
Computer-Aided Optimization of Resource-Efficient and Flexible Power-to-Syngas Processes

Dissertation

zu Erlangung des akademischen Grades

Doktoringenieur

(Dr.-Ing.)

von **M.Sc. Andrea Maggi**

geboren am 10.02.1992 in Cernusco sul Naviglio (Italien).

Genehmigt durch die Fakultät für Verfahrens- und Systemtechnik der
Otto-von-Guericke-Universität Magdeburg.

Promotionskommission:

<i>Vorsitz</i>	apl. Prof. Dr.-Ing. habil. Gabor Janiga
<i>Gutachter</i>	Prof. Dr.-Ing. Kai Sundmacher
<i>Gutachter</i>	Prof. Dr.-Ing. Achim Kienle
<i>Gutachter</i>	Prof. Dr.-Ing. Jens Bremer

Eingereicht am 28.01.2025

Promotionskolloquium am 27.03.2025

Abstract

The intermittent nature of renewable energy sources is forcing engineers to solve chemical process design tasks with innovative computer-aided process engineering (CAPE) tools. The aim of this thesis is to extend and implement optimization approaches for the synthesis, sizing and control of potentially interesting plant concepts which make use of an unsteady supply of renewable energy and potentially limited feedstock. In particular, synthesis gas, or syngas, is addressed, as it constitutes a relevant intermediate for the production of chemicals and synthetic fuels. A gap in the existing literature can be reported on the systematic analysis of process candidates for the separation of a raw syngas mixture from inert and unreacted gases, such as methane, carbon dioxide and water. First, multi-objective and superstructure optimization tools are used to determine the topology, energy input, and carbon efficiency of candidate reactor-separator layouts that attain either minimum absolute carbon emissions, with or without green renewable power, or minimum total energy demand. The thermodynamic study opens the ground for flexibility analyses. In this framework, a novel power-to-syngas plant concept for Fischer-Tropsch makeup gas specification is identified with the optimization tool previously developed. The new plant configuration is designed to increase the atomic efficiency of a water electrolyzer by valorizing both of its outlets. Hydrogen is fed to a reverse water-gas shift reactor when renewable energy is available. Oxygen, part of which is stored beforehand, is fed to an adiabatic tri-reforming reactor. Both reactors operate together to stabilize the syngas production rate and composition under the fluctuation of renewable energy. Such case is thus used to benchmark an optimal control approach for the stabilization of syngas specifications. The discussion then expands to the general implications of process flexibility in system design, supported by results from multi-period optimization of the design and operation of a highly electrified methanol plant powered by local renewable energy. This novel application of the method to a detailed model of the entire process-system aims to ensure the identification of a feasible design at the maximum profit and constitutes a powerful method to screen different extents of flexibility. When the plant is operated at maximum flexibility, without buffering strategies in place, the base load must be provided by external electricity: its purchase price is a determining factor for the competitiveness of this plant concept as an alternative to a plant operated at steady-state with large buffering devices and an oversized renewable energy park and electrolyzer.

Zusammenfassung

Die intermittierende Natur der erneuerbaren Energiequellen zwingt die Ingenieure, neue Probleme mit innovativen CAPE-Methoden für die Systementwicklung zu lösen. Ziel dieser Arbeit ist die Erweiterung und Implementierung von Optimierungsverfahren für die Synthese, Dimensionierung und Steuerung potenziell interessanter Anlagenkonzepte, die eine un stetige Versorgung mit erneuerbarer Energie und potenziell eingeschränkte Ressourcen nutzen. Insbesondere wird das Synthesegas –Syngas– betrachtet, da es ein relevantes Zwischenprodukt für die Herstellung von Chemikalien und synthetischen Brennstoffen darstellt. Eine Lücke in der Literatur besteht in der systematischen Analyse von Prozesskandidaten für die Trennung eines Synthesegasgemisches von inerten und nicht reagierten Gasen wie Methan, Kohlendioxid und Wasser. Zunächst werden mit Hilfe von Mehrziel- und Superstruktur-Optimierung der Energieeinsatz und die Atomeffizienz von Reaktoren-Separatoren Kandidaten Layouts bestimmt, bei denen entweder die minimalen Kohlenstoffemissionen oder der minimale Gesamtenergiebedarf erreicht werden. Die thermodynamische Studie eröffnet den Weg für Flexibilitätsanalysen. In diesem Rahmen wird ein neuartiges Power-to-Syngas Anlagenkonzept für Fischer-Tropsch mit dem bestehenden Optimierungstool identifiziert. Die neue Anlagenkonfiguration ist darauf ausgelegt, die Atomeffizienz eines Wasserelektrolyseurs zu erhöhen, indem seine beiden Ausgänge genutzt werden. Wasserstoff wird einem RWGS Reaktor zugeführt, wenn erneuerbare Energie verfügbar ist. Sauerstoff, der zum Teil vorher gespeichert wird, wird einem adiabatischen Tri-Reforming-Reaktor zugeführt. Beide Reaktoren arbeiten zusammen, um die Syngasproduktionsrate und -zusammensetzung unter den Schwankungen der erneuerbaren Energie zu stabilisieren. Dieser Fall wird daher zum Benchmarking eines optimalen Steuerungsansatzes für die Stabilisierung der Synthesegasspezifikationen verwendet. Die Diskussion wird dann auf die allgemeinen Auswirkungen der Prozessflexibilität bei der Systemauslegung ausgedehnt, unterstützt durch Ergebnisse aus der Multiperiodenoptimierung der Auslegung und des Betriebs einer hoch elektrifizierten Methanolanlage, die mit lokaler erneuerbarer Energie betrieben wird. Diese neuartige Anwendung der Methode auf ein detailliertes Modell des gesamten Prozesssystems kann die Identifizierung eines machbaren Entwurfs mit maximalem Profit gewährleisten und stellt eine leistungsfähige Methode zur Untersuchung verschiedener Flexibilitätsgrade dar. Abschließend kann ein Kompromiss zwischen Pufferung und flexiblem Betrieb die maximale Profitabilität der Anlage bestimmen. Wenn die Anlage mit maximaler Flexibilität betrieben wird, ohne dass Speichervorrichtungen vorhanden sind, muss die Grundlast durch externen Strom bereitgestellt werden: Sein Einkaufspreis ist ein entscheidender Faktor für die Wettbewerbsfähigkeit dieses Anlagenkonzepts als Alternative zu einer stationär betriebenen Anlage mit großen Speichervorrichtungen und einem überdimensionierten erneuerbaren Strompark und Elektrolyseur.

Contents

1	Introduction	1
1.1	Background challenges	1
1.2	The importance of Computer Aided Process Engineering (CAPE) in decision-making	3
1.3	Guiding research questions	6
2	Technological background	8
2.1	The applications of syngas in industry	8
2.2	Chemical reactors for syngas production: state of the art	9
2.3	Carbon dioxide and biogas reformers: novel reforming concepts	10
2.4	Water electrolyzer	12
2.5	Sustainable feedstock	14
2.6	Separation methods	15
2.7	Optimization of Power-to-X systems	16
2.8	Optimization in process synthesis	17
2.9	Optimization for sizing and control of flexible plants	19
2.10	Novelty and relevance of this thesis	21
2.11	Sustainability of the electrical power supply in optimization	23
2.12	Terminology in this thesis	23
3	Retrofitting a steam reforming plant for sustainable syngas production	24
3.1	Introduction	24
3.2	Superstructure of reactor-separator system	26
3.2.1	Reactors operating conditions, plant feedstock and outlets	26
3.2.2	Exclusion of the water-gas shift reactor for pure hydrogen production	27
3.2.3	Feasible separation methods	28
3.2.4	Steam reforming of methane: separation sequence	28
3.2.5	RWGS reactor: separation sequences	29
3.3	Modeling approaches	29
3.4	Optimization problems	30
3.4.1	The cost of carbon efficiency	33
3.5	Multi-objective optimization by combination of Objective (A) and (B): renewable power is available	34
3.5.1	Minimum absolute carbon emissions with renewable power - Objective (B) .	36
3.5.2	Separation train: optimal topologies - Objective (B)	38

3.5.3	Minimum absolute carbon emissions with renewable power - Objective (A)	40
3.5.4	Intermediate solutions: weight factor within the interval 0.21 - 0.62	44
3.6	Multi-objective optimization by combination of Objective (A) and (B): electricity from powerplant	45
3.6.1	Exclusion of the steam reformer: operating electrolysis and RWGS with powerplant electricity	46
3.7	Inclusion in the objective function of the carbon dioxide stream recycled from combustion outlets	47
3.8	Conclusions and outlook	49
3.9	Chapter summary	50
4	MILP approach for the analysis and screening of large Power-to-Syngas reactor-separator networks	52
4.1	Introduction and background	52
4.2	Novelty and general system framework	53
4.3	System description	55
4.4	Methods	57
4.4.1	General modeling assumptions for reactors and separators	57
4.4.2	Modeling of reactors	57
4.4.3	Mass balances	57
4.4.4	Energy balances	59
4.4.5	Modeling of separators	60
4.4.6	Mass balances	61
4.4.7	Energy balances	62
4.5	Modeling of interconnections	66
4.5.1	Mass and energy balances: mixture block	67
4.5.2	Motivation for the modeling approach	68
4.5.3	Logical constraints	70
4.5.4	Formulation of the optimization objectives	71
4.6	Feedstock: biogas	73
4.6.1	Dealing with redundancies	74
4.6.2	Coexistent reactors, non-redundant separators. Minimum total energy	75
4.6.3	Coexistent reactors, non-redundant separators. Minimum thermal energy	78
4.6.4	Heat recovery: combustion of excess bio-methane	81
4.6.5	Single reformer, non-redundant separators. Minimum total energy	83
4.7	Feedstock: carbon dioxide	85
4.8	Conclusions and outlook	89
4.9	Chapter summary	90
5	Process flexibility (I) - Optimal control of syngas production for Fischer-Tropsch applications	92
5.1	Introduction	92

5.2	Plant layout and dynamics	93
5.2.1	Plant control	97
5.2.2	Pre-definition of the renewable power ramp: case relevance	99
5.3	Modeling assumptions on a plant level	100
5.4	General reactor modeling approach	101
5.5	Reactor design	102
5.5.1	Design of TRI	103
5.5.2	Design for RWGS	104
5.5.3	Oxygen utilization	105
5.6	General plant modeling approach	105
5.7	Optimal control for the plant model	106
5.7.1	Numerical time integration	107
5.7.2	Optimization setting and initialization	108
5.7.3	Comparison between parareal and a fine integrator: computational frame- work	109
5.7.4	Numerical results	110
5.8	Conclusions and outlook	113
5.9	Chapter summary	114

6 Process flexibility (II) - Multi-period design optimization of a Power-to-Methanol

Process	116	
6.1	Introduction	116
6.1.1	Scaled profitability	119
6.2	Methodological background	120
6.2.1	The methanol synthesis	121
6.3	Plant layout	122
6.4	Power supply and optimization setups	123
6.4.1	Design and operating variables	126
6.5	Mathematical models of process units	127
6.5.1	SOEC	127
6.5.2	Reactors	129
6.6	Optimization objectives, scenarios and solver	130
6.6.1	Objective functions	130
6.6.2	Case-studies	132
6.6.3	Formulation of multi-period design optimization problem	133
6.6.4	NLP solver	136
6.7	Optimization results	136
6.7.1	Results for CASE.FLEX: maximum flexibility without heat integration	137
6.7.2	Results for CASE.BUFF: steady-state operations without heat integration	141
6.7.3	Role of the external electricity price on the competitiveness of the flexible process	144

6.7.4	Results for CASE.EFF: maximum efficiency for B.I and B.II, no heat integration	145
6.7.5	Results for CASE.FLEX.HI: maximum profit with heat integration	146
6.7.6	Desalination of seawater	146
6.8	Discussion	147
6.9	General remarks and outlook	149
6.10	Chapter summary	149
7	Conclusions and impact of the thesis	151
A	Appendix A	
	Supplement to Chapter 3	154
A.1	Equilibrium reactors and condensers	154
A.2	Modeling of surplus methane	154
A.3	Inclusion in the objective function of CO ₂ recycling stream from combustion gases .	155
B	Appendix B	
	Supplement to Chapter 4	157
B.1	Modeling of interconnections between separators and component nodes	157
	B.1.1 Interconnection of consecutive mixture blocks	157
	B.1.2 Replicas of downstream separation systems	158
	B.1.3 Substance nodes	160
	B.1.4 Outlet and syngas nodes	161
C	Appendix C	
	Supplement to Chapter 5	163
C.1	Process synthesis	163
C.2	Reaction rates for tri-reforming of methane	164
C.3	Reaction rates for RWGS	165
C.4	Overall heat transfer coefficient RWGS	166
C.5	Graphical results optimal TRI and RWGS configurations	167
D	Appendix D	
	Supplement to Chapter 6	169
D.1	Wind park parametrization	169
	D.1.1 Wind turbine power curve	169
	D.1.2 Monthly wind velocity	169
D.2	Mixers, heat exchangers, compressors, flash separator	170
	D.2.1 Mixers, heat exchangers, compressors	170
	D.2.2 Flash separators	171
D.3	System models parametrization	172
	D.3.1 Modeling of SOEC	172
	D.3.2 Modeling of flash separator F2 (methanol recycle loop)	174

D.3.3	Source term σ_α in reactor models	175
D.3.4	Reaction rates for reverse water-gas shift (RWGS)	176
D.3.5	Reaction rates for methanol reactor (METHL)	177
D.3.6	Analytical solution for the compressibility factor in gas phase (METHL) . . .	178
D.3.7	Analytical solution for the compressibility factor in gas phase (COMPR) . . .	179
D.3.8	Overall heat transfer coefficient U (METHL)	179
D.3.9	Interstitial velocity for tubular reactors (METHL and RWGS)	181
D.4	Cost functions	182
D.4.1	Tubular reactors	182
D.4.2	SOEC	183
D.4.3	Compressor	183

Bibliography

186

List of symbols

Greek alphabet

$\alpha_{\text{eff}}, \alpha_w$	heat transfer coefficient (effective, wall)	$\text{W m}^{-2} \text{K}^{-1}$
$\alpha_{\text{mix,phase}}, \alpha_{\alpha,k}$	EOS coeff. (mixture, pure α at node k)	
$\beta_{\text{mix,phase}}, \beta_{\alpha,k}$	EOS coeff. (mixture, pure α at node k)	
$\gamma_{\text{mix,phase}}, \gamma_{\alpha,k}$	EOS coeff. (mixture, pure α at node k)	
γ	ratio of specific heats at constant p and v	
ϵ	void fraction in packed-bed reactors	$\text{m}_{\text{bulk}}^3 \text{m}_{\text{reactor}}^{-3}$
ζ_{α}	molar fraction of α	
η	generic efficiency	
η_{PP}	power plant efficiency	
$\eta_{\text{PtCH}_3\text{OH}}$	power-to-methanol efficiency based on LHV	
θ_j	extent of reaction j / feed flowrate	
$\lambda_{\text{mix}}, \lambda_{\text{bed}}, \lambda_{\text{cat}}$	thermal conductivity (gas mixture, bed, catalyst)	$\text{W m}^{-1} \text{K}^{-1}$
Λ_r	effective radial thermal conductivity	$\text{W m}^{-1} \text{K}^{-1}$
$\Lambda_{(1,2,3,4)}$	lumping factors for SOEC models	
μ_{mix}	average viscosity in bulk phase	Pa s^{-1}
$\nu_{\alpha,k}$	stoichiometric coefficient of component α in reaction k	
ξ_{F}	ratio between vapor and feed molar flowrate (flash)	
$\xi_{\text{A/(B,C)}}$	split factor to separation task A/(B, C)	
(π)	superscript denoting variables shared across periods	
Π_i	i th period	
$\rho_{\text{cat}}, \rho_{\text{gas}}$	density (catalyst, gas)	$\text{kg}_{\text{cat}} \text{m}_{\text{cat}}^{-3}$
σ_{α}	(overall) molar generation rate for single component α	$\text{mol kg}_{\text{cat}}^{-1} \text{s}^{-1}$
τ_i	set of discretized time steps collected in period i	
\mathcal{T}	final integration time	s
Φ_{D}	vector of (structural) optimization variables	various
χ	conversion in chemical reaction	
ω	pseudo price for multi-objective optimization	
ω_j	probability of period j	

Latin alphabet

$a_{\text{mix,phase}}$	EOS parameter (mixture, binary interaction of pair i - j ,	
$a_{i,j,\text{phase}}$	pure component α)	
$a_{\alpha,\text{phase}}$		
A	kinetic pre-exponential factor	various
\mathbf{AE}, \mathbf{AE}	algebraic equation (single, set)	various
$A_{\text{EOS,phase}}, A_{\text{EOS},\alpha,k}$	EOS parameter (mixture, pure component α)	
$A_{\text{SOEC}}^{(\pi)}, A_{\text{cross}}$	area SOEC, cross sectional area reactor	m^2
$b_{\text{mix,phase}}$	EOS parameter (mixture, binary interaction of pair i - j ,	
$b_{i,j,\text{phase}}$	pure component α)	
$b_{\alpha,\text{phase}}$		
$B_{\text{EOS,phase}}, B_{\text{EOS},\alpha,k}$	EOS parameter (mixture, pure)	
bed	bed (adsorption)	
C_{gas}	gas concentration (for reactors, in bulk phase)	$\text{mol}_{\text{gas}} \text{m}^{-3}$
$C_i^{(\pi)}, \dot{C}_i^{(\pi)}$	cost of unit i , annualized	$\text{€}, \text{€ year}^{-1}$
$\dot{C}_{22,\text{CH}_3\text{OH},\Pi_j}$	annualized revenue at period j	€ year^{-1}
$\tilde{C}_{\text{p,gas}}, \tilde{C}_{\text{p},\alpha}$	molar heat at constant pressure (bulk, α)	$\text{J mol}^{-1} \text{K}^{-1}$
COP, COP _{id}	coefficient of performance (ideal)	
CRE	climate related energy	
$D_{\text{cat},k}^{(\pi)}, D_{\text{T},k}^{(\pi)}$	diameter of reactor k (catalyst, reactor tube)	m
DE, DE	differential equation (single, set)	various
DEN	denominator in the rates of reaction	
des	desorption	
DOF	degree of freedom	
E	kinetic activation energy	J mol^{-1}
ev	evaporation	
f	generic function	various
$\dot{H}, \dot{H}_{\text{in/out}}$	flow enthalpy (generic, inlet/outlet)	J s^{-1}
$\tilde{H}_{\alpha}, \tilde{H}_{i,\alpha}$	molar enthalpy of component α (generic, i -th stream)	J mol^{-1}
$\Delta H_{\text{R}}, \Delta H_{\text{ev}}$	enthalpy of reaction, latent heat of vaporization	J
$i^{\text{SOEC}}, i_{\text{av,cat/an}}$	current density SOEC (total, exchange cathode/anode)	A m^{-2}
k_i	kinetic constant of reaction i	various
K_{α}	adsorption constant of species α	various
$K_{\text{eq},i}$	equilibrium constant of reaction i	
$L_{\text{T},k}^{(\pi)}$	tubes length of reactor k	m
LB, UB	vector of bounds to variables (lower, upper)	various
LB ^(π) , UB ^(π)	vector of bounds to design variables (lower, upper)	various
LB , UB	vector of bounds to operating variables (lower, upper)	various

LHV	low heating value	J mol^{-1}
M_α	molecular weight of component α	g mol^{-1}
M	big M for linear programming	
N	number of units (MILP formulation)	
$N_{\text{T,METHL}}^{(\pi)}$	number of tubes in the methanol reactor	
$\dot{N}_{\text{tot},i}, \dot{N}_{i,\alpha}$	flowrate (stream i , component α in stream i)	mol s^{-1}
NP	number of periods	
ops	operation	
$p, p_{\text{in/out},k}$	total pressure (generic, inlet or outlet unit k)	Pa
$\tilde{q}_{\text{des},\alpha}^*$	molar heat of desorption for component α	J mol^{-1}
\tilde{q}	thermal power per unit of molar flowrate	J mol^{-1}
\dot{Q}	total thermal duty demand (LP/MILP formulations)	W
\dot{Q}_{E}	thermal duty to generate electricity in a powerplant of given efficiency	W
\dot{Q}_{CL}	cold duty demand for the generic condenser CL	W
r	H_2 -to-CO ratio	
R_i	molar reaction rate for reaction i	$\text{mol kg}_{\text{cat}}^{-1} \text{s}^{-1}$
R_{gas}	universal gas constant	$\text{J mol}^{-1} \text{K}^{-1}$
S	split factor	
t	time	s
$T, T_{\text{in/out},k}, T_{\text{cool,METHL}}$	temperature (generic, in/out unit k , coolant)	K
U	overall heat transfer coefficient	$\text{W m}^{-2} \text{K}^{-1}$
v, v_{wind}	interstitial velocity (reactor), wind velocity	m s^{-1}
$V_{\text{tot,SOEC}}, V_i$	SOEC voltage (total, single i -th contribution)	V
$\dot{W}_{\text{tot}}(t), \dot{W}_{\text{tot},j}, \dot{W}_k$	power input (at time t , average period j , to unit k)	W
\dot{W}_{id}	ideal power input	W
\tilde{w}	electrical power per unit of molar flowrate	J mol^{-1}
$\mathbf{x}^{(\pi)}, \bar{\mathbf{x}}^{(\pi)}$	DOFs shared across periods (vector, matrix)	
$\tilde{\mathbf{x}}, \bar{\tilde{\mathbf{x}}}$	DOFs not shared across periods (vector, matrix)	
z	axial coordinate	m
$Z_{\text{mix,phase}}, Z_{\alpha,\text{phase},k}$	compressibility (mixture, α at node k)	

Process identifiers

AA	amine absorption
AD	anaerobic digestion
AEL	alkaline electrolyzer
CD, cond	condensation
CL	cooler
COMB	catalytic oxidation of methane
CPR	train of adiabatic compressors

CR, CRYO	cryogenic operation
DR	methane dry reforming
EL	electrolyzer
F	flash separator
FTS	Fischer-Tropsch synthesis
HE	electrical heat exchanger
METHL	methanol reactor
MIX	mixer
MS	membrane separator
PEM, PEMEL	proton exchange membrane electrolyzer
POX	methane partial oxidation
R	refrigerant
RE, REN	renewable resource (wind power)
reg	regeneration
RMETH	reverse methanation reaction
RWGS	reverse water-gas shift reactor or reaction
S	splitter
SR	methane steam reforming
SOEC	solid-oxide electrolyzer
TPSA	temperature-pressure swing adsorption
TR	throttle valve
TRI	tri-reforming of methane
TSA	temperature swing adsorption
VPSA	vacuum pressure swing adsorption
WGS	water-gas shift reaction

Introduction

1.1 Background challenges

Nobel laureate Svante Arrhenius' first theorization of the greenhouse effect of carbon dioxide in 1896 [1] failed to generate interest among the scientific peers of his time [2]. Since then and for several decades, these findings have been ignored. It was only with the second half of the 20th century, as several large communities on the planet witnessed their own metamorphosis into consumer societies, that the correlation between the ongoing global warming and greenhouse gas (GHG) emission became matter of systematic studies and monitoring. In the 1980s, newly established international organizations meant to observe and predict the trends of global warming conferred public resonance to these themes. The Intergovernmental Panel on Climate Change (IPCC), a hub between policy makers and the scientific community, was founded. This organization has more recently been involved in monitoring activities to support policy makers in their goal of keeping global warming well below 2 °C and possibly below 1.5 °C, compared to the pre-industrial levels, as a result of the Paris Agreements [3, 4]. However, it has recently been reported that this recommended threshold has been exceeded in 2024 by a temperature increase of 1.6 °C compared to the pre-industrial era [5]. Human-induced global warming has caused changes in the climate, land and ocean temperatures, and there is substantial evidence of an increase in frequency and intensity of extreme meteorological events, such as precipitations and droughts in the mediterranean region [6]. Ecosystems are substantially affected by these anomalies, which clearly jeopardize the agricultural production yield, introducing unevenness in the distribution of wealth. A clear example can be represented by the effect of the severe drought in Europe (2022), causing a drop of about 15 % in yield for grain maize, soybean and sunflowers [6], and a consequent chain increase in prices.

In this context, the European dependency on delocalized and expensive fossil fuels forces a fast pace-shift towards alternative supplies. According to the Environmental Protection Agency of United States (EPA), 25 % of the global GHG emissions are generated for electricity and heat production, 21 % and 14 % by the industrial and transportation sector, respectively [7].

Consequently, among the options against global warming enumerated in the ICPP Summary for Policymakers 2022, the use of wind and solar energy for electricity generation may have the largest impact on the path towards the targeted reduction of net emissions by 2030, overall by circa 8 GtCO_{2,eq} yr⁻¹, followed by fuel switching in the industry sector, by 2 GtCO_{2,eq} yr⁻¹ (Figure SPM.7 in [8]). All this considered, the electrification of relevant industrial sectors, in combination

with the defossilization of feedstock and decarbonization of energy supply, constitute important mitigation approaches.

Stemming from this multifaceted background, Power-to-X (P2X) technologies are intended to attain substantial mitigation effects by converting renewable electrical power and a sustainable carbon source into climate-neutral synthetic fuels or chemicals. An important P2X application is the supply of E-fuels to the aviation, shipping and heavy duty transportation sector, which cannot be otherwise electrified. Furthermore, spikes in the production of renewable electricity can be conveniently stored as liquid chemicals and fuels (Power-to-Liquid), or gas, to be injected into transportation grid (Power-to-Gas).

In P2X technologies, hydrogen assumes a central role as energy carrier and reducing agent in chemical processes. This is reflected by the unprecedented momentum in related policies and projects launched around the world. The main focus is on increasing the capacity of electrolyzers and building an infrastructure to deliver hydrogen to industrial sites, for transportation and for heating residential and commercial buildings. In the manufacturing of chemicals and fuels, a more sustainable carbon source must replace fossil precursors fed to the process system, then reduced by green hydrogen to the desired product.

One option is the use of carbon dioxide, captured from the atmosphere (air-capture) or obtained from the anaerobic digestion of biomass, then reduced by green hydrogen to carbon monoxide, thus contributing to the synthetic gas mixture (syngas), an essential intermediate for further downstream processes. Syngas consists of carbon monoxide and hydrogen at a well defined molar ratio, function of its target application. Some authors define syngas as a ternary mixture, also including carbon dioxide. Alternatively, syngas can be obtained sustainably from the oxidation of biogenic methane or biomass in Renewables-to-X processes (R2X). Besides green projects, blue technologies based on carbon capture and utilization have been proposed as prompt industrially relevant solutions in conjunction with the generation of renewable hydrogen.

This brings us to a fundamental problem: the urgency imposed by policy makers on businesses to comply with energy transition scenarios, and the consequent attempt to generate valid solutions on the short term, such as hybrid approaches. These solutions still benefit from the know-how gained in the past, from the economy of scale, and from low fixed costs. However, they heavily rely on operating costs related to the import of fossil gas, and are thus vulnerable to international events. On the contrary, highly electrified processes rely on the fixed costs of renewable power production, which are dependent on domestic market regulations [9]. Upfront fixed costs for the installation of wind and solar power farms constitute the dominant contribution, up to 75 % of the total costs. As a benchmark, fixed costs of gas-fired combined cycle powerplants is less than 10 % of the total, the remaining share being constituted by fixed operating costs such as fuel supply. The shift in progress towards renewable supply will thus determine a dominance of fixed costs in the future, requiring deep modifications in the established business models [9], although a steady fall trend in the installation costs involved in the generation of renewable power is reported, up to 85 % and

55 % for solar and wind between 2010 and 2019, respectively [10]. Low upfront installation costs may enable competitive delocalization strategies based on off-grid renewable-power.

As commented in a recent study issued by the International Renewable Energy Agency IRENA (2022) on renewable power generation and utilization in the European market [11], the window of opportunities that fossil gas-based technologies benefited from in the transition towards a more sustainable economy is rapidly closing, as fixed cost of renewable power generators drop and the price of natural gas increases. Nonetheless, state-of-the-art reforming and partial oxidation plants for the generation of syngas rely on stable operations at their nominal load, whereas, the availability of renewable resources forces P2X processes to cope with the unstable, intermittent nature of their power supply. This clearly expands the interest on balancing strategies of the volatility of electric power, such as sector coupling, batteries, hydrogen storage [11]. Nonetheless, buffering devices integrated in the conversion system for the generation of chemicals or fuels add an important contribution to the overall leveled manufacturing cost of the product, also in terms of renewable energy consumption which cannot be re-generated, e.g., for the compression or liquefaction of hydrogen to the storage requirements. Alternatively, the P2X process can be designed and operated to offer a flexible response to the instability of its own power supply, making the best use of excess supply from the grid, and reducing its operating regime if the supply is scarce. Flexible P2X systems have undersized buffers or operate in their absence.

In the next section, the role of computer-aided chemical engineering is outlined and the scope of this thesis is framed around the aforementioned aspects defining the grand challenges introduced by the ongoing energy transition scenarios.

1.2 The importance of Computer Aided Process Engineering (CAPE) in decision-making

The market demand for production under stringent quality and environmental constraints require unprecedented modifications in the technological proposal for production processes and for existing plants. On a daily basis, we see solid business concepts being challenged and conventional companies closing or restructuring entire production lines, often starting feasibility studies to be ahead of the competition in their niche for years to come. In parallel, the fast-pace scouting of emerging technologies and startups potentially enables larger industrial players to give body to paradigm shifts in production applications. The computational power of modern computers combined with sharp problem formulations should be used to unlock promising opportunities, and to safely navigate through the degrees of freedom, in terms of process synthesis, design and operations. In addition, as the pathways to new products such as E-fuels and hydrogen require disruptive infrastructure changes and are initially seeded with significant capital raises, methodologies supporting each project stage play an important role, demonstrating to stakeholders and institutions that the product can be certified to international and national standards. Hence

the importance of CAPE, short form for computer-aided process engineering, becomes clear in the systematic multiscale prediction, description and analysis of complex systems: CAPE focuses on algorithms, procedures and frameworks, which automate the operating and design decisions [12]. At the nano- and micro-scale, material and catalyst modeling allows for a satisfactory description and prediction of novel systems by means of material property predictors, micro-kinetic and heterogeneous models, which can determine the sensitivity of operating regimes on the selectivity of an entire unit operation. Up to the meso-scale, by means of discretized domains it is possible to debottleneck and improve the design of what often constitutes a major contributor to the energy requirement: the catalytic reactor, either cooled or heated, thus possibly avoiding large compression and recycle-compressor power demands. A systemic analysis by means of partial differential equations (PDE) is important to scale-up reactors and to predict implications of process operation [12]. At the meso- and macro-scale for industrial production, given all unit operation specifications, the use of process simulators is of great importance to determine a realistic overall plant efficiency and compare possible scenarios. PDE are often implemented in computational fluid dynamic simulation softwares, although such calculations often underlay proprietary vendors' offers, not disclosed to clients in the selection of the project, who are primarily interested in understanding energy requirements for nominal inputs and outputs, and can thus justify budget requests. Therefore it is often the case that nano- and micro-scale are decoupled from meso- and macro-scale at the plant level in large implementations, due to the fact that single unit operations belong to confidential proprietary packages, not accessible to business developers or engineering, procurement and construction companies. In some cases however, large plant sections belong to a single licensor, which has adopted CAPE tools to integrate micro- and macro-scale to determine an efficient and profitable solution. All this considered, computers can support decision making by providing solutions to simulation and optimization problems in process synthesis and operations.

In a preliminary process design phase, engineering teams need to compare alternative conceptual flowsheets. These activities have a major impact on the overall project costs, although it is estimated that only 15-20% of the total funds are devoted to this [13]. A given reaction step or feedstock can be the decisive factor on the competitiveness of the project in the free market. The evaluation of alternatives requires the selection of a suitable mathematical approximation for the unit operations and subsequently to carry out analyses based on project performances. The selection and monitoring of relevant key performance indicators (KPIs) plays a crucial role. A layer of complexity may be introduced by the typical feature of conflicting trends for different KPIs, which can be considered in the form of Pareto-optimal sets. A typical example is the inverse proportionality between distillation reboiler duty, related to energy costs, and capital cost. Process synthesis by complete enumeration of alternative layouts by KPIs evaluation can be performed directly in dedicated process simulation environments. Dedicated softwares typically offer a user-friendly interface to combine unit-blocks sequentially and assist in attaining sequential or plant-wise simultaneous solutions of equation sets, invoking thermodynamic packages and allowing a certain extent of customization for unit internals. The advantage in such CAPE simulation tools is undoubtedly the fact that they are state-of-the-art environments, allowing for relatively agile

management of detailed thermo- and fluid-dynamics, determining reliable KPI values. On the other hand, they may be unsuitable when the search space across process opportunities is large, and when a considerable degree of freedom on feedstock or product range exists, which in simulation software is addressed by means of sensitivity analyses. In these cases, the complete enumeration of single-layout evaluations based on forward simulations must be substituted by superstructure optimization, where CAPE can assist with different algorithmic approaches. An overlaying mathematical optimization routine can support the systematic evaluation of KPIs and boundary conditions calling for forward-simulations of candidate layouts implemented in dedicated simulation softwares. Optimization routines may be offered within the simulation software package itself, although this may lead to unsatisfactory results due to the high nonlinearity of typical problems and the impossibility to optimize for structural variables. As a result, many authors have developed frameworks to let an external, reliable superstructure optimization routine call a process simulation run within an established simulation software [14, 15, 16, 17, 18]. These approaches are generally computationally expensive, as they imply multiple calls to detailed, sequential plant simulations at each optimization iteration, although they are extremely attractive when the number of process alternatives is relatively small and high-fidelity outputs are required. However, large search domains in terms of number of layouts are common in the early stages of the project when little information is available about the internals of the unit blocks. Here, it is often required to describe a unit operation with simple linear models, especially when vendors are only willing to share CAPEX and nominal operation duties, feedstocks requirements and outlets. Such high-level descriptions may be sufficient to identify a single plant candidate, or a subset, that merit further investigation based on more accurate models.

In the next project stage, CAPE traditionally supports decision-making in equipment sizing at nominal loads in detailed process simulations for the identification of more accurate budgetary offers from vendors. Process flow and piping & instrumentation diagrams are the reference for the front-end engineering phase, where preliminary simulation results allow clients and procurement companies to sharpen the overall investment requirement and total installed cost, and to constitute a solid base for tendering. Structural analysis, piping rack design and stress tests can be now performed by dedicated CAPE applications for the civil engineering. Also at this project stage, our times impose to re-frame the approach we adopt in defining detailed process specifications. Renewable feedstocks and electrification introduce temporal variability in the supplies. Novel CAPE process design tools must assist engineering teams in identifying appropriate trade-offs in sizing and resource management while meeting feasible operations. This aspect will be addressed in a later chapter that aims to fill the gap left by the current practice of oversizing process units at peak supply.

Once the plant is operational, control softwares ensure that safety and quality are attained. As individual control actions often affect several process variables, old controllers based on relays and contactors have gradually been replaced by digital CAPE tools that ensure a flexible and fast response action on a single actuator (PLC, programmable logic controller) or a more structured response involving multiple actuators and based on high-level programming languages (DCS,

distributed control system). Computational speed is key to a successful implementation, even more when transient load regimes become the normal operation mode in upcoming scenarios dominated by an intermittent renewable power supply.

1.3 Guiding research questions

This thesis is dedicated to the computer-aided modeling and optimization of Power-to-Syngas processes and aims at contributing to the extension of existing CAPE methodologies for process optimization on a plant scale. Furthermore, after formalization of the technological background in Chapter 2, these tools are adopted to address the following research questions relevant to the energy transition:

1. What is the impact that retrofitting has on the energy consumption of an existing natural gas reforming plant in the context of flexible plant operations?
2. What is the energy consumption of optimal reactor-separator sequences for the production of syngas from biogas or air-captured CO₂, selected from a large number of candidates?
3. How does the inherent intermittency of renewable power influence the design and operation of a Power-to-X plant?
4. What is the trade-off between buffering and process flexibility?

Both questions 1 and 2 fall within the domain of process synthesis, to which methodologies for screening system alternatives belong. For this reason, they are considered in the first part of this thesis in Chapter 3 and 4, respectively. In particular, Chapter 4 formalizes, generalizes and expands on methodological aspects more compactly introduced in Chapter 3. Although the inclusion of fixed costs is of uttermost importance in the viability evaluation of real projects, as discussed in the previous Section 1.2, the first part of this thesis does exclusively account for total energy and power consumption. In fact, solutions which do currently have no room of applicability at their current market value, especially due to the low TRL level, may have a profound impact on the technical offer in the long run as CAPEX will drop with mass manufacturing. Also the cost of feedstock is subject to market availability, and can vary over time. For instance, biogenic carbon dioxide is necessary for the production of green E-fuels, but its demand for E-fuel projects will increase in likely future market scenarios, causing its availability to drop and price to increase. Furthermore, retrieving accurate cost data for individual pieces of equipment from the available literature can be problematic, especially when the operations involve proprietary technologies or at a low stage of development, as is the case for a number of reactors and separators included in the superstructure formulation presented in Chapter 4. Therefore, a cost-based analysis within a methodological and scientific framework of this type may require the introduction of a considerable extent of

uncertainty, due to the estimation of future market price of emerging technologies, consequently possibly excluding interesting technical opportunities based on thermodynamics: market and policy makers have a strong influence on the economic viability of a good, a product or a process by means of subsidies or simply the law of demand and supply.

Question 3 is addressed in the second part of this dissertation which makes use of distributed models for the more accurate description of given plant layouts. First, Chapter 5 shows how the intermittency of renewable power can be leveraged by the use of both product streams from a water electrolyzer, provided that the system is optimally controlled. This flexible plant concept for the production of a stable syngas supply for Fischer-Tropsch synthesis, inherited from Chapter 4, constitutes a suitable benchmark to test the potential of a fast integrator for optimal control applications. From a methodological perspective, the implementation of `pararea1` as underlying integrator to optimally stabilize the syngas flowrate over time is proposed for the first time in this technical application relying on DAE system-description: the chapter intends to compare `pararea1` with a fine integrator operating on the whole temporal domain.

Finally, Chapter 6 continues the elaboration of Question 3 by showing the impact of renewable energy on design and operation decisions for power-to-X plants. A novel application of multi-period design optimization [19] constrained by a detailed, distributed model of an entire Power-to-Methanol plant is discussed: this methodological framework is proposed to identify the cost-optimal sizing and feasible operation of a flexible plant running on intermittent renewable energy. This case is compared to a plant running on a single, annually averaged renewable load secured by buffering devices, thus addressing Question 4.

The case study presented in Chapter 6 opens the floor for concluding remarks on the implications of process flexibility, then elaborated in Chapter 7, which binds the research topics to a common ground and concludes the dissertation.

Technological background

2.1 The applications of syngas in industry

In the 19th Century, syngas was provided from coal gasification and directly utilized as a fuel for heating and lighting. However, it was due to the scarcity of natural gas and oil and to the huge demand for chemicals and fuels that alternative chemical synthesis routes from this mixture were identified between the World Wars: the ammonia synthesis from hydrogen and nitrogen at high pressures was discovered by Haber and Bosch (1910), Fischer and Tropsch identified and implemented the synthesis of syngas to liquid hydrocarbons on iron catalyst (1923), routes to methanol and other alcohols were hereafter identified, as well as the hydroformylation of olefins to aldehydes in 1938 [20]. Table 2.1 summarizes typical downstream processes and temperature/pressure ranges.

Table 2.1.: Syngas downstream applications, molar ratios, temperature and pressure requirements [21].

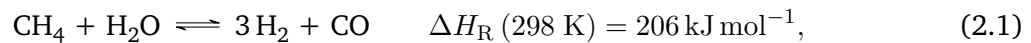
Downstream Application	Molar ratio H ₂ /CO	<i>T</i> (K)	<i>p</i> (bar)
Phosgene [22]	0.0	323	1-3
Monsanto process [23]	0.0 - 0.2	423-473	30-60
Hydroformylation [24]	1.0 - 1.2	393-463	40-300
Reduction of iron ore [25]	1.3 - 1.5	878-1100	atmospheric
Fischer-Tropsch [26]	1.6 - 2.3	473-513	20-40
Alcohol synthesis (methanol) [27]	2.0 - 2.3	200-550	50-200

A higher hydrogen content in the synthesis gas may be required for the reduction of iron ore and for the ammonia synthesis (pure hydrogen).

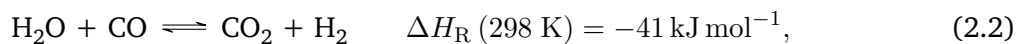
Later on, with the increasing availability of oil, the syngas routes to chemicals and fuels were abandoned in favor of more profitable refining processes. Interestingly enough, the current climatic and geopolitical context forces the society to step 100 years back and to resort to synthesis pathways identified by the engineers of the past. Furthermore, the fact that syngas can be generated from a number of carbon carriers, such as natural gas, captured carbon dioxide, biomethane, coal and biomass, implies high flexibility of its production pathways. At the same time, this introduces many degrees of freedom in the selection of the processes.

2.2 Chemical reactors for syngas production: state of the art

Steam reforming has been a dominant technology for hydrogen production due to the high H₂/CO ratio in the outlets. In this process, methane or higher hydrocarbons are catalytically converted with steam:

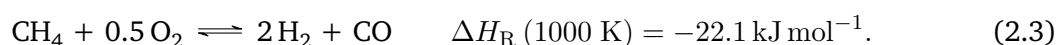


which occurs at high temperature and intermediate pressure, 850 °C and 15 – 30 bar. The strongly endothermic reaction takes place in multi-tubular, fire-heated reactors, followed by a mild exothermic shift in a second reactor stage to attain complete conversion of CO and H₂O into H₂ and CO₂, subsequently separated by swing adsorption:



For syngas applications other than hydrogen, the syngas ratio is too high. Therefore, further syngas downstream conditioning is required and performed by suitable separation systems, and excess hydrogen might be possibly stored. As natural gas is the prevailing state-of-the-art feed, it requires to be desulfurized on a zinc oxide bed prior to entering the steam reforming nickel catalyst bed, to prevent from poisoning and consequent deactivation. Due to the high energy requirement, this technology has a high environmental impact in terms of carbon footprint if the shell-side feed is a mixture of air and natural gas, also due to the emissions of nitrogen oxides.

Another role of primary importance in the production of syngas is the catalytic partial oxidation of natural gas, conducted in heterogeneous reactors. This reaction is slightly exothermic and generates a syngas ratio of 2, optimal for gas-to-liquid (GtL) applications:



Nevertheless, other reactions can influence the selectivity to the desired product. These reactions are primarily the total oxidation of methane, carbon monoxide and hydrogen. Their high exothermicity can influence the catalyst stability. Both in partial oxidation and in steam methane

reforming, carbon deposition contributions at high temperature and low pressures are possible but not favored. Furthermore, homogeneous reactions are also involved [28] at high pressures. Therefore, the partial oxidation reaction is preferably run at low pressures. Nickel supported by alumina is a candidate catalyst, contributes more than rhodium to coke deposition. The short residence times and high temperatures attained in noble metal coated monolith reactors show higher selectivity and are suitable for high syngas production in small volumes [28].

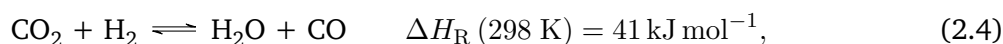
Autothermal reforming exploits the heat produced by the partial oxidation of methane: steam is injected, thus adding the strongly endothermic steam methane reforming to the reaction system, which absorbs the heat produced in the first reaction section to reform the gases on a catalyst bed [29]. Furthermore, steam hinders the deposition of soot on the catalyst bed located after the burner [30]. The first combustion section is operated at 2000 °C, whereas the reforming bed tolerates temperatures of 1000-1200 °C [30].

Although the autothermal reforming of methane is not directly accounted for in this dissertation, its compact review is relevant to another important technology included in the thesis and reviewed in the next section: tri-reforming of methane.

2.3 Carbon dioxide and biogas reformers: novel reforming concepts

The shift from natural gas towards more sustainable feedstocks led to the conceptualization of novel chemical reactors involving the reaction of direct hydrogenation of carbon dioxide to syngas (reverse water-gas shift), the direct reformation of purified biogas (dry reforming of methane), and the autothermal reforming of biogas (tri-reforming of methane).

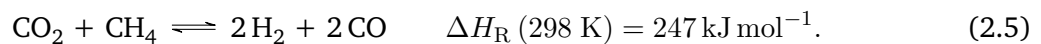
Reverse water-gas shift is the mildly endothermic hydrogenation of carbon dioxide into carbon monoxide and water.



It can be activated by steam reforming or methanation catalyst, i.e., supported nickel, at high temperatures. This catalyst choice however leads to the reverse methanation and a consequent production of methane as a side product. Thermodynamics shows that the relevant working area to avoid a significant generation of methane, high temperatures and low pressures are required. At atmospheric pressure and with a H_2/CO_2 ratio of 3, the interesting operating regimes are above 1100 K [31]. Consequently, if this hydrogenation step is preceded by high temperature, medium

or high pressure steam electrolysis, thermodynamic could favor the generation of methane in the reverse water-gas shift reactor, due to the contribution of methanation and reverse steam-reforming. These reaction proceed with a decrease in the number of moles, thus favored at high pressures. This is an important aspect to be accounted for in the analysis of the results generated in Chapter 6. Other catalysts of interest are copper-based or supported ceria [32]. Therefore, the RWGS reactor can valorize the CO₂ captured from point sources provided that a source of pure hydrogen is available. Hydrogen can be blue, if generated by fossil-based technologies such as methane steam reforming supported by carbon-capture technologies, or green, if provided by a water or steam electrolyzer.

Not only carbon dioxide, but also methane constitute a greenhouse gas. It can be generated by anaerobic digestion as bacteria decompose organic wastes and paper, and consists of an almost equimolar mixture of carbon dioxide and methane. Normally, methane is the prevailing component in a ration 3/2. For this reason, dry-reforming of methane has gained attention, as it converts a one-to-one feed mixture of CH₄ and CO₂ into a one-to-one mixture of H₂ and CO at atmospheric pressure:



For this reactor, several studies have investigated the use of different catalysts, although Ni-supported catalyst appear to be the most relevant candidates in terms of availability and costs. The highly endothermic nature of this process forces the system to be operated at high temperatures (900-1300 K) and at high energy input. At these operation regimes, standard Ni-based catalyst prove more susceptible to deactivation than noble metal catalysts [33, 34] which, conversely, are not at hand and costly. In fact, deactivation by coking and cold spots within the catalyst bed constitute major limitations to the industrialization of this technology [34].

As mentioned, the major limitation constituted by coke deposition in a dry-reforming reactor could be mitigated by noble metal catalyst formulations. Additional approaches implementing state-of-the-art reforming catalysts have been proposed. The injection of steam on the catalyst bed, combined with the partial oxidation contribution due to oxygen or air injection at the catalyst surface, appeared to be a viable technology option. As a matter of fact, oxygen and steam contribute to shift the equilibrium of carbon formation reactions towards their reactants:



although coke is omnipresent at low temperatures, below 1000 K at low pressures [35]. Tri-reforming can absorb flue gases containing CO_2 , H_2O , uncombusted CH_4 , O_2 , possibly N_2 , and convert it into syngas, provided the required integration of reactants. Clearly, other candidate feedstocks are biogas, and captured carbon dioxide [36]. Tri-reforming is carried out at high temperatures (1000-1200 K) and low pressures [37], as selectivity towards H_2 and CO becomes relevant in this temperature range or above [38], and the reactions involved proceed with increase in number of moles. Nevertheless, in industrial practice pressures up to 30 bar are to be considered [35]. The tubular, fixed-bed catalytic reactor can have a single or multiple injection points axially [37] to allow for a more uniform axial temperature profile. According to the feed composition, the reaction may be conducted adiabatically [37, 39, 40] or diabatically: the operation mode is highly dependent on the reaction conditions, i.e., feed composition, temperature and pressure, due to the complex interplay between individual the exothermic (water gas-shift, partial or total oxidation) and endothermic processes involved (steam reforming, dry reforming of methane) [35]. Singha et al. [41] characterized nanocrystalline Ni-ZrO₂ catalysts for tri-reforming, particularly suited to accept flue gases without the need for previous separation. In the context of partial oxidation, study by Pantaleo et al. [42] proposes the use of CeO₂-supported nickel catalysts: the catalyst activity and stability reveals to be deeply affected by the crystallite size and interaction between nickel oxide and ceria. Furthermore, high conversion and selectivity were obtained. The analysis of a synergistic combination of partial oxidation and dry reforming of methane was explored by Kang et al. [43]: a non-stoichiometric dry reforming feed-stream (excess methane over carbon dioxide) is fed to a fixed bed reactor, previously oxidized by air. The subsequent oxidation of methane accompanies the endothermic dry reforming reaction, with a resulting decrease in energy demand.

2.4 Water electrolyzer

As reported earlier in the compact review presented on reverse water-gas shift, hydrogen must be provided in order to reduce carbon dioxide. Green hydrogen is generated entirely by conversion of renewable power by water electrolysis.

Three are the technologies available: alkaline water electrolysis (AEL), polymer electrolyte membrane (PEM, or PEMEL) and solid oxide electrolyzer cell (SOEC, operated with steam at high temperature) [44, 45, 46, 47]. PEMEL electrolyzers exploit a proton exchange membrane to separate anode and cathode, acting as solid acidic electrolyte. On the contrary, an AEL requires a liquid basic solution as electrolyte. The alkaline electrolysis is a widely established technology, although mainly operated at steady state. The large ohmic resistances determine relatively low current densities of $0.2 - 0.4 \text{ Acm}^{-2}$, which makes a traditional AEL a rather bulky device [48] if compared to PEMEL. If AEL and PEMEL are established technologies, SOEC is still in the development phase [49]. This is due to the challenging reaction conditions of SOEC, also called high-temperature steam electrolysis, as operating temperature range between $700 - 900 \text{ }^\circ\text{C}$. The

corrosive environment requires proper material development. To attain this temperature range, a suitable source of waste heat must be available within the plant: high temperature allows to attain very high stack efficiencies if compared with PEMEL and AEL: nominal stack efficiencies for AEL and PEMEL are in the range of 70 %, and for SOEC up to 100 % the theoretical efficiency [47, 50, 46]. On the contrary, PEMEL and AEL are operated at lower temperatures: 40 – 90 °C and 20 – 100 °C, respectively [46]. Commercial PEMEL systems can operate currently in the delivery pressure range up to 30 – 40 bar [51], although high pressures reduce the electrolyzer efficiency due to increasing mass losses due to back-permeation of H₂ and O₂ [52]. Furthermore, there are prototypes and studies which suggest delivered pressures above 100 bar may be achieved [51]. This is due to the feature of polymer electrolyte, being able to withstand high pressure gradients without the need of pumping incoming water to the desired H₂ pressure level. Such high delivery pressures from PEMEL may be attained by electrochemical compression, which comes at the expenses of the energy requirement but spares in H₂ compressor CAPEX [53]. However, this seems to reduce the yield due to the tendency of H₂ to diffuse back to the O₂ compartment, thus increasing the specific power demand in comparison to non-differential systems. Furthermore, it introduces challenges due to mechanical stress, corrosion, hydrogen embrittlement, operation complexity and slower dynamic response [49]. Hancke et al. [53] report that, despite the recent interest and contributions in this field of research, there is still a lack of understanding in PEMEL differential pressure system performance, which still lags behind in the current market offer. On the contrary, AEL are limited in the attainable pressure due to the implementation of a porous membrane: balanced anodic/cathodic pressure operations are required, as higher pressures result in cross permeation of electrolyte and gases, leading towards inefficiency and potential safety risks [44, 51]. Therefore, AEL operating pressures can reach up to 30 bar [49]. Similarly, SOEC performances are reported up to 20 – 30 bar [54, 49].

A very relevant aspect is the load range these devices can tolerate, in the perspective of green, flexible operations. Currently, this value ranges between 5-120 % of a nominal load (PEMEL) or 30-120 % (SOEC), although the spans are expected to expand in the next decades: 5-300 % for PEMEL and 0-200 % for SOEC [55]. Current and projected minimum part-load for AEL are 25 % and < 10 %, respectively [49]. Other sources report a range of 10 – 40 % [56], thus setting a more restricted feasibility windows than PEMEL in flexible operations. Below this range, H₂ and O₂ quality reduce significantly due to contamination of the other component, leading into safety risks.

Cold start-up time may be relevant when considering to ensure the base-load by means of hydrogen storage tanks. In this scenario, the electrolyzer is shut down when no renewable power is fed. Unless waste heat is available for preserving the required temperature, AEL and PEMEL require up to 15 min for start-up, whereas SOEC from 60 min [49].

2.5 Sustainable feedstock

An alternative source of carbon for the P2X and GtL applications is found in biogas, generated by anaerobic digestion of bio- and agricultural waste. Digestors are used nowadays to treat industrial waste water, sewage sludge, agricultural wastes, hence converted into fertilizers. Increasingly, anaerobic digestion is applied for degrading heavy organic pollutants such as chlorinated compounds [57]. Biogas produced from anaerobic digestion and landfill produces a mixture of methane and carbon dioxide. The composition of biogas depends on the type of substrate it is provided from. Landfill gas provides methane in the range of 35-65 % and carbon dioxide of 15-40 %, whereas biogas from anaerobic digestion provides 60-70 % (CH₄) and 30-40 % (CO₂), respectively [58]. Raw biogas contains also traces of ammonia, hydrogen sulfide, nitrogen. These components are contaminants, and constitute a hazard for humans and downstream process systems, i.e., catalyst poisoning and corrosion. The purification process of biogas is named upgrading. Sometimes, upgrading indicates the generation of biomethane, cleaned from contaminants and separated from carbon dioxide. Technologies for the upgrade to biomethane are reviewed in Sun et al. [59], whereas Abatzoglou et al. [60] reviewed separation methods to remove toxic contaminants (NH₃, H₂S, Siloxane). The latter is particularly relevant to this thesis, since the work presented in the next sections assumes that biogas, pre-purified of its contaminants and consisting of a stream of carbon dioxide and methane, is fed to the conversion systems. Therefore, purification is decoupled from the production of syngas.

The purification and desalination of water prior to water electrolysis are imperative steps to ensure the stability and durability of the process. Typically, deionised water is required. Its source influences the selection of the purification method [61]. Reverse osmosis (RO) is required to desalinate seawater, with a power input of 3-6 kWh m⁻³ [62, 63, 61], the highest among all purification processes. In addition, a high volume of water is lost during RO, about 35% of the feed [61]. Unless the plant is located offshore or in proximity of the coastal line, transportation requires to be accounted for in the balance of plant. On the contrary, surface water does not always require energy-intensive treatment prior to utilization, although its availability may be limited and seasonal.

Water electrolysis can provide green hydrogen and oxygen if supplied with renewable power. The latter is required to sustain total or partial oxidation reactions, as a reactant or in the utility line as comburent for heat generation purposes. Air normally serves the purposes. Alternatively, oxycombustion systems make use of pure oxygen. Air involves the introduction of a large amount of nitrogen, which imposes the selection of larger unit operations. Nitrogen oxides are formed and must be removed. On the contrary, its absence from the oxidant mixture results in higher concentrations of carbon dioxide, which facilitates its capture after the condensation of water vapor [64, 65]. However, the temperatures are higher than those normally attained in air combustion systems. Therefore, although oxycombustion can run in conventional combustion systems, the partial recirculation of exhaust gases is required. Steam can be injected for the same purpose

[65]. Fuel combustion in enriched air can also contribute to simpler carbon capture strategies and smaller process volumes due to the reduced volume of nitrogen. All this considered, oxycombustion is an interesting candidate in the framework of sustainable processes, to be preferred as long as pure oxygen can be provided comparatively inexpensively and sustainably. However, oxygen is separated from air by means of energy-intensive air separation cryogenic units (ASU). This is not required for Power-to-X processes, where pure oxygen can be co-generated in the electrolyzer, provided that its partial pressure at the anode is sufficiently low.

2.6 Separation methods

Raw biogas and syngas mixtures must be purified before undergoing further processing steps down to the desired product. The chemical species of interest are separated from unreacted carbon dioxide, methane, water vapor, and from excess hydrogen. Prior to its conversion into syngas, biogas is purified from catalyst poisons, such as hydrogen sulfide, sulfur oxides, ammonia. In some cases, bio-methane and carbon dioxide are partially or completely separated from each other. The separation of a key component from another or more species becomes possible when a driving force can be exploited, that is, a key property K_k must distinguish the species uniquely:

$$K_{k,\alpha \neq k} = \frac{K_k}{K_{\alpha \neq k}} \gg 1, \quad (2.8)$$

which indicates that property K for key component k is larger than for any other component α . The type of key property defines the suitable separation method for the given feed and target component [66]. Relevant separation methods for mixtures in the gas phase are reported in this section [67, 66]. In some cases, the task of separating a key component from a mixture can be performed by more than one separation method.

Adsorption is based on the selective binding of components on the surface of a solid. In physisorption, the key property is the molecular diameter. Molecules whose diameters are of the same order of magnitude of the pores on the solid surface are selectively separated from larger components. On the contrary, chemisorption is based on the chemical affinity between the species of interest and the solid surface. A high surface area is required to provide the gas phase with a high adsorption capacity. Equilibrium is established between molecules in gas and in solid phase. Therefore, the equilibrium constant derived from Langmuir, Freundlich or a BET isotherm is the key property for this separation method and can provide enough information on the selectivity of the adsorbent towards the key component of interest.

In absorption operations, one or more components in a gas mixture are selectively removed by contact with a liquid phase. As for adsorption, this process may be physical or chemical. The key property of physical absorption is the relative solubility of the key component with respect to other species, whereas for chemical absorption the key component must react with the liquid phase. For physical absorption, Henry's law is the most used.

Membrane separators allow the selective permeation of one or more species, which migrate from the retentate to the permeate side. Porous membranes separate according to the size of the particles, whereas dense (nonporous) membranes exploit the difference in solubility and mobility of the key component. Composite membranes combine a dense with a porous layer for the permeation of more than one component. The driving force is the (partial) pressure between retentate and permeate.

Key property in cryogenic operations is the higher relative volatility of the key component at low temperatures. Compression stages may be involved, as well as the preliminary purification steps from components which can freeze along the pipelines.

2.7 Optimization of Power-to-X systems

The multitude of process steps involved in the generation, separation and conditioning of syngas and in its downstream applications, as well as the system design and operations, invoke the use of systematic approaches for the determination of the best process alternatives. The desired solution is related to a specific target that the process should attain, defined by an objective function, to be minimized, or maximized. The values of the objective function are influenced by the degrees of freedom of the process. Each process variable is constrained within given ranges, or bounds. Different variables are related among each other by equality and inequality constraints. Typical examples of equality constraints are represented by the models of unit operations and interconnections, whereas inequality constraints identify those portions of the domain where technologically relevant and mathematically feasible solutions can be attained.

The generic optimization problem reads:

$$\begin{aligned}
 \min_{\mathbf{x}, \mathbf{p}} \quad & f(\mathbf{x}, \mathbf{p}) \\
 \text{s.t.} \quad & \mathbf{h}(\mathbf{x}, \mathbf{p}) = \mathbf{0}, \\
 & \mathbf{g}(\mathbf{x}, \mathbf{p}) \leq \mathbf{0}, \\
 & \mathbf{LB} \leq \mathbf{x} \leq \mathbf{UB},
 \end{aligned} \tag{2.9}$$

where f , the objective function depending on the system variables (vector \mathbf{x}) and the parameters (vector \mathbf{p}), is minimized and is constrained by the process model equations, h , and feasibility conditions, g . Variables are forced between lower and upper bounds, respectively, **LB** and **UB**.

The mathematical formulation for the optimization of a Power-to-X system, or program, may include integer variables (\mathbf{y}) defined over the domain \mathbb{Z} .

$$\begin{aligned}
 \min_{\mathbf{x}, \mathbf{y}, \mathbf{p}} \quad & f(\mathbf{x}, \mathbf{y}, \mathbf{p}) \\
 \text{s.t.} \quad & \mathbf{h}(\mathbf{x}, \mathbf{y}, \mathbf{p}) = \mathbf{0}, \\
 & \mathbf{g}(\mathbf{x}, \mathbf{y}, \mathbf{p}) \leq \mathbf{0}, \\
 & \mathbf{LB} \leq \mathbf{x} \leq \mathbf{UB}, \\
 & \mathbf{y} \in \mathbb{Z}
 \end{aligned} \tag{2.10}$$

A mixed domain identifies mixed-integer optimization problems (MIP). Furthermore, if the optimization problem in Equation 2.10 is completely linear, both in its objective function and constraints, the problem is a linear program (LP or MILP). On the contrary, if at least one equation is nonlinear, the problem is a nonlinear program (NLP or MINLP). Nonlinear programs may admit more than one locally optimal solution. Sufficient condition for a global optimal solution are that the objective function f and inequality constraints g are convex, and that the equality constraints h are linear [13]. Clearly, a linear or mixed-integer linear problem admits a global optimum.

Mathematical optimization methods are at the core of the CAPE applications introduced in section 1.2 and applied to process synthesis, design, and flexible operations. The following sections illustrate the fundamental research pillars of these branches and highlight the novel contributions that the present thesis intends to bring.

2.8 Optimization in process synthesis

Process synthesis is a creative activity that requires the identification of the best candidate among viable alternative resources and pathways to produce a desired product. At first, a primitive problem must be formulated based on business opportunities in terms of production scale and feedstock [68]. Concrete examples are given by the research Question 2 in Section 1.3 for a retrofitting and new plant synthesis case, respectively. For E-fuels production processes, such as those considered in this work, the exact identification of the geographical location of the plant may be not relevant to the primitive problem, since E-fuels such as methanol are essentially hydrogen carriers and can be produced in remote locations. If so, it is important to identify a class of locations with some essential feature in common. As for Question 2 and E-fuel projects in general, cheap renewable power and biogenic carbon must be available, and optionally, access to grid

electricity. Alternatively, a specific geographical location may be defined from the very beginning as a business opportunity arises. Plant retrofitting is an example, and the primal problem may be not too dissimilar from Question 1 of Section 1.3: for instance, the managers of a given steam reforming facility with access to cheap PPAs from renewable power and to a source of biogenic carbon dioxide want to leverage public subsidies for the inclusion of green hydrogen production within the battery limits. These primitive problems have many possible solutions, even though many candidates can be excluded already in a pre-feasibility analysis after sufficient information has been gathered. Biegler et al. emphasize the need to perform a thorough search for information "since a design problem is rarely entirely new" [13]. Although not relevant to the first chapters of this thesis dedicated to process synthesis, where production scales have been normalized to generalize the approach, thus focusing on specific, not absolute, energy consumption, information on the scale of the process driven by market analyses allow to gather correct CAPEX information from vendors and, where needed, to design the manufacturing processes for the raw materials [68]. Moreover, considering the real manufacturing scale of a process is required when costs are determining factors in decision-making, as larger purchase orders come with lower specific costs. The next step is the identification and evaluation of process alternatives. This approach can be taken from a base-case simulation, or from a set of pre-postulated competing candidate layouts. In the former case, a base design can be improved by means of evolutionary methods, which enforce a sort of sensitivity analysis based on small modifications to the base-case: the initial flowsheet must be reasonable, as process synthesized by evolutionary methods depend on it, and may be derived by other methods [69]. The latter case falls in the domain of structural parameter approach, or superstructure optimization, where all possible interconnections are embedded within a single optimization problem [69]. Douglas [70] formalized a hierarchical decomposition approach for process synthesis, where a sequential decision approach is taken to identify the candidate solution based on experience-driven decisions and heuristics. The decision-sequence prescribes the definition of feedstocks, products, side-products in a batch or continuous fashion, reactor type, interconnections and recycles, separators for the given mixtures, and finally heat recovery network. At each stage, a KPI analysis on plant profitability and based on process simulations determines whether it is worthy to explore further decision levels. Hierarchical decomposition represents an alternative to superstructure synthesis. However, a sequential approach based on heuristics and experience may cut counter-intuitive but relevant solutions out of the search candidates, often deriving from the integration of different decision levels, such as reactor and separator sequence, plant and heat integration. On the other hand, a superstructure optimization may lack of sufficient process details, for instance, in simple linear or quadratic descriptions, or may present severe convergence issues or local optimality in case high-fidelity nonlinear descriptions are adopted together with integer variables, thus the need of an appropriate mathematical formulation depending on the case study and the scope of work. Therefore, efforts have been made to integrate hierarchical decomposition and mathematical optimization into hybrid approaches, as by Daichendt and Grossmann [71] and Zhang [72]. Contrarily to superstructure optimization, where a possibly large but pre-defined set of alternative layouts is set, the so called "ab initio" approaches aim at combining a number of process units by means of evolutionary programming with non-linear programming [73]. If on the one hand this approach has the advantage of not

relying on pre-defined structures, and thus possibly attaining counterintuitive feasible designs, it does not guarantee convergence due to the combinatorial complexity.

Superstructure-based process synthesis has evolved from the first synthesis-superstructure by Umeda et al. [74], who postulated a general problem for reactor-distillation sequence based on shortcut models in continuous variables. This approach developed then for the solution of subsystems [75], utility and heat-exchange networks [76, 77, 78, 79, 80], separation sequences [81, 82, 83], and for entire plant layouts. Sargent, Grossmann, Westerberg and Floudas have been pioneers in the field of process synthesis. Fundamental is the systematic representation of the system for conceptual design. On this regard, it is important to cite the conceptual framework illustrated by Yeomans and Grossmann [84]. The authors illustrated the "state-task network" (STN) representation, relevant to Chapter 4, traditionally split into VTE (variable task-equipment), if a single equipment can perform several tasks, and OTOE (one task one equipment), if one equipment can exclusively address a given task. In addition, they discussed the state-equipment representation (SEN), where all possible unit operations are reported just once and are interconnected by stream flows through nodes. Such high-level system representations can be translated into logical statements [85]. The major issue found in the application of mixed integer programming is the efficient modeling of discrete decisions, where logics could offer an alternate framework. Generalized disjunctive programming - GDP, first discussed in a contribution by Raman and Grossmann [86], offers a approach facilitates the representation of discrete decisions. It combines Boolean logics with continuous variables, where discrete decisions in the continuous space, e.g., the activation of unit operation A while B and C are not selected, are represented within disjunctions, whereas logic propositions determine the rules according to which a selection has been made, e.g., at most one unit is active (A can be active, if B and C are certainly inactive). A GDP formulation must be translated into a MIP to yield solutions to the synthesis problem, for instance, the so denominated "big-M" representation. However, the efficiency of this approach depends on the valid selection of the constant M, which is an additional problem-dependent parameter to be carefully selected. Furthermore, there may be more efficient formulations of the GDP-correspondent MIP problem, that is a problem with a tighter relaxation of the mixed-integer bounds into a continuous formulation called during MINLP iterations. This was shown in a contribution by Lee and Grossmann, which introduced a different relaxation approach: the convex-hull of non-linear disjunctions [87]: here, the optimal solution of the relaxation obtained by convex-hull representation was better than the solution of the relaxed "big-M" formulation due to a tighter domain of the relaxation, thus improving the convergence efficiency of any suitable MINLP algorithm.

2.9 Optimization for sizing and control of flexible plants

High level formulations of plant layout alternatives are typical in superstructure optimization approaches. However, once the promising layout has been identified, a refinement of the modeling

scheme is required for plant sizing and operations, and distributed models must be adopted within simulation or optimization frameworks. Typically, plant sizing is attained with sequential details and improvements added to a base-case forward simulation within a simulation software, as anticipated in Section 1.2. Traditional references for such approaches are found in many well-known textbooks, such as "Process Design Principles" [68], "Systematic Methods of Chemical Process Design" [13], and "Analysis, synthesis, and design of chemical processes" [88]. At first, detailed thermodynamic frameworks need to be specified, and basic mass and energy balances are determined on input-output boxes invoking full conversion reactors, sharp split separators; temperatures and pressures are based on bubble and dew points. This first description is based on actual production levels and give an idea of the required resources and external utilities. Then, the level of detail is gradually increased. For reactors, the description goes from equilibrium reactors to ideal reactors, and then distributed models including pressure drop information. Similar for distillation processes, the first shortcut approaches will be substituted by rigorous models for the columns with detailed thermodynamics and fluid-dynamics calculations at each tray. Sensitivity analysis can support in evaluating improved structural and operational variables to attain desired KPIs. In a sensitivity study, the key inputs were traditionally modified manually. However, current simulators can perform them automatically within a range of selected values for one or multiple variables. An alternative to sensitivity analysis is the use of mathematical optimization via non-linear programming (NLP). This can be performed within a simulation software environment, by evaluation of the outputs of sequential-modular (SM) forward simulations or in equation-oriented mode (EO), where all problem equations contribute to the constraints of the NLP in Equation 2.10, the latter being more desirable for large flowsheets with many recycle loops. Alternatively, the whole process may be modeled in programming languages which provide embedded NLP solvers, or allow to call for external solvers, with the advantage of having full control on models and versatility in problem formulation for special classes applications. Chapter 1 introduced the scenarios evoked by intermittency in the energy source. Clearly, robust design and fast control tools are needed to face the challenges that variable loads introduce design and control of production systems.

The dynamic representation of a process is fundamental for the understanding of the modeled plant and for real-time plant control applications. Introduction Section 1 mentioned the role of distributed control systems (DCS) in modern system architectures. Also here, mathematical programming supports decision-making in the conduction of control actions based on dynamic model outputs, corrected as time proceeds by the incoming values of boundary conditions [89]. Model predictive control (MPC) is a class of such techniques, especially well-suited for complex multi input-multi output problems [90, 91, 92]. Again, the important feature is the prediction of future behaviours of the plant as the incoming perturbation assumes a different value, and the controller outputs correct the system with respect to minimize the difference between the controlled variables of interest and the setpoint. At each instant of time, calculations are repeated and the prediction updated based on the current data (moving horizon) [89]. Due to the regular repetition of the forecast for the control actions, each consisting in the solution of dynamic simulations and NLP problems, high-performance computers are essential, as well as fast underlying integration

strategies for the nested forward simulation problem. Parallel computing techniques can exploit multi-core computing to divide and conquer PDE problems, where time is an essential feature, such as in live-plant optimally controlled operations and MPC.

Clearly, efficient optimal control approaches must be applied to systems, which were optimally designed to tolerate swings in the operating modes due to the prevailing contribution of volatile renewable power. Robustness may be described as "the property of a component to remain healthy and operable if it is not utilized in a proper way for a certain time" [93], although this implies that flexible Power-to-X systems have to be operated improperly on a daily or hourly time scale, as they are affected by the volatility (of cost or availability) of renewable electrical power: what is noise and disturbance in traditional process engineering becomes the normality in flexible E-fuels synthesis plants. Therefore, it is critical to identify a robust design early in the project [94]. The design must be capable of tolerating load fluctuations and deliver the product at the required quality. Turton et al. [88] indicate that plant operations do not correspond to the conditions specified in the design due to multiple reasons, such as change in external effects (feed materials, product specifications and flowrates), equipment replacement or improvement, oversizing of the units to ensure that typical nominal flowrates can be ensured over time and degradation. For this reason, performance curves are prepared in order to support the understanding the unit performances within given ranges. In order to construct the curves, material and energy balances are used along with design equations. In addition, operability thresholds are added such as minimum or maximum temperature and velocity along a reactor tube, flooding thresholds in packed columns, maximum residence time in an oven or reactor to avoid coking/cracking, etc [88]. Such performance curves are essentially sensitivity analyses based on fixed unit sizes. As already reported in this section, sensitivities can be converted in model-based optimization approaches, constrained by the same models and feasibility constraints that allow vendors to generate the performance curves of their technical proposals, thus allowing the designer to systematically explore the feasible operation domain while accounting for fixed parameters and interplay between units simultaneously. Efficiency is also an interesting parameter that may be inferred from unit provider datasheet at different sizes and embedded in the optimization, such that inefficient operating modes for the given sizes are penalized.

2.10 Novelty and relevance of this thesis

The process synthesis sections of this paper presented in Chapters 3 and 4 firmly lay their foundations in the milestones discussed in Section 2.8, bringing in the novelty of a systematic approach in the field of sustainable syngas production by adapting the state-task network OTOE representation of sharp split separators with the inclusion of any feasible separation method for each separation task. Regardless of the technological readiness level (TRL), the feasibility of a separator is given by the analysis of key chemical or physical property relevant to the separation technology (relative adsorptivity, permeability, volatility, absorptivity, and kinetic

diameter). As discussed in Section 1.3, fixed costs are not considered in the analysis to focus on scientifically relevant aspects such as energetic efficiency, thus maintaining a market-independent perspective: as already discussed in Section 1.3, capital cost estimates are subject to change due to market development, e.g., law of supply and demand, policies dictating the price of single unit components if imported from abroad, readiness level. Therefore, these studies presented aim at the identification of pathways that are energetically favorable in the context of intermittent cheap green power by exploitation of suitable objective function formulations. Whenever a large number of process candidates or scenarios are considered in multi-objective or superstructure optimization, a high-level mathematical description of single unit operations can still capture the essential features relevant to the analysis at hand, provided that appropriate modeling assumptions are adopted. For this reason, Chapters 3 and 4 treat Power-to-X systems from a high level perspective, where fully linear modeling approaches are involved, with continuous (LP) and mixed-integer (MILP) variables.

On the contrary, in Chapters 5 and 6 the analysis is reduced to a given process, whose design and operation mode can be determined by a detailed nonlinear description, resulting in nonlinear programming problem formulations (NLPs).

Chapter 5 analyzes the application of optimal control to a novel flexible process concept for syngas production for Fischer-Tropsch. Aim is to stabilize the product over intermittent energy supply and to test the performance and limitations of a parallel computing approach, although special care must be posed in the problem formulation, as emerges from the conclusions.

However, the significant time spent by the plant in part-load, as well as the interconnection of highly electrified processes driven by a limited, fluctuating source of electrical power, require CAPE approaches meant to simultaneously identify unit sizes and operation set-points, at nominal and part-loads. Chapter 6 implements multi-period design optimization for the first time on a realistic description of a fully electrified methanol process, where flexible operations are buffered by a liquid storage for the mixture methanol-water before distillation. This methodology is used to compare the profitability of extreme case scenarios: maximum process flexibility up to liquid methanol/water storage compared to buffering H_2 or power (batteries) and steady-state operations.

This thesis shows that the challenges posed by the intermittency of renewable energy supply and by alternative feedstocks require an intensive use of computer-aided approaches, where the novelty is often represented by methodological extensions to adapt to the nature of these cases.

2.11 Sustainability of the electrical power supply in optimization

In the first evaluations proposed in this thesis in Chapter 3 and 4, extreme-case scenarios are assumed for the high-level superstructure analyses based on thermodynamics. It is either implied that electrical power is provided entirely by carbon-neutral natural resources, or by the combustion of fossil fuels, e.g., natural gas from the grid, thus associated with a positive carbon footprint. The first case can be translated into the use of locally generated green electricity, while the second case can be translated into the supply of grid electricity, only for the 48 % green in the German market [95], for the 39 % green in Europe on average [96].

When renewable electricity is assumed, combustion steps along the process coordinate are penalized in favor of highly electrified solutions which make use of renewable power. A fall by 56 %, 48 % and 68 % between 2010 and 2020 in the global averaged levelized cost of electricity for on-shore, off-shore and concentrated solar renewable power projects, respectively [10], were reported by IRENA. Therefore in such optimization scenarios, profitability is not being accounted for. This relies on the fact that the cost of electricity in the future will not be a critical aspect to consider in screening various processes. Nonetheless, this approach is completed later on in the dissertation in Chapter 6, where the profitability is included in the comparative analysis of a flexible plant concept.

2.12 Terminology in this thesis

A clarification is here reported concerning the terminology adopted in this thesis. The use of the term *power* in the context of Power-to-X and Power-to-Syngas denotes the conversion of electricity. However, the same term is used for the physical definition of power, as energy per unit of time. In this sense, power can be *electrical* (from electricity) or *thermal power* (from combustion). The sum of electrical and thermal power constitutes the total power supply.

Retrofitting a steam reforming plant for sustainable syngas production

3.1 Introduction

The growing trend toward process electrification to reduce carbon dioxide emissions requires the implementation of novel industrial-scale production pathways that can flexibly adapt to the intermittent nature of renewable electricity. Retrofitting well-established processes is a prompt step toward defossilization.

From this perspective, the production of green hydrogen from water electrolysis can support valid alternatives to state-of-the-art processes such as steam methane reforming, a highly endothermic process that relies on natural gas to supply the reaction heat and to provide hydrogen. However, from a thermodynamic perspective, splitting water into its elements H_2 and O_2 via electrolysis requires considerably more energy than reducing methane to H_2 and CO in a steam reformer, although an electrolyzer is run mainly in electricity. Energy requirements are discussed in the next Section 3.2.1.

This chapter proposes a retrofitting case to enable sustainable syngas production, where linear programming is applied to identify energy or atom efficient reactor-separator configurations and operations modes. A water electrolyzer and a reverse water-gas shift reactor are added to a preexisting steam reforming plant to leverage the use of available renewable power and biogas. The reverse water-gas shift reactor is followed by a superstructure representation of the separation train, which encompasses multiple attainable routes based on thermodynamics.

This allows to

- lower the H_2/CO ratio of steam reforming, too high for most downstream processes as reported in Table 2.1, without the need to inject carbon dioxide directly in the steam reformer, which enhances the RWGS reaction contribution in the catalytic bed at the expenses of an increased rate of fouling [97];
- use renewable energy when externally purchased green electricity is relatively inexpensive if compared to a reference fossil fuel by running the electrolyzer in combination with RWGS;

- attain a lower specific thermal energy requirement per syngas produced when renewable electricity is relatively expensive: the heat of reaction required by RWGS is lower if compared to SR, and, if combined, both reactors contribute to the production of CO.

Excess hydrogen from steam reforming can substitute energy-intensive green hydrogen for carbon dioxide reduction in the reverse water-gas shift step whenever cheap renewable power is not enough or is too expensive to run the electrolyzer.

For the synthesis process, the plant relies on biogas, a mixture of CO₂ and CH₄, which can be integrated by an additional stream of biogenic CO₂, either provided by the hot utility loop when excess bio-methane from the synthesis is burned, or delivered by any other external source outside of the battery limits. However, locally available biomass may be scarce, which potentially limits the opportunity to run the process entirely on biogas, also for hot utility generation. As a consequence, natural gas can be integrated to generate the hot utility for thermal demands. Therefore, possible limitations in biomass availability require that the carbon economy of the system is systematically optimized. Renewable power can also be limited due to availability constraints, thus, grid electricity can be supplied, possibly at a high relative cost.

All this considered, the inclusion of an additional reverse water-gas shift step equipped with a new efficient separation train may prove beneficial, boosting the plant adaptability potential to new biogenic feedstock, renewable energy sources and widening the range of attainable product specifications.

It is assumed that the plant is flexible enough to ensure product specifications by dynamically adapting the flow patterns and loads to fluctuations in the cost of externally purchased green electricity and in the cost of the reference fossil fuel for combustion. Although this may constitute a CAPEX-favorable approach, limitations in load-swing feasibility may require a certain extent of energy storage. However, this may not be readily appreciated in a preliminary, high-level process synthesis study, where lumped and equilibrium models cannot capture the actual implications of flexible operations, object of the second part of this Dissertation.

The next sections are dedicated to the definition of the technological framework to allow for a combined analysis of the interactions between reactors and separators under different optimization scenarios. Finally, solutions, discussion and limitations of the study will be reported. Methodological aspects proposed in this chapter are elaborated further in Chapter 4, where the modeling approach is extended beyond to a larger number of reactors and separators for process synthesis problems.

3.2 Superstructure of reactor-separator system

3.2.1 Reactors operating conditions, plant feedstock and outlets

The steam reforming of methane (SR) and reverse water-gas shift (RWGS) reactors are modeled as isothermal equilibrium Gibbs stages at 1200 K, 30 bar, 227 kJ mol⁻¹ and 900 K, 15 bar, 36 kJ mol⁻¹ respectively. The reaction energy requirement is calculated based on the enthalpy difference between inlets and outlets at the process operating conditions. Carbon dioxide is accounted for in the equilibrium calculations for steam reforming, which then embeds two independent stoichiometric relations. For the electrochemical conversion of H₂O into H₂, an electrical power input of 385 kJ mol_{H₂}⁻¹ [50] for 60% stack efficiency [98] is accounted for in a low-pressure electrolyzer at 333 K and atmospheric pressure. Methane is provided by the anaerobic digestion of biomass (AD), thus separated from an equimolar mixture of CH₄ and CO₂, biogas, at atmospheric pressure and temperature.

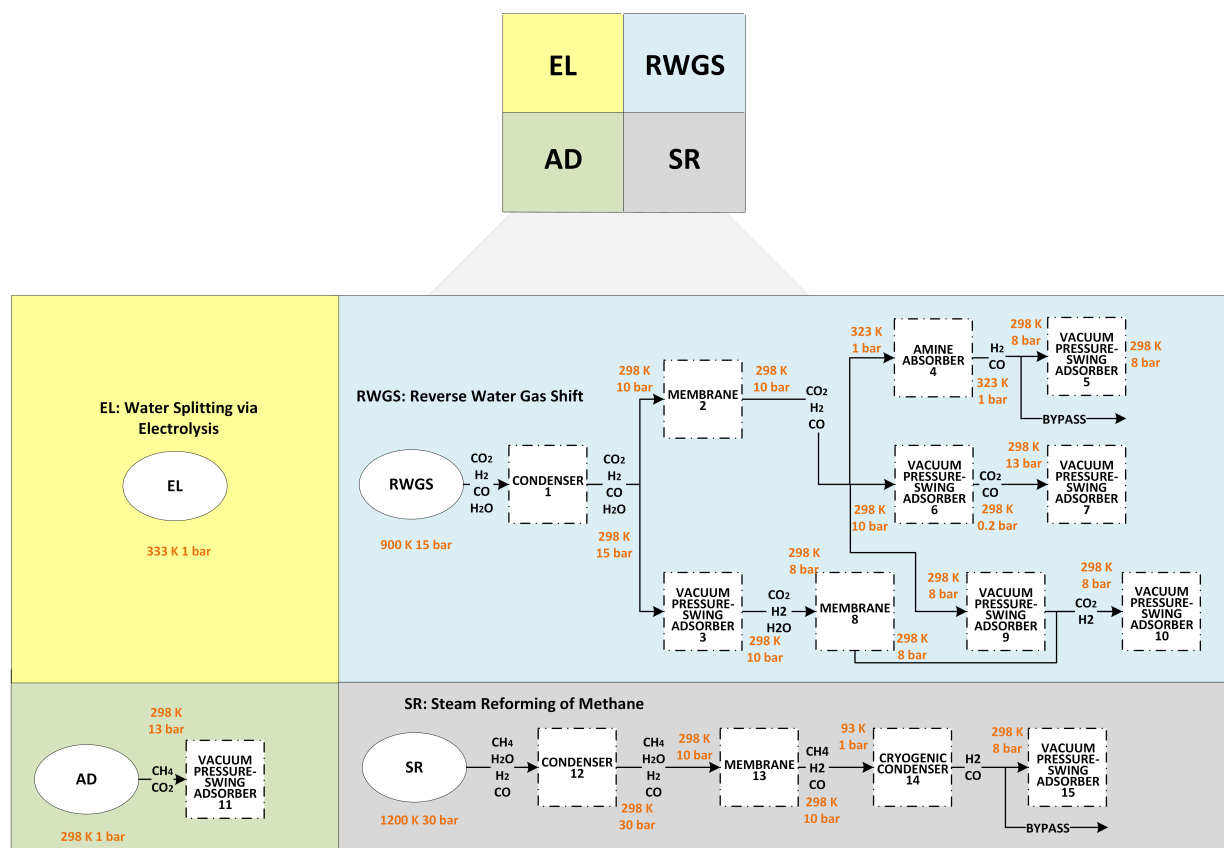


Figure 3.1.: Schematic representation of the separators involved after each reactor. Temperature and pressure levels are reported in orange. Abbreviations: electrolyzer (EL), reverse water-gas shift (RWGS), anaerobic digestion (AD), steam methane reformer (SR).

Figure 3.1 shows the reactor-separator sequences which constrain the optimization problems. Unit operations and connectivity are described in this section.

Combustion of CO to lower the syngas ratio is not accounted for. This is due to the fact that the synthesis of CO costs combustion energy required to sustain endothermic process steps for its synthesis, and the combustion of CO back to CO₂ creates an inefficient loop. Furthermore, it does not add any value for the generation of H₂.

As stated in Section 3.1 and in Table 2.1, syngas can be fed to a number of downstream applications, each requiring a syngas ratio $r = \text{H}_2/\text{CO}$ comprised within well defined boundaries. Therefore, syngas ratio conditioning is required and achieved by flowrate-adjustment at the reactors and electrolyzer. Nevertheless, in this study temperature and pressure of the syngas stream are not raised to the required values for the designated downstream application. Instead, energy evaluations are performed exclusively based on the syngas ratio, independently on the targeted downstream application.

Excess CH₄ can leave the plant after compression at 300 bar to be potentially utilized within the battery limits later on. Excess oxygen undergoes cryogenic storage at 73 K and can be thus sold as valuable byproduct. Excess carbon dioxide contributes to positive emissions and is subject to penalization in the optimization framework, as reported in Section 3.4.

3.2.2 Exclusion of the water-gas shift reactor for pure hydrogen production

The state of the art process to obtain pure H₂ after a reforming reactor such as steam reforming of natural gas is the water-gas shift reactor followed by PSA separation of CO₂ [99]. However, this approach is not considered in this superstructure formulation. In the perspective of green (i.e. climate-neutral) production systems, resource availability and efficiency play a crucial role. If so far natural gas or coal has been the primary source of hydrogen atoms, regardless of tight availability constraints and environmental costs of the footprint associated with the separated CO₂-stream, in the perspective of green production systems biogas must be considered as a locally limited resource. For this reason, meeting the entire pure H₂ demand by feeding only half of its flow (CH₄) to a steam reformer to extract H₂ *via* water-gas shift and create an additional stream of unused CO₂, which adds up to the surplus CO₂ from biogas itself, should not be considered a reasonable process scheme. However, in the broader discussion of availability constraints, these considerations may change given a specific project location, such that water may be more scarce than biogas and the entire production must rely on standard methods. However, specific cases are beyond the scope of this investigation, which assumes that water availability is not a limiting factor, while atomic efficiency must be considered.

3.2.3 Feasible separation methods

Feasible separation methods for specific feed mixtures are identified from the literature. In this and the following chapter, the notation denotes with (A,B,C), the task of separating A from the incoming mixture (A,B,C) will be denoted with A/(B,C).

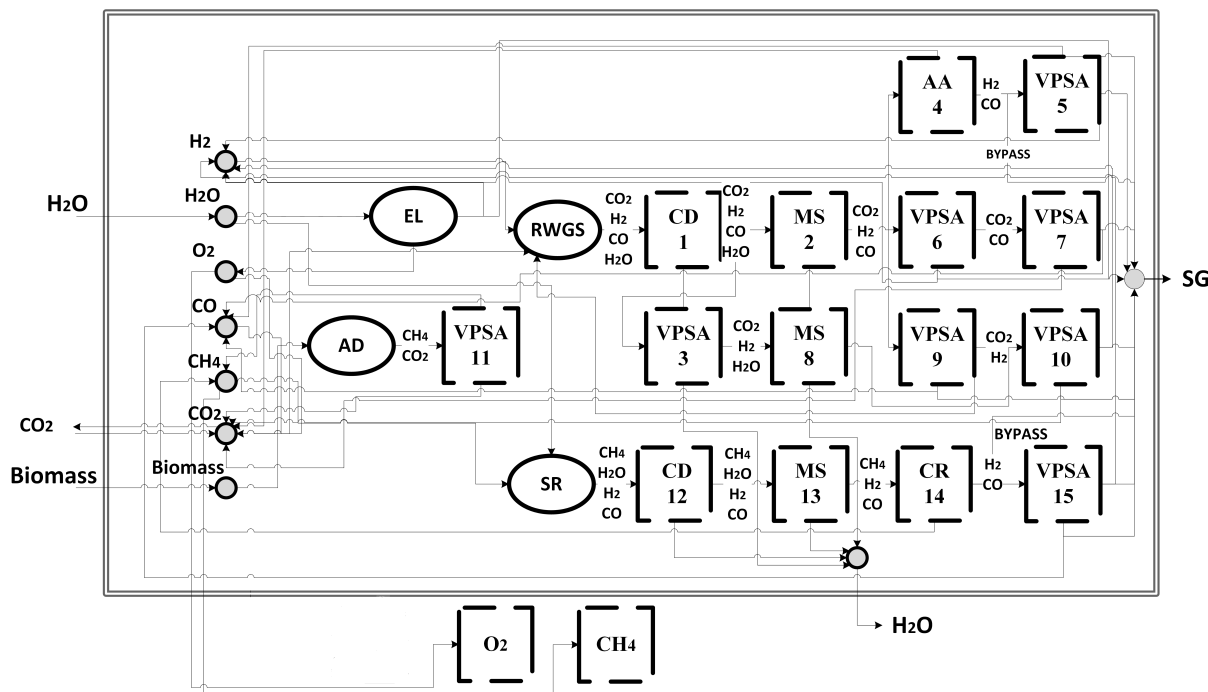


Figure 3.2.: Fully connected superstructure. Substance nodes (grey circles) accept feedstock and recycles, to be delivered to the reactors (ovals). Excess H_2 , O_2 and CH_4 are stored (dashed boxes). Water and syngas (SG) leave the plant as co-product and product, respectively. Acronyms for process units: electrolyzer (EL), anaerobic digester (AD), steam reformer (SR), vacuum pressure swing adsorption (VPSA), water condenser (CD), membrane separator (MS), amine absorption (AA), cryogenic separator (CR).

Figure 3.2 identifies reactors and separation tasks with an acronym and a sequential number. This representation is an expansion of Figure 3.1, highlighting process interconnections and nodes. It must be emphasized that, for this preliminary case-study on retrofitting, the superstructure permits a single viable separation method for each separation task. An extension of this approach to multiple separation methods per task is presented in the next chapter on superstructure optimization.

3.2.4 Steam reforming of methane: separation sequence

This section of the plant is pre-existing and subject to retrofit. Therefore, the separation sequence that follows SR is predefined and does not present alternative branches: this sequence does not constitute a superstructure in itself.

Separation sequences of gas phase mixtures can be negatively affected by the presence of water, which can condense along the process pathways, leading to clogging. Therefore, most of the moisture should be removed at the reactor outlet by temperature-driven condensation (CD). For this reason, SR is followed by water condensation (CD 12) followed by a membrane dehydration step (MS 13). Afterwards, $\text{CH}_4/(\text{CO}, \text{H}_2)$ separation is performed by cryogenic condensation (CR 14) [100], possibly followed by recycling of CH_4 . Lastly, VPSA 15, possibly bypassed, allows for syngas conditioning.

Biogas provides methane to SR: after anaerobic digestion, it is separated into CH_4 and CO_2 by VPSA 11 [101].

3.2.5 RWGS reactor: separation sequences

After condensation (CD 1), the outlet stream from RWGS includes CO , unreacted CO_2 and H_2 , and traces of H_2O , ca. 0.3%_{vol}. High permeability of water is reported in poly-dimethyl siloxane [102], as well as lower permeabilities for the other components of the mixture [103]. Therefore, a membrane separator (MS 2) can be implemented for gas dehydration after condensation. Following the membrane separator for the fine removal of water is a tree of alternatives for syngas separation and conditioning. Branches can be easily identified in the panel represented in Figure 3.1. The available separation routes are:

1. $\text{CO}_2/(\text{H}_2, \text{CO})$ by amine absorption (AA 4) [104] and $\text{H}_2/(\text{CO})$ (VPSA 5 [105]) and/or bypass to the product;
2. $\text{H}_2/(\text{CO}_2, \text{CO})$ (VPSA 6 [105]) and $\text{CO}/(\text{CO}_2)$ (VPSA 7 [106]);
3. $\text{CO}/(\text{CO}_2, \text{H}_2)$ (VPSA 9 [107]) followed by $\text{CO}_2/(\text{H}_2)$ on activated carbons or by recycle of the reactants (CO_2, H_2) (VPSA 10).

Alternatively, after condensation (CD 1) water is not completely removed. Instead, VPSA (3) selectively separates CO from ($\text{CO}_2, \text{H}_2, \text{H}_2\text{O}$) [107], followed by a polymeric membrane (MS 8 [102]) for the removal of H_2O and separator VPSA 10 to entrain CO_2 .

3.3 Modeling approaches

Reactors and separators are assembled into a single superstructure, where temperature and pressure levels in each unit are fixed prior to the optimization and are shown in Figure 3.1.

In the optimization problems formulated in this and the following chapter, the required carbon uptake is always regulated by a hard constraint that fixes the product stream flow rate across scenarios, where the composition of H₂-to-CO varies.

Chemical component nodes receive and deliver process streams. The reactor outlets are at their equilibrium compositions. Furthermore, the assumption of sharp-split separators allows to calculate the flow rate of each process stream as a function of the mole fractions after condensation at the reactor outlet. A stoichiometric feed is assigned to the reactors. Since no compression is considered before the water is condensed, the selected pressure level at the reactors also defines the amount of water fed to the membrane separators. The partial pressure of water in the membrane separator must be less than its vapor pressure to prevent condensation. The molar fraction of water condensing in CD 1 and CD 12 is calculated using Raoult's law for ideal gases (calculation in Supplementary Section A.1).

For RWGS and SR, the thermal energy requirements are calculated from the reaction enthalpy at T_{RWGS} and T_{SR} , respectively. Normalized temperature and pressure, i.e., ambient temperature and pressure, are assigned to the substance-nodes. Therefore, a recycle stream will reach the ambient conditions before being heated and compressed to the actual requirements at the reactors. Separation methods such as VPSA and amine absorption comprise sequences of operation and regeneration steps, each being associated with predefined (T, p) values. (T, p) changes between consecutive tasks are accomplished by adiabatic compression and heating from external utilities. Expansion and cooling are not considered in the energy calculations, which justifies the most conservative scenario setting for externally supplied heat and power. An exception is made for cryogenic condensation and storage, whose power demand is calculated from the definition of coefficient of performance (COP), 60% of its ideal value [108]. Furthermore, vacuum is normalized by adiabatic compression, from 0.2 bar to ambient pressure, before any other compression stage occurs to attain the required final pressure at the next unit. Pressure drops in the single membrane module is calculated as 13% of the feed pressure, and a sequence of 10 stages is assumed. Permeate pressure is always atmospheric. Lastly, the regeneration heat for an amine scrubber requires $0.198 \text{ MJ mol}_{\text{CO}_2}^{-1}$ and is conducted at 1.5 bar and 393 K [109].

3.4 Optimization problems

The scope of retrofitting a steam reforming plant by adding an electrolyzer and a RWGS reactor, together with a biogenic feedstock of limited availability, is to attain more sustainable operations. This can essentially result from

- minimizing the total energy requirement, independently on the source of electricity;

- maximizing the overall utilization of carbon atoms as feedstock or for utility generation, thermal and electrical;
- minimizing any surplus in CO₂ and CH₄ from biogas;
- minimizing biogas utilization, if locally limited;
- minimizing the contribution of endothermic processes, locally for thermal energy inputs and remotely for any electrical input coming from power-plants.

The contribution of endothermic processes can be quantified by the equivalent amount of CO₂ generated within a combustion process. Accounting for natural gas or bio-methane as reference fuel, it can be assumed that one mole of CH₄ yields one mole of CO₂. Therefore, dividing the thermal power $\sum \dot{Q}$, given as summation of the single contributors, by the lower heating value of CH₄ (LHV_{CH₄}), the corresponding CO₂ is obtained:

$$\dot{N}_{\text{CO}_2, \text{th}} = \frac{1}{\text{LHV}_{\text{CH}_4}} \sum \dot{Q}. \quad (3.1)$$

If a powerplant generates the required electric power to the plant $\sum \dot{W}$ when the renewable power is scarce, its efficiency η_{PP} is integrated in the calculation:

$$\dot{N}_{\text{CO}_2, \text{el}} = \frac{1}{\text{LHV}_{\text{CH}_4}} \frac{1}{\eta_{\text{PP}}} \sum \dot{W}. \quad (3.2)$$

As reported in the introduction to this chapter, additional makeup biogenic CO₂ may be required and is allowed to the process. Makeup CO₂ can also be recycled from the hot utility loop, as long as exclusively provided from bio-methane, and as fossil carbon is not present in the off-gases.

System configurations that maximize carbon efficiency are those allowing the least surplus of carbon-containing molecules. Their cumulative contribution is denoted as absolute carbon emission (CEabs) in molar flowrate, with or without renewable electricity, respectively:

$$\dot{N}_{\text{CE,abs},(\exists\text{REN})} = \sum_{j \in \{\text{CH}_4, \text{CO}_2\}} \dot{N}_{j,\text{surplus,system}} + \dot{N}_{\text{CO}_2,\text{th,tot}} - \dot{N}_{\text{CO}_2,\text{th,bio,recycle}} \quad (3.3)$$

$$\dot{N}_{\text{CE,abs},(\nexists\text{REN})} = \sum_{j \in \{\text{CH}_4, \text{CO}_2\}} \dot{N}_{j,\text{surplus,system}} + \dot{N}_{\text{CO}_2,\text{th,tot}} + \dot{N}_{\text{CO}_2,\text{el}} - \dot{N}_{\text{CO}_2,\text{th,bio,recycle}} \quad (3.4)$$

Equations (3.3,3.4) indicate that excess CO_2 and CH_4 from the process lines of the synthesis process ($\dot{N}_{j,\text{surplus,system}}$) and the CO_2 generated in the utility lines from combustion processes and externally, in a powerplant for electricity generation, contribute to CEabs. However, if bio- CH_4 is burned, it can be recycled as makeup CO_2 , provided that no natural gas is fueled. Surplus CH_4 is what remains from the process lines of the synthesis and from combustion in the utility lines (locally, for thermal energy, more details in Supplementary Section A.2).

As it is formulated, CEabs is not necessarily an indicator of the actual carbon footprint of the process, as surplus CH_4 and biogenic CO_2 from the synthesis possibly contribute, although normally assumed as carbon-neutral. However, it is a good indicator of resources utilization, as it allows to lump in the same problem the minimization of CO_2 emissions due to energy production, Equation (3.1) and (3.2), with surplus carbon from the synthesis.

Therefore, minimizing CEabs is an intuitive approach to identifying an efficient process and these equations will constitute the optimization objective, shortly to be introduced. However, it should be noted that the negative term $\dot{N}_{\text{CO}_2,\text{th,bio,recycle}}$ in Equations (3.3,3.4) has profound implications. Essentially, maximizing the recycle of CO_2 from the combustion of bio- CH_4 as feedstock makes it the preferred fuel over natural gas and reduces the dependency on an external CO_2 stream from a pipeline or a different process system outside the battery limits. Although this is a legitimate approach and will be discussed later in this work (Section 3.7), it will always favor topologies and operation modes that maximize the contribution of endothermic processes, preferably fueled with bio- CH_4 , over solutions that maximize the use of electricity. Especially if biogas is locally limited, using it as a fuel to generate the required amount of CO_2 for the synthesis may be less feasible than integrating an external source of captured CO_2 in a highly electrified system. In other terms, if the negative term is excluded from the objective functions, the minimization of Equation (3.3) actually favors electricity over combustion, possibly saving biogas, whereas, on the contrary, combustion will be favored over electricity when Equation (3.3) is minimized due to the massive penalization of grid electricity (powerplant efficiency is $\eta_{\text{PP}} = 0.34$ [110]).

Considering the above, for a first optimization approach, the recycle stream $\dot{N}_{\text{CO}_2,\text{th,bio,recycle}}$ is excluded from the objective functions of the linear programs. However, for the correct interpretation of results, optimal solutions are post-processed to admit, wherever possible, the biogenic CO_2 waste stream from combustion as feedstock for the synthesis process, along with externally supplied makeup CO_2 .

Three relevant optimization objectives read:

$$\min \quad \dot{W} + \dot{Q} \quad (\text{A})$$

$$\min \quad \dot{N}_{\text{CE,abs},(\exists\text{REN})} + \dot{N}_{\text{CO}_2,\text{th,bio,recycle}} \rightarrow \dot{N}_{\text{CE,abs},(\exists\text{REN})}^* \quad (\text{B})$$

$$\min \quad \dot{N}_{\text{CE,abs},(\# \text{REN})} + \dot{N}_{\text{CO}_2,\text{th,bio,recycle}} \rightarrow \dot{N}_{\text{CE,abs},(\# \text{REN})}^* \quad (\text{C})$$

Problem (A) represents the minimization of the total power requirement, with or without renewable energy, where no distinction is made between electrical (\dot{W}) and thermal power (\dot{Q}). In essence, this formulation represents the cost of energy, in case the cost of electricity, even if it is provided by renewable sources, is comparable to the cost of an external fuel for heat supply. As earlier stated, neither thermal nor electrical power recovery is considered: gas expansion and cooling are not accounted for in the objectives. Aim is to identify energy efficient configurations, regardless of the atom efficiency. Problems (B) and (C) are the minimization of absolute carbon emissions, when CO_2 is generated accounting for a reference fuel (methane) as thermal power source: electricity can either be fully provided by zero-emissions sources, i.e. solar and wind, Problem (B), or by the reference powerplant running on natural gas, Problem (C). Formulations (B) and (C) are intended to emphasize that $\dot{N}_{\text{CO}_2,\text{th,bio,recycle}}$ is excluded from the objective functions, without affecting the formulation of absolute carbon emissions in molar flows as in Equations (3.3,3.4), since this term cancels out: the definition of CEabs can be used in its original form for the interpretation of results. Objective (C) minimizes the electric power demand, while (B) does not, thus potentially leading to highly electrified topologies at the expenses of the total energy demand. Although in general (A), (B) and (C) are completely different objectives, it is expected that (A) and (C) determine similar or identical results if energy efficiency dominates over atom efficiency, typical of strongly endothermic processes with few process candidates.

3.4.1 The cost of carbon efficiency

The objective functions are combined to define multi-objective optimization tasks, where a pseudo cost ω represents the relative cost of externally purchased renewable electricity compared to a reference fossil fuel such as natural gas. The value of ω allows for a generalized OPEX analysis, while still allowing for the identification of important policy implications on the cost of natural gas and the impact of purchase agreements for green power (PPAs) on process operations. Therefore, if available, renewable electricity has no carbon footprint and may be relatively inexpensive $\omega \rightarrow 0$, or relatively expensive $\omega \rightarrow 1$. If green electricity is not available, the optimization scenarios attribute a carbon footprint to grid electricity, as well as a relative cost ω . If renewable power is available, the final multi-objective function combines Objective (A) and (B), and reads:

$$\min \quad (\dot{W} + \dot{Q})\omega + (\dot{N}^*_{\text{CE,abs,}(\exists\text{REN})}) (1 - \omega), \quad (\text{A})+(\text{B})$$

The combination (A)+(B) in a multi-objective optimization program represents the trade-off between sustainability of renewable electricity and its cost: the minimization of carbon emissions ($\omega \rightarrow 0$) may result in high energy requirement, acceptable only if the cost of renewable power is low. If this is not the case, intermediate configurations for $\omega \rightarrow 1$ should be enforced.

If renewable power is unavailable, it combines (A) and (C):

$$\min \quad (\dot{W} + \dot{Q})\omega + (\dot{N}^*_{\text{CE,abs,}(\# \text{REN})}) (1 - \omega), \quad (\text{A})+(\text{C})$$

For each syngas ratio, an optimization problem is solved.

Linear programs were implemented and solved in MATLAB2018b by the dual-simplex algorithm.

3.5 Multi-objective optimization by combination of Objective (A) and (B): renewable power is available

Figure 3.3 illustrates the results from the combination of Objectives (A), the total energy (y-axis), and (B), the absolute carbon emissions into a single linear multi-objective optimization problem: Objective (A)+(B), which accounts for the use of carbon-free renewable electrical power (as defined in Section 3.4). The x-axis reports net CO₂ emissions, as motivated in Section 3.3). The syngas ratio $r = \text{H}_2/\text{CO}$ is defined in $\{0, 6\}$. Brightening tones of blue denote increasing syngas ratios. For any given syngas ratio, a Pareto-front of four solutions is outlined as the value of the weight factor ω spans within the range $[0, 1]$. Each Pareto-optimal solution determines a well-defined operation and topology of the plant. The extreme solution points coincide with the minimization of objective (A) (total power, low on the y-axis, pseudo cost $\omega = 1$, in purple) and (B) (minimum absolute carbon emissions, pseudo cost $\omega = 0$, in green). At $\omega = 0$, solutions lay vertically on the ordinate axis, indicating that absolute carbon emissions are absent. Total energy consumptions for setups identified at extreme values of the weight factor $\omega = \{0, 1\}$ differ by a factor 1.6-1.9. Additionally, two sets of intermediate Pareto-optimal solutions are shown. The solution highlighted by a dashed red line corresponds to a configuration with a negligible improve in total energy requirement at substantial larger absolute carbon emissions. Although it may be tempting to exclude this option from the reasonable candidates, this requires a deeper analysis, proposed in the upcoming Section 3.5.2 on separation topologies. The remaining solution

indicated by a dashed box differs from the configuration at the minimum total power demand for syngas ratios equal or greater than 2, whereas they overlap for $r = \{0, 1\}$ (the darker markers). For increasing syngas ratios $r > 3$ towards pure H_2 generation, all solutions along the Pareto front tend to converge to a point of zero net CO_2 emissions at a comparable power demand of $0.46 MJ mol_{\text{syngas}}^{-1}$. This trend towards zero net CO_2 emissions can be motivated by the increasing dominance of water electrolyzer for pure H_2 production.

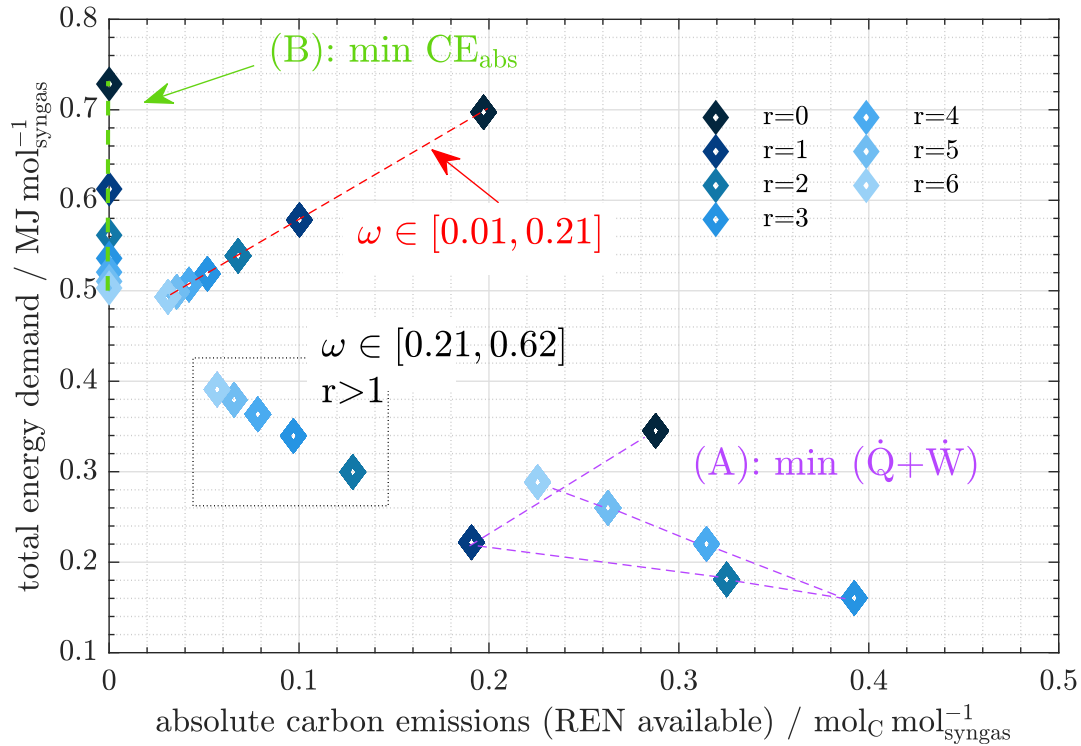


Figure 3.3.: Renewable electricity is available: multi-objective optimization results combining total energy and absolute carbon emissions minimization by means of a weight factor ω . At extreme values of ω , the multi-objective optimization results are indicated with colors, where the objective function coincides with the minimization of Objective (A) (total energy, for $\omega = 1$, in purple) and (B) (absolute carbon emissions, for $\omega = 0$, in green), respectively. Different ω values generate two sets of intermediate solutions (in red and within the black rectangle). Discretization of ω : 1×10^4 points. The H_2 -to- CO ratio is indicated with r .

In the next sections, system configurations and individual energy demands are being discussed, primarily focusing on the extreme cases of the Pareto-front, with a comment on the implications of intermediate set for $\omega \in [0.21, 0.62]$. At first, topological results are reported with focus on the activation and interaction of plant macro-sections, e.g., RWGS and SR reactors with related separation trains, electrolyzer (EL), and anaerobic digestion (AD) with biogas upgrade. Details on the topological results for the individual separation trains follow.

3.5.1 Minimum absolute carbon emissions with renewable power - Objective (B)

Figure 3.4 reports the breakdown of the total energy demand, electrical and thermal, by single plant section if the absolute carbon emissions value is to be minimized in presence of renewable electricity – Objective (B). Therefore, the cumulative energy demands coincide with the solutions highlighted in green in Figure 3.3. The total energy demand is specific molar (syngas) for increasing H₂-to-CO ratios.

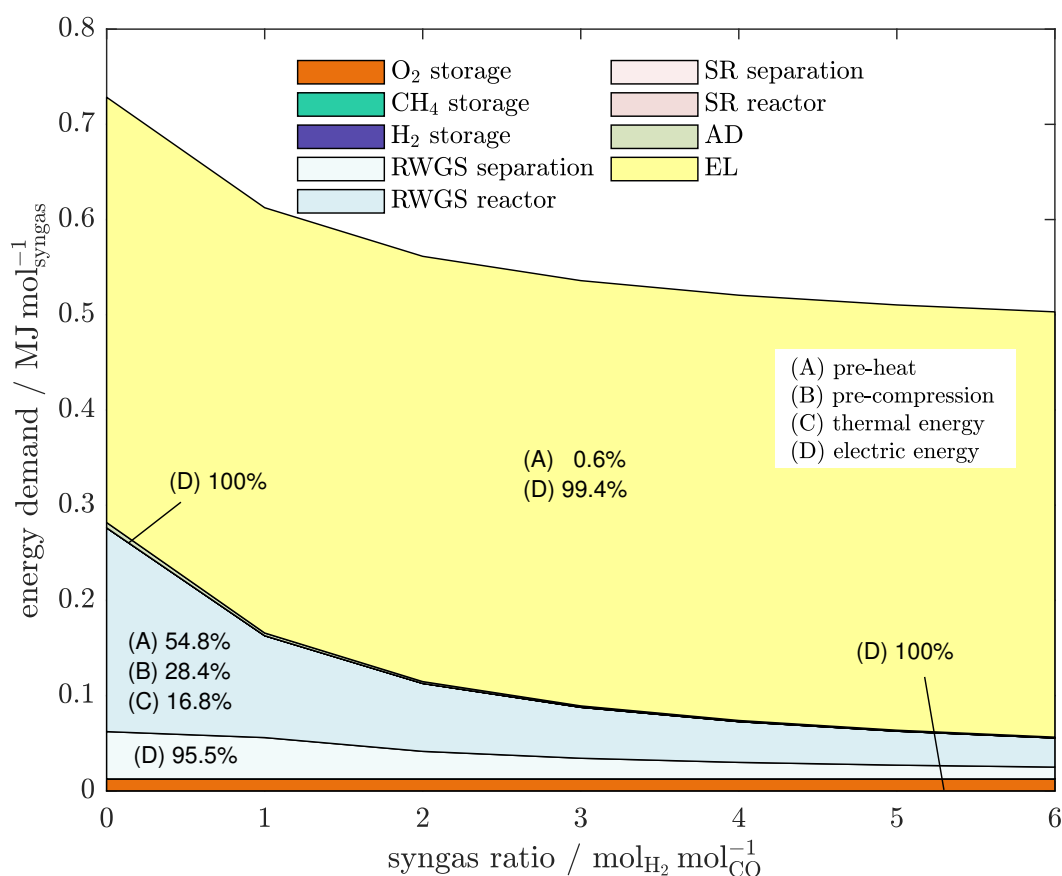


Figure 3.4.: Minimum absolute carbon emissions and relatively inexpensive, available renewable power – Objective (B) ($\omega = 0$): power contributions of reactors, separation sections, and storage systems for surplus O₂, CH₄.

Results show that the pre-existing standard steam reforming section is not being operated. In contrast, the prevailing duty is represented in yellow by the electrolyzer, which can make almost exclusive use of renewable electricity, with a thermal contribution for pre-heating of 0.6%. Therefore, the generation of CO₂ from combustion in this step is negligible. The EL unit generates H₂, partly contributing to the outlet syngas stream, but also required for the reduction of CO₂ in the RWGS reactor, whose thermal and electrical duties are reported in blue (reactor) and light

blue (separation section). Oxygen, the second end of the EL outlets, is then stored as valuable byproduct (in orange), to be exported or used in other plants in the surroundings. As CO is exclusively produced by CO₂ reduction in the RWGS step, the total energy demand at RWGS (thermal) drops along the x-axis, as does the CO for lower syngas ratios. Conversely, the energy demand at EL is essentially constant within the domain, and so is the energy required to store O₂: the overall demand for H₂ within the process is unvaried, as it either contributes directly to the product syngas or it reduces one mole of CO₂ to generate one mole of CO.

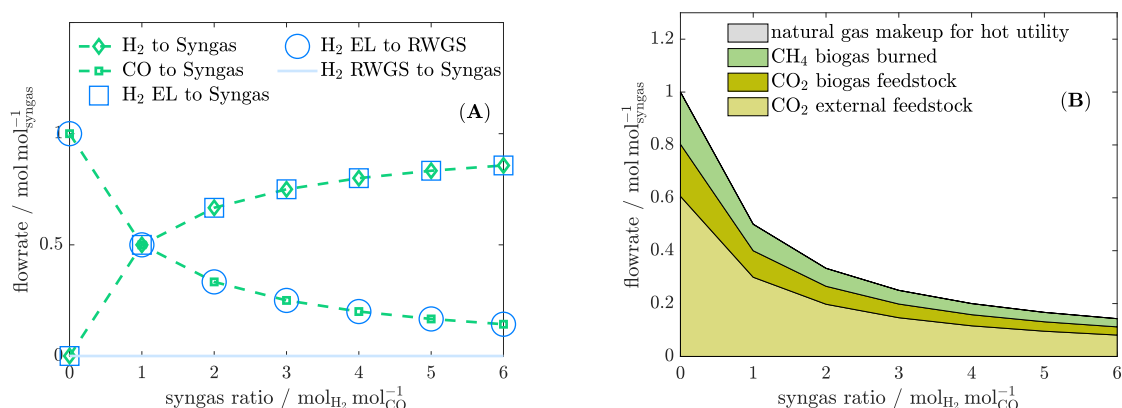


Figure 3.5.: (A) Relevant specific molar flowrates as a function of the syngas ratio for minimum absolute carbon emissions in presence of renewable power – Objective (B); (B) feed policies for CH₄ (from biogas or from natural gas), and CO₂, from biogas or external.

The specific fluxes reported in Figure 3.5(A) confirm that the electrolyzer is operated at a fixed H₂ flow for any syngas ratio: the cumulative contributions of H₂ flowrates at EL outlet directed to the product and to the RWGS for CO₂ reduction marked with blue squares and circles, respectively, is unitary. The H₂ flow fed to RWGS coincides with the outlet CO to syngas, consistent with the presence of a recycle stream for unreacted H₂ and CO₂.

Figure 3.5(B) shows that most of the biogenic carbon required at the product is provided externally. The admission of biogas is limited by the fact that the selected process is mildly endothermic. Therefore, its heat demand can be fulfilled by combustion of bio-CH₄ before the requirement for CO₂ at the RWGS reactor for CO generation is fulfilled by the remaining bio-CO₂, recycled from bio-CH₄ combustion and also provided after biogas upgrade. This is mathematically constrained by Equation A.3 in the Appendix, also reported here for clarity:

$$\dot{N}_{\text{CH}_4, \text{surplus, burned}} \leq \dot{N}_{\text{CO}_2, \text{th, tot}}, \quad (3.5)$$

which states that the maximum amount of bio-CH₄ burned cannot be larger than what is imposed by the total thermal demand of the system. This finding is consistent with the choice expressed

in Section 3.4 to exclude the recycle stream of bio-CO₂, obtained from the combustion of biogas for heat generation, from the objective functions. As already discussed, this choice favors highly electrified processes for the minimum carbon emissions when renewable power is available and relatively inexpensive, Objective (B), thus identifying configurations which limit the need for combustion in general, and combustion of bio-CH₄ in particular. On the contrary, if the recycle flow $\dot{N}_{\text{CO}_2, \text{th}, \text{bio}, \text{recycle}}$ is favored in the target, potentially highly endothermic setups based on the combustion of bio-CH₄ and still zero absolute carbon emissions can be expected, which may or may not be desirable depending on the availability of biogas and external CO₂.

3.5.2 Separation train: optimal topologies - Objective (B)

Figure 3.6 highlights in blue the selected path for pure CO production ($r = 0$). For other syngas specifications, the path is highlighted in green. Figure 3.6 and the following illustrations of the topology selected after RWGS are intended to highlight the selected separators. For this reason, the product streams are not shown. Instead, Section 3.5.1 reports the actual trend in feedstock supply and destination of H₂ from the electrolyzer. The breakdown of energy demand in the form of heat and electricity for the RWGS reactor-separation train at different syngas ratios r is reported in Figure 3.4: the separation train requires mostly electric energy inputs (95%), due to the penalization of carbon emissions from combustion for heat generation.

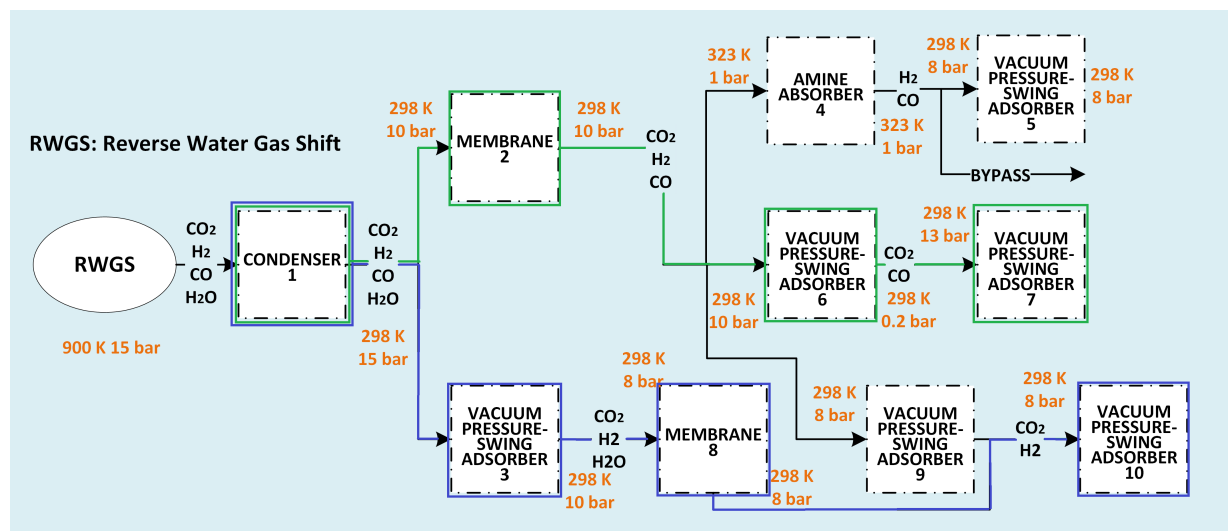


Figure 3.6.: Optimal topology for the separation train (Objective (B)).

As to be expected, path 1-2-4-5 is not selected due to the comparatively higher thermal demand of the amine absorber. In all selected topologies, the mixture is separated completely, which may not be desirable from a CAPEX and a total energy perspective. Alternatively, if separator VPSA 9 or membrane 8 are selected, the binary mixture (H₂, CO₂) obtained may be entirely recycled back to the RWGS reactor. Therefore, from a CAPEX and total energy perspective, one of these routes may be more viable. To inspect this approach, a minor penalization of the thermal energy supply is

imposed by setting the weight factor ω to 0.01. This is sufficient to attain the solutions highlighted in red in Figure 3.3.

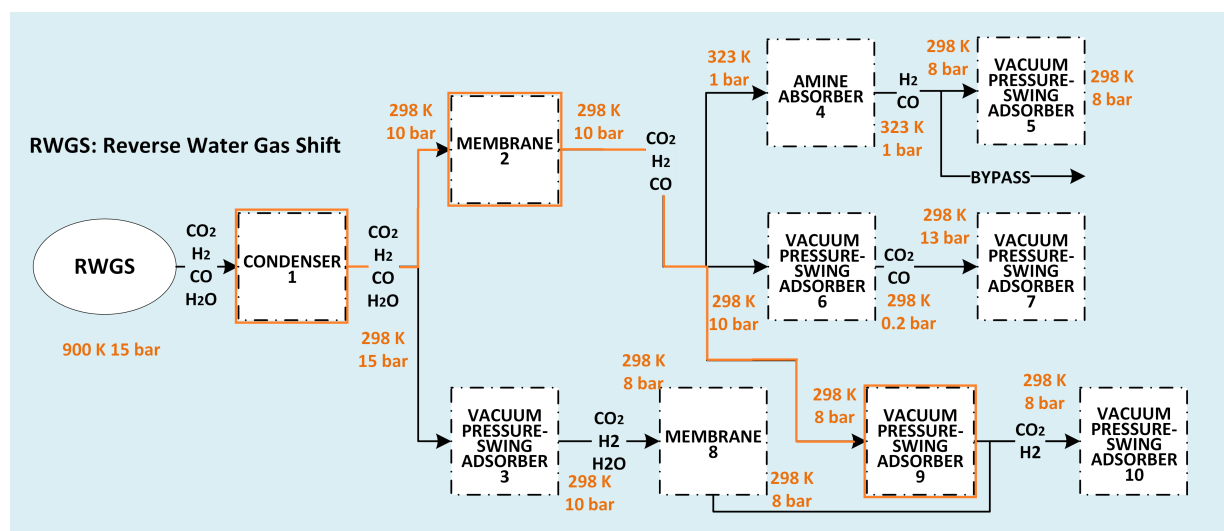


Figure 3.7.: The optimal topology for intermediate Pareto-optimal solutions at $\omega \in [0.01, 0.21]$ is highlighted in orange, for any value of the syngas ratio r .

Figure 3.7 highlights the selected separation sequence at $\omega \in [0.01, 0.21]$. As previously assumed, the separation train implies the complete recycle of the binary mixture (H_2, CO_2) back to the reactor feed. For this separation path, due to the (marginal) penalization of electricity at this value of the weight factor ω , the required electrical energy drops to 90.7%, thus requiring a higher share of thermal energy if compared with topologies in Figure 3.6. However, this is not the reason for the significant increase in absolute carbon emissions shown in Figure 3.3, as the thermal energy requirement of this separation train is a minimal contribution to the overall energy requirement (Figure 3.8(B))

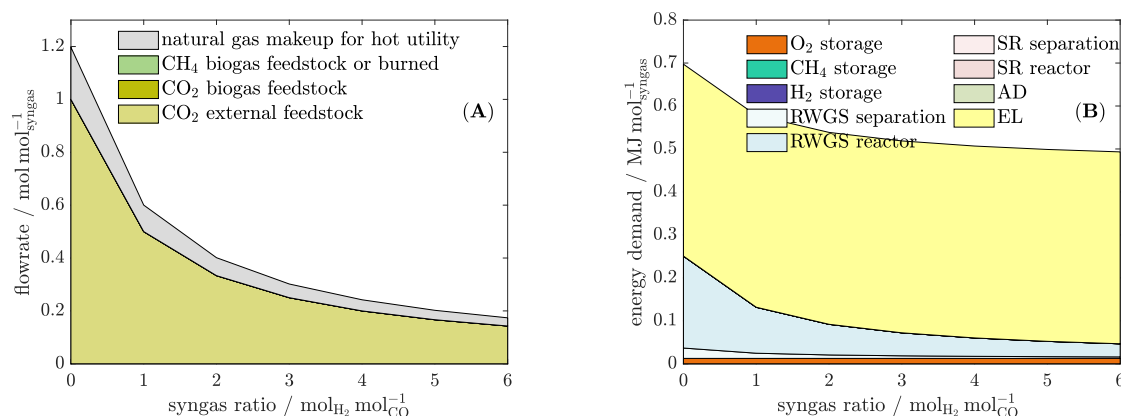


Figure 3.8.: (A) Feed policies for CH_4 (from biogas or from natural gas), and CO_2 , from biogas or external at $\omega \in [0.01, 0.21]$; (B) energy demand.

Figure 3.8(A) shows that biogas is not admitted as feedstock to the process. On the contrary, external CO₂ makes up for the carbon demand of the process entirely, whereas the heat demands are completely fulfilled by an additional stream of natural gas. This is now motivated by the minor penalization of the electrical supply. Since anaerobic digestion and biogas upgrading section require a small amount of electric power, the optimizer excludes them from the solution, thus favoring external natural gas to sustain the process.

All this considered, if biogas is available locally, anaerobic digestion should be forced in the solution pathway to avoid the use of natural gas. However, the energetically most attractive separation sequence after RWGS is the latter, reported in Figure 3.7.

So far it has been assumed that electric energy is not penalized, due to the fact that renewable power can be assumed at zero carbon footprint. However, this does not account for the cost of energy: although comparatively inexpensive where readily available, the price of PPAs varies according to regional availability and demand. If the renewable power is locally generated, it is penalized by its levelized cost of energy. The next sections investigate the results of Problem (A), which weights the electric energy by the same factor as the thermal energy contribution.

3.5.3 Minimum absolute carbon emissions with renewable power - Objective (A)

Figure 3.9 reports the energy contributions resulting from the minimization of the total energy demand – Objective (A). Up to a syngas ratio of 3, the stoichiometric outlet of a steam reforming, the electrolyzer is not operated. Instead, from an energetic perspective it is more convenient to divide the task of producing CO between steam reforming, highly endothermic but yielding an excess of H₂, and RWGS, the latter lowering the total energy demand due to its moderate endothermic contribution. In blue, the demand at RWGS is reported. In grey, the contribution of steam reforming, which continues for syngas ratios above 3. In this region, RWGS is not active: to attain high syngas ratios it is energetically more convenient to generate the required amount of CO via steam reforming, although thermally demanding, than to produce an excess of H₂ via electrolysis for CO₂ reduction in the RWGS reactor, although less demanding from the thermal energy requirement. The benefit of a reduced thermal duty by RWGS operations over SR would then be lost due to the dramatic increase in electric duty to be supplied by the electrolyzer. As EL is being operated, excess O₂ is stored (the area in orange). The separators require considerably less energy than the reactors.

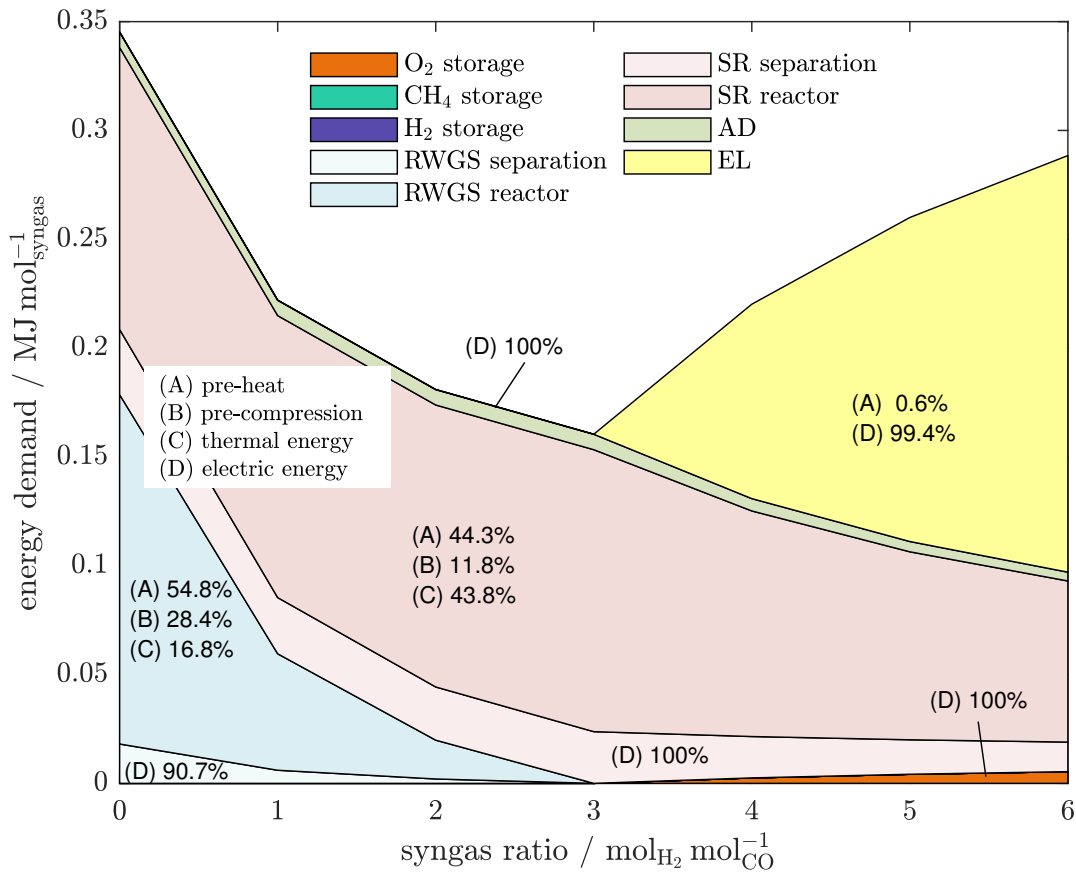


Figure 3.9.: Energy demands for minimum total power – Objective (A) ($\omega = 1$): power contributions of reactors, separation sections, and storage systems for surplus O_2 and CH_4 .

Relevant trends in H_2 production are shown in Figure 3.10(A). Up to a syngas ratio of 3, the whole H_2 requirement in syngas is covered by SR (curve "H₂ to Syngas", in green), which also supplies H_2 for the reduction of CO_2 in RWGS ("H₂ from SR to RWGS"). Above a syngas ratio of 3, the electrolyzer activates to complement the syngas requirement for H_2 together with SR. Therefore, also in this case the RWGS separation train will have to recycle the binary (H_2, CO_2) mixture back to the reactor inlet.

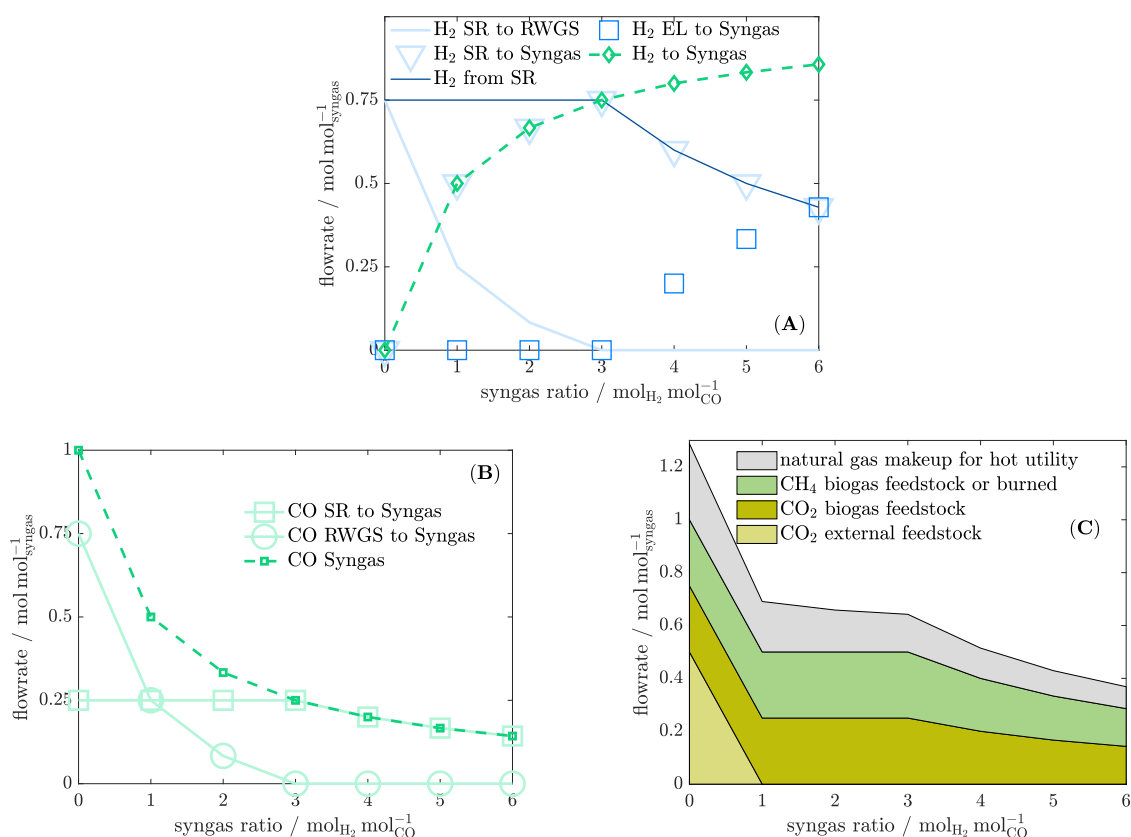


Figure 3.10.: (A) Molar flowrates of the H₂ streams: total H₂ from the steam reformer outlet (H₂ from SR), share of H₂ from SR fed to the RWGS reactor for CO₂ reduction (SR to RWGS), and to the product stream (SR to Syngas). In green, H₂ stream to the product (H₂ to Syngas) and from EL to syngas (blue square markers); (B) CO flowrates to the product (CO to Syngas), from the reformers outlets to Syngas (CO from SR and RWGS to Syngas); (C) CH₄ and CO₂ feedstock to the reactors (in tones of green), where excess CH₄, if available, can be burned to produce thermal energy.

The synergy between RWGS and SR can be appreciated in Figure 3.10(B), which reports the specific flowrates of CO production. Below a target ratio of 3, the flowrate of CO produced by SR is constant, whereas the contribution of RWGS decreases. As illustrated in Figure 3.10(A), SR supplies the entire flowrate of H₂ required in the syngas stream (light-blue dashed curve, marked with triangles, and green curve, marked with diamonds), which means that RWGS completely recycles the unconverted H₂ back to its feed. Clearly, above the syngas ratio of 3, the electrolyzer operates proportionally to the syngas ratio whereas SR adapts to the decreasing trend in CO contents in the syngas stream.

Figure 3.10(C) reports the feedstock requirements of the process. As no surplus of bio-CH₄ is left after the synthesis that could be used for heat generation purposes, the plant always relies on natural gas. However, as discussed in the previous Section 3.5.2, this contribution can be substituted by additional bio-CH₄, if enough biomass is available, thus contributing to the required makeup of CO₂ at syngas ratio $r = 0$. Figure 3.11 shows the contributions to the absolute carbon

emissions, with a peak at $r = 3$, corresponding to the maximum utilization of steam reforming. Its stoichiometric outlets coincide with the syngas ratio: the SR reactor requires the available bio-CH₄ as feedstock, therefore additional fuel is required to power the process step. Excess CH₄ from the synthesis in light blue is not shown in the figure. This indicates that CH₄ is preferably used for the synthesis, bringing CO₂ into the system in the required biogas stream and resulting in a CO₂ surplus from the synthesis steps.

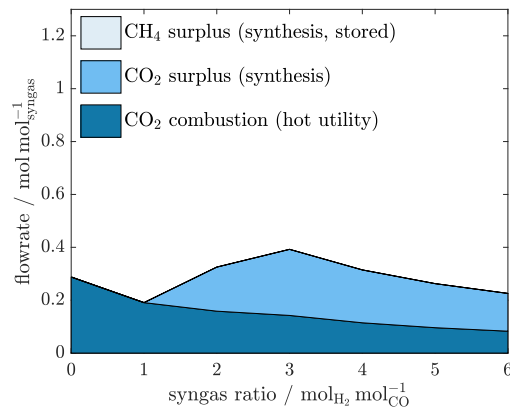


Figure 3.11.: Absolute carbon emissions by contribution. In dark blue, CO₂ is produced by combustion processes for thermal energy generation; an intermediate tone of blue indicates the excess CO₂ from the synthesis, therefore not being reduced to CO. In light blue, CH₄ surplus not utilized in the synthesis which is preferably burned and, if the thermal demand is then completely fulfilled, the remaining is stored.

In this setup, no appreciable differences are to be reported concerning topology of the separation system, which correspond to the solution shown in Figure 3.7.

3.5.4 Intermediate solutions: weight factor within the interval 0.21 - 0.62

Figure 3.12 shows the specific energy contributions for the intermediate Pareto front solutions reported in Figure 3.3 and highlighted by the black dashed rectangle: for syngas ratios $r \leq 1$, no difference can be observed if compared to solutions at the minimum total energy (Objective (A), $\omega = 1$). However, $r > 1$ and for $\omega \in [0.21, 0.62]$, the electrolyzer starts operating, thus reducing the carbon emission of the process at the cost of the overall energy demand. However, this operation mode may prove interesting if profitability and flexibility are accounted for. Operational implications based on the identified solutions will be further investigated in Section 3.8.

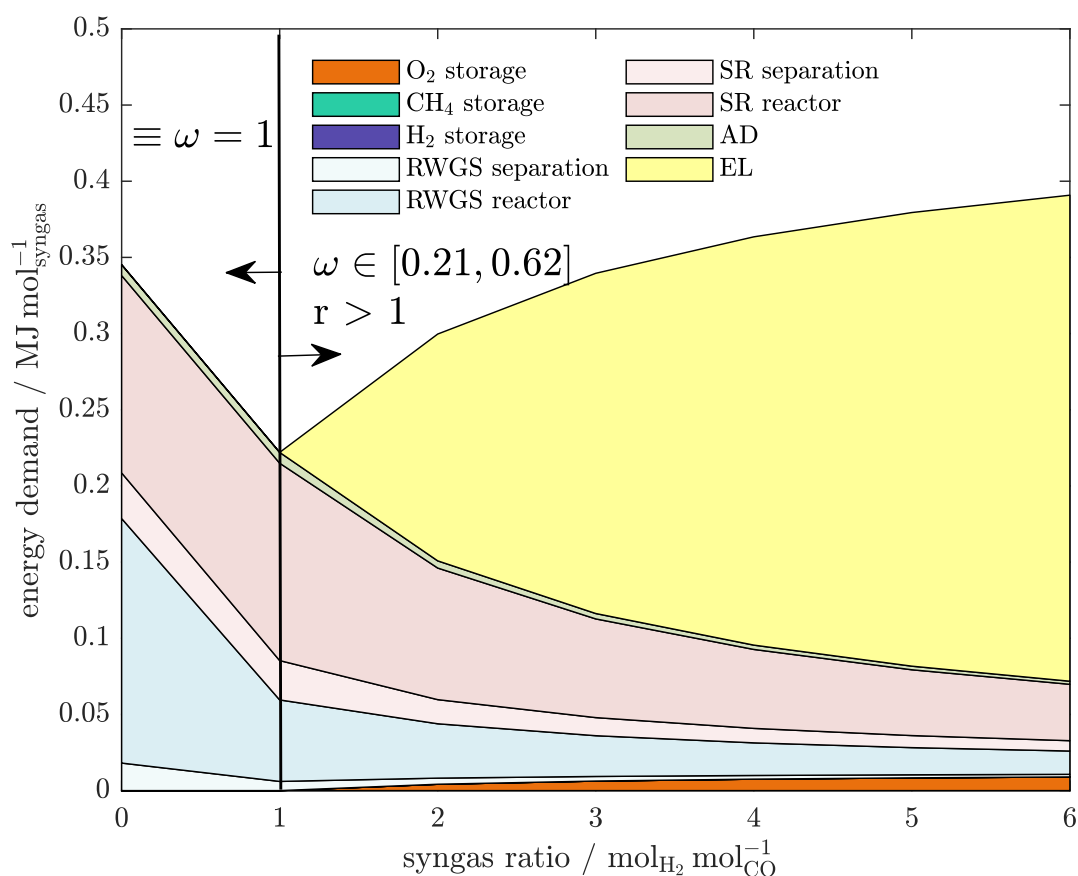


Figure 3.12.: Pareto-optimal solutions for $\omega \in [0.21, 0.62]$ and H₂-to-CO $r > 1$. The region $r \leq 1$ is labeled with $\equiv \omega = 1$: for syngas ratios $r \leq 1$, results at $\omega \in [0.21, 0.62]$ coincide with results at $\omega = 1$ (minimum total energy). Therefore, process configurations and related energy demands at $r \leq 1$ are the same for any value of the weight factor $\omega \geq 0.21$.

3.6 Multi-objective optimization by combination of Objective (A) and (B): electricity from powerplant

Figure 3.13 reports the multi-objective solution when renewable energy is not available and grid electricity is imported instead. In this case, no Pareto-front can be outlined. All solutions for different values of the weight factor ω coincide due to the fact that configuration at the minimum total carbon emissions and at the minimum energy coincide. This indicates the strong dominance of carbon emissions for energy generation over carbon emissions due to an inefficient use of the feedstock.

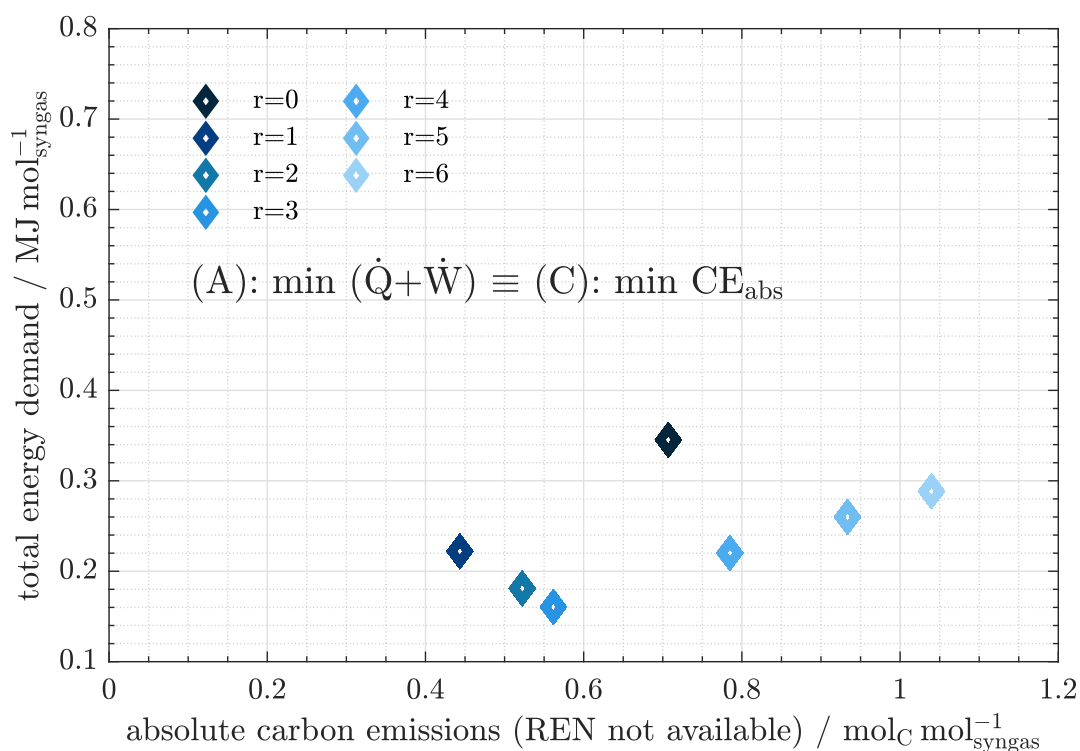


Figure 3.13.: Renewable electricity is not available: multi-objective (A)+(C). The Pareto-front is absent, as the minimization of energy and carbon efficiency identify the same configurations: as indicated within the figure, results from the minimization of Objective A and C coincide.

Therefore, process topologies and operation regimes coincide with those identified in Section 3.5.3, and the energy requirements for the process sections were already reported in Figure 3.9 for Objective (A). Solutions in Figure 3.13 correspond to those shown in Figure 3.3 at the minimal total energy with available renewable power. However, in the newly introduced scenario, the carbon footprint of grid electricity translates the points along the abscissa towards a region of higher absolute carbon emissions. Furthermore, for $r > 3$, solutions in Figure 3.3, Problem (A), are now not only translated, but also mirrored on the y-axis, attaining larger absolute carbon emissions for increasing syngas ratios: here, the electrolyzer starts to operate, which increases the

demand for electric energy, as well as the total energy requirement. The minimum total energy requirement across different optimization scenarios can be found at syngas ratio $r = 3$, i.e., the stoichiometric output of the steam reformer (cf. Section 3.5.3).

The translation along the x-axis can be also understood from Figure 3.14(A), reporting the absolute carbon emissions by contribution, corresponding to Figure 3.11 for solutions at the minimum energy in day time, with the addition of the powerplant contribution in dark blue. The cumulative value of absolute carbon emissions has a positive slope for $r \geq 3$, which clarified what already discussed. Figure 3.14(B) shows that no surplus bio-CH₄ is available for combustion, and an additional fuel is required (biogas, where availability does not set a limitation).

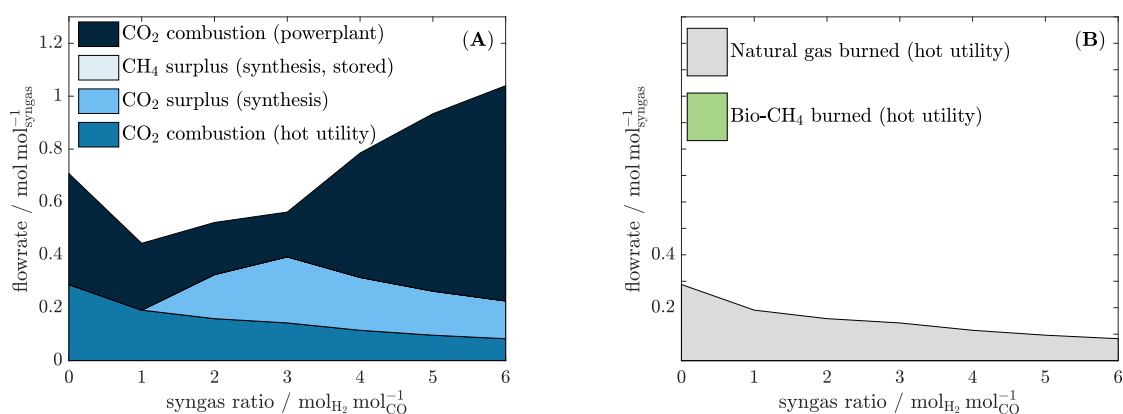


Figure 3.14.: (A) Absolute carbon emissions by contribution. From the darkest tone of blue: CO₂ generated from the combustion of CH₄ in a powerplant for electricity generation, CO₂ produced by combustion processes for thermal energy generation, excess CO₂ from the synthesis not being reduced to CO, CH₄ surplus not utilized in the synthesis and preferably burned (not present); (B) combustion of natural gas and of surplus bio-CH₄: if biogas availability is constrained, the plant should resort to natural gas for heat generation. In this case, no surplus CH₄ from the synthesis is available for the purpose of heat generation.

3.6.1 Exclusion of the steam reformer: operating electrolysis and RWGS with powerplant electricity

Sections 3.5 and 3.5.1 show that the coupling of an electrolyzer with a RWGS reactor require a substantial external CO₂ intake to operate on renewable power. This configuration maximizes the use of electricity over combustion and minimizes the use of biogas, provided that an external source of CO₂, possibly of biogenic origin, is available. The implementation of this process must ensure the use of renewable power. Figure 3.15 reports energy requirement and net CO₂-emissions in case this system were to be implemented as stand-alone process, and for a long-lasting unavailability of renewable resources. If the process does not have the ability to rely on buffered renewable electricity, product quality must be ensured at the expense of sustainability, as the process would rely solely on external energy. As a consequence, the net CO₂-emissions pattern is the highest among those reported, although the total energy requirement remains unvaried and reflects the

findings at the Pareto front in Figure 3.3 (green curve), but translating the trend to the positive side of the x-axis.

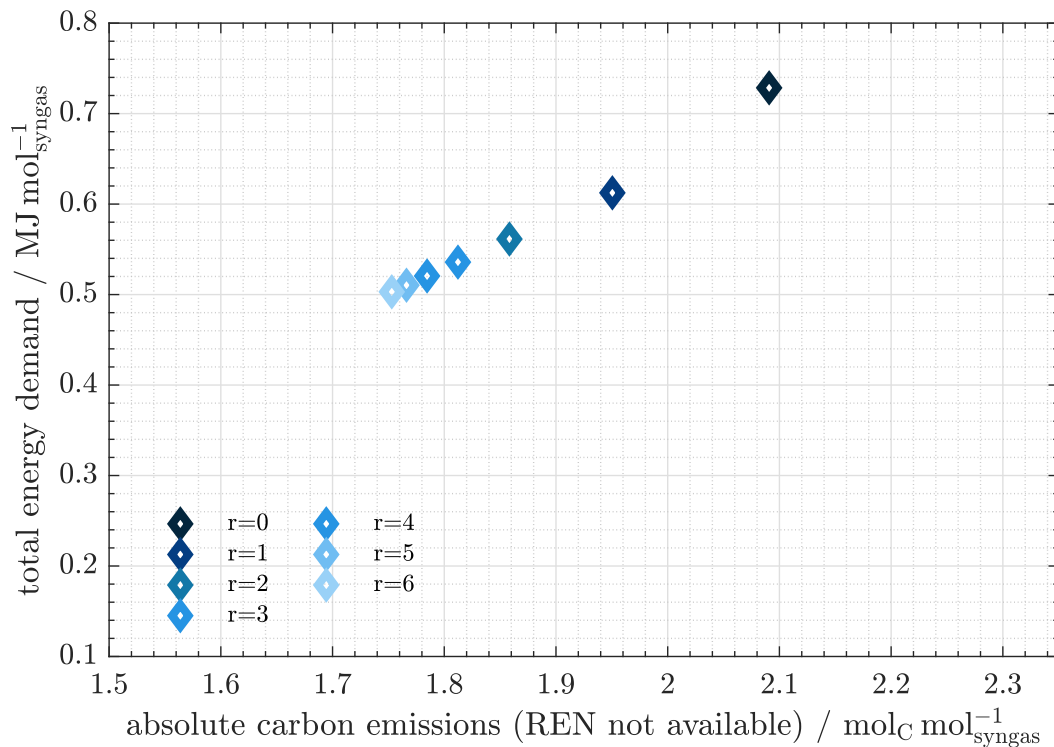


Figure 3.15.: Total power demand and net CO₂ emission if the most sustainable process solution in presence of renewable power were to be operated with natural gas-based electricity from power plant.

3.7 Inclusion in the objective function of the carbon dioxide stream recycled from combustion outlets

Section 3.4 formulated the optimization problems (A,B,C) without including $\dot{N}_{\text{CO}_2, \text{th}, \text{bio}, \text{recycle}}$, representing the recycle of biogenic CO₂ in combustion gases from hot utility generation, into the objective functions for the minimization of absolute carbon emissions. Aim was to identify highly electrified solutions when renewable power is available, without favoring the recycle of bio-CO₂ from the combustion off-gases back to the RWGS reactor inlet which, in turn, favors combustion over electrified processes (cf. Section 3.4). This section reports results obtained from

the implementation of the actual, net absolute carbon emission value as minimization objective:

$$\min \dot{W} + \dot{Q} \quad (\text{A})$$

$$\min \dot{N}_{\text{CE,abs},(\exists\text{REN})} \quad (\text{B})$$

$$\min \dot{N}_{\text{CE,abs},(\notin\text{REN})} \quad (\text{C})$$

Solutions previously identified at the minimum energy requirement in the previous sections are not expected to exhibit any modification, as bio-CH₄ was entirely converted into the required CO in the product stream.

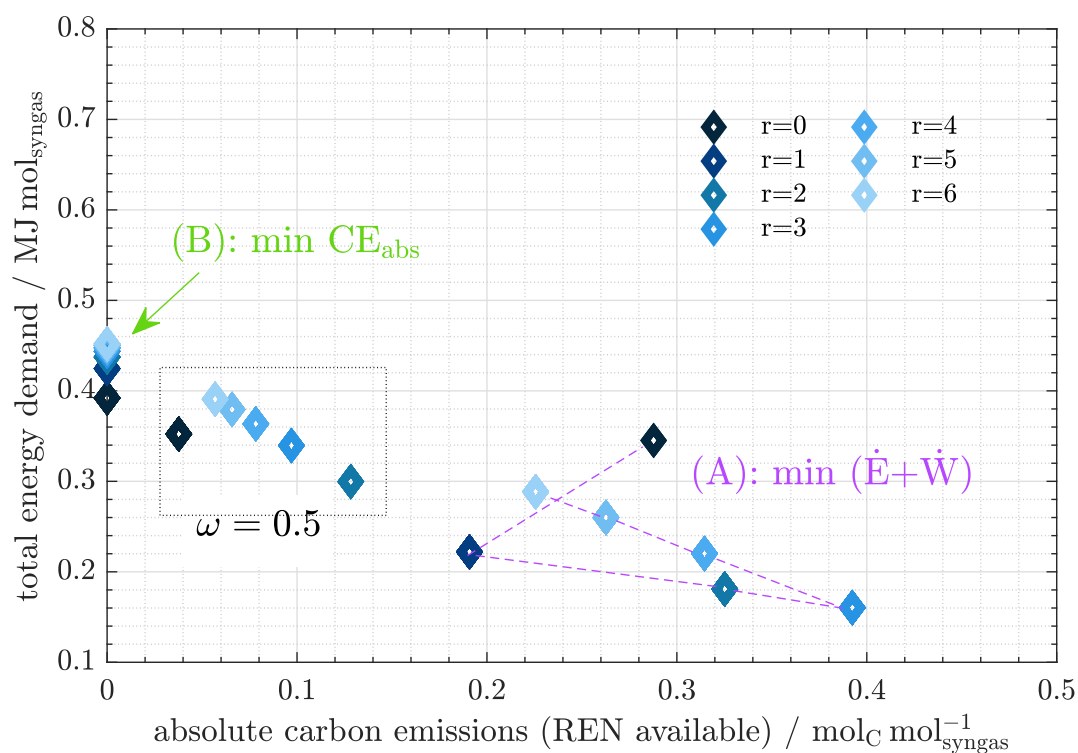


Figure 3.16.: Multi-objective solutions, renewable power is available. Recycle of bio-CO₂ from the utility stream is admitted at the reactors feed and favored in the objective function for the minimization of absolute carbon emissions.

Figure 3.16 reports 3 Pareto-optimal solutions. At positive carbon emissions, they coincide with the solutions already discussed in detail (cf. Figure 3.3, at $\omega \geq 0.21$). However, solutions at null absolute carbon emissions are now considerably less energy demanding. Therefore, only solutions at CE_{abs}= 0 are being discussed in this Section, whereas figures for CE_{abs}> 0 are reported in the Supplementary Section A.2.

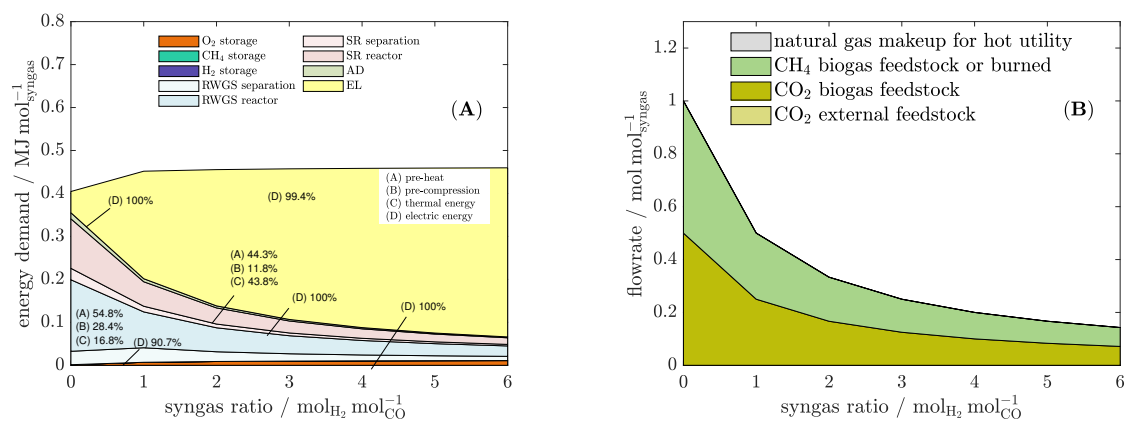


Figure 3.17.: Energy (A), CO₂ and CH₄ demand (B) for the process at minimum absolute carbon emissions with renewable electricity and inclusion of recycled bio-CO₂ from the hot utility within the objective function.

As shown in Figures 3.17(A,B), the steam reforming is operated, and biogas can entirely fulfill the heat and product requirements. Here, EL operates for any value of the syngas ratio of the given set. Even though this configuration requires considerably less energy than the corresponding plant discussed in Section 3.5.1 and operating EL and RWGS with the exclusion of SR, the latter required considerably less local biomass, provided that renewable power is not subject to availability constraints or is substantially inexpensive and a source of CO₂ externally supplied is ensured and price-competitive. If biomass is considerably limited, the current configuration must heavily rely on natural gas from the grid to ensure a steady syngas supply.

3.8 Conclusions and outlook

The approach presented in this Chapter allows to address the first fundamental research question presented in Section 1.3: "What is the impact that retrofitting has on the energy consumption of an existing natural gas reforming plant in the context of flexible plant operations?".

Several operating regimes have been identified for the retrofitting of the steam reforming train. For syngas ratios $r \leq 1$, reverse water-gas shift is always selected. When renewable power is available and the recycle of CO₂ from the combustion of bio-CH₄ is not favored in the objective function minimizing the total carbon emissions, including unreacted CO₂ and CH₄, and CO₂ in the combustion off-gases, the steam reforming section is not selected and the required H₂ is supplied by an electrolyzer operated at low temperature. This problem formulation identified the most electrified solutions. However, when the total energy or the total carbon emissions are minimized and renewable power is not available, steam reforming is always selected at any value of H₂-to-CO. This plant section reduces the duty of the water electrolyzer for supplying the required H₂ for CO₂ reduction in RWGS and to reach product specifications. The optimal separation train after RWGS is a sequence of water condensation, membrane separation to complete H₂ removal, followed by

a VPSA which removes CO, and recycle of the binary mixture (CO₂,H₂) back to reactor inlets (Figure 3.7). However, two additional separation sequences were identified if electric power is not penalized in the objective, which should then be included in a profitability analysis once the location of the project, thus local availability and cost of resources, feedstock, and vendor information regarding the budget offer of these process units, are identified.

According to the availability of resources, i.e., renewable power and biomass, and costs of the resources, the selected process topology must be able to switch between different operating points. In particular, setting a steam reformer in hot standby to ensure the most profitable and sustainable operations when renewable power is abundant and biomass is scarce (configuration EL+RWGS) may be not a feasible approach, due to the fact that these plants require to observe a minimum admissible load, or base-load. However, depending on the circumstances, the plant may be in this mode for an extended period of time and the steam reformer may be set on standby without affecting the economics of the project.

Therefore, different steady states for the plant requires that the detailed design ensures feasibility in any of them, and efficient control strategies must drive the transition. Furthermore, buffering strategies may be required to ensure that the process runs in the most profitable or safest mode. This brings back to the fundamental questions proposed in Section 1.3 and addressed later in this thesis with different CAPE tools.

Although the proposed superstructure proved to be an agile preliminary tool for screening energy demands and contributions for different renewable electricity scenarios in this retrofit context, it does not embed an exhaustive selection of possible separators for the given raw syngas mixtures. The fact that each separation task is here associated with a single, feasible separation method may exclude non-trivial separation solutions in a more general feasibility analysis of Power-to-Syngas systems. Furthermore, more reactors can be included in the superstructure to offer a complete selection of process candidates, not necessarily limited to a retrofit problem of an existing plant section. The formulation of a larger reactor-separator superstructure requires the definition of a complexity constraint, which can be used to restrain the number of potentially selected units to a predefined maximum, thus converting the LP into a MILP problem.

3.9 Chapter summary

In this chapter, an existing steam reforming process is retrofitted with the inclusion of an electrolyzer and a RWGS step followed by a train of possible separators. This modification allows for the resulting system to be operated more sustainably in presence of renewable power by enhanced electrification. Linear programming (LP) is used to investigate the potential of flexibly operating the system under intermittent renewable electrical power. Optimization results identify synergies between electrolysis, steam reforming of methane and RWGS. Unreacted H₂ and CO₂ are recycled

by VPSA after RWGS, whereas CO from RWGS and SR, and H₂ from SR and EL leave as syngas. EL is highly energy-demanding but sustainable if renewable electricity is available and relatively inexpensive compared to natural gas. On the contrary, this trend is reversed for electricity provided via power-plant. Therefore, the implementation of EL and RWGS would be unable to ensure a sustainable production for scenarios where renewable electricity is not sufficiently available, unless buffering devices or a flexible syngas production process and downstream were involved. In such cases, process-systems comprising EL, RWGS and SR allow for lower CO₂ generation levels and energy demand in that SR can substitute or complement EL as H₂ source for RWGS.

MILP approach for the analysis and screening of large Power-to-Syngas reactor-separator networks

4.1 Introduction and background

Chapter 3 proposed the use of a linear programming approach to determine the energy demand and carbon footprint of a retrofitted steam reforming plant, in the presence or absence of renewable energy. This approach is here formalized and extended to a wider range of process candidates. After reviewing the relevant contributions available in the literature, the methodology developed for this analysis is outlined. Results show that with biogas and a large availability of renewable electricity, plant configurations mainly run via electricity, which constitutes up to 97% of the total power for partial oxidation of methane interacting with water electrolysis. Alternatively, lower total demands are attained at higher thermal duties when electricity is also penalized: the endothermic-synthesis reactors are operated. With carbon dioxide as the only feedstock, the total energy demand substantially increases due to the large consumptions of direct-air capture (DAC) and water electrolysis, although different DAC technologies or biogenic CO₂ sources allow this process to be fully electrified, as shown in Chapter 3. The resulting topologies always favor membrane separation, adsorption and, more limitedly, cryogenics over absorption technologies.

As reported in Chapter 2 and summarized in several excellent review articles [111, 112, 113], many efforts have been devoted to holistic approaches for system analysis based on superstructure optimization. In the framework of solid and urban waste valorization into H₂ and power, several authors recently dedicated their efforts to propose mathematical programming problems for the identification of optimal conversion pathways such as gasification, pyrolysis, anaerobic digestion, and incineration using lumped models and with particular focus on costs and setting primary importance on the reactive systems chosen from a limited number of alternatives rather than reactor-separator sequences, critical for the production of high quality precursors for the chemical synthesis [114, 115]. Another source of thermal energy in the valorized form of bio-fuel is biomass from microalgae, which was considered in a contribution by Gani's group on process synthesis for the maximization of the gross operating margin and minimization of waste streams *via* MINLP-based superstructure optimization using lumped models [116]. Again, focus was to deliver the best reactor configuration, whereas the separation sequence was pre-determined. An important contribution in the field of syngas production from biomass has been recently given

by Kenkel et al. [117], who proposed a MILP modeling approach for biomass-to-X processes, encompassing different electrolyzer types and reactors, also including Fischer-Tropsch (FT) and methanol synthesis within the battery limits with a simplified heat integration approach. These superstructures do account for CO₂-based FT and methanol synthesis, highly investigated research topics, but not yet readily implemented on industrial scale. Furthermore, as for the aforementioned contributions, focus has been given to the reactors, whereas separation methods have been selected for the given task. A broad literature field deals with the problem of optimal separation networks, where distillation is predominantly being investigated when superstructure-based optimization is adopted, and fixed feed compositions are separated into pure products. If multiple inputs to the separation train are present, they are often treated independently in multiple single-input sequences [118, 119]. However, an approach which rigorously includes all available separation methods for a relevant number of candidate reactors for the production of synthetic gas from biogas is yet to be found in literature.

4.2 Novelty and general system framework

In this chapter, an extension to the methodology based on the state-task network (STN) representation of one-task-one-equipment (OTOE) is applied to the superstructure very compactly represented in Figure 4.1. The novelty lies in the fact that several separation methods are formulated for each separation task. This further branches the search-space, aiming at systematically including state-of-the-art process candidates, such as amine or methanol scrubbing and cryogenics, with less established technologies, e.g., the selective adsorption of CO out of a given multicomponent feed and membrane operations. Another novelty is that the selection of multiple reformers implies the generation of multiple effluent streams at different temperatures, pressures and compositions, which need for separation. Unless they are merged with a mixer after pressure normalization, they may undergo different separation pathways. Therefore, this extended OTOE approach can identify a separation sequence for each selected reactor, potentially resulting in energy savings that may justify the CAPEX for additional, smaller separators. However, the integration of integer variables and logical constraints can force the configurations to have a single separation sequence shared by multiple reformers. In addition, logical constraints can force the optimizer to select a single reactor at a time. The approach is described in detail in the next section.

This is then applied to generate and condition the syngas to the state required at the downstream applications reported once again in Table 4.1, where temperature and pressure of the downstream process selected from the range in Table 2.1. Although efforts have been made in the simultaneous layout and heat-integration optimization [120, 121, 122], the latter introduces remarkable complexity if a rigorous pinch analysis is to be integrated to a very large search space of alternative layouts. This can be handled subsequently in a more traditional methodological fashion, thus after the superstructure optimization is performed. For this reason, the current chapter focuses on layout optimization. In the present contribution, a superstructure optimization approach is

used to identify which reaction and separation steps should be chosen to produce syngas with a minimum overall energy demand. Special emphasis is put on differentiating between energy inputs in the form of heat and electricity. Biogas from anaerobic digestion, water and carbon dioxide from direct air-capture are considered as renewable raw materials. Essentially, biogas is a carbon-neutral resource, thus, it does not contribute significantly to the increase in atmospheric carbon dioxide levels, as reported by Paolini et al. [123]. As chemical reaction steps, water electrolysis, methane steam reforming, dry reforming, partial oxidation, tri-reforming and reverse water-gas shift are considered and possible synergies allowed. For the subsequent separation of the mixtures, both state-of-the-art as well as new and emerging technologies are considered. The aim is to highlight most promising flowsheets for current and future implementation, for the downstream applications reported in Table 4.1. As the main efforts are directed towards the identification of reactor-separator sequences out of an extensive number of process candidates, this implementation is limited to equilibrium reactors, although it could be extended to different reactor-feed policies and temperature/pressure levels if the states at the reactors are discretized.

Table 4.1.: Syngas downstream applications, molar ratios, temperature and pressure requirements. Data are retrieved and adapted from Table 2.1.

Downstream Application	Molar ratio H ₂ /CO	(<i>T</i> (K) , <i>p</i> (bar))
Phosgene	0	(323,3)
Monsanto Process	0.01	(473,60)
Hydroformylation	1.1	(428,170)
Iron Ore	1.4	(973,1)
Fischer-Tropsch	1.95	(30,473)
Methanol	2.15	(140,473)

As it will be clarified in the second chapter on flexible process design, the methanol synthesis is not normally conducted in pure CO but rather with a feed mixture of CO₂ and CO to reduce the exothermicity of H₂ reacting in pure CO, thus reducing the thermodynamic limitation by operating at lower temperatures. Ullmann recommends to refer to a stoichiometric number *S* slightly above 2 for the definition of feed requirements, where, in molar terms,

$$S = \frac{H_2 - CO_2}{CO + CO_2}. \quad (4.1)$$

If $S \gg 2$, H₂ accumulates in the recycle loop, if $S \leq 2$, the selectivity is hindered.

However, for the sake of comparability with the other processes, in this study CO₂ is not admitted in the product line, thus $S \equiv r = 2.15$.

4.3 System description

Syngas is produced by chemical conversion steps followed by separation and conditioning of the molar H_2/CO ratio. Figure 4.1 represents a simplified flowsheet of the system described in this Section. Purified biogas (BG) from anaerobic digestion and CO_2 from direct air-capture are the candidate carbon sources.

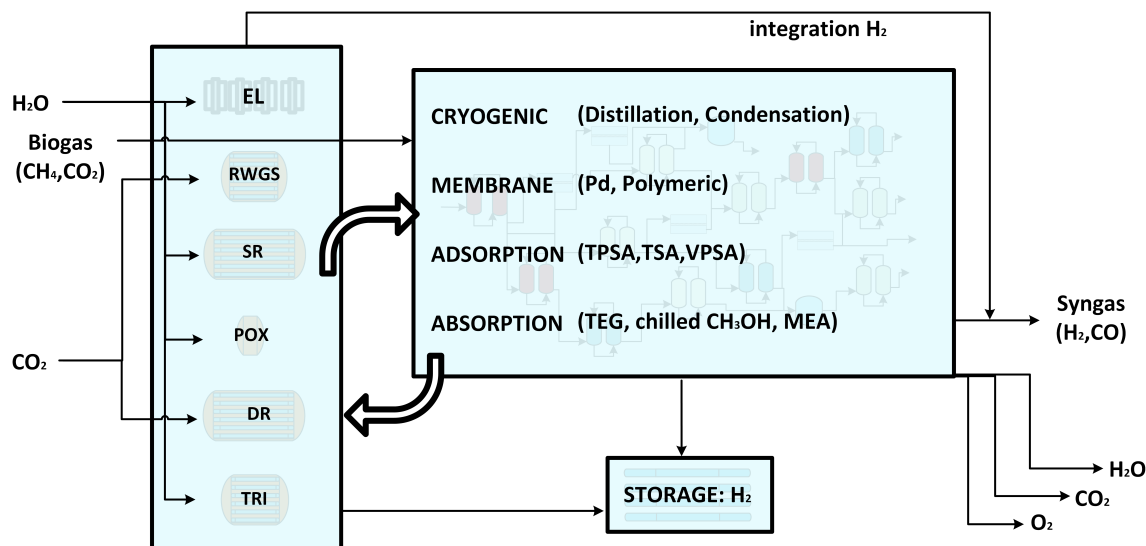


Figure 4.1.: Illustrative process flowsheet. EL = electrolyzer; RWGS = reverse water-gas-shift reactor; SR = steam reforming of methane; POX = partial oxidation of methane; DR = dry reforming of methane; TRI = tri-reforming of methane; TPSA, TSA, VPSA = temperature/pressure/vacuum swing adsorption; TEG = ethylene glycol absorption; MEA = mono-ethanol amine.

A pool of reactors generates raw syngas from the feedstocks. Biogas purification steps are not included in the analysis. Nevertheless, a 2-to-3 CO_2/CH_4 biogas mixture can be fed directly to dry-reforming (DR) or tri-reforming (TRI), or separated into its components CO_2 and CH_4 , reactants for reverse water-gas-shift (RWGS), methane steam-reforming (SR) and methane partial oxidation (POX). In this chapter, a biogas mixture containing 60% of CH_4 is selected as trade-off, given a typical range which spans between 50% and 75% for CH_4 and a complementary amount of CO_2 . CO_2 from direct air capture can be fed to the RWGS reaction. With the exception of DR, the other chemical reactors require H_2O , O_2 or H_2 . Consequently, a make-up stream of H_2O is also allowed which either feeds SR and TRI or is split into pure H_2 and O_2 via polymer electrolyte membrane electrolysis (EL). The raw syngas is composed of unreacted components and side-products. Therefore, recycle and outlet streams are introduced. Excess O_2 can be utilized for the generation of thermal energy by oxy-combustion or released into the atmosphere, although this aspect is not relevant to the objectives of this study. Unreacted CO_2 is also released. However, such emissions are biogenic due to the selected carbon sources for the process. Excess H_2 is pressurized and stored at 300 bar [124]. EL can provide green H_2 directly to the outlet syngas stream, bypassing the battery of reactors. A surplus CO is not admitted, considering that biogas,

the only source for carbon to syngas, is a limited resource.

The product separation can be accomplished by a number of state-of-the-art or emerging technologies. For a single separation task – e.g., separation of component A from an initial mixture ABC – the superstructure comprises one or more separation methods. As an example, the task of separating H₂ from CO₂ can be accomplished by five competing methods: layered bed pressure-swing adsorption, polymeric membranes, palladium membranes, physical and chemical scrubbing, as illustrated in Figure 4.2.

This study is intended to provide a conservative energy analysis of the system. Therefore, electricity is not recovered by expansion and cooling utility consumption is not accounted for. The power required for pumping cooling water is assumed to be negligible compared to the major energy contributions in the system.

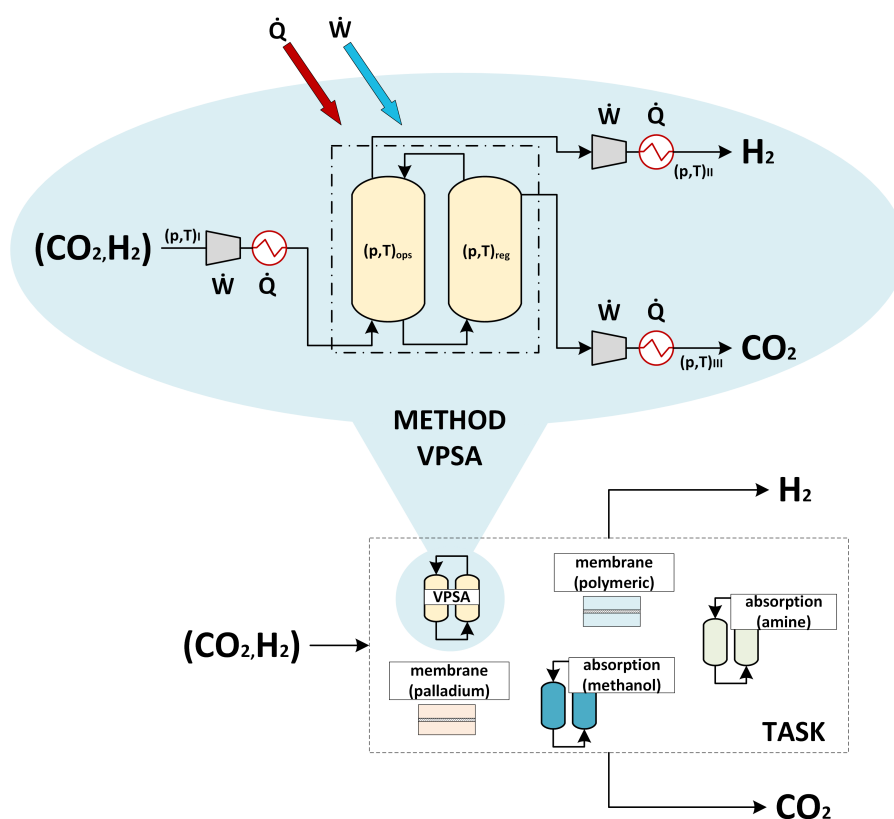


Figure 4.2.: Exemplification of separation tasks and methods embedded in the superstructure. For instance, the task of separating CO₂ from H₂ can be accomplished by five separation methods: VPSA, palladium membrane, polymeric membrane, chemical and physical absorption. Temperature and pressure are adjusted at the feed to each separation method from the previous temperature and pressure level, i.e., from the previous separator or reactor. Method-specific energy requirements can be accounted for (red and blue arrow for thermal and electrical input, respectively).

4.4 Methods

4.4.1 General modeling assumptions for reactors and separators

Similarly to Chapter 3, energy consumptions and flowrates are specific, therefore based on the molar flowrate of syngas. Reactor temperature, pressure and feed composition are assigned prior to optimization, and they are modeled as Gibbs reactors prior to the optimization. In particular, side reactions contribute defining the outlets from SR, DR and POX. On the contrary, due to the intrinsic system complexity, representative temperature, pressure, inlet and outlet composition for TRI are retrieved from literature [125] for a slightly endothermic operating mode. The conversion of water at EL is assumed as complete.

Sharp-split separators are assumed, where the generic separator is decomposed into one operation and one regeneration step. Similarly to the reactors, temperature and pressure levels at the separators are assigned prior to optimization. Streams flowing between two consecutive separators are penalized due to their energy demand (thermal and electrical contributions). The separators may be accompanied by specific energy requirements, such as the heat of regeneration for adsorption beds, cryogenic work, etc. Compression steps are adiabatic, and expansion as well as cooling do not contribute to the identification of energy demands. Most importantly, the components approximately should obey the ideal gas law.

The scope of this study is to underline dominant process paths in a topological perspective. For this reason, the optimization of operating conditions for each process-element is not part of the analysis.

4.4.2 Modeling of reactors

The complete set of parameters implemented at a reactor-level is reported in Table 4.2. The current Section discusses the rationale behind its identification.

4.4.3 Mass balances

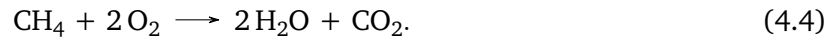
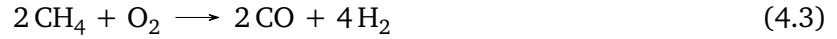
For the description of the outlet composition of an isothermal system at thermodynamic equilibrium, it is sufficient to define the following set of algebraic equations, for each given independent stoichiometric relation j :

$$f_j(T, p, \lambda) = 0, \quad \forall j \in J, \quad (4.2)$$

where f is a function of the system temperature, pressure and the extent of reaction λ_j . Hence, for the RWGS reactor, $J = \{j \mid j = \{\text{RWGS}\}\}$; for SR $J = \{j \mid j = \{\text{SR.SR}, \text{SR.WGS}\}\}$ and for

DR $J = \{j \mid j = \{\text{DR.DR}, \text{DR.RWGS}\}\}$, where the second entry reflects a given independent stoichiometric relation (WGS: water-gas shift reaction stoichiometry). The outlet composition can thus be determined. Given that (T, p) are fixed and that the feed to the reactor is stoichiometric, the ratio between outlet and inlet flowrates remains constant for any given inlet flowrate. As a result, the outlet molar flowrate is linearly proportional to the feed flowrate and the compositions are fixed for all streams.

POX is run within an adiabatic reactor with irreversible reactions of partial and total oxidation:



Due to the adiabatic behavior, Equation set (4.2) is not sufficient to characterize the equilibrium. For this process-step, T is the outlet temperature which is calculated from the following energy balance

$$\dot{H}_{\text{in}}(T_{\text{in}}) - \dot{H}_{\text{out}}(T) = 0, \quad (4.5)$$

expressing the conservation of energy in terms of enthalpy change. Furthermore, atomic balances for the elements saturate the degrees of freedom, leading to the set of equations

$$f_j(T, p, \dot{N}) = 0, \forall j \in J := \{\text{DR}, \text{SR}\}, \quad (4.6)$$

$$\dot{H}_{\text{in}} - \dot{H}_{\text{out}} = 0, \quad (4.7)$$

$$\dot{N}_{i,\text{in}} - \dot{N}_i = 0, \forall i \in I := \{\text{C}, \text{O}, \text{H}\}, \quad (4.8)$$

which is solved for T and \dot{N} (vector of molar outlet flowrates). Here, C, O, H belong to set I and denote the chemical elements carbon, oxygen and hydrogen, respectively. As for RWGS, SR and DR, feed composition, temperature and pressure are fixed and the outlet composition and reactor temperature can be calculated.

Inlet and outlet composition in TRI are retrieved from a relevant case in Song et al. [125]. For a selected feed composition of $\text{CH}_4 : \text{CO}_2 : \text{H}_2\text{O} : \text{O}_2 = 1 : 1 : 1 : 0.1$, the paper reports a syngas ratio H_2/CO of 1.48 and equilibrium conversions of 53.1%, 99.8% and 26.7% for CO_2 , CH_4 and H_2O , respectively, at 850°C and 1 atm. Knowing from the rank evaluation of the stoichiometric matrix (rank 3 and 6 components involved) that the reacting system can be described by means of 3 independent equilibrium relations (methane dry-reforming TRI.DR, methane steam-reforming TRI.SR and partial oxidation of methane TRI.POX), the evaluation of their extent of progression allows to calculate the resulting outlet composition. The extent of reaction of steam reforming is calculated from the conversion of water. Assuming a unitary total feed flowrate to the reactor, the extents of the independent reaction j per unit of feed flowrate shall be denoted by θ_j . For steam reforming, it reads $\theta_{\text{TRI.SR}} = 0.086$. Similarly, the total consumption of O_2 defines $\theta_{\text{TRI.POX}} = 0.064$. Finally, knowing the total conversion of CH_4 and

its consumption in the independent reactions TRI.SR and TRI.POX, it is possible to determine its consumption due to the dry-reforming contribution (TRI.DR), which coincides with its extent of progression $\theta_{\text{TRI.DR}} = 0.1714$. The outlet compositions from TRI and the ratio between inlet and outlet flowrates are reported in Table 4.2.

4.4.4 Energy balances

The process system includes heated reactors sustaining endothermic processes (RWGS, SR, DR, TRI) and an adiabatic reactor (POX). In all the cases, preconditioning of the feed streams to the reactors is performed by compression and pre-heating, thus enabling the internal energy of reactants to reach the requirements for chemical conversion.

Each heated reactor requires a thermal power input, expressed as linear function of the total feed flowrate as

$$\sum_{j \in J} \lambda_j \Delta H_j(T) = \dot{N}_{\text{in}} \sum_{j \in J} \theta_j \Delta H_j(T), \quad (4.9)$$

where θ_j is the constant ratio between the extent of reaction j and \dot{N}_{in} , the feed flowrate. POX is adiabatic and requires no modeling of excess heat. For TRI, the summation appearing in the right-hand-side of Equation (4.9) is determined from the standard reaction enthalpy of the independent reactions – dry reforming (TRI.DR), steam reforming (TRI.SR) and partial oxidation of methane (TRI.POX) – and from their extent of progression of reaction per unit feed flowrate, calculated in the previous section, which read:

$$\begin{aligned} & \theta_{\text{TRI.DR}} \Delta H_{\text{TRI.DR}} + \theta_{\text{TRI.SR}} \Delta H_{\text{TRI.SR}} + \theta_{\text{TRI.POX}} \Delta H_{\text{TRI.POX}} = \\ & = 0.1714 \cdot 247 \text{ kJ mol}_{\text{feed}}^{-1} + 0.086 \cdot 206 \text{ kJ mol}_{\text{feed}}^{-1} + 0.064 \cdot (-35.6 \text{ kJ mol}_{\text{feed}}^{-1}) = \\ & = 58 \text{ kJ mol}_{\text{feed}}^{-1} \end{aligned} \quad (4.10)$$

The electrolyzer requires power in the form of electrical energy input. As reported in Bensmann et al. [98], the Gibbs free energy of reaction is equal to the reversible power requirement, which is divided by an efficiency factor of 72% to obtain the real demand. As for the reactors, EL requires feed preconditioning to reach the operative temperature at atmospheric pressure.

Reactor specifications are reported in Table 4.2.

Table 4.2.: Parameters for the description of reactors. θ represents the ratio between extent of reaction and feed flowrate. Specific heat demand (\tilde{q}) and electrical energy demands (\tilde{w}) per mole-flowrate of feed are included.

Reactor	Components	Inlet molar composition %
RWGS	H ₂ ,CO ₂ ,H ₂ O,CO	[50 50 0 0]
SR	H ₂ ,CO ₂ ,H ₂ O,CO,CH ₄	[0 0 50 0 50]
POX	H ₂ ,CO ₂ ,H ₂ O,CO,CH ₄ ,O ₂	[0 0 0 0 66.7 33.3]
DR	H ₂ ,CO ₂ ,H ₂ O,CO,CH ₄	[0 50 0 0 50]
TRI	H ₂ ,CO ₂ ,H ₂ O,CO,CH ₄ ,O ₂	[0 32.26 32.26 0 32.26 3.22]
EL	H ₂ ,H ₂ O,O ₂	[0 100 0]

Reactor	Components	Outlet molar composition %	Molar ratio outlet:inlet flowrate
RWGS	H ₂ ,CO ₂ ,H ₂ O,CO	[27.43 27.43 22.56 22.56]	0
SR	H ₂ ,CO ₂ ,H ₂ O,CO,CH ₄	[56.18 2.56 11.69 15.31 14.26]	1.55
POX	H ₂ ,CO ₂ ,H ₂ O,CO,CH ₄ ,O ₂	[58.57 1.32 4.33 30.14 5.65 0]	1.80
DR	H ₂ ,CO ₂ ,H ₂ O,CO,CH ₄	[28.5 10.8 5.4 39.2 16.1]	1.51
TRI	H ₂ ,CO ₂ ,H ₂ O,CO,CH ₄ ,O ₂	[45.3 9.38 14.68 30.6 0.04 0]	1.61
EL	H ₂ ,H ₂ O,O ₂	[66.7 0 33.3]	1.5

Reactor	T (K)	p (bar)	\tilde{q} (kJ mol ⁻¹)	\tilde{w} (kJ mol ⁻¹)	θ_j %
RWGS	1000	5	$35 \cdot \theta_{RWGS}$	0	$\theta_{RWGS} = 22.6$
SR	1173	30	$227 \cdot \theta_{SR} - 33 \cdot \theta_{WGS}$	0	$\theta_{SR} = 27.8;$ $\theta_{WGS} = 4.0$
POX	1328 (in: 773)	30	adiabatic	0	–
DR	1000	5	$260 \cdot \theta_{DR} + 35 \cdot \theta_{RWGS}$	0	$\theta_{DR} = 25.6;$ $\theta_{RWGS} = 8.1$
TRI	1123	1	$58 \cdot \dot{N}_{in}$	0	–
EL	333	1	0	327	–

4.4.5 Modeling of separators

An extensive literature survey was conducted to identify unit-specific calculations. Therefore, the energy requirements are characterized for each specific case, resulting in linear grey-box models. The superstructure embeds the following families of separation methods: temperature- and (vacuum) pressure-swing adsorption (TSA, VPSA), absorption (glycol, amine, methanol), membrane separation (polymeric, palladium) and cryogenic operations (chilled methanol, cryo-

genic distillation). Table 4.4 introduces the set of separators allowed within the control-volume and their parameters selection.

4.4.6 Mass balances

The sharp-split assumption allows for a linear mathematical description only if the composition at the beginning of the separation train is fixed. For this reason, the modeling choice of fixing temperature and pressure at the Gibbs reactors introduced in Section (4.4.1) is justified. This approach has been adopted in literature [13] for the screening of distillation sequences, while the current contribution extends the method to a wider choice of separators. The underlying mathematical formulation reads:

$$\dot{N}_A = \dot{N}_{(A,B,C)} \frac{\zeta_A}{\zeta_A + \zeta_B + \zeta_C} = \dot{N}_{(A,B,C)} \xi_{A/(A,B,C)}, \quad (4.11)$$

where a generic component A is ideally separated out of a mixture ABC, and the split factor ξ is given by the ratio of the mole fractions ζ at the outlet stream of the reactor. The splits modeled in the framework are listed in Table 4.5, together with the corresponding feasible separation methods and literature references. It is here stressed that not all of the separation techniques are at high readiness level. A few separators are considered feasible for specific separation tasks if characteristic properties, such as kinetic diameter, relative permeability, dew points etc., suggest so. Nevertheless, most of the separators are state-of-the-art technologies in industry or in laboratory-scale applications.

Table 4.3.: The separation tasks are here sorted by the number of components in the feed, N_{spec} , and reactor type. Reactors DR, SR, TRI, POX share the same separation tasks. A single asterisk * indicates the separation tasks whose methods are shared between DR, SR, TRI, POX. Double asterisk those shared between RWGS and the other reformers **. The task of separating biogas into CH_4 and CO_2 and possibly adopted in the downstream of the reformers DR, SR, TRI, POX, is indicated by a triple asterisk ***. Details on the separation methods available are collected in Table 4.5.

N_{spec}	reactors		
	RWGS	DR,SR,TRI,POX	biogas
5	-	$(\text{H}_2, \text{CH}_4)/(\text{CO}_2, \text{CO}, \text{H}_2\text{O})^*$ $(\text{H}_2)/(\text{CO}_2, \text{CO}, \text{H}_2\text{O}, \text{CH}_4)^*$ $(\text{H}_2\text{O})/(\text{CO}_2, \text{H}_2, \text{CO}, \text{CH}_4)^*$	-
4	$(\text{H}_2)/(\text{CO}_2, \text{CO}, \text{H}_2\text{O})$ $(\text{H}_2\text{O})/(\text{CO}_2, \text{H}_2, \text{CO})$ $(\text{CO}_2, \text{H}_2\text{O})/(\text{H}_2, \text{CO})$	$(\text{H}_2\text{O})/(\text{CO}_2, \text{CO}, \text{CH}_4)^*$ $(\text{CH}_4)/(\text{CO}_2, \text{CO}, \text{H}_2\text{O})^*$ $(\text{H}_2)/(\text{CO}_2, \text{CO}, \text{CH}_4)^*$ $(\text{CO})/(\text{CO}_2, \text{H}_2, \text{CH}_4)^*$	-
3	$(\text{CO})/(\text{CO}_2, \text{H}_2\text{O})^{**}$ $(\text{H}_2\text{O})/(\text{CO}_2, \text{CO})^{**}$ $(\text{CO}_2)/(\text{H}_2, \text{CO})$ $(\text{H}_2)/(\text{CO}_2, \text{CO})$ $(\text{CO})/(\text{CO}_2, \text{H}_2)$	$(\text{CO})/(\text{CO}_2, \text{H}_2\text{O})^{*,**}$ $(\text{H}_2\text{O})/(\text{CO}_2, \text{CO})^{*,**}$ $(\text{CO}_2)/(\text{CO}, \text{CH}_4)^*$ $(\text{CO})/(\text{CO}_2, \text{CH}_4)^*$ $(\text{CO}_2)/(\text{H}_2, \text{CH}_4)^*$ $(\text{H}_2)/(\text{CO}_2, \text{CH}_4)^*$	-
2	$(\text{CO}_2)/(\text{H}_2\text{O})^{**}$ $(\text{CO}_2)/(\text{CO})^{**}$ $(\text{H}_2)/(\text{CO})$ $(\text{CO}_2)/(\text{H}_2)$	$(\text{CO}_2)/(\text{H}_2\text{O})^{*,**}$ $(\text{CO}_2)/(\text{CO})^{*,**}$ $(\text{CO}_2)/(\text{CH}_4)^{*,***}$ $(\text{CO})/(\text{CH}_4)^*$ $(\text{H}_2)/(\text{CH}_4)^*$	$(\text{CO}_2)/(\text{CH}_4)^{***}$

4.4.7 Energy balances

The generic separator is divided into operation and regeneration step. A membrane separates the permeate from the retentate stream, a gas-liquid absorption process is followed by stripping and an adsorption step via VPSA/TSA is periodically switched into regeneration mode by vacuum generation or heating, respectively. Therefore, each method is associated with two distinct (T, p) values, respectively for operation $(T, p)_{\text{ops}}$ and regeneration $(T, p)_{\text{reg}}$: the feed stream, as well as the outlet from the operation-step, are at $(T, p)_{\text{ops}}$. In order to model the adjustment of the internal energy between consecutive separators, heating or cooling, compression or expansion are considered. For thermal energy calculations, the heat capacity \tilde{C}_p is calculated as a weighted average for pure components, accounting for the actual mixture composition and the initial and

final temperature.

As formerly stated in Section (4.3), power recovery by expansion and cooling are not considered as long as they occur above the atmospheric conditions ($T = 298 \text{ K}$, $p = 1 \text{ bar}$). Nevertheless, the expansion of gas may require inter-heating steps. Similarly, compression may require cooling. The temperature attained after isentropic transformation is calculated as:

$$T_{2,\text{id}} = T_1 \left(\frac{p_2}{p_1} \right)^{\frac{R}{\bar{C}_p}}, \quad (4.12)$$

where R is the universal gas constant. The real temperature is calculated assuming an efficiency factor of $\eta = 80 \%$. In agreement with the conservative framework, the power requirement for compression is over-estimated by a single, isentropic step, as well as the temperature out of compression and expansion. As an example, whenever a process stream delivers gas to higher (T, p) values, the pressurization can be deployed to partly satisfy the need for thermal power input. For an adiabatic compression step, the specific molar electrical work is estimated as:

$$\tilde{w} = \frac{\gamma}{(\gamma - 1)} RT_1 \left(\left(\frac{p_2}{p_1} \right)^{\frac{\gamma - 1}{\gamma}} - 1 \right) \frac{1}{\eta}, \quad (4.13)$$

$$\gamma = \frac{\tilde{C}_p}{\tilde{C}_v} \quad (4.14)$$

where $\eta = 0.8$ is the efficiency, γ is the ratio of specific heats at constant pressure and constant volume [126]. Equation (4.13) defines a coefficient which multiplies the gas flowrate, i.e. the mathematical description is linear. The same formula is adopted to model vacuum operations as in Grande et al. [126], e.g. vacuum normalization in VPSA, or membrane separators. For the latter, the pressure in the retentate is assumed to be 20 times higher than in the permeate side, set at $p = 0.1 \text{ bar}$ is assumed [127]. In order to describe the energy demand of each separator, additional, method-specific calculations are included.

The non-ideal coefficient of performance (COP) describes the ratio between the thermal power absorbed by the refrigerant and the real electrical power required at the compressor in a cryogenic loop. The definition of COP reads:

$$\text{COP}_{\text{real}} = \text{COP}_{\text{id}} \eta = \frac{Q}{W_{\text{id}}} \eta = \frac{T_{\text{ev}}^R}{T_{\text{cond}}^R - T_{\text{ev}}^R} \eta, \quad (4.15)$$

where \dot{W}_{id} is the ideal electrical power requirement. In an ideal case, it corresponds to a reverse Carnot cycle between the cryogenic evaporation temperature of the refrigerant, T_{ev}^R , and the temperature at which the refrigerant releases its internal energy by condensation, T_{cond}^R . The ideal COP is corrected by a thermodynamic efficiency factor η of 60% [108]. \dot{Q} is the thermal power

acquired by the refrigerant during cryogenic evaporation and lost by the cooling process fluid in order to reach the required cryogenic temperature. A proportionality coefficient for the estimation of the power requirement in cryogenic operations is derived by rearranging Equation 4.15:

$$\tilde{w} = \frac{1}{\text{COP}_{\text{id}}\eta} \tilde{q} = \frac{1}{\eta} \frac{T_{\text{cond}}^R - T_{\text{ev}}^R}{T_{\text{ev}}^R} \tilde{C}_p (T_{\text{amb}} - T_{\text{cryo}}). \quad (4.16)$$

In Equation 4.16, a distinction is made between the cryogenic temperatures T_{cryo} and T_{ev}^R , the former being 15 K higher than the latter, thus ensuring the heat transfer.

TSA operations consist of cyclic switch between operation and regeneration at high temperature of the adsorbent bed. Consequently, the relevant contributions for regenerations are the heat of desorption for the entrained components \dot{Q}_{des} and the heat input to raise the bed temperature \dot{Q}_{bed} :

$$\dot{Q}_{\text{TSA}} = \dot{Q}_{\text{bed}} + \dot{Q}_{\text{des}} = (\tilde{q}_{\text{des}} + \tilde{q}_{\text{bed}}) \dot{N}_{\text{feed}} \quad (4.17)$$

$$\tilde{q}_{\text{bed}} = (T_{\text{reg}} - T_{\text{op}}) \sum_{k \subset K} \left(\frac{1}{\theta_i} \hat{C}_{p,\text{bed},l} M_i \zeta_i \right), \quad (4.18)$$

$$\tilde{q}_{\text{des}} = \sum_{k \subset K} \left(\tilde{q}_{\text{des},i}^* \zeta_i \right). \quad (4.19)$$

For Equation 4.18 and 4.19, sets k and K are introduced:

$$k \subset K, k = \{i, l \mid i = \{\text{components adsorbed by adsorbent-type } l\}, l = \{\text{adsorbent-type } l\}\}. \quad (4.20)$$

In Equation (4.18), $\theta_i^{-1} M_i$ is the molar mass of adsorbent required to adsorb component i , which is multiplied by the specific heat per unit of mass of adsorbent \hat{C}_p . Furthermore, M_i is the molecular weight of component i . In Equation (4.19), $\tilde{q}_{\text{des},i}^*$ is the molar heat of desorption for component i .

Layered-beds are also considered, which necessitates the subscript l and the summation operator in Equations (4.18) and (4.19).

Gas-liquid absorption processes require high-temperature regeneration. It is often the case that the absorption operation is performed in pressurized vessels. Unit-specific calculations must account for the change of the internal energy of the fluid sent to regeneration. The specific thermal power input reads:

$$\tilde{q}_{\text{rec}} = \theta_{\text{rec}} \tilde{C}_{p,\text{entrainer}} (T_{\text{reg}} - T_{\text{op}}), \quad (4.21)$$

where θ_{rec} is the ratio between the flowrate of entrainer required per unit of entrained key component (circulation rate). The description of amine and glycol absorption resort to Equation

4.21. The absorption of CO₂ in methanol occurs at cryogenic conditions, whereas the regeneration is operated at ambient temperature. As a consequence, this specific separator is described by the relations already introduced for cryogenic systems.

Table 4.4.: Separation methods and identifiers adopted in Table 4.5. Deviations from the reported values for $(T \text{ (K)}, p \text{ (bar)})$ are possibly implemented in the constraints, e.g. membranes for H₂ separation adjacent to the reactor are operated at temperatures higher than 298 K (Pd membrane, polymeric membrane).

Separator	ID	$(T, p)_{op}$ (K, bar)	$(T, p)_{op}$ (K, bar)	$\tilde{C}_{p,entrainer}$ J kg ⁻¹ K ⁻¹	θ kg kg ⁻¹	\tilde{q}_{reg} kJ mol ⁻¹	COP	ref.
TPSA (Al ₂ O ₃ + CuCl/Z)	I	(298, 8)	(393, 1)	Al ₂ O ₃ : 240 CuCl/Z: 240	Al ₂ O ₃ : 5.5 CuCl/Z: 5.5	H ₂ O: 48 CO ₂ : 34 CO: 35 CH ₄ : 11	-	[128]
TSA (Silica Gel)	II	(298, 1)	(393, 1)	silica: 920	silica: 8	H ₂ O: 31	-	[128]
TPSA (Al ₂ O ₃)	III	(298, 8)	(393, 1)	Al ₂ O ₃ : 240	Al ₂ O ₃ : 5.5	H ₂ O: 48	-	[128]
TSA (ASMS-3A+ CuCl/Z)	IV	(298, 8)	(393, 1)	ASMS-3A: 920 CuCl/Z: 240	ASMS-3A: 8 CuCl/Z: 5.5	H ₂ O: 23 CO ₂ : 23 CO: 35	-	[129, 130]
VPSA	V	(298, 8)	(298, 0.1)	-	-	-	-	-
Membrane (Polymeric)	VI	(298, 2)	(298, 0.1)	-	-	-	-	-
Membrane (Palladium)	VII	(298, 21)	(298, 1)	-	-	-	-	-
Absorption (Glycol)	VIII	(308, 10)	(473, 1)	TEG: 2225	49	H ₂ O: 320	-	[131]
Absorption (Methanol)	IX	(233, 30)	(298, 1)	-	-	-	40 (1.2 kJ mol ⁻¹)	[132]
Absorption (Amine)	X	(313, 1)	(393, 2)	MEA: 3325	3.5	CO ₂ : 41	-	[104]
Cryogenics (CH ₄ /CO ₂)	XI	(263, 40)	(223, 40)	-	-	-	54 (1.93 kJ mol ⁻¹)	[133]
Cryogenics (CH ₄ /H ₂)	XII	(103, 1)	(103, 1)	-	-	-	775 (23 kJ mol ⁻¹)	[132]

Table 4.5.: Numbered list of splits allowed in the superstructure and available separation methods. (*) MEDAL™ Air Liquide - hydrogen purification; (**) MEDAL™ Air Liquide - biogas purification.

(ID)	Splits	ID available methods	references
(1)	(H ₂ ,CH ₄)/(CO ₂ ,CO,H ₂ O)	IV	[134, 106, 107]
(2)	(H ₂)/(CO ₂ ,CO,H ₂ O,CH ₄)	VII	[135, 102]
(3)	(H ₂ O)/(CO ₂ ,H ₂ ,CO,CH ₄)	VI	[136, 137, 102, 103]
(4)	(H ₂ O)/(CO ₂ ,CO,CH ₄)	VI,VIII,II	[138, 136, 137, 103, 128]
(5)	(CH ₄)/(CO ₂ ,CO,H ₂ O)	II	[134, 106, 107, 139]
(6)	(H ₂)/(CO ₂ ,CO,CH ₄)	V,VI,VII	[105, 134, 106, 107, 140, 135, 141, 142], (*)
(7)	(CO)/(CO ₂ ,H ₂ ,CH ₄)	V	[134, 106, 107]
(8)	(CO ₂ ,H ₂ O)/(H ₂ ,CO)	III,X	[141, 104, 143]
(9)	(H ₂ O)/(CO ₂ ,H ₂ ,CO)	VI,VIII,II	[138, 136, 137, 102, 103, 128]
(10)	(H ₂)/(CO ₂ ,CO,H ₂ O)	I,VII	[144, 135, 141, 139, 142, 128]
(11)	(CO)/(CO ₂ ,H ₂ O)	V	[144, 106, 107]
(12)	(H ₂ O)/(CO ₂ ,CO)	VI,VIII,II	[138, 136, 137, 102, 103, 128]
(13)	(CO ₂)/(H ₂ ,CO)	V,IX,X	[145, 141, 146, 104, 147, 148, 149, 150], (**)
(14)	(H ₂)/(CO ₂ ,CO)	VI,V,VII	[144, 151, 101, 152, 138, 142, 153], (*)
(15)	(CO)/(CO ₂ ,H ₂)	V	[144, 106, 107]
(16)	(CO ₂)/(CO,CH ₄)	V	[154]
(17)	(CO ₂)/(H ₂ ,CH ₄)	V	[101, 154]
(18)	(H ₂)/(CO ₂ ,CH ₄)	V,VII,VI	[134, 140, 135, 141, 142, 155, 156], (*)
(19)	(CO)/(CO ₂ ,CH ₄)	V	[144, 106, 107]
(20)	(CO)/(CH ₄)	V	[134, 106, 107]
(21)	(H ₂)/(CH ₄)	VI,XII,V	[140, 146, 157, 150], (*)
(22)	(CO ₂)/(CH ₄)	VI,V,X,XI	[141, 104, 154, 133, 158], (**)
(23)	(CO ₂)/(H ₂ O)	II,VIII,VI,	[138, 136, 159, 137]
(24)	(CO ₂)/(CO)	V	[160, 144, 134, 106, 107, 146, 154]
(25)	(CO ₂)/(H ₂)	V,X,IX,VI,VII	[144, 140, 135, 141, 152, 146, 104, 147, 148, 142], (*), (**)
(26)	(CO)/(H ₂)	V,VI,VII	[160, 105, 144, 134, 106, 107, 145, 151, 140, 135, 141], (*)

4.5 Modeling of interconnections

This section discusses the conceptual structures which enable to build the final set of problem-constraints in a mixed-integer linear form.

Methodological details concerning the formulation of interconnection between separation blocks and substance nodes are specified in the Supplementary Section B.

4.5.1 Mass and energy balances: mixture block

For a generic mixture ϕ , there are two sets of mass balances:

$$\xi_{\phi,i} \dot{N}_i - \sum_j \dot{N}_{j,i} = 0 \quad \forall i \in I, \quad (4.22)$$

$$\dot{N}_j - \sum_i \dot{N}_{j,i} = 0 \quad \forall j \in J. \quad (4.23)$$

Sets I and J in Equations 4.22 and 4.23 incorporate the feed streams to the separators which generate and accept ϕ , corresponding to flowrates \dot{N}_i and \dot{N}_j , respectively; $\xi_{\phi,i}$ is the split factor associated with separator i and its outlet mixture ϕ . Parametric coefficients of molar thermal energy and work (see Section 4.4.5) are multiplied by the corresponding flowrates $\dot{N}_{j,i}$ of the separator connecting unit i to j . The linear description of the change in (T, p) between consecutive separators is formulated as:

$$\dot{Q}_{j,i} - \tilde{q}_{j,i} \dot{N}_{j,i} = 0, \quad (4.24)$$

$$\dot{W}_{j,i} - \tilde{w}_{j,i} \dot{N}_{j,i} = 0, \quad (4.25)$$

where $\dot{Q}_{j,i}$ and $\dot{W}_{j,i}$ denote the thermal and electrical power inputs required to shift from separator i to separator j .

Set Φ (capitalized) is introduced. It encompasses Equations 4.22,4.23,4.24,4.25, related to the specified mixture ϕ .

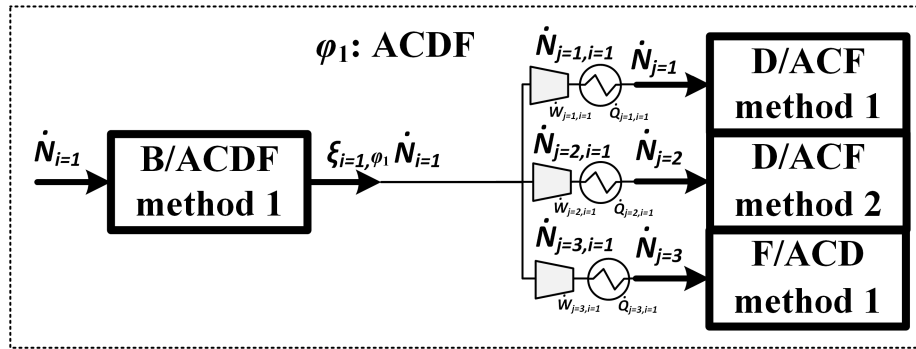


Figure 4.3.: Representation of a mixture block delivering mixture ϕ (lowercase) with a single sharp-split separator.

Figure 4.3 exemplifies concept and nomenclature with a generic quaternary mixture of components ACDF, generated by separator B/ACDF from mixture ABCFD via stream $i = 1$ with flowrate $\dot{N}_{i=1}$. Three separators accept mixture ACDF and are fed by streams $j = \{1, 2, 3\}$ with flowrates $\dot{N}_{j=\{1,2,3\}}$. Flowrates $\dot{N}_{j=\{1,2,3\},i=1}$, as well as thermal and electrical power inputs, $\dot{Q}_{j=\{1,2,3\},i=1}$ and $\dot{W}_{j=\{1,2,3\},i=1}$, are associated with the transition from separator B/ACDF to D/ACF (method 1 and 2) and F/ACD. In this specific case and for a given separator j out of the mixture block,

Equation 4.23 reduces to $\dot{N}_j - \sum_i \dot{N}_{j,i} = \dot{N}_j - \dot{N}_{j,i=1} = 0$ due to the fact that a single separator B/ACDF delivers mixture $\phi = \text{ACDF}$.

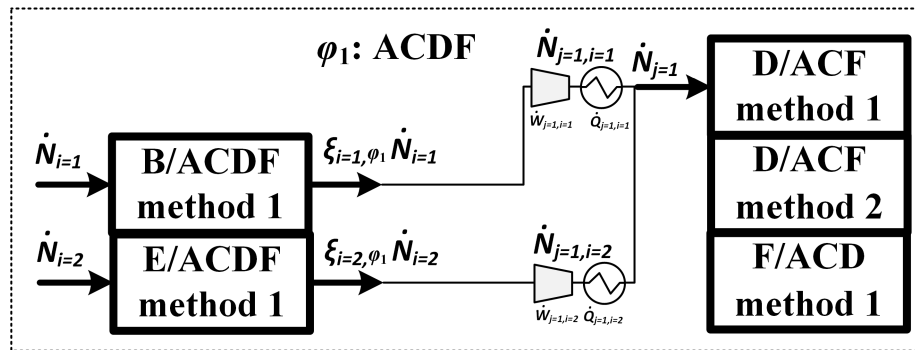


Figure 4.4.: Compact representation of a mixture block delivering mixture ϕ with two sharp-split separators.

On the contrary, Figure 4.4 illustrates the case in which a second separator $i = 2$ delivers the same mixture $\phi = \text{ACDF}$. In this case Equation 4.23 reads $\dot{N}_{j=1} - \sum_i \dot{N}_{j=1,i} = \dot{N}_{j=1} - (\dot{N}_{j=1,i=1} + \dot{N}_{j=1,i=2}) = 0$. The additional connecting flowrate $\dot{N}_{j=1,i=2}$ allows the definition of thermal and electrical power requirements associated with the transition from separator E/ACDF to D/ACF (method 1).

As a given mixture ϕ can be generated by multiple separators in a separation train, the superstructure is classified as a network representation of the separation process [13].

4.5.2 Motivation for the modeling approach

Separators included in the downstream of different reactors are replicated within the superstructure. By extension, this applies to entire separation trains whose feed streams share the same components, although they differ in composition, temperature and pressure. This approach, exemplified in Figure 4.5(A), differs from a typical formulation of similar optimization problems, where the superstructure of a sequence of separators is shared between the downstreams of several reactor candidates, as shown in Figure 4.5(B).

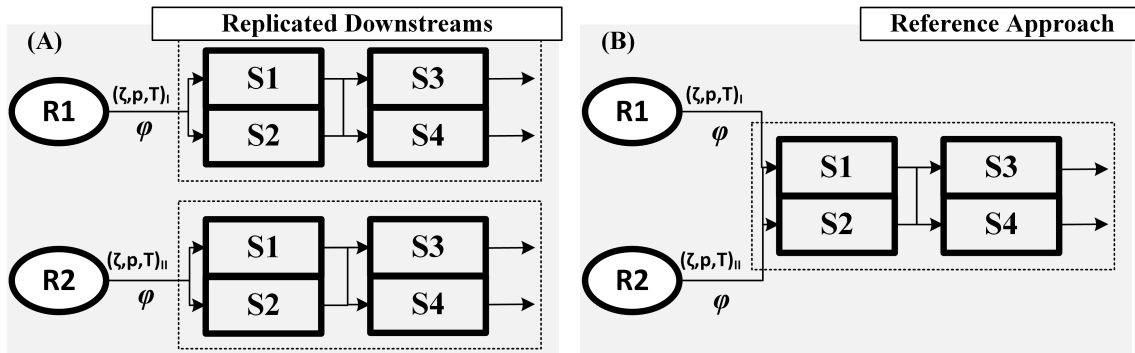


Figure 4.5.: (A) Superstructure approach adopted in this chapter, where replicas of the downstream sections are fed by the same components (mixture ϕ) with different composition, pressure and temperature (ζ, T, p) from reactor R1 and R2, respectively; (B) reference formulation not replicating the separators.

With the current implementation, redundancies may be present in the solution of the downstream section. Alternative separation routes for mixtures which share the same components at different states (composition, temperature and pressure) and flowrates can coexist when more than one reformer is active at the minimum total energy consumption. This is shown qualitatively in Figure 4.6(A), where red boxes define the optimal separation routes.

Thus, relevant information concerning the preferred type of separation methods selected at the absolute minimum energy demand can be obtained, regardless of the number of redundant unit operations presented in the selected flowsheet. A cost-based objective function may possibly induce the optimizer to select a single separation method for the given split, as explained in Section B.1.2.

This may however be not the case if the energy savings of operating multiple reactors are considerable, and in retrofitting problems, where a pre-existing reformer is co-operated with a newly installed reactor, e.g., SR and RWGS, as proposed in the previous chapter, SR and TRI or any other combination.

In this analysis, fixed costs are not considered. Instead, dedicated complexity-reduction constraints can force the solution towards simpler process configurations, thus mimicking the effect of a cost-based optimization on the plant complexity. Such constraints invoke the binary variables and belong to the category of logical constraints. Figure 4.6(B) and (C) show an exemplification of this solution and its equivalent by linear combination of the energy demand (cf. Section B.1.2).

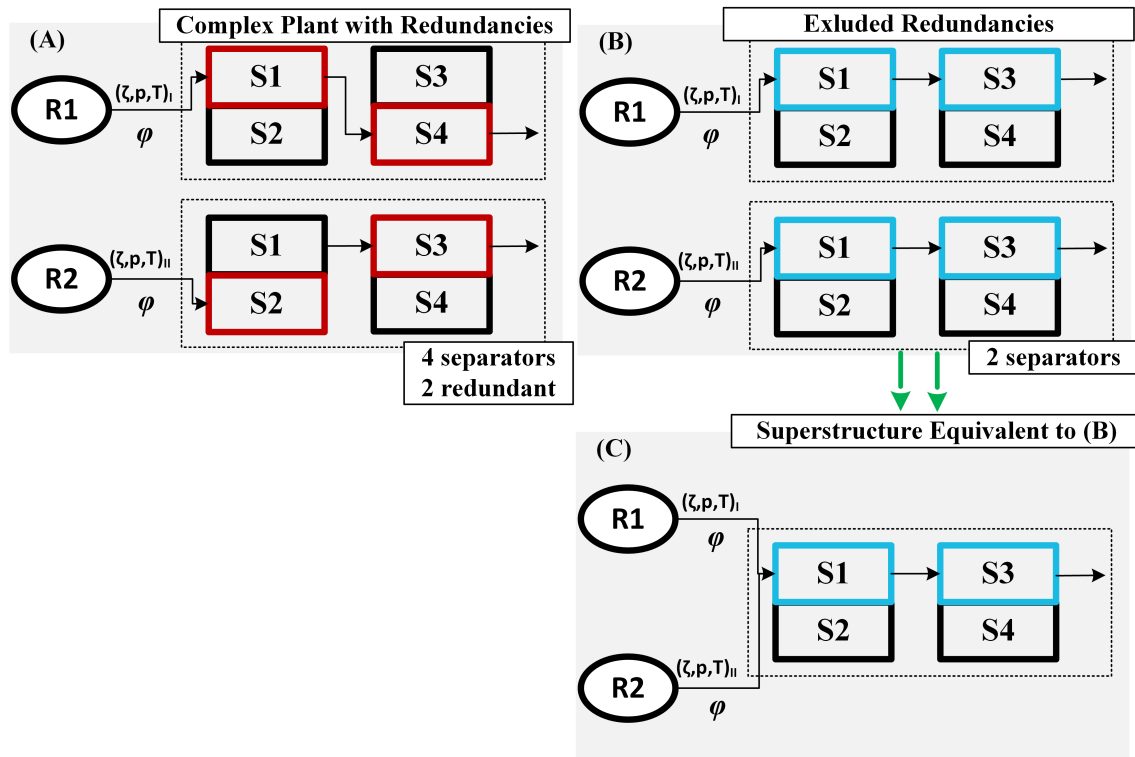


Figure 4.6.: (A) Qualitative representation of a possible solution from an energy-based objective function, where different feed states to the separation trains define two redundant units; (B) no redundant units are allowed in the solution due to the problem formulation; (C) equivalent representation without redundancies.

4.5.3 Logical constraints

Logical constraints involving binary variables are imposed such that at most one separation method per task is active:

$$\sum_{i \in I} y_i - 1 \leq 0, \quad (4.26)$$

$$\dot{N}_i - M y_i \leq 0, \quad \forall i \in I, \quad (4.27)$$

where set I collects the separation methods available for the given task. When the binary variable y_i in Equations 4.26 and 4.27 is zero, the feed flowrate \dot{N}_i to separator i , belonging to the set I of the available methods for the task, is also zero. On the contrary, if $y_i = 1$ the separator is active. M is a constant whose value is of the same order of magnitude as the feed flowrate. If the value of M exceeds the underlying flowrate for several orders of magnitude, numerical issues might be encountered and the condition of mutual exclusivity among separators may be violated.

As shown in Section 4.5.2, even though RWGS, SR, POX, DR, TRI could share the same separators, five distinct separation-trains are implemented, which allows for linearity to be preserved. In case the selected route for separation strongly depends on the outlet composition from the reactor, redundancies may occur if more reactors are simultaneously operated. For instance, membrane and adsorption technologies may entrain the same key component out of a given mixture in the downstream of two distinct reactors. Therefore, the optimal separation sequence can be homogenized by introducing complexity-reduction constraints. For each separator j shared among N different separation-trains, an inequality is implemented:

$$\frac{1}{N} \sum_{i \in I} y_i - y_j^{\text{CC}} \leq 0. \quad (4.28)$$

The new binary variable y_j^{CC} appears in the final inequality constraint which sets the maximum number of units allowed within the plant N_{max} :

$$\sum_{j \in J} y_j^{\text{CC}} + \sum_{k \in K} y_k - N_{\text{max}} \leq 0. \quad (4.29)$$

Equation 4.29 combines the binary variables associated to the possibly redundant units, set J , with the binaries of unique units, set K , i.e., reactors and separators appearing in a single separation sequence. For $N_{\text{max}} = +\infty$, unitary binaries can be paired with units whose feed flowrate is zero. In case constraint 4.29 is active, $N_{\text{max}} \leq N_{\text{unconstrained}}$ and the plant is forced towards higher power requirements. Therefore, each binary variable assumes unitary value only if the corresponding unit operation is active and N_{max} coincides with the actual number of operating units.

Solutions which do not enforce the complexity constraint Equation 4.29 must present lower energy requirements if compared to those stemming from constrained configurations. In the next section, optimization results with unconstrained flowsheet complexity, constrained complexity with multiple reformers, and constrained complexity with a single active reformer are reported and compared.

4.5.4 Formulation of the optimization objectives

Similarly to Problem (A) presented in the retrofitting approach in Section 3.4 of this dissertation, the current problem formulation minimizes the summation of thermal \dot{Q} and electrical power inputs \dot{W} . In its most general formulation, the electrical power term is multiplied by a weighting factor ω , comprised between $[0, 1]$:

$$\min_{\dot{N}, \mathbf{y}} (\dot{Q} + \omega \dot{W}). \quad (4.30)$$

For decreasing values of ω , the electricity demand becomes less relevant to the objective. This reflects a transition to plant layouts that favor the use of sustainable, carbon-neutral electrical power sources. For $\omega = 0$, the process configuration minimizes the thermal inputs regardless of the cost of electricity. Optimization variables (vectors in bold) are molar flowrates, \dot{N} , and binary variables, in vector \mathbf{y} .

In this chapter, topological results and total power consumptions are explored exclusively at the boundaries of the weighting factor, namely at $\omega = 1$, which defines Problem (A):

$$\min_{\dot{N}, \mathbf{y}} (\dot{Q} + \dot{W}), \quad (\text{A})$$

and $\omega = 0$, which defines Problem (B):

$$\min_{\dot{N}, \mathbf{y}} (\dot{Q}). \quad (\text{B})$$

The minimization of the sum between electrical and thermal energy in Problem (A) stands for a scenario where electricity is supplied from the grid, in the worst case from the combustion of fossil fuels. On the contrary, the minimization of the thermal energy identifies the most electrified and sustainable solution when cheap renewable electricity is supplied from external sources or produced on-site, although this configuration may come at a high overall energy demand. As already anticipated in Chapter 3, highly electrified processes at high overall energy requirement must be stabilized by buffering devices or implemented with flexible plant concepts, thus compensating for possible drops in renewable energy supply. Otherwise, the plant may then have to rely on grid supplies, where energy mix in which coal- and gas-fired power plants still play a significant role when renewables are scarce (Section 2.11).

At first, biogas is considered as the only source of carbon supplied to the plant, optionally separated into its components CH_4 and CO_2 by separation task (22) in Table 4.5. Alternatively, only carbon dioxide is supplied to the system. The energy demand of the direct air capture is added to the energy demand of the syngas plant in this scenario. Objectives and constraints are linear and decision variables are continuous or integer. The resulting MILP problems were solved in MATLAB®

2018b using the function *intlinprog*. The algorithm solves and tightens LP relaxations before implementing heuristics and branch-and-bound strategies.

4.6 Feedstock: biogas

Plant topologies obtained for Objective (A) and (B) and unconstrained plant complexity are reported in Table 4.6 (A) and (B), respectively.

Table 4.6.: Topological results for unconstrained plant complexity, where multiple reformers can be selected simultaneously and interact with each other. The number of redundant units is derived according to the criteria presented in Section 4.6.

(A) $\min_{\dot{N},y} (\dot{Q} + \dot{W})$					
Downstream	Reactors	Separation Methods	N_{units}	$N_{\text{redundancies}}$	tot. / $\text{kJ mol}_{\text{syngas}}^{-1}$
Phosgene	RWGS,DR	V,VI	10	2	204
Monsanto	RWGS,DR	V,VI	10	2	225
Hydroformylation	SR,DR,TRI,EL	IV,V,VI	12	4	146
Iron Ore	SR,DR,TRI,EL	V,VI,VII	12	4	124
Fischer Tropsch	SR,DR,TRI,EL	V,VI	9	1	124
Methanol	SR,DR,TRI,EL	IV,V,VI	11	3	137

(B) $\min_{\dot{N},y} (\dot{Q})$					
Downstream	Reactors	Separation Methods	N_{units}	$N_{\text{redundancies}}$	tot. (thermal) / $\text{kJ mol}_{\text{syngas}}^{-1}$
Phosgene	POX,EL	V,VI,XII	7	1	668 (17.3)
Monsanto	POX,EL	V,VI,XII	7	1	692 (17.2)
Hydroformylation	POX,EL	V,VI,XII	7	1	338 (8.3)
Iron Ore	POX,EL	V,VI,XII	7	1	218 (17.5)
Fischer Tropsch	POX,EL	V,VI,XII	7	1	218 (5.9)
Methanol	POX,EL	V,VI,XII	7	1	220 (5.5)

The number of units accounts for redundancies in the arrangement of the separation systems. Polymeric membranes, palladium membranes for selective hydrogen separation and VPSA are the prevailing separation methods selected in the different downstreams. In addition, a TSA separator with double active material (ASMS-3A and CuCl) is identified by Objective (A) to accomplish separation task (1): $(\text{H}_2, \text{CH}_4)/(\text{CO}_2, \text{CO}, \text{H}_2\text{O})$, where $(\text{CO}_2, \text{CO}, \text{H}_2\text{O})$ is entrained. At the minimum thermal power supply Objective (B), the only adiabatic system (POX) is selected in combination with EL. The separation sequences downstream of EL and POX involves always 3 methods: polymeric membrane, VPSA and cryogenics for the separation of methane from hydrogen.

The important outcome of this optimization result is that membrane separators and PSA units are favored over scrubbing. The energy intensive cryogenic separation of methane from H_2 requires comparatively less thermal energy supply: it is always selected in the separation sequence which follows the partial oxidation reactor (POX), never selected when the total energy is minimized (A). TSA (separation method IV) is selected only once for the separation $(H_2, CH_4)/(CO_2, CO, H_2O)$ after dry reforming and steam reforming at the minimum total energy.

The next section indicates how redundancies in the separation sequences are avoided by enforcing Equation 4.29.

4.6.1 Dealing with redundancies

At the minimum total energy, $\min(\dot{Q} + \dot{W})$, and low syngas ratios (phosgene and Monsanto processes), the optimizer identifies 10 units: RWGS, DR and 8 separators – see Table 4.6(A), column N_{units} . However, Table 4.3 shows that two separators can be shared between the separation trains after RWGS and DR: $(CO)/(CO_2, H_2O)$ followed by $(CO_2)/(H_2O)$, or alternatively, $(H_2O)/(CO_2, CO)$ followed by $(CO_2)/(CO)$, as the chemical species involved are shared in the downstream of the two reactors. Therefore, when defining the maximum number of units allowed within the plant (N_{max} in Equation 4.29), 2 reactors (RWGS and DR), 2 separators shared in their downstream (as just shown), and 3 additional separators not shared in the downstreams are considered, which amounts to a total of 4 separators dedicated to a initial mixture of 5 components (DR) and 3 separators after RWGS for a 4 species mixture. In addition, the plant must have the option to partially or completely separate biogas into its components by task CO_2/CH_4 . In total, 8 units must be allowed in the solution of constrained plant complexity for a system which allows the coexistence and interaction of two reformers, RWGS and DR. For all other syngas applications and for the same Problem (A), SR, DR and TRI are indicated in the solution together with EL (Table 4.6). These reformers share the same components in their downstreams (Table 4.2). For this reason, the topological configuration with plant complexity restrained to 3 reformers and an electrolyzer may involve at most 4 separators for the quinary mixture, one of which serves for biogas upgrading (task CO_2/CH_4), for a total of 8 units.

Similarly, when Objective (B) is enforced (maximum electrification), 4 separation tasks are active after POX. Biogas upgrade involves the use of an additional separator, and electrolysis generates pure oxygen for POX. Therefore, 7 unit operations are active at the optimum, although the separation of CO_2 from CH_4 could be also involved in the downstream of POX, thus reducing the number of units to 6.

All this considered and based on the number of unit operations reported in the solutions, the number of redundancies can be identified. The number of units for the unconstrained complexity scenario N_{units} as well as the number of redundant units $N_{\text{redundancies}}$ is collected in Table 4.6. Therefore, a second optimization run can be started, where Equation 4.29 is now included in the

set of constraints and N_{\max} is imposed according to the redundancies, as it has been discussed in this section. At the optimum, redundancies may still be present due to a new combination of reactors. In such cases, the procedure must be repeated fixed a new (smaller) value for N_{\max} .

This iterative process brings to the resulting plant configurations reported in Tables 4.7 and 4.8, which highlight the separation steps involved in the downstream sequences (numbered according to Table 4.5) and the method chosen (in roman numbers, recalling Table 4.4).

4.6.2 Coexistent reactors, non-redundant separators. Minimum total energy

The minimization of the total energy - Problem (A) - with constrained topological complexity leads to similar results in terms of selected separation methods, as reported in Table 4.7: scrubbing systems are not part of the solution, whereas VPSA and membrane separators (palladium and polymeric membrane) prevail. Moreover, for hydroformylation applications, the double-bed TSA for the simultaneous adsorption of CO_2 , CO and H_2O is selected. With the exclusion of the hydroformylation application, where biogas is directly fed to the reformers without previous separation, biogas is always partially upgraded by means of polymeric membranes (method VI).

Table 4.7.: Plant topology and power consumption when more reactor can be simultaneously selected but redundancies in the separation systems are removed. The total number of units allowed is iteratively constrained to a maximum N_{\max} , until the first configuration without redundant units is identified. The percent value of thermal energy (T%), electrical energy (E%) and the total energy in $\text{kJ mol}_{\text{syngas}}^{-1}$ (tot.) are reported. Biogas is the only feedstock.

$$(A) \min_{N,y} (\dot{Q} + \dot{W})$$

Downstream	Reactors (Separators)	N_{units}	T %	E %	tot. $\text{kJ mol}_{\text{syngas}}^{-1}$
Phosgene	RWGS(9 _{VI} ,15 _V ,);DR(3 _{VI} ,6 _{VI} ,19 _V ,22 _{VI});biogas(22 _{VI})	8	69.8	30.2	209
Monsanto	RWGS(9 _{VI} ,15 _V ,);DR(3 _{VI} ,6 _{VI} ,19 _V ,22 _{VI});biogas(22 _{VI})	8	59.8	40.2	239
Hydroformylation	DR,SR(1 _{IV} ,11 _V ,21 _V ,23 _{VI})	6	76.9	23.1	147
Iron Ore	EL;DR,SR,TRI(3 _{VI} ,6 _{VI} ,19 _V ,22 _{VI});biogas(22 _{VI})	8	75.7	24.3	125
Fischer Tropsch	EL;SR,TRI(3 _{VI} ,7 _V ,18 _V ,22 _{VI});biogas(22 _{VI})	7	63.5	36.5	128
Methanol	EL;SR,TRI(3 _{VI} ,7 _V ,18 _V ,22 _{VI});biogas(22 _{VI})	7	57.0	43.0	139

Among the converters, the electrolyzer represent the largest energy sink (Table 4.4.4). For this reason, the generation of H_2 via electrolysis tends to be limited by the implementation of endothermic reformers. This is similar to what is proposed in Chapter 3, where for a similar scenario (renewable electricity is unavailable) excess H_2 from an existing steam reforming facility reduces CO_2 in a RWGS reactor and the electrolyzer is not activated. Dry reforming is selected at lower syngas ratios $r \in [0, 1.1]$, whereas steam reforming at higher values $r \in [1.1, 2.15]$, as they deliver a low and high H_2/CO ratio of 0.72 and 3.6, respectively. The high thermal duty required

by SR and DR is then mitigated by the co-selection of less endothermic reformers, which also serves to reduce the syngas ratio to the required level. At low ratios, RWGS is active to absorb the excess H₂ generated by the dry reformer. At high ratios, TRI is operated, which partly makes use of the O₂ generated by EL.

The total energy demand is not significantly higher than the demand reported for unconstrained topologies for comparison with Table 4.6. Therefore, solutions with constrained topological complexities are to be preferred from the perspective of fixed cost economics.

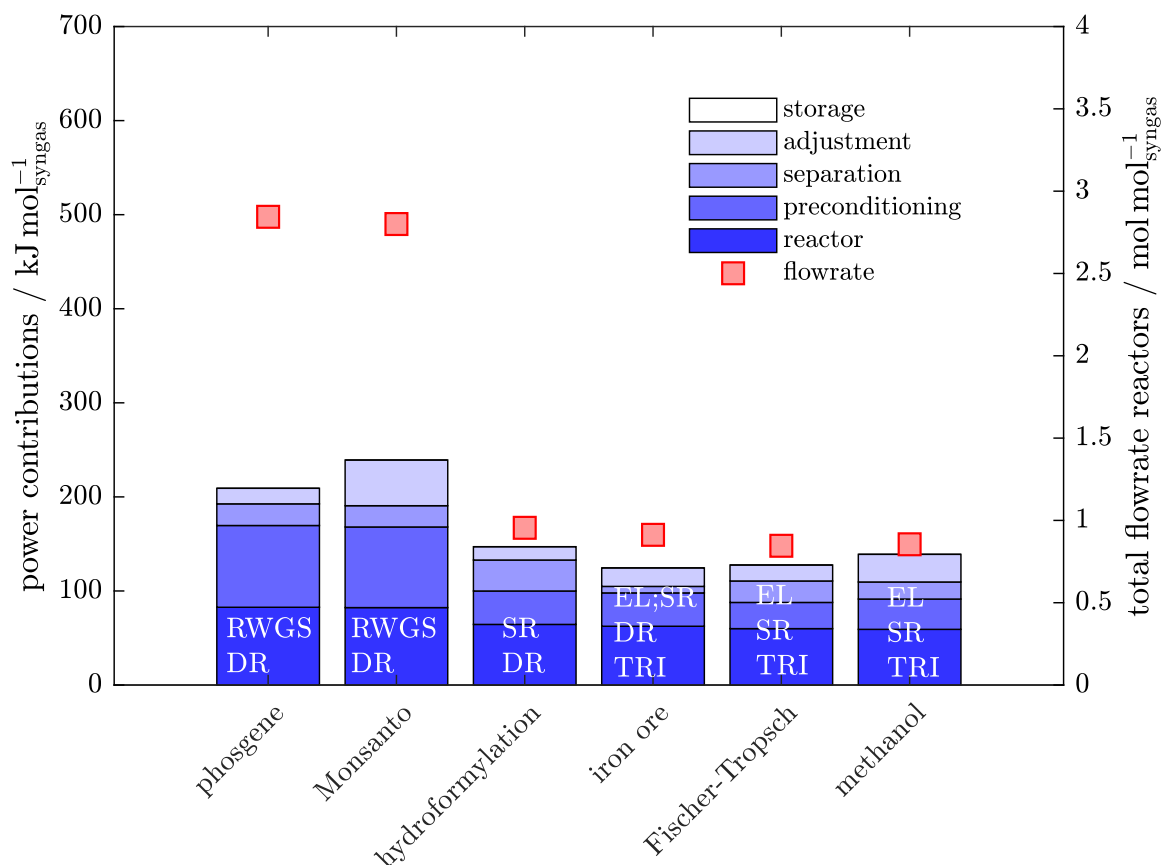


Figure 4.7.: Contributions to the total power requirements for $\min_{N,y} (\dot{Q} + \dot{W})$, biogas as feedstock. Plant complexity is constrained in the separation system, but two or more reformers can be selected simultaneously and interact at the minimum energy demand. The entry "flowrate" indicates the summation of feed flowrates to the reactors.

Figure 4.7 reports the different contributions to the total energy demand for the current optimization scenario with constrained topology, where no distinction is made between thermal and electrical energy supply. Different tones of blue denote the requirements for different plant sections. In dark blue, the reactor energy supply (*reactor*), including EL, is based on the equilibrium data reported in Table 4.4.4; *preconditioning* allows the feed gas (makeup or recycled) to reach a suitable state at the reactor inlet. *Separation* involves all intermediate contributions to switch from

the outlet state of a separator to the inlet of the following one, as well as the unit-specific energy demands, as reported comprehensively in Table 4.4. After reaction and separation, the syngas stream is adjusted to temperature and pressure level required by the downstream application (*adjustment*). Any amount of H₂ produced and not utilized for the syngas production is stored at high pressure (300 bar). Topologies at the minimum total energy supply do not allow for any surplus of H₂ to be generated and stored. The resulting interconnections between different reformers in parallel allow to preserve comparable total energy demands for different syngas ratios and downstream applications, although it loosely decreases for increasing syngas ratios. As CO can leave the plant exclusively in the syngas stream, its outlet flowrate is directly proportional to the overall feed to the reformers and, consequently, to the energy demand of the optimized topology. The decreasing total flowrate fed to the reactors, EL included, is reported in red markers in Figure 4.7.

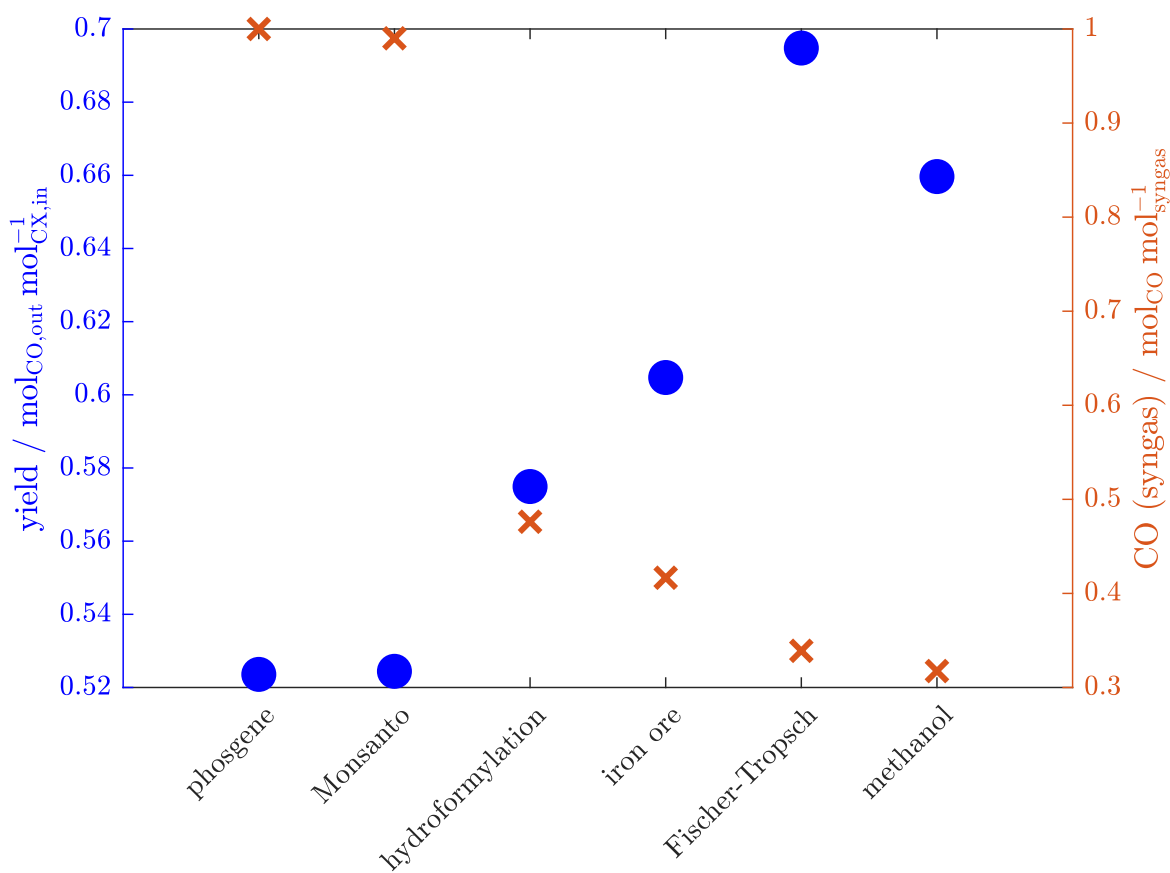


Figure 4.8.: Yield to CO and molar carbon content in the syngas stream. For syngas applications at low syngas ratios r , RWGS and DR are active. This combination determines the lowest yield and the highest processed flowrates to the reactors, which justifies the increased energy consumption for preconditioning of the inlet, as shown in Figure 4.7.

Furthermore, the combination of RWGS and DR at low syngas ratios has an inferior overall yield to CO, defined as the ratio between CO in the outlets and the summation of all carbon sources (CO₂ and CH₄) in the inlet:

$$\text{YIELD} = \frac{\sum_{i \in I} \dot{N}_{\text{CO},i,\text{out}}}{\sum_{i \in I} (\dot{N}_{\text{CO}_2,i,\text{in}} + \dot{N}_{\text{CH}_4,i,\text{in}})}, \quad (4.31)$$

where $I := \{\text{RWGS}, \text{DR}, \text{SR}, \text{TRI}, \text{POX}\}$. Figure 4.8 shows the yield in function of the downstream syngas application. The low yield for applications at high CO content in the syngas (phosgene and Monsanto) partly contributes to the higher flowrates to the reformers, which in turn determine the significantly higher preconditioning duties at low syngas ratios, shown in Figure 4.7. The low carbon yield is due to the fact that RWGS is favored from an energy perspective (low in thermal demand) but, together with DR, requires more CO₂ than CH₄ as carbon supplier for CO generation. Since the feedstock is purely biogas, there is a large surplus in bio-CH₄ which can be burned to provide the heat requirement. This aspect is analyzed and discussed in Section 4.6.4 on heat recovery.

4.6.3 Coexistent reactors, non-redundant separators. Minimum thermal energy

Problem (B) for the maximum system electrification is now enforced. Preliminary results with unconstrained complexity identified 7 units, including the POX reformer supplied with pure oxygen from the electrolyzer. One redundancy can be accounted for, as the separation of a mixture of 5 components can be accomplished by 4 units, one of which serves as biogas upgrader CH₄/CO₂, for a total of 6 units including reformer and electrolyzer. The resulting configurations are reported in Table 4.8.

Table 4.8.: Plant topology and power consumption when more reactor can be simultaneously selected but the number of units allowed is iteratively constrained to a maximum N_{max} , until the first configuration without redundant units is identified. The percent value of thermal energy (T%), electrical energy (E%) and the total energy in $\text{kJ mol}_{\text{syngas}}^{-1}$ (tot.) are reported. Biogas is the only feedstock.

(B) $\min_{N,y}(\dot{Q})$					
Downstream	Reactors (Separators)	N_{units}	T % ($\text{kJ mol}_{\text{syngas}}^{-1}$)	E %	tot. $\text{kJ mol}_{\text{syngas}}^{-1}$
Phosgene	EL;POX(3 _{VI} ,6 _{VII} ,19 _V ,22 _{VI})	6	3.13 (20.0)	96.87	639
Monsanto	EL;POX(3 _{VI} ,6 _{VII} ,19 _V ,22 _{VI});biogas(22 _{VI})	6	2.98 (19.8)	97.02	665
Hydroformylation	EL;POX(3 _{VI} ,6 _{VII} ,19 _V ,22 _{VI});biogas(22 _{VI})	6	2.85 (9.52)	97.14	333
Iron Ore	EL;POX(3 _{VI} ,7 _V ,18 _{VI} ,22 _{VI});biogas(22 _{VI})	6	7.41 (18.37)	92.59	247.8
Fischer Tropsch	EL;POX(2 _{VII} ,4 _{VI} ,19 _V ,22 _{VI});biogas(22 _{VI})	6	3.38 (6.78)	96.62	200.3
Methanol	EL;POX(2 _{VII} ,4 _{VI} ,19 _V ,22 _{VI});biogas(22 _{VI})	6	3.0 (6.34)	97	211

The thermal energy consumption reported in parentheses is slightly higher than the same value for unconstrained complexity in Table 4.6(B) due to the topological constraint on the number of units, forcing the solution towards higher thermal duties. Nevertheless, with the exception of the iron ore application, the total energy demand is now lower than in the unconstrained case, although this is not attributable to the optimization objective or constraints being enforced. The selected separation methods for this scenario are VPSA and membranes. Biogas is always upgraded by a membrane separator.

The advantage of operating with lower gas volumes due to the replacement of air with pure oxygen at the reformer feed is offset by a low atomic efficiency of the Power-to-Syngas process. The syngas ratio generated by partial oxidation is 1.95, which make higher or equal to the requirement of target applications. Therefore, EL produces an excess of H_2 , inversely proportional to the syngas ratio requirement but always present, as long as the electrolyzer is operated for the generation of O_2 . In this process configuration, H_2 is essentially a valuable by-product, although the process is significantly less efficient if the atom efficiency is to be restricted exclusively to syngas, as introduced in the following definition:

$$\eta_{\text{atom}} = \frac{(\text{H} + \text{C} + \text{O})_{\text{syngas}}}{(\text{H} + \text{C} + \text{O})_{\text{feed}}} = \frac{(2\dot{N}_{\text{H}_2} + \dot{N}_{\text{CO}} + \dot{N}_{\text{CO}})_{\text{syngas}}}{\left((4\dot{N}_{\text{CH}_4} + 2\dot{N}_{\text{H}_2\text{O}}) + (\dot{N}_{\text{CH}_4} + \dot{N}_{\text{CO}_2}) + (\dot{N}_{\text{H}_2\text{O}} + 2\dot{N}_{\text{CO}_2}) \right)_{\text{feed}}} \quad (4.32)$$

Figure 4.9 shows the values of atom efficiency comparatively for the two problems, (A) and (B). As explained, the configuration at minimum thermal energy input being discussed in this section, i.e., when EL is meant exclusively to provide pure O_2 to POX, presents lower efficiencies. More

in general and for any configuration, low molar ratios (H_2/CO) in the syngas correspond to low efficiencies, as the hydrogen fed to the plant is meant to reduce CO_2 to CO , or comes with the carbon carrier CH_4 but does not contribute to syngas. For combined POX and EL operations resulting from Objective (B), the lower atom efficiency in this case is also motivated by the excess in CO_2 from biogas not reduced by the reformer, exclusively fed by CH_4 and O_2 . When DR and RWGS are operated, i.e., Problem (A) at low syngas ratios, a surplus of CH_4 is present. This aspect is particularly important, as any excess of bio- CH_4 can be involved in a broader analysis, where this carbon neutral fuel can substitute fossil fuels for the energy supply, electrical and thermal. This is exemplified in Section 4.6.4.

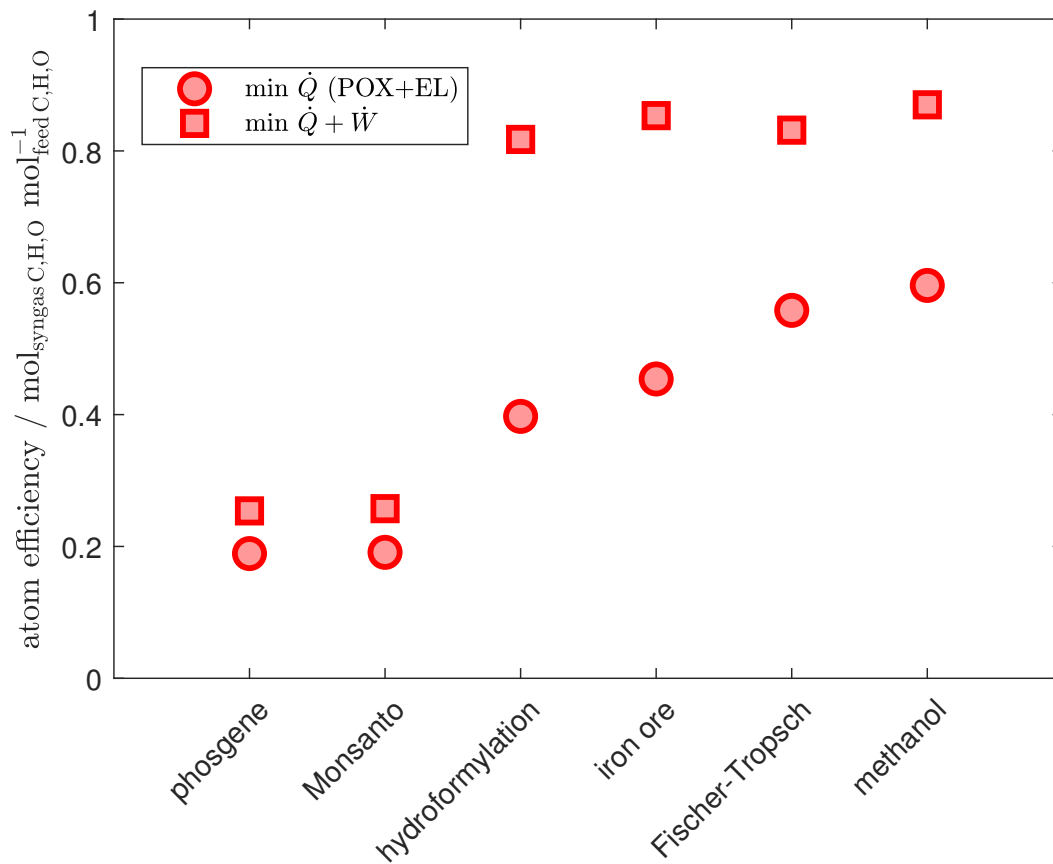


Figure 4.9.: Atom efficiency for Problem (A) $\min_{N,y} (\dot{Q} + \dot{W})$ and (B) $\min_{N,y} (\dot{Q})$ for constrained topological complexity in the separation train (no redundancy in the separators), where multiple reformers can be active at the same time (cf. Figure 4.7).

Figure 4.10 reports the specific energy contributions at the maximum electrification (Problem (B), $\min_{N,y} \dot{Q}$). The atomic inefficiency associated with the excess of H_2 translates into a higher demand for electrical energy at the electrolyzer and for the storage of excess H_2 , for any syngas application. Reactor duty in dark blue largely dominates the total energy demand due to the high volume of O_2 and required for partial oxidation: this duty is mainly absorbed by EL.

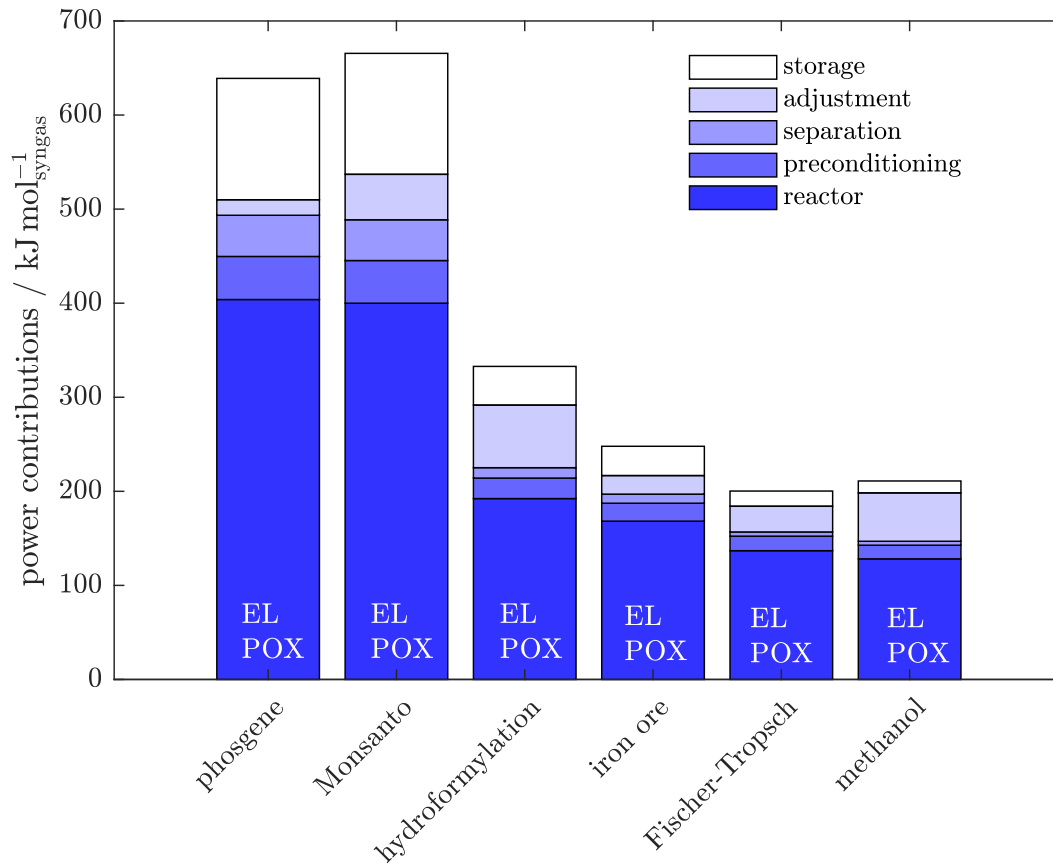


Figure 4.10.: Contributions to the total power requirements for $\min_{N,y} \dot{Q}$, biogas as feedstock. Plant complexity is constrained in the separation system and more reactors can be selected simultaneously.

4.6.4 Heat recovery: combustion of excess bio-methane

Biogas is completely or partially upgraded into bio-CH₄ and CO₂ and used as carbon source for the syngas. Excess bio-CH₄ can be used locally to generate carbon-neutral hot thermal utilities, or it can be injected into the natural gas grid and contribute in gas-fired power plants to generate electricity. Therefore, the net (external) thermal energy demand can be determined by subtracting the combustion duty of excess bio-CH₄ from the total demand at the syngas plant. The carbon footprint of the process can be determined assuming that the heat recovered from excess bio-CH₄ is the only carbon-neutral thermal contribution. Any emission of CO₂ from the process lines derives from biogas, thus carbon-neutral, and not accounted for in the balance.

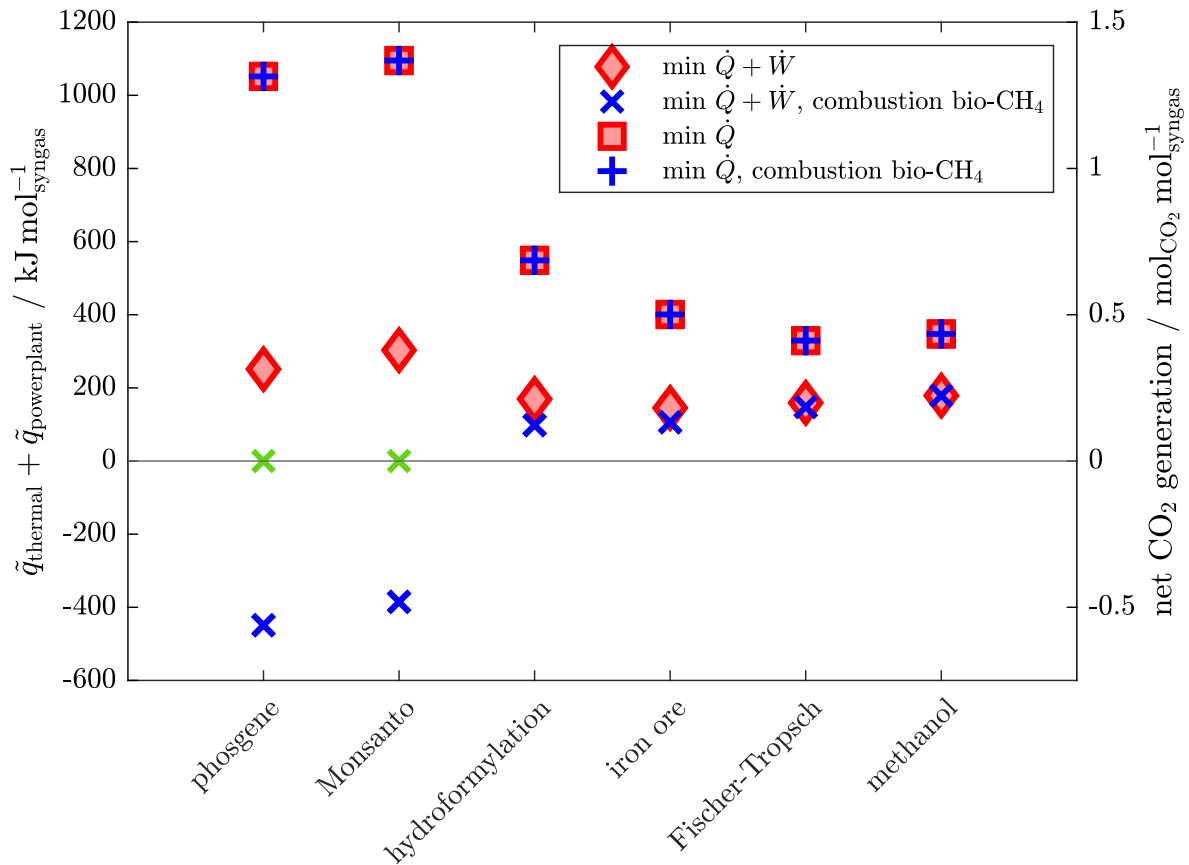


Figure 4.11.: Net thermal power demand and CO₂ generation for the two objectives, $\min_{N,y} (\dot{Q} + \dot{W})$ and $\min_{N,y} \dot{Q}$ and constrained complexity with possible interactions among reformers. Biogas is the only carbon source, and surplus bio-CH₄ is optionally burned to recover clean energy. Electricity is generated in a gas-fired power-plant of 60 % efficiency in a worst-case scenario of unavailable renewable power. In green, net CO₂ generation when the net energy requirement is negative.

Figure 4.11 reports the results of this analysis applied to the constrained complexity analyses discussed in the previous Sections 4.6.3 and 4.6.2 where, for any topology, including the highly electrified EL-POX plant configuration (Problem (B), $\min \dot{Q}$), the worst case scenario is presented: this highly energy demanding process is run with grid electricity, generated externally in a gas-fired power plant with a heat-to-electricity efficiency of 60 %. Irreversibilities in the generation of hot utility from bio-CH₄ are neglected, and it is implied that the low heating value of bio-CH₄ is fully available as such. The summation of all thermal duties, including the requirement at the gas-fired power plant for the supply of electricity, are reported on the y-axis. In the figure, a negative specific thermal energy demand implies that excess bio-methane can exceed the energy requirement at the syngas plant. This occurs when the syngas ratio required is low (phosgene and Monsanto), and the plant is run in DR and RWGS, as reported earlier in Section 4.6.3. The green symbols correspond to this scenario in net CO₂ generation, as the combustion of biogas is carbon-neutral

and cannot determine negative emissions. For different syngas applications, the combustion of excess bio-methane does not play a relevant role in lowering the overall energy requirement and CO₂ emissions. Clearly, the points belonging to the solution of Problem (B) must coincide: as reported in the previous section, bio-CH₄ is completely utilized in POX and none can be burned. The overall energy demand in this scenario is five times larger than in the solution of Problem (A). It follows that such highly electrified process solutions should entirely rely on renewable electricity to prove sustainable.

4.6.5 Single reformer, non-redundant separators. Minimum total energy

As reported in Section 4.6.2, the optimizer identified the interplay between different reformers as optimal solution at the minimum total power demand. The complexity reduction in the separation sequence discussed in Section 4.6.1 is here extended to the reformers. If the interaction among reformers proves optimal from an energy perspective, the choice may not prove profitable when CAPEX is included. This section is intended to present results with an additional constraint on the number of unit operations involved in the minimization of the total energy - Problem (A).

The complexity constraint sets the plant topology to a maximum of 6 units, which account for 1 reformer, 4 separators (at most, for a mixture of 5 species as resulting from POX, TRI, DR, SR), EL. Additionally, a new logical constraint forces the choice to a single reformer:

$$\sum_{i \in I} y_i = 1 \quad (4.33)$$

with $I := \{\text{RWGS}, \text{TRI}, \text{POX}, \text{SR}, \text{DR}\}$, mutually exclusive units. The solution is reported in Table 4.9. Here the optimal separators are sequences of VPSA and polymeric membranes. Where the combination of RWGS and DR resulted at low syngas ratios (phosgene and Monsanto), DR is exclusively selected. For higher ratios, the combination of EL and TRI is selected. At high syngas ratios, biogas is directly fed to TRI without upgrade, which underlines the reason of interest towards TRI, as this reformer does not generally need the biogas separation unit.

Table 4.9.: Plant topology and power consumption for the minimization of the total power demand (Problem A), biogas as feedstock. When not indicated, biogas is fed without upgrading to the reactor. In this case, only one reformer can be selected, possibly in conjunction with EL. Maximum number of units: 6.

$$(a) \min_{\dot{N}, y} (\dot{Q} + \dot{W})$$

Downstream	Reactors (Separators)	T %	E %	tot. kJ mol ⁻¹ _{syngas}
Phosgene	DR(3 _{VI} ,6 _{VI} ,19 _V ,22 _{VI});biogas(22 _{VI})	70.1	29.9	232
Monsanto	DR(3 _{VI} ,6 _{VI} ,19 _V ,22 _{VI});biogas(22 _{VI})	61.6	38.4	262
Hydroformylation	EL;TRI(3 _{VI} ,7 _V ,17 _V ,21 _V)	56	44	188
Iron Ore	EL;TRI(3 _{VI} ,6 _{VI} ,19 _V ,22 _{VI});biogas(22 _{VI})	72.7	27.3	141
Fischer Tropsch	EL;TRI(3 _{VI} ,7 _V ,17 _V ,21 _V)	48.3	51.7	156
Methanol	EL;TRI(3 _{VI} ,7 _V ,17 _V ,21 _V)	38.6	61.4	182

Figure 4.12 shows the energy requirements for these configurations in shades of blue. The selected reactors are marked in white on the columns. At low syngas ratios, a surplus of H₂ is present and contributes to the energy demand for storage. For syngas ratio requirements above the ratio generated from the TRI reformer (H₂/CO = 1.5), the reactor duty in dark blue increases proportionally with the flow at EL, which provides with the complementary amount of H₂ required in the final syngas stream. In the same figure, the energy demands related to the current scenario are compared with the results from allowing multiple reformers to be active simultaneously without redundancies in the separation sequences, as defined in Section 4.6.2. In the latter case, the selected reactors are recalled in green frames above the stacked columns.

From the comparative analysis of the two cases it can be seen that the energy requirements at low syngas ratios (phosgene and Monsanto) exclusively restricted to the reactor-separator sequence (Figure 4.12) are essentially comparable, although excess H₂ produced now by the operations restricted to the exclusive implementation of DR must be stored, and thus increases the energy costs. On the contrary for operations non restricted to a single reformer, the RWGS reactor consumes excess H₂ generated in DR, thus lowering the energy requirement at the reactors. For all other syngas applications, the storage of H₂ storage plays no role and the interaction of reformers may offer more consistent energy savings, standing up to about 20 % of the total energy demand.

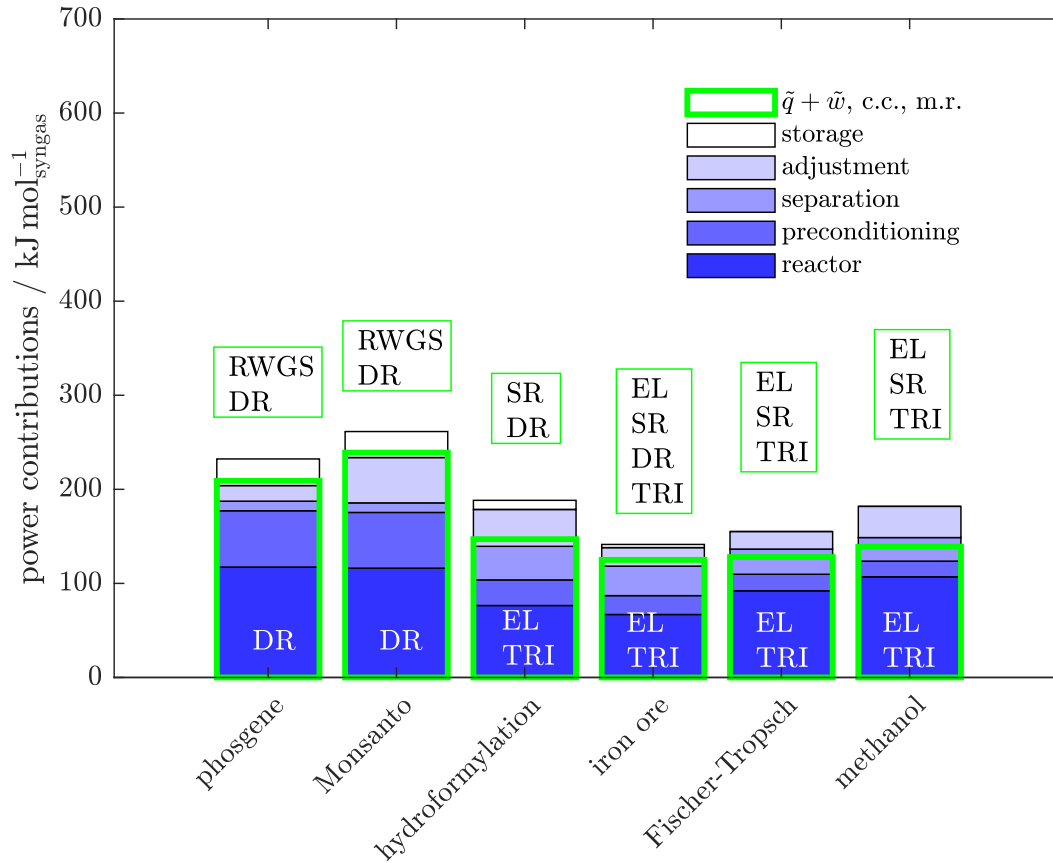


Figure 4.12.: Contributions to the total power requirements for $\min_{N,y} (\dot{Q} + \dot{W})$, biogas as feedstock. The solution is constrained to a single reformer, optionally with EL. In green, the reference solution for constrained plant complexity (c.c.), where more reformers (m.r., indicated in the green boxes) can be selected and interact, also reported in Table 4.7, and in Figure 4.7.

4.7 Feedstock: carbon dioxide

So far, biogas has been considered the only source of carbon for the system. The supply of bio-CH₄ opened to a complex range of process options in terms of reactors and separators, embedded in a superstructure and optimized to the minimum energy demand. In this section, CO₂ is considered as the only carbon carrier, which boils down the process options significantly: RWGS is the only reactor which converts CO₂ exclusively, and EL must supply H₂. Any amount of O₂ surplus can be safely released to the atmosphere, determining a loss in atomic efficiency. Even if biogas were to be supplied to RWGS, as analyzed in the previous Chapter 3, the excess bio-CH₄ would be enough to sustain the demand for heat, but not the demand for carbon: an external source of CO₂ needed to be included. Additionally, it is assumed in this analysis that CO₂ is captured from air (DAC) by means of low-temperature (LT) solid sorbent, which performs DAC with a thermal and electrical power input of 277 kJ mol⁻¹_{CO₂} (1750 kWh ton⁻¹_{CO₂}) and 39 kJ mol⁻¹_{CO₂} (245 kWh ton⁻¹_{CO₂}), respectively.

The values are adapted from Fasihi et al. [161]. Table 4.10 shows that the combination of EL and RWGS, the only technology available for the given feedstock, is followed by combinations of membranes (polymeric and Pd), and VPSA operations. Being the process topology highly constrained due to the absence of bio-CH₄. Objectives (A) and (B) produce similar results. The optimum topologies are highly electrified solutions, where the electricity inputs span between 77 % and 91 % of the total energy requirement. If compared with the corresponding configurations for optimal topologies accepting biogas as feedstock and allowing multiple reformers (Table 4.7), the power demands are conspicuously larger due to the presence of DAC, whose share spans between 19 % and 37 % of the total energy requirement of the plant. The DAC technology selected for this study requires electricity for 12.5 % of its total energy demand [161]. However, this shall be considered as a high-level reference: many are the DAC technologies on the market, from fully electrified electrochemical systems, to thermal absorption processes and moisture-swing for thermal regeneration. A more detailed analysis of potential heat and electrical integration should be considered according to specific projects and locations.

Table 4.10.: Plant topology and power consumption, divided into thermal percentage (T%), electrical percentage (E%) and total power for the syngas plant (tot.). Additionally, consumptions for direct air-capture (DAC) are reported.

(a) $\min_{N,y} (\dot{Q} + \dot{W})$						
Downstream	Reactors (Separators)	T %	E %	tot. kJ mol ⁻¹ _{syngas}	DAC kJ mol ⁻¹ _{syngas}	
Phosgene	EL;RWGS(9 _{VI} ,13 _V ,24 _V)	22.2	77.8	528	316	
Monsanto	EL;RWGS(9 _{VI} ,13 _V ,26 _{VII})	21.4	78.6	532	313	
Hydroformylation	EL;RWGS(9 _{VI} ,13 _V ,26 _{VII})	12.5	87.5	435	151	
Iron Ore	EL;RWGS(9 _{VI} ,13 _{VI} ,24 _V)	15.6	84.4	425	132	
Fischer Tropsch	EL;RWGS(9 _{VI} ,13 _V)	9.8	90.2	403	107	
Methanol	EL;RWGS(9 _{VI} ,13 _V)	9.1	90.9	410	101	

(b) $\min_{N,y} \dot{Q}$						
Downstream	Reactors (Separators)	T %	E %	tot. kJ mol ⁻¹ _{syngas}	DAC kJ mol ⁻¹ _{syngas}	
Phosgene	EL;RWGS(9 _{VI} ,15 _V ,25 _{VII})	21.2	78.8	534	316	
Monsanto	EL;RWGS(9 _{VI} ,15 _V ,25 _{VII})	19.9	80.1	564	313	
Hydroformylation	EL;RWGS(9 _{VI} ,13 _V ,26 _{VII})	12.5	87.5	437	151	
Iron Ore	EL;RWGS(9 _{VI} ,13 _V ,26 _{VI})	14.3	85.7	439	132	
Fischer Tropsch	EL;RWGS(9 _{VI} ,13 _V ,26 _V)	9.5	90.5	414	107	
Methanol	EL;RWGS(9 _{VI} ,15 _V ,25 _V)	8.8	91.2	422	101	

Figure 4.13 can be considered representative for the solutions of Problem (A) and (B), as the energy contributions in the two cases are essentially the same. It shows that the energy input at the reactor section is almost constant for different applications. The slight decrease is due to the smaller flowrates fed to RWGS for increasing syngas ratios, as the mild endothermicity of RWGS has a moderate impact on the overall energy demand at the reactors, thus at most 23 % of the

combined duty of EL and RWGS. As the flowrate of RWGS decreases inversely to the syngas ratio, so does the preconditioning of its feed stream (lighter blue in the figure). Although the flowrate of CO₂ required at RWGS is inversely proportional to the syngas ratio, as reflected by the trend of energy demand at the DAC in Table 4.10, the flowrate processed at EL does not vary: it either feed H₂ to RWGS or to the final syngas stream.

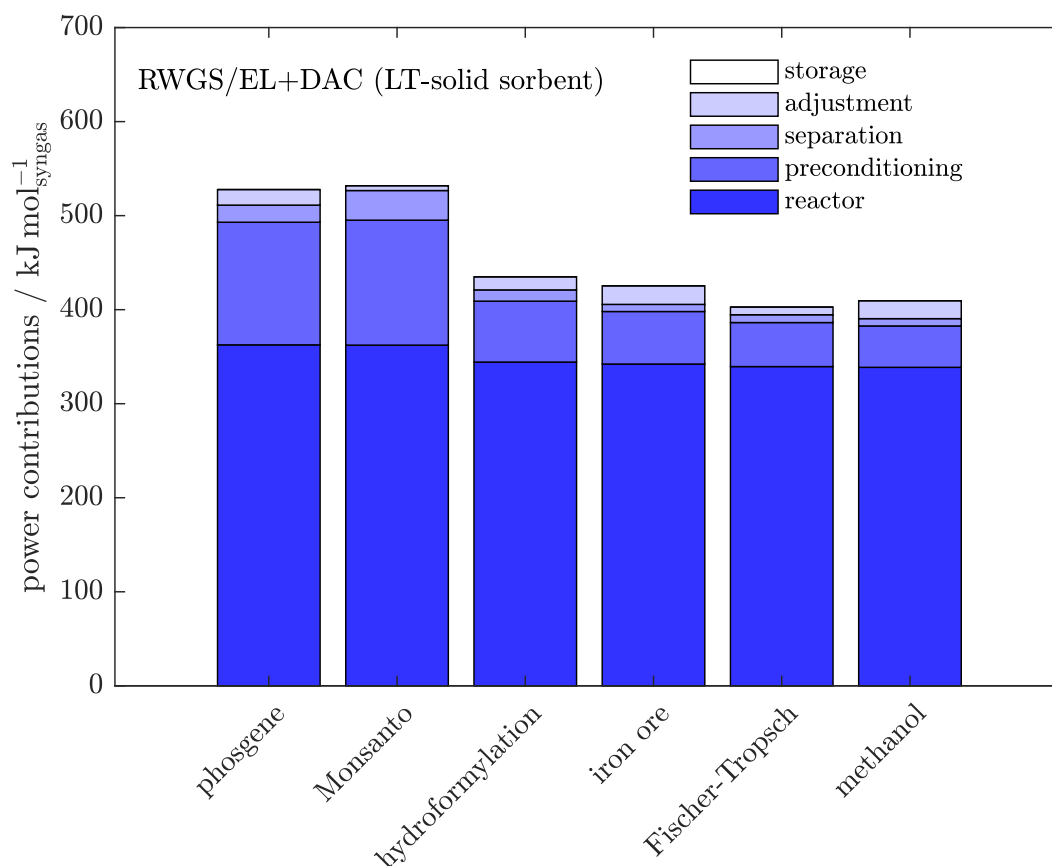


Figure 4.13.: Energy demand if exclusively CO₂ from DAC is fed to the plant for $\min_{N,y} (\dot{Q} + \dot{W})$. A maximum of 5 units is allowed by complexity constraint Equation 4.29. The contributions in this figure do not include DAC energy requirements.

The higher extent of electrification of CO₂-based processes over solutions fed by biogas can be appreciated in Figure 4.14, where the total thermal duties for the two cases are collected. Topologies accepting biogas as feedstock require a higher thermal duty even at the minimum total energy as in this case it is shown. Although the combination of RWGS and EL requires a higher total energy demand, it systematically reports lower thermal requirements, as shown in Figure 4.14. Exception can be made for low syngas ratio applications, where the combustion of excess bio-CH₄ resulting from the interaction between RWGS and DR (biogas as feedstock) can sustainably provide the plant with the total energy it requires, as it was shown in Figure 4.11 of Section 4.6.4.

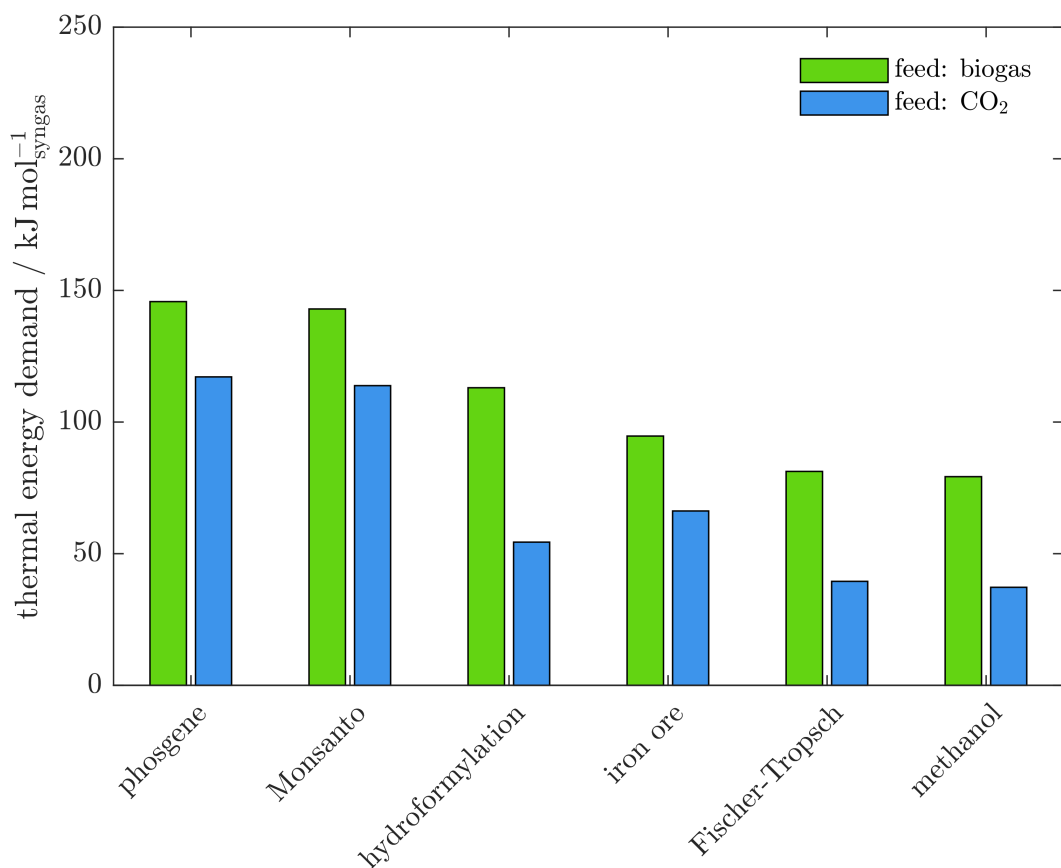


Figure 4.14.: Total thermal requirements. Comparison of the interaction between reformers at the minimum total energy, with biogas as feedstock to multiple reformers without redundant separators (in green, extracted from the results in Table 4.7) and with direct air-captured CO₂ to the combination of EL and RWGS (in blue, from Table 4.10(A)). The latter accounts also for the thermal input requirement at DAC, which is a conservative assumption: the selected DAC technology requires a considerable amount of thermal energy, while many DAC systems proposed on the market can be fully electrified or thermally integrated within the system with waste heat at low temperatures.

Figure 4.14 shows that although the energy content of a biogas stream is higher than that of a pure CO₂ stream, the thermal energy demand is lower when pure CO₂ is fed to the system when total energy is minimized. This is due to the fact that reducing CO₂ in an RWGS reactor (case: feed CO₂) requires less energy than reforming CH₄ in steam and dry reforming reactors, as reported in table 4.7 (case: feed biogas).

The higher energy content of biogas results in a lower thermal energy demand compared to a pure CO₂-fed plant when biogas is fed into an adiabatic partial oxidation reactor. However, this solution requires the injection of oxygen, which must be provided by an electrolyzer to avoid the introduction of inert N₂ with air into the system, which drives up the electrical energy demand

and thus the total energy cost of the process. This solution is suboptimal in the context of total energy minimization, which determined the results shown in Figure 4.14.

4.8 Conclusions and outlook

At low syngas ratios and for pure CO production from biogas (phosgene and Monsanto processes), the interaction between the reverse water-gas shift reactor and dry-reformer without the contribution of water electrolysis, identified at the minimum total energy, implies the presence of a stream of surplus bio-CH₄, possibly burned to generate carbon-neutral thermal and electrical energy (Figure 4.11). If the topology is forced to a single reformer, dry-reforming is selected but a surplus of H₂ is generated and has to be stored. This contributes to a lower atom efficiency towards syngas and to an increased energy demand, as shown in Figure 4.12. For syngas applications at higher H₂-to-CO ratios, combinations of reformers can ensure energy savings with respect to single-reformer implementations, where tri-reforming combined with water electrolysis prevails in the latter scenarios.

At higher syngas ratios however, configurations at the minimum thermal energy and maximum electrification are obtained when the two ends of an electrolyzer, either pure H₂ or O₂, are used in a RWGS reactor (Table 4.10) or in a partial oxidation reformer (Table 4.8), as discussed in Sections 4.7 and 4.6.3, respectively.

Such highly electrified solutions require large contributions of the electrolyzer with surplus of H₂ or O₂, if exclusively a partial oxidation reformer or a RWGS reactor were to be installed with the electrolyzer.

As a matter of fact, the exclusive implementation of one of the two processes, RWGS or partial oxidation with water electrolysis, determines a low efficiency in the utilization of the power demand at the electrolyzer for syngas generation, as either a surplus of O₂ or H₂ is present (Figure 4.9). It should be noted that the tri-reformer can also be operated adiabatically to attain the correct H₂-to-CO ratio for methanol and Fischer-Tropsch applications, resulting in a surplus of H₂ as in the case of POX shown in Figure 4.10.

The inefficient utilization of material streams at EL affects the overall system performance, as this unit operation is the most energy demanding of the entire process. The stoichiometry of EL indicates that oxygen constitutes 33 % of its outlets, and is completely utilized in POX, which generates a syngas ratio of 1.95, already suitable for methanol or Fischer-Tropsch synthesis. Consequently, the H₂ stream produced at EL is a valuable byproduct that, however, lowers the Power-to-Syngas efficiency. Similarly, the sole installation of RWGS implies that the whole H₂ stream from EL (67 % of its outlets) is used for syngas production as reducing agent in the reactor, or by direct integration in the product stream, and thus bypassing the plant. In this case, O₂

is a valuable byproduct. Surplus O_2 could be fed to the combustion chamber to sustain the endothermic process steps (RWGS reactor). However, this would still lead to a considerable surplus of valuable byproduct that may be directly utilized within the plant (Figure 4.15).

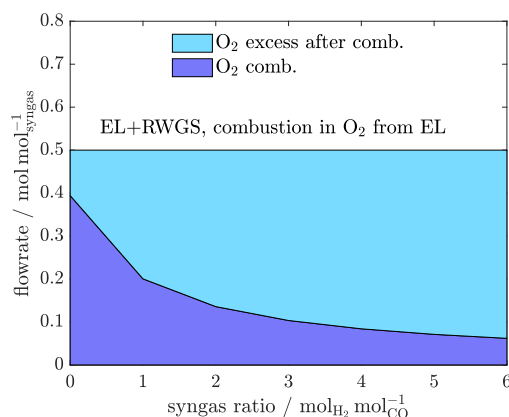


Figure 4.15.: Oxygen can be supplied to the oxy-combustion chamber of the RWGS reactor, where heat is supplied to allow the endothermic reaction to take place (in purple). The remaining O_2 , while valuable, has no use in the system (in blue).

For process configurations where the electrical input constitutes a predominant share of the total, proper flexibility and/or buffering strategies to manage the fluctuating nature of a renewable power source must be put in place. Design and control methods must then be applied to well defined syngas applications, stepping down from high-level descriptions of large process networks to a more accurate description of the single steps involved.

The next chapter illustrates how process flexibility, in conjunction with a certain extent of buffering, can offer a technical solution to the inefficient utilization of the material streams generated by the water electrolyzer to generate a syngas to Fischer-Tropsch. In this case, the partial oxidation of pure bio-methane (POX) is substituted by an analogous tri-reforming reactor operated in adiabatic mode, where the amount of O_2 injected is sufficient to sustain an adiabatic operating regime.

4.9 Chapter summary

In this chapter, a superstructure optimization approach is used to investigate Power-to-Syngas reactor-separator sequences for the minimum energy requirement, thus allowing to address the second research question formulated in Section 1.3: "What is the energy consumption of optimal reactor-separator sequences for the production of syngas from biogas, selected from a large number of candidates?". Mixed-integer, linear modeling constraints are imposed for two alternative feedstock scenarios: biogas or CO_2 from direct air-capture (LT-solid sorbent). A general objective function combines thermal and electrical power input linearly. The electrical power contribution is weighted by a pseudo-price $\omega \in [0, 1]$. For $\omega \rightarrow 1$, electricity is penalized, as it might

be obtained from non-renewable sources, for instance, generated in power plants run in natural gas. On the contrary, when $\omega \rightarrow 0$ the plant is supposed to rely on carbon-free renewable electricity. The resulting MILP problems are solved for the extreme-case scenarios: Objective (A) for $\omega = 1$ and Objective (B) for $\omega = 0$. Results show that the higher total power demand from enforcing Objective (B) (renewable power) is compensated by the predominance of the share of electricity, up to 97 %, possibly increasing after heat integration. Furthermore, topological configurations from Objective (B) include two reactors for any syngas application, a general EL electrolysis module and partial oxidation of methane in oxygen, whereas an interaction among different reformers results with the minimization of the total energy demand as in Objective (A). Surplus bio-CH₄ can relieve the demand for external fossil-based fuel, especially for downstream applications requiring low syngas ratios at the minimum total energy. Membranes and adsorption-based separators prevail over absorption and scrubbing methods. Cryogenics possibly result with configurations run in renewable power. The combination of electrolysis and reverse water-gas shift reactor supplied by direct air-captured CO₂ increases the total power requirements, although the electricity demand always prevails over the thermal inputs, even accounting for the thermal contribution of a DAC technology based on thermal regeneration, thus a conservative assumption. At low syngas ratios, the interaction between dry reforming and the RWGS reactor result in the most energy efficient and sustainable solution if excess bio-methane is used to provide thermal energy inputs and to contribute to carbon-neutral electricity. At high syngas ratios, the lowest share of thermal energy is required when the two outlet streams from the electrolyzer are utilized in a mutually exclusive way, feeding either H₂ to the RWGS reactor, or O₂ fed to a partial oxidation reactor, thus determining a surplus production of valuable electrolyzer products.

Process flexibility (I) - Optimal control of syngas production for Fischer-Tropsch applications

5.1 Introduction

The high-level analyses proposed in Chapters 3 and 4 approached the systems from a purely thermodynamic perspective. This allowed the screening of numerous process candidates under extreme-case scenarios, when either clean, low-cost renewable energy is available, and thus highly electrified process setups are identified at the minimum thermal power, or when expensive grid electricity comes at a high environmental cost, e.g., when provided externally from gas-fired power plants fueled by natural gas. Although this approach consented a numerically cheap evaluation of the entire system, it did not yet incorporate temporal and spatial coordinates, essential in the actual process design and operations. The second part of this dissertation is intended to cover these aspects.

Conclusions of the last Chapter 4 indicated that partial oxidation and reverse water-gas shift reactor in combination with a water electrolyzer offer high electrification potential, although an excess production of H_2 and O_2 introduces an extent of under-utilization of the electrolyzer, which is the most energy demanding piece of equipment. Unless large battery storage devices are foreseen in the plant, implementing both partial oxidation and RWGS reactors, where the electrolyzer supplies with the required stream of H_2 and O_2 , could be a viable approach, provided that effective control system ensure product specifications under dynamic operations.

Scope of the study presented in this chapter is to illustrate the novel process setup and to identify relevance and features of an optimal control approach to ensure plant specifications, when the system is subject to fluctuations in the renewable power.

In the first part, a fluctuating renewable power supply of real time-scale and magnitude is integrated with a distributed plant model based on the outcomes of Chapter 4. The system is controlled to meet the desired syngas specifications (productivity and composition) for Fischer-Tropsch applications.

After the relevance of fast computations in model-based plant control strategies is discussed, results from a collaboration with TU-Chemnitz are presented, where Dr. Garmatter set and run optimal control routines to test the performance and computational speed of `pararea1`, a promising parallel-in-time integrator, if benchmarked with a reference fine implicit integrator of higher order running over the same time domain. Results show that, although the parallelization strategy halves the computational time required, utilizing differential-algebraic equations significantly limits the attainable computational speed. Therefore, it may be more effective to reformulate the problem as a ordinary-differential equation set, which implies the introduction of modeling simplifications and, possibly, minor inconsistencies in the material and momentum balances.

For this chapter, a standard procedure for reactor design, based on individual nominal loads, is applied. This does not account for the impact that the instability of a renewable power source may have on the identification of the optimal design of the unit operations involved. This non trivial task is also influenced by the high level of interconnection between system units, typical within highly electrified Power-to-X systems meant to absorb peaks and drops in the supply of available power without any energy surplus. Therefore, the allocation of renewable power within the plant influences not only the design of process units, but also their operation. Consequently, design, operations and allocation of fluctuating renewable power must be simultaneously combined plant-wise within a single optimization problem. All this considered, the second chapter dedicated to process flexibility combines the aforementioned aspects for the design and setpoints definition of a flexible Power-to-Syngas process for the synthesis of methanol.

5.2 Plant layout and dynamics

The synthesis of Fischer-Tropsch (FTS) represents a milestone in the production of synthetic hydrocarbon fuels. It converts a feed stream of syngas with molar ratio H_2/CO of 2 into liquid fuels: olefines and paraffines. The feed stream must be purified of the presence of other components typically present in crude syngas: H_2O , a byproduct of the synthesis, hinders the conversion; CO_2 behaves as an inert component when fed with CO on standard cobalt catalysts, and lowers selectivity toward long-chain hydrocarbons when hydrogenated directly due to the predominance of the contribution of methanation [162]; CH_4 is essentially an undesired product. In order to purify the feed, the choice on the separation sequence to be implemented is here identified by means of the tools developed in Chapter 4. Details on the derivation of the current process layout are reported in the Supplementary Section C.1.

As concluded in the previous chapter, the use of an electrolyzer reveals highly electrified process configurations when cheap renewable electricity is available, for instance generated by a wind farm installed in the vicinity of the chemical facility. In this plant scheme, H_2 from the electrolyzer and CO_2 provided by (direct-air) carbon capture, or from biogas, can be converted into syngas in a non-adiabatic fixed bed reactor (reverse water-gas shift). Its mild endothermicity allows a

moderate thermal input to support the production of CO. Therefore, among the externally-heated reforming technologies, a RWGS reactor offers the highest versatility in term of potential carbon feedstock (biogas, biogenic CO₂ or from DAC) and represents, together with an adiabatic partial oxidation reforming process, the most electrified solution.

However, besides H₂, EL generates O₂ which can be used to sustain the endothermicity of RWGS with a clean combustion, facilitating the carbon capture with a more concentrated CO₂ in the exhaust off-gas. However, as reported in Figure 4.15, for a syngas ratio of 2, only 13.5 % of the O₂ stream from the electrolyzer is needed for a clean combustion of CH₄, whereas the most part of O₂ is not utilized within the process.

The former chapter concluded that a partial oxidation technology could be coupled with RWGS to allow for a more efficient utilization of the electrolyzer. Two partial oxidation reactors were included in the superstructure analysis, either fed by pure methane (denoted by POX, or simply partial oxidation) or by a mixture of biogas and water (tri-reforming, TRI). For TRI, a conservative assumption related to the energy requirement assumed an understoichiometric feed of O₂, not sufficient to sustain the reforming reactions adiabatically. Therefore, a thermal energy input was considered. However, when the process is fed by a sufficiently higher flowrate of O₂, it can be run without additional need for fuel. In absence of pure O₂, air can be fed to the system, although a different process design consisting of larger unit operations is preferable due to its dilution. Alternatively, air or enriched air fed to a plant designed and optimized for pure O₂ would determine a lower productivity of syngas. TRI is particularly interesting, as it allows to feed biogas without the need for previous upgrading separation, whereas partial oxidation requires the preliminary separation of methane from carbon dioxide. In addition, a lower flowrate of biogas is required to generate the same amount of CO in that not only CH₄, but also CO₂ contributes in the supply of carbon to syngas.

Due to the lower energy demand required to store O₂ over H₂, and to the fact that a partial oxidation system can also operate in air or O₂-enriched air if the stored O₂ drops low, the proposed Power-to-Syngas process involves the storage of O₂. In contrast, the flow rate of H₂ fluctuates according to the trend of the renewable power supply. By means of this buffering scheme, the RWGS reactor and tri-reformer should be operated dynamically to ensure a stable productivity and syngas composition, in order to offset the fluctuations of the energy supply.

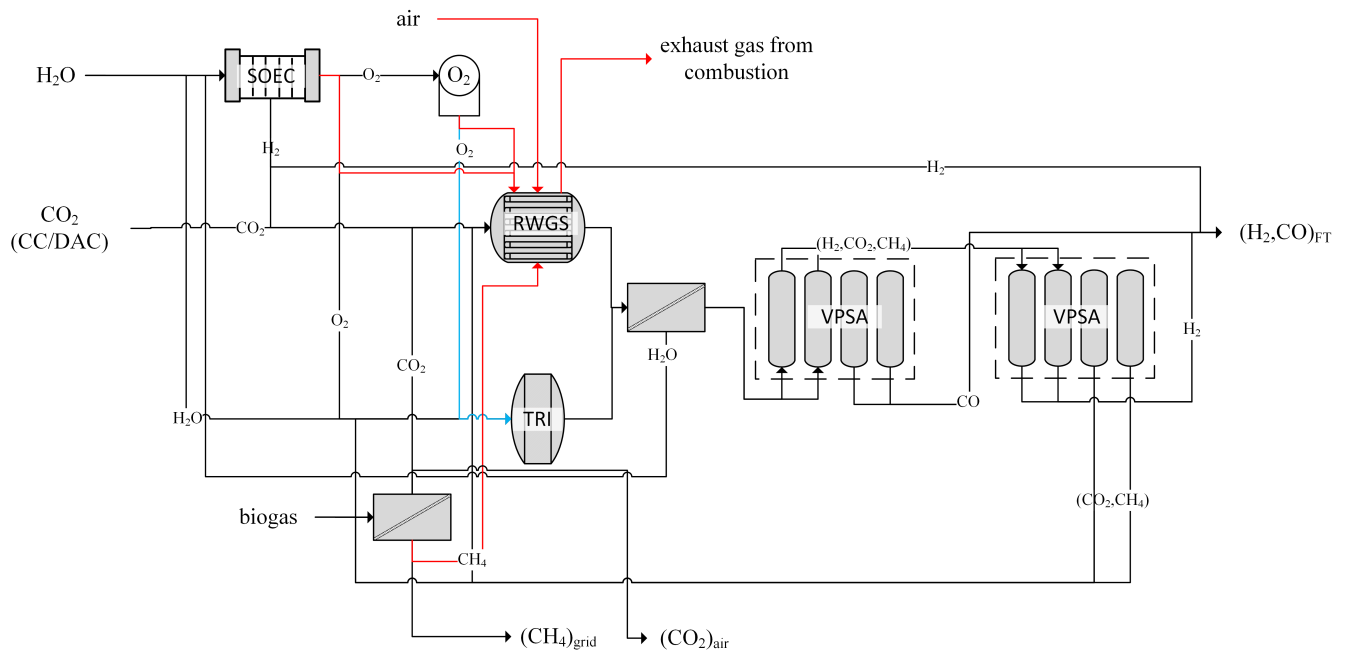


Figure 5.1.: Plant layout: the RWGS and TRI reactors produce raw syngas, where H_2 and O_2 are supplied via electrolysis, e.g., an efficient SOEC. H_2 may be fed to RWGS and/or bypass the reactor to the syngas product stream whereas excess O_2 may be stored in a buffering device. CO_2 could be obtained from biogas using a suitable separation strategy.

Figure 5.1 reports the plant configuration for the synthesis of raw syngas and its purification. Raw syngas is the mixture produced at junction of the two reactors. The upstream section comprises an electrolyzer (solid-oxide), the RWGS multitubular reactor and the TRI adiabatic step. Furthermore, biogas is optionally upgraded in a polymeric membrane. In this layout it is shown that CO_2 can be provided from the upgraded biogas stream, whereas excess CH_4 is burned to sustain the reaction. The additional required CO_2 stream can be provided directly from carbon-capture technologies, e.g., from adjacent production facilities, or from DAC. The utility lines to the combustion chamber of the RWGS reactor are reported in red. Air, enriched air or pure O_2 is combined with CH_4 from the biogas upgrade for combustion. Oxygen is stored, fed to the TRI reactor (black connectors), or fed to the utility line (red connectors) to support RWGS. The separation sequence after RWGS and TRI is determined based on the results of a new superstructure optimization, where the total power is minimized, and the plant is forced to operate exclusively the TRI reactor and an electrolyzer. This solution suggests the installation of a polymeric membrane dehydrator after the reformer, separating H_2O from H_2, CO, CO_2 , and CH_4 , followed by a sequence of VPSAs for the sequential separation of CO and H_2 , thus integrated into the outlet syngas stream. The last VPSA partly recycles the binary mixture (CO_2, CH_4) back to the TRI reactor, and partly feeds with the same mixture a membrane separator for the biogas upgrade. The same separation sequence can process the RWGS reactor outlets. Therefore, the total number of unit operations, including reactors, electrolyzer and separators, is 7, as the plant layout in Figure 5.1 shows.

The plant is supposed to switch between alternative configurations according to the availability of renewable power.

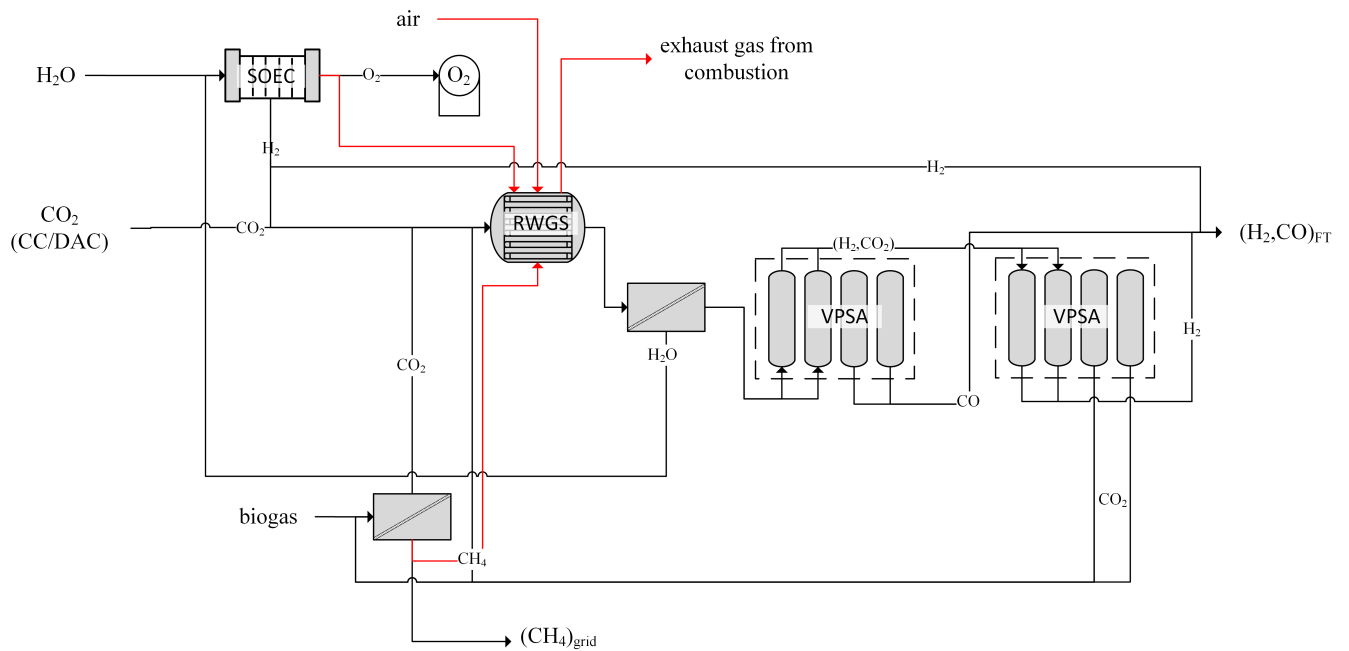


Figure 5.2.: Plant operation when electricity is scarce and RWGS is supplied with H_2 from EL. Methane from biogas can provide heat to the RWGS reaction.

Figure 5.2 defines the systems response in a scenario where the renewable power is at peak supply. In this case, the buffer tank for O_2 storage is filled, EL supplies H_2 to the RWGS reactor which is heated by combusted bio- CH_4 or biogas.

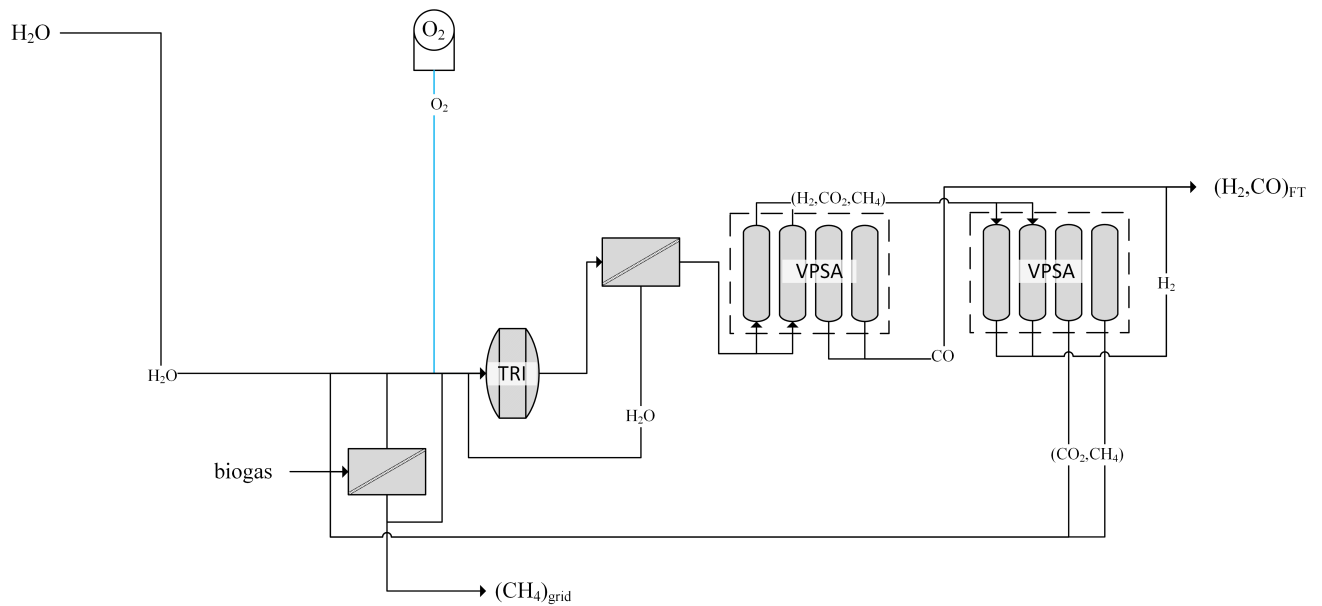


Figure 5.3.: Plant operation when electricity is scarce and Tri-reforming is combined with stored O_2 .

On the contrary, Figure 5.3 illustrates the switch in operating regime when the plant faces a shortage in renewable power supply. In this case, the storage device releases O_2 , which feeds the TRI reactor. EL is not operated.

5.2.1 Plant control

Figure 5.4 recalls the complete plant layout, where the final syngas specifications are reported in red. The plant must provide a mixture of H_2 and CO with a molar ratio of 2, at about 110 ton day^{-1} . This stream is stably supplied to the Fischer Tropsch reactor downstream. As analyzed in the previous section, the swing between the operating regimes shown in Figures 5.2 and 5.3 requires to be optimally controlled. For this reason, this chapter deals with a optimal control approach restricted to the production section of the plant, identified by the blue box outlined in dashes in the illustration above. Syngas specifications are to be attained directly at the outlets of the reactors, given a hourly fluctuation in the available renewable electricity supply.

parallel step. The next section frames the modeling approach and the assumptions adopted.

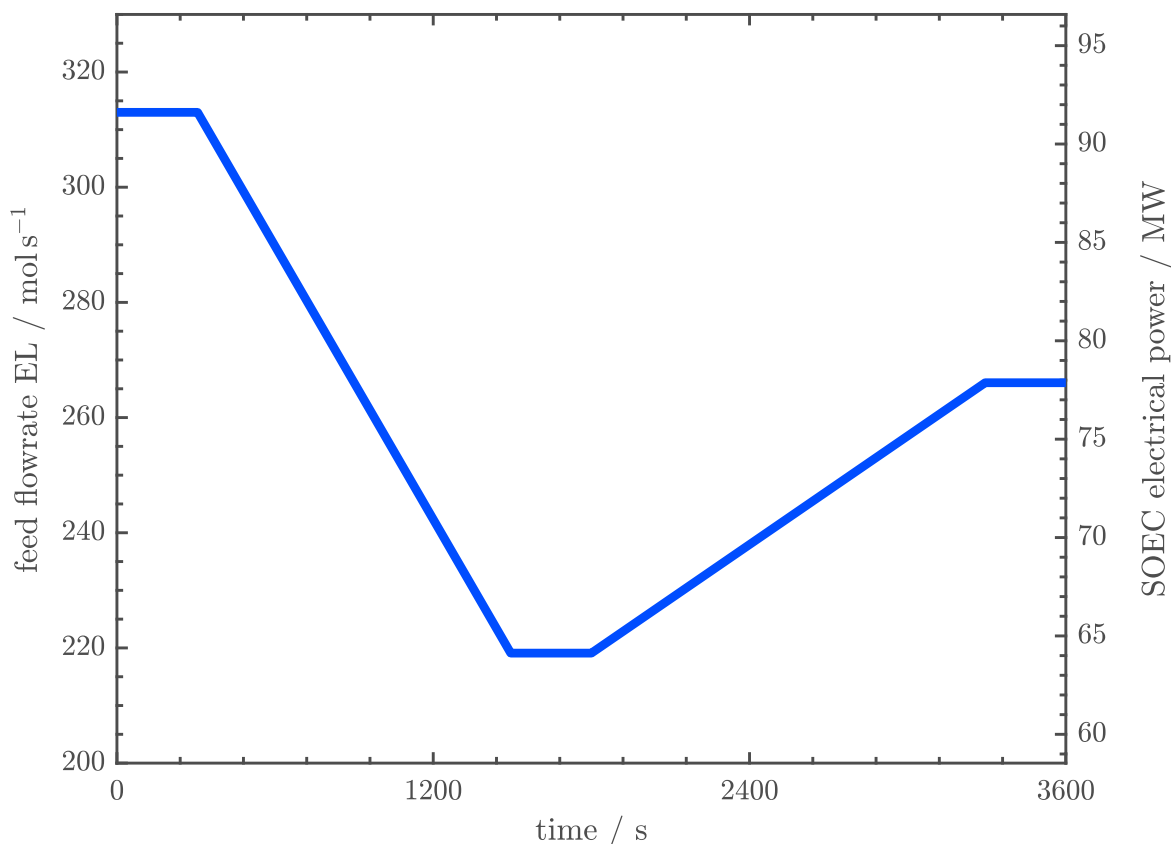


Figure 5.5.: Temporal trend of the electricity supply and molar feed flowrate to SOEC.

5.2.2 Pre-definition of the renewable power ramp: case relevance

Identifying dynamics in the incoming renewable power profiles as shown in Figure 5.5, and thus "hard-coding" them within the modeling system for a significant portion of the temporal domain is relevant in industrial practice. Flexible processes based on renewable energy, such as concentrated solar plants, typically rely on weather forecasts on different time scales, such as months, days, hours. Shorter time spans are typical for receding horizon optimal control, which enables safe and profitable real-time plant operations. In real-time applications, a good compromise between fineness of the discretization grid and length of the time scale of the receding domain must ensure that accurate control decisions are identified in a reasonable time. On the other hand, optimizations based on longer time-horizons, often embedding uncertainties (robust optimal control), support strategic plant management decisions based on quantitative information.

5.3 Modeling assumptions on a plant level

The first important assumption is that dynamics at the separation sequence can be safely neglected, as the raw syngas mixture collected at the intersection of the two reformers is essentially stable over time in composition and total flowrate. This shall be verified later on in the evaluation of the outcomes (cf. Figure 5.7). Therefore, syngas purification is not involved in the optimization nor in the modeling of the plant, as already anticipated.

Furthermore, Figure 5.4 exclude EL and the O₂ storage device from the blue box of the units considered. As concluded in the previous Chapter 4, water electrolysis absorbs the vast majority of the overall plant electrical input. It is then safe to assume that the trend of, e.g., wind power is directly reflected in the flowrate of H₂ generated from EL and fed to the plant, either to RWGS or directly adjusting a low syngas ratio in the outlet stream. Moreover, the EL is ideal in that it converts its feed of steam completely into H₂ and O₂.

The storage device is not sized, although the rate of O₂ accumulating in this system is formulated as the difference between O₂ from EL feeding TRI and RWGS (shell-side, for heat generation). The accumulation rate of O₂ in the storage is relevant to the estimation of the compression energy required.

The second feedstock (biogas) is a binary mixture of CH₄ and CO₂. Biogas may contain traces of ammonia and hydrogen sulfide which should be removed before any catalytic operation. These process steps are required. Nevertheless, considering that purification operations would constitute a decoupled optimization problem from the syngas stabilization, i.e., to minimize the concentration of catalyst poisons at their outlets, and considering that the time-scale related to the effects of catalyst deactivation due to poisoning differs from the one related to short-term power fluctuation here investigated, purified biogas is considered in the control volume of the process system analyzed in this study. Furthermore, biogas could vary in its CH₄ concentration, as it may be provided by different biomass feedstock over time, or collected within the plant from different geographical areas in the region. For this reason and for the parametrization of TRI, a lower and upper bound is considered in order to design the plant for the most suitable biogas composition. In case this composition were not perfectly aligned with the actual feed gas, the ratio could be easily adjusted *via* membrane modules, already implemented to generate a stream of CO₂ intended for RWGS. As a lower bound for the methane concentration in the binary mixture of CO₂ and CH₄ fed to TRI, 55 % is selected, whereas 75 % is the upper bound, a rather high but possible value, as reported by the European Biogas Association [167] and by the International Energy Agency [168] [169].

5.4 General reactor modeling approach

At first, the reformers are designed at their nominal load to attain the syngas setpoint without the contribution of the other reactor. Distributed reactor models are introduced, discretized and solved. While RWGS is simulated, TRI is also optimized to determine the configuration which maximizes its selectivity.

This section introduces the main governing equations of the reactors as well as further reactor-specific assumptions. Extensive details regarding the modeling of kinetics and heat transfer can be found in the supplementary materials – see Supplementary Section C.

Introducing the set of chemical components $\mathcal{S} := \{\text{CO}_2, \text{H}_2, \text{CO}, \text{H}_2\text{O}, \text{CH}_4, \text{O}_2\}$, the reactors are described by dynamic, one-dimensional, pseudo-homogeneous material and energy balances. The material balance for component α in molar formulation reads:

$$\frac{\partial \zeta_\alpha}{\partial t} = -v \frac{\partial \zeta_\alpha}{\partial z} + \frac{1 - \epsilon}{\epsilon} \frac{\rho_{\text{cat}}}{C_{\text{gas}}} \left(\sigma_\alpha(\zeta_\alpha, T) - \zeta_\alpha \sum_{\alpha \in \mathcal{S}} \sigma_\alpha(\zeta_\alpha, T) \right), \quad (5.1)$$

whereby the molar fraction ζ_α is governed in time and space. Equation (5.1) has to be fulfilled for all $(t, l) \in (0, t_{\text{end}}] \times (0, L)$, where $L > 0$ specifies the length of the reactor (z is the axial coordinate), $t_{\text{end}} > 0$ is the final time (t is the temporal coordinate).

The energy balance is used to derive the following partial differential equation, describing the change of the temperature in terms of the time and space coordinates:

$$\frac{\partial T}{\partial t} = \frac{-v \epsilon C_{\text{gas}} \tilde{C}_{\text{p,gas}} \frac{\partial T}{\partial z} - 4 \frac{U}{D_{\text{T}}} (T - T_{\text{ext}}) - (1 - \epsilon) \rho_{\text{cat}} \sum_{k \in K} \tilde{H}_k R_k \eta_k}{\epsilon C_{\text{gas}} \tilde{C}_{\text{p,gas}} + (1 - \epsilon) \rho_{\text{cat}} \hat{C}_{\text{p,cat}}}, \quad (5.2)$$

defined for all $(t, T) \in (0, t_{\text{end}}] \times (0, T_{\text{max}})$, where axial dispersion is neglected. Equation (5.2) introduces a summation term defined for the relevant kinetics $k \in K := \{\text{reverse water-gas shift (RWGS)}, \text{water-gas shift (WGS)}, \text{steam-reforming of methane (SR)}, \text{reverse methanation (RMETH)} \text{ and } \text{catalytic oxidation of methane (COMB)}\}$. The term σ_α , concurring to (5.1), is the overall molar generation rate for the single component α and is function of the local states (ζ_α, T) . It can be expanded as:

$$\sigma_\alpha = \sum_{k \in K} \nu_{\alpha,k} R_k \eta_k. \quad (5.3)$$

State-of-the-art kinetics reported by Xu et al. [170] and De Groote et al. [171] are implemented for TRI. Combustion kinetics within TRI were adapted from [172] by De Smet et al. [28] for supported Ni catalysts. Effectiveness factors for this heterogeneous model are constant and were retrieved from De Groote et al. [171]. Reversible kinetics of RWGS were taken from Richardson et al. [33], thus based on a $\text{Rh}/\gamma - \text{Al}_2\text{O}_3$ catalyst. The effectiveness factor of 0.3 observed by the authors is also incorporated in the calculations for this contribution. For adiabatic operations, i.e., inside the TRI reactor, the overall heat transfer coefficient U is 0, whilst it is $U \neq 0$ for the RWGS mildly-endothermic, multitubular reactor.

The axial mole-averaged interstitial velocity v is defined by a total mass balance in quasi-steady state assumption. Mole and mass-averaged velocities coincide if dispersion is neglected. Thus, the molar-based axial velocity defined between the reactor feed (superscript ⁰) and the generic reactor section reads

$$v = \frac{\sum_{\alpha \in \mathcal{S}} \dot{N}_{\alpha, \text{in}} M_{\alpha}}{C_{\text{gas}} A_{\text{cross}} \epsilon \sum_{\alpha \in \mathcal{S}} \zeta_{\alpha} M_{\alpha}}. \quad (5.4)$$

The momentum balance, typically dominated by friction, reduces to the Ergun equation

$$\frac{dp}{dz} = -\frac{(1-\epsilon)^2}{\epsilon^3} \left[150v \frac{\epsilon(1-\epsilon)}{D_{\text{cat}}^2} \mu_{\text{mix}} + 1.75 \frac{1-\epsilon}{\epsilon^3} \rho_{\text{gas}} \frac{v^2 \epsilon^2}{D_{\text{cat}}} \right]. \quad (5.5)$$

The time-dependency of momentum is neglected. Equations (5.1), (5.2), and (5.5) are completed by Dirichlet-type boundary conditions at each reactor inlet, respectively

$$\zeta_{\alpha}(t, z=0) = \zeta_{\alpha, \text{in}}, \quad T(t, z=0) = T_{\text{in}}, \quad p(t, z=0) = p_{\text{in}}, \quad (5.6)$$

where $\zeta_{\alpha, \text{in}}$, T_{in} and p_{in} are the molar fraction of component α , temperature and pressure at the reactor feed, pre-specified and constant over time.

These reactor models are discretized by upwind finite difference method. Therefore, Equation 5.5 is implicit in the pressure, and constitute an algebraic constraint in a DAE system.

5.5 Reactor design

Based on the modeling approach illustrated in Section 5.4, reactor designs for RWGS and TRI are identified separately, ensuring that the desired productivity of $270 \text{ ton}_{\text{CO}} \text{ day}^{-1}$ and a syngas ratio of $\text{H}_2/\text{CO} = 2$, suitable for Fischer-Tropsch synthesis, are attained in each case. The molar flowrate of syngas is $330 \text{ mol}_{\text{syngas}} \text{ s}^{-1}$ ($111 \text{ mol}_{\text{CO}} \text{ s}^{-1}$).

5.5.1 Design of TRI

A preliminary optimization problem is set to identify suitable values of the design parameters that maximize the selectivity towards syngas. Here, Equations (5.1) and (5.2) are implemented in their steady-state formulation such that time derivatives vanish. The resulting modeling equations serve as equality constraints in the following nonlinear programming (NLP) problem:

$$\begin{aligned}
 & \max_{\Phi_{D,\text{TRI}}} \quad \left. \frac{\dot{N}_{\text{H}_2} + \dot{N}_{\text{CO}}}{\dot{N}_{\text{CH}_4} + \dot{N}_{\text{CO}_2} + \dot{N}_{\text{H}_2\text{O}}} \right|_{\text{out,TRI}} \\
 & \text{s.t.} \quad 0 = h_{\text{TRI}}(y_{\text{diff,TRI}}(t), y_{\text{alg,TRI}}(t)) \\
 & \quad \{y_{\text{diff,TRI}}(t), y_{\text{alg,TRI}}(t)\} \leq \text{UB} \\
 & \quad \{y_{\text{diff,TRI}}(t), y_{\text{alg,TRI}}(t)\} \geq \text{LB}
 \end{aligned} \tag{5.7}$$

where vector $\Phi_{D,\text{TRI}}$ collects the optimization variables: tube length L , tube diameter D_{T} , feed molar flowrates $\dot{N}_{\alpha,\text{in}}$ ($\alpha \in \mathcal{S}$), temperature T_0 and pressure p_0 . Function $h_{\text{TRI}}(y_{\text{diff}}(t), y_{\text{alg}}(t))$ consists of the conservation laws in discretized form, and of the Ergun equation.

The syngas composition is bound: $\text{H}_2/\text{CO} \in [1.95, 2.1]$. The productivity of carbon monoxide is constrained ($270 \text{ ton}_{\text{CO}} \text{ day}^{-1}$). Problem parameters, constraints and bounds are defined in Matlab v2018b, combined with CasADi v3.5.3, a symbolic framework for algorithmic differentiation and numeric optimization developed by Andersson et al. [173]. The nonlinear program is solved by IPOPT v3.12.3, running with the linear solver mumps [174]. The solver IPOPT identifies local optima. Therefore, in order to identify a global solution, optimization variables are randomized within bounds. Preliminary simulations in steady-state based on the randomized guesses are then run to provide IPOPT with reasonable initial guesses. Optimal solutions are then compared and the design set ensuring the best objective is selected. The reactor is discretized with 150 equally-spaced points. Optimization variables, bounds and optimal values are reported in Table 5.1.

Table 5.1.: List of relevant optimization variables for design problems, bounds, and results for TRI.

Variable	LB	UB	value at optimum	unit (SI)
$\dot{N}_{\text{CO}_2,\text{in}}$	10	70	38.6	mol s^{-1}
$\dot{N}_{\text{H}_2\text{O},\text{in}}$	10	120	102.7	mol s^{-1}
$\dot{N}_{\text{CH}_4,\text{in}}$	30	150	115.8	mol s^{-1}
$\dot{N}_{\text{O}_2,\text{in}}$	5	60	51.9	mol s^{-1}
D_{T}	0.104	1.6	1.6	m
L	0.1	1.1	1.1	m
T_{in}	700	1050	1050	K
p_{in}	25×10^5	40×10^5	25×10^5	Pa

The selected bounds for the feed pressure to TRI are in line with the findings on the role of coke formation in catalytic partial oxidation of methane by De Groote et al. [171] and with the

prevailing literature on partial oxidation and tri-reforming. Above 25 bar and for elevated inlet temperatures, coke deposition is neglected.

Moreover, the selected lower bound for the feed pressure at TRI, which coincides with its optimal value reported in Table 5.1, is consistent with the requirement of a typical Fischer-Tropsch synthesis reactor, i.e., no pressurization is required before this downstream syngas application.

At the best local optimum, the molar selectivity towards H₂ and CO as defined in the objective is 2.28. The feed ratio between CH₄ and the sum of CO₂ and CH₄ is 0.75, which corresponds to the upper bound defined for the molar content of CH₄ in this binary mixture, as elaborated in Section 5.3.

Graphical trends at the steady-state are reported, for trireforming and RWGS, in the Supplementary Section C.5.

5.5.2 Design for RWGS

The set of relevant design parameters and operating conditions is reported in Table 5.2.

Table 5.2.: List of design parameters and nominal operating conditions for RWGS.

Variable	value	unit (SI)
$\dot{N}_{\text{CO}_2,\text{in}}$	0.495	mol s ⁻¹
$\dot{N}_{\text{H}_2,\text{in}}$	0.495	mol s ⁻¹
D_T	0.11	m
L	1.5	m
N_{tubes}	500	–
T_{in}	950	K
p_{in}	2×10^5	Pa
$T_{\text{shell,RWGS}}$	1073	K

Accounting for its axial drop, the feed pressure selected is slightly above atmospheric, in agreement with the range of validation for the kinetic model by Richardson et al. [33]. At the prevailing temperature, pressure and feed composition, the selected feed and shell-side temperature are high enough to prevent from a thermodynamically relevant contribution of the methanation reaction, therefore neglected. The number of spatial discretization points for RWGS simulations and optimal control is 150.

Assuming that the EL (SOEC) operates at 1073 K, the ideal electrical power demand, which equals the Gibbs free energy of reaction, is $188 \text{ kJ mol}_{\text{H}_2}^{-1}$. Therefore, the nominal flowrate of H₂ to RWGS ($247.5 \text{ mol}_{\text{H}_2}\text{s}^{-1}$) is ensured if an efficient SOEC is supplied with 46.53 MW. However, Posdziech et al. [175] identified a SOEC efficiency of 82 %, based on the lower heating-value of H₂ (LHV_{H₂}), corresponding to $240 \text{ kJ mol}_{\text{H}_2}^{-1}$, which outlines a power demand of 72.4 MW. For

the given operation, a syngas ratio H_2/CO of 2 is attained if an integration of $85 \text{ mol}_{H_2} \text{ s}^{-1}$ is accounted for, which corresponds to an ideal total power demand at SOEC of 62 MW, based on the Gibbs free energy, and 97 MW, based on the LHV_{H_2} efficiency. CH_4 is a candidate fuel to sustain the heat demand of RWGS, possibly provided from bio- CH_4 as carbon-neutral source. Given that its lower heating value (LHV_{CH_4}) is 800 kJ mol^{-1} , an estimate of the required flowrate is provided by the following calculation, accounting for the reactor discretization (N_z points in axial coordinate and axial discretization segments of length Δz):

$$\dot{N}_{CH_4, RWGS, shell} = \frac{1}{LHV_{CH_4}} \left(\sum_{i=1}^{N_z, RWGS} 4 \frac{U_i}{D_T} (T_{ext} - T_i) \right) \Delta z \frac{D_T^2 \pi}{4} N_{tubes}, \quad (5.8)$$

resulting in 5.8 mol s^{-1} of CH_4 , 5% of the molar flowrate required for nominal operations of TRI towards the maximum selectivity to syngas (see Table 5.1). If biogas has a molar concentration of 60% in CH_4 , $9.7 \text{ mol}_{BG} \text{ s}^{-1}$ must be separated. Consequently, nominal RWGS operations require considerably less CH_4 than TRI, the latter virtually demanding no electricity other than compression duties.

5.5.3 Oxygen utilization

Given that the stoichiometric combustion of $5.8 \text{ mol}_{CH_4} \text{ s}^{-1}$, recommended in Section 5.5.2, requires $11.6 \text{ mol}_{O_2} \text{ s}^{-1}$, nominal RWGS operations generate an excess of $155 \text{ mol}_{O_2} \text{ s}^{-1}$ which can be buffered to allow for the operation of TRI when renewable electricity is scarce. Assuming that RWGS (TRI is off) and TRI (RWGS is off) are respectively operated for 50% of a given time-horizon, the ratio of O_2 generated (not intended for combustion) to O_2 fed to TRI (Table 5.1) is $155/52 = 2.98$: 1.98 moles of surplus per mole of oxygen fed to TRI. The surplus stored is possibly further decreased to sustain thermal utility generation within the plant or sold at market value.

5.6 General plant modeling approach

After discretizing the reactors by equally-spaced finite volumes in the spatial direction and approximating the advection contributions with the upwind scheme, the resulting system of modeling equations is a semi-explicit differential-algebraic equation (DAE) system of index 1 on the time

horizon $[0, t_{\text{end}}]$. For readability, vectors and matrices shall be denoted by plain text notation and introduced as such within the text. Thus, it can be written in the form

$$\begin{aligned}\dot{y}_{\text{diff}}(t) &= f(t, y_{\text{diff}}(t), y_{\text{alg}}(t)), \\ 0 &= g(t, y_{\text{diff}}(t), y_{\text{alg}}(t)),\end{aligned}\tag{5.9}$$

where \dot{y}_{diff} is an abbreviation for $\frac{dy_{\text{diff}}(t)}{dt}$ and suitable initial values for (5.9) will be discussed in Section 5.7. Here:

- $y_{\text{diff}}(t) \in \mathbb{R}^d \times [0, t_{\text{end}}]$ collects all *differential variables*, i.e., all variables that are differentiated with respect to time. These are the mole fractions coming out of the discretizations inside the RWGS and TRI reactor.
- $y_{\text{alg}}(t) \in \mathbb{R}^q \times [0, t_{\text{end}}]$ collects all *algebraic variables*. These are the pressure values inside the reactors as well as the outlet molar flowrates from the reactors and the H₂-integration into the plant outlet stream.
- $f : \mathbb{R} \times \mathbb{R}^d \times \mathbb{R}^q \rightarrow \mathbb{R}^d$ is a function, collecting all differential equations.
- $g : \mathbb{R} \times \mathbb{R}^d \times \mathbb{R}^q \rightarrow \mathbb{R}^q$ is a function, collecting all algebraic equations.

The discretization scheme for balance equations is backward in space (upwind scheme). Therefore, the Ergun equation for the pressure profile 5.5 is implicit and algebraic. Further algebraic contributions are introduced with the optimal control setup in the next section.

5.7 Optimal control for the plant model

The control vector $u = (u^{\text{RWGS}}, u^{\text{TRI}})^{\top} \in \mathbb{R}^2$ contains the inlet flowrates to the RWGS and TRI reactors, where feed compositions, temperature and pressures are fixed at the optimal design values. These control variables are adjusted to meet the set point at any given time. The inlet molar flowrate to SOEC, denoted as $\dot{N}_{\text{SOEC},\text{in}}$, is pre-defined in the model. Therefore, the flow rate of H₂ to be integrated into the product stream is obtained:

$$\dot{N}_{\text{H}_2,\text{int}} = \frac{u^{\text{RWGS}}}{2} - \dot{N}_{\text{SOEC},\text{in}},\tag{5.10}$$

where the composition of u^{RWGS} , the total inlet flowrate to RWGS, is an equimolar mixture of CO₂ and H₂ as prescribed in Section 5.5.2. Finally, the accumulation of O₂ inside the buffer can be calculated as

$$\dot{N}_{\text{O}_2,\text{buff}} = \frac{\dot{N}_{\text{SOEC},\text{in}}}{2} - \dot{N}_{\text{O}_2,\text{RWGS},\text{shell}} - \dot{N}_{\text{O}_2,\text{TRI},\text{in}},\tag{5.11}$$

where $\dot{N}_{\text{O}_2, \text{TRI}, \text{in}}$ is the mole fraction of O_2 in the TRI inlet stream and $\dot{N}_{\text{O}_2, \text{RWGS}, \text{shell}}$ is the oxygen required to burn the required amount of methane calculated in Equation 5.8.

In OCP, control vector u and the EL inlet flowrate $\dot{N}_{\text{SOEC}, \text{in}}$ are time-dependent functions. As a result, they are discretized in time such that the amount of control variables scales with the time steps.

5.7.1 Numerical time integration

The main idea of `parareal` is to decompose the global time domain $[0, t_{\text{end}}]$ into N_t smaller subdomains. Given initial values on each of these subdomains, the global time-dependent problem in each iteration of the method splits up into N_t many local problems on these subdomains, which can then be solved in parallel. The initial values can be generated using a *coarse integrator*, which should be *cheap* but can be inaccurate, and the subproblems are then solved in parallel using a *fine integrator*, which has to be *accurate* and is thus more expensive. Afterwards, the next iterate of `parareal` is generated *via* a correction step, where the fine solutions of the subproblems are used to correct the coarse sequential integrator.

Introducing the general time grid $0 := t_0 < t_1 \cdots < t_{N_t} := t_{\text{end}}$ with variable step sizes $h_n := t_{n+1} - t_n$, $n = 0, \dots, N_t - 1$, $\mathfrak{G}(t_{n+1}, t_n, h_n, w_n^k)$ denotes the coarse integrator, that integrates on the subdomain $[t_n, t_{n+1}]$ with step-size h_n and provides an inaccurate approximation to $w(t_{n+1})$, the solution of (5.9), using the initial values w_n^k . Here, k indicates the iteration number of `parareal`. The fine integrator has to be more accurate and can thus be more expensive. This can be achieved by using a higher order integration method or by operating on a refinement of the time grid or a combination of both. In this study, the fine integrator will always be a higher order method and it can additionally operate on a refinement of the time grid such that $\mathfrak{F}(t_{n+1}, t_n, R_{\text{ref}}, w_n^k)$ denotes the fine integrator, that integrates on $[t_n, t_{n+1}]$ using $R_{\text{ref}} \in \mathbb{N}$ time steps and provides a more accurate approximation to $w(t_{n+1})$ using the initial values w_n^k . Thus, for $R_{\text{ref}} = 1$ both integrators use the same grid and for $R_{\text{ref}} \geq 2$ the fine solver \mathfrak{F} uses a refined grid. With this notation at hand, `parareal` is described in Algorithm 1.

Algorithm 1 parareal ($w_0, N_t, K, R_{\text{ref}}, \varepsilon_{\text{tol}}, \mathfrak{G}, \mathfrak{F}$)

```
1:  $k = 0, w_0^0 = w_0$ 
2: for  $n = 0, \dots, N_t - 1$  do
3:    $w_{n+1}^0 = \mathfrak{G}(t_{n+1}, t_n, h_n, w_n^0)$  ▷ first initial values
4: end for
5: for  $k = 1, \dots, K_{\text{max}}$  do
6:   parfor  $n = 0, \dots, N_t - 1$  do
7:      $\mathfrak{F}_{n+1}^k = \mathfrak{F}(t_{n+1}, t_n, R_{\text{ref}}, w_n^k)$  ▷ parallel step
8:   end parfor
9:   for  $n = 0, \dots, N_t - 1$  do
10:     $w_{n+1}^{k+1} = \mathfrak{G}(t_{n+1}, t_n, h_n, w_n^{k+1}) + \mathfrak{F}_{n+1}^k - \mathfrak{G}_{n+1}^k$  ▷ correction step
11:   end for
12:   if  $\|w^{k+1} - w^k\| / \|w^k\| \leq \varepsilon_{\text{tol}}$  then
13:     return  $w^{k+1}$ 
14:   end if
15: end for
16: return  $w^K$ 
```

Algorithm 1 is terminated either after a fixed amount of $K_{\text{max}} \in \mathbb{N}$ iterations or as soon as the relative change in the iterate $\|w^{k+1} - w^k\| / \|w^k\|$ is below some tolerance $\varepsilon_{\text{tol}} > 0$. Note that in line 10, the values of the coarse integrator $\mathfrak{G}_{n+1}^k = \mathfrak{G}(t_{n+1}, t_n, h_n, w_n^k)$ have been calculated in the previous iteration already and thus can be reused. Regarding the integrators, \mathfrak{G} should be fast but at the same time an implicit method. The backward (implicit) Euler method is chosen as coarse integrator, whereas for the fine integrator \mathfrak{F} a higher order method is required: Lobatto IIIC is used, of order 4 [176].

5.7.2 Optimization setting and initialization

As reported earlier in Section 5.7, the control vector u (feed streams to the reformers) and the inlet flowrate to SOEC $\dot{N}_{\text{SOEC}, \text{in}}$ are time-dependent functions, hence the control dimension p scales with the number of time steps. In particular, the controls are piecewise constant. On the contrary, the trend of future renewable power supply is a pre-defined piecewise linear function, and it is assumed that is directly proportional to the power absorbed by SOEC, and consequently to its inlet and outlet flowrates. These trends are represented in Figure 5.5.

The fluctuation starts at 94 % of the maximum SOEC power intake required for nominal RWGS operations, drops to 65 % at the minimum and stabilizes then at 80 %.

OCP is then supposed to stabilize the plant to the desired setpoint for the desired syngas ratio $\text{SR}_d \in \mathbb{R}$ and flowrate $\text{SF}_d \in \mathbb{R}$ in the product stream. Introducing the notation for the setpoint as

$SR(t)$ and $SF(t)$ for syngas ratio and flowrate, respectively, the objective function for the optimal control problem, constrained by the reactors models previously defined in Section 5.4 (a DAE set), reads:

$$\min_{u(t) \in \mathbb{R}^2} J_2(u(t)) := \frac{1}{2} \int_0^T c_{SR} (SR(t) - SR_d)^2 + c_{SF} (SF(t) - SF_d)^2 dt. \quad (\text{OCP})$$

Here, $c_{SR} := \frac{\max\{SR_d, SF_d\}}{SR_d}$ and $c_{SF} := \frac{\max\{SR_d, SF_d\}}{SF_d}$ are scaling constants that ensure that both contributions to the objective function are equally weighted.

Assuming that the plant had benefited from a stable and abundant supply of renewable power, (OCP) is initialized with the solution of the DAE problem described in Section 5.6. At the beginning of the time-horizon, the SOEC electrolyzer is supplied with 92 MW, corresponding to a feed of $313 \text{ mol}_{\text{H}_2\text{O}} \text{ s}^{-1}$ (based on the efficiency outlined in Section 5.5.2). At $t = 0$, the controls are set to $465 \text{ mol}_{\text{RWGS}, \text{in}} \text{ s}^{-1}$ and $20 \text{ mol}_{\text{TRI}, \text{in}} \text{ s}^{-1}$. A time-horizon of 1 h is selected to reflect a realistic change in availability of renewable resource, e.g., wind power. The number of equidistant steps h_n in the time-grid is set to $N_t = 200$. The tolerance threshold set for the optimization is 10^{-3} , whereas the termination of parareal iterations occur at $\varepsilon_{\text{tol}} = 10^{-6}$ (line 12 in Algorithm 1).

5.7.3 Comparison between parareal and a fine integrator: computational framework

As anticipated in Section 1.3, aim of this chapter is to identify and test a promising optimal control strategy, given the implications of renewable intermittency in flexible plant operations. Therefore, an optimization based on parareal is compared to the same optimization, where DAE integrations are performed with the fine solver \mathfrak{F} over the whole refined temporal domain (benchmark case). Computations are performed on a machine with 60 Intel(R) Xeon(R) CPU E7-4880 v2 @ 2.50GHz cores. The coarse integration within the parareal scheme (Algorithm 1), as well as the fine integration in the benchmark case, are running on single core and single thread, whereas 50 cores are used for the parallel step of parareal. The number of cores should scale with the number of discretization steps N_t set for the coarse solver (\mathfrak{G} in Algorithm 1), so that each core can run the fine integration \mathfrak{F} and perform the parareal iterates on a single coarse step. In this application, each core operates on 4 coarse integration steps, as $N_t/N_{\text{cores}} = 4$. Therefore, the total number of coarse integration steps is 200. To each temporal discretization point of the coarse grid correspond 2 time-steps of the fine integrator within the parareal loop ($R_{\text{ref}} = 2$ for a total of 400 fine discretization steps in parareal iterations). As anticipated, for the benchmark case the fine integrator runs on this refined grid with 400 steps. For the solution of (OCP), Matlab's `fmincon` routine with its SQP solver is called. The necessary derivatives of \tilde{F} are calculated with ADiMat [177]. The integral in (OCP) is approximated *via* the trapezoidal rule. Furthermore, the

tolerance for the Newton-solver inside \mathfrak{G} (coarse solver) is lifted to 10^{-4} where the tolerance inside \mathfrak{F} (fine solver) is 10^{-8} . This is justified, as the inaccuracy in the Newton method for the coarse solver obviously decreases its convergence time, although accuracy of the overall parareal method is ensured by the correction steps. as indicated in Algorithm 1.

5.7.4 Numerical results

The benchmark optimization, which runs exclusively the fine integrator \mathfrak{F} over the entire temporal domain, requires 6.56 h, whereas the implementation of parareal determines a speedup of 1.7 and reduces the solution time to 3.85 h. Due to the time-dependent dynamics, parareal requires 2 iterations, although the iteration error in line 12 of Algorithm 1 after the first iteration is on average very close to the tolerance for parareal iterations ($\varepsilon_{\text{tol}} = 10^{-6}$). As a consequence to parallel computations in the parareal loop, the average times spent in the coarse and fine solver per iteration are 233.46 s and 31.16 s, respectively.

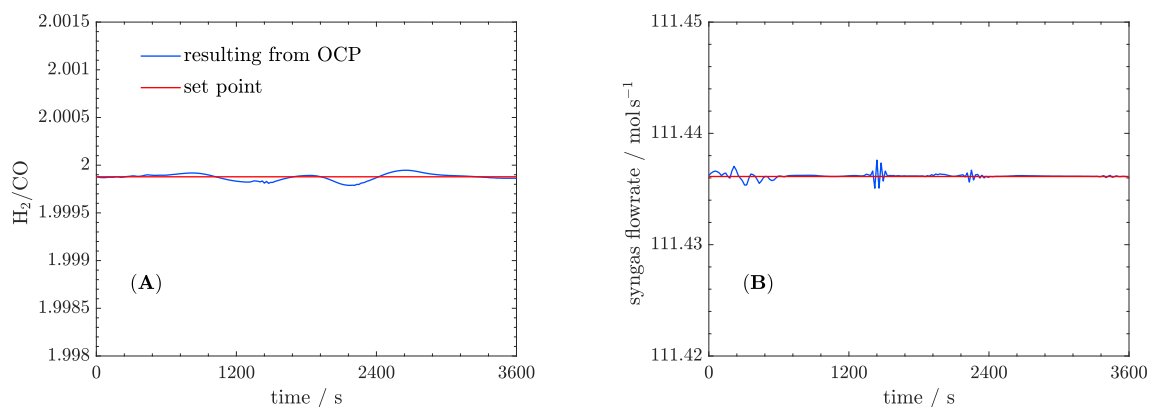


Figure 5.6.: Setpoint attainment with parareal: (A) syngas ratio; (B) flowrate of CO in the syngas stream.

Figures 5.6 show that the setpoints, i.e., syngas composition (A) and flowrate (B), are attained over the entire time-domain at the optimum. Such trends obtained with parareal are preserved in the solution from the benchmark optimization running on the fine integrator over the complete time domain.

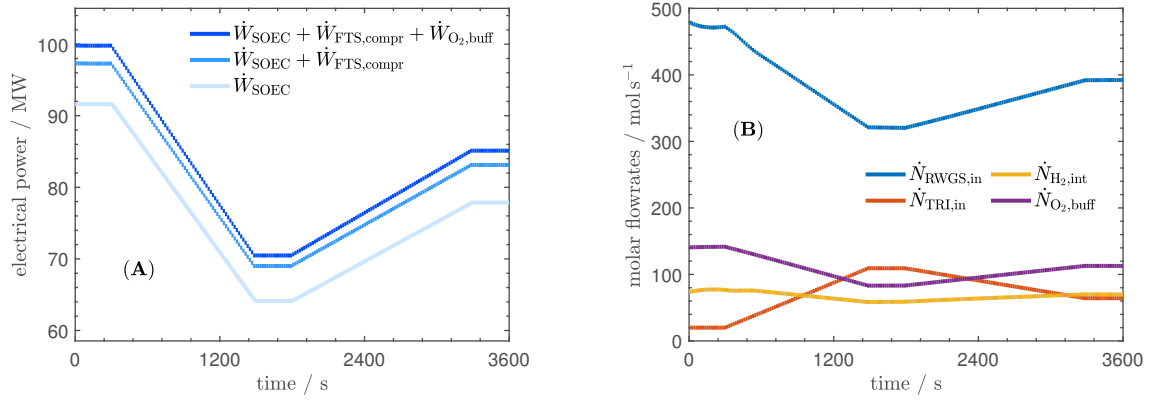


Figure 5.7.: (A) Power demand at SOEC (\dot{W}_{SOEC}), for the compression to the Fischer-Tropsch reactor requirements ($\dot{W}_{FTS,compr}$) and to buffer O_2 at 300 bar in gaseous form ($\dot{W}_{O_2,buffer}$); (B) total feed flowrate to RWGS and TRI, flowrate for the integration of H_2 directly to the syngas stream ($\dot{N}_{H_2,int}$), accumulation rate of O_2 in the buffering device ($\dot{N}_{O_2,buffer}$).

Figure 5.7 (A) shows stacked power demand over time in incremental contributions and darker tones of blue, which justifies the assumption initially made, that the fluctuation in renewable power directly translates into the trend at the electrolyzer, representing the dominant energy sink in syngas generation. In light blue, the demand at SOEC is reported (\dot{W}_{SOEC}). The power required to adapt the gas to FTS requirements ($\dot{W}_{FTS,compr}$) is then added on top of it. This value is obtained assuming that the separation system recommended in the layout presented in Figure 5.1 can be neglected and that the raw syngas mixture is fed directly to the FTS. In this scenario, the duty to attain the required operating pressure in FTS can be approximated as an isothermal transformation, e.g., at 373 K:

$$\begin{aligned} \dot{W}_{FTS,compr} \text{ (W)} &= - \int_{amb}^{FTS(25 \text{ bar})} p d\dot{V} = \\ &= \left(\dot{N}_{TRI,in} + \dot{N}_{RWGS,out} + \dot{N}_{H_2,int} \right) \cdot R_{gas} \cdot (373 \text{ K}) \cdot \ln \frac{25 \text{ bar}}{1 \text{ bar}}, \end{aligned} \quad (5.12)$$

where it is assumed that the gas is compressed after RWGS, operated at low pressure as reported in Figure C.2 (C). This duty constitutes about 7% of the SOEC energy requirement. Furthermore, the figure reports the additional demand for the compression of excess O_2 ($\dot{N}_{O_2,buffer}$) to storage requirement at 300 bar. Once again, the values are obtained from an isothermal formula (5.12), where the flowrate of O_2 is calculated with Equation 5.11:

$$\dot{W}_{O_2,buffer} \text{ (W)} = - \int_{amb}^{storage(300 \text{ bar})} p d\dot{V} = \dot{N}_{O_2,buffer} \cdot R_{gas} \cdot (373 \text{ K}) \cdot \ln \frac{300 \text{ bar}}{1 \text{ bar}}. \quad (5.13)$$

In this scenario setting, the power requirement to store O_2 drops from 2.7% to 2.1% of the demand at the highest (at $t = 0$) and lowest peak in renewable power supply, respectively. Clearly, a minor power contribution for the storage may translate in a major increase in the fixed costs, not considered in this first chapter on process flexibility. The drop in percent contribution for the storage of O_2 scales with the accumulation rate of O_2 in the buffering device, reported in purple in Figure 5.7 (B). The moderate swing in the supply of renewable power from a high availability level ($t = 0$) is such that oxygen accumulates in the storage throughout the entire temporal domain for the current scenario of fluctuating electricity. At the minimum power supply and as suggested from the feed flowrates illustrated in the same figure, TRI contributes for 25% to the syngas production, not yet enough for storage release (negative accumulation trend). Furthermore, the power supply to SOEC, in conjunction with the stabilization effect of OCP on the product stream, determine other trends in Figure 5.7 (B), which express the feed flowrates to RWGS and TRI (blue and red), as well as the amount of H_2 integrated directly into the product line, in yellow.

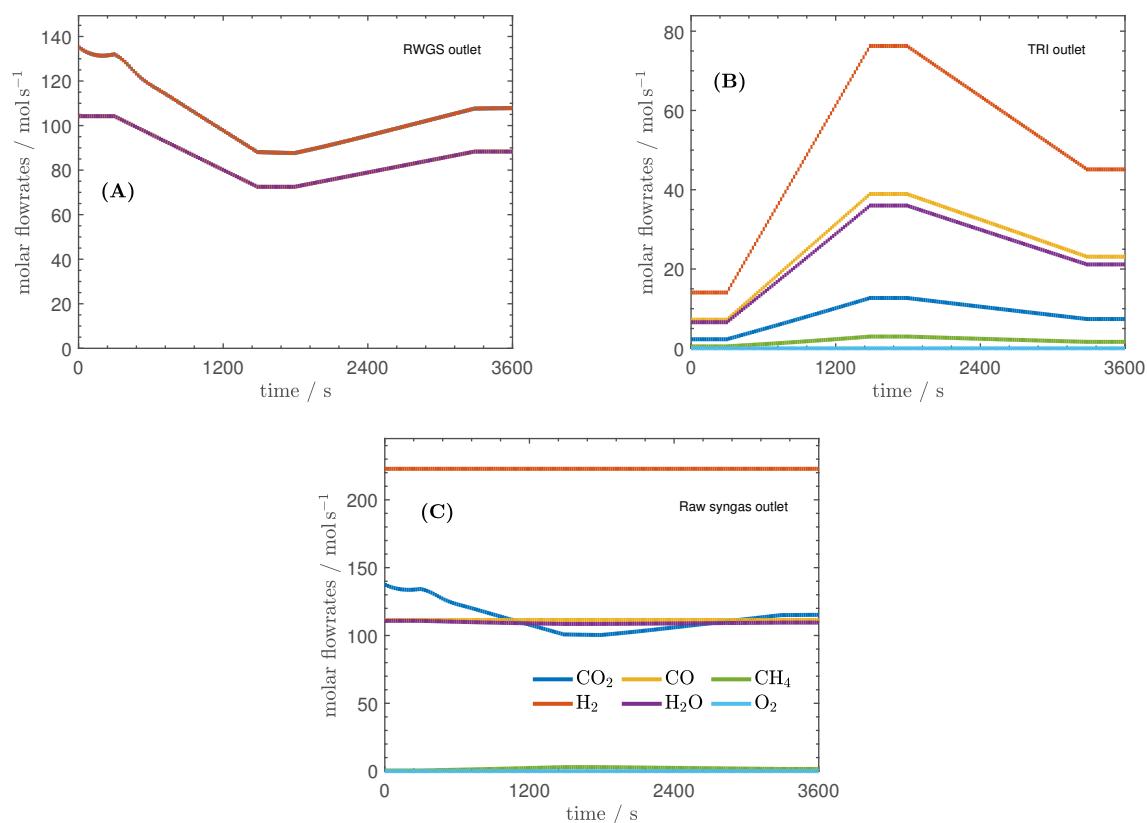


Figure 5.8.: Molar flowrates at the outlet of RWGS (A) and TRI (B) and in the syngas stream (C) over the time domain at the optimum.

If the trends at reactors outlets change over time as a response to the fluctuating energy supply as shown in Figures 5.8(A,B), the composition trend in the raw syngas stream is essentially preserved. In Figure (C), a larger fluctuation in the CO_2 flowrate is present, although CH_4 and O_2 are essentially converted, H_2O is produced in both reactors and thus stable at their interception, and syngas is stabilized by OCP. A larger drop in available power will mainly reduce the concentration

of CO₂ and increase CH₄ to some extent. Essentially, it can be concluded that the separation system proposed in the layout of Figure 5.1 should be able to tolerate minor changes in composition over time.

5.8 Conclusions and outlook

Although the comparative test between `parareal` and fine integrator shows that the former performs almost double as fast, the computational time of the coarse solver in `parareal` is a limiting factor, as the integration of a DAE system is still too expensive, even with a first order method.

As outlook, debottlenecking strategies expected to significantly reduce the time spent in the coarse solver should be investigated:

- the analysis of different numerical schemes for a cheaper integration of DAE systems, such as implicit-explicit integrators (IMEX [178, 179]) ;
- a reformulation of the equations-system, from a DAE into an ODE system;
- the application of model-order reduction (MOR) for the coarse steps, but relying on the full model for the fine integration.

In this particular case, the nature of this system formulation as a DAE is due to the upwind discretization scheme for spatial derivatives. If this discretization approach is applied rigorously, the Ergun Equation 5.5 is implicit in the pressure, which contributes to density and velocity on the right hand side. This could be relaxed by discretizing this pressure drop equation forward in space, to allow the explicit formulation of the pressure, and the conversion of the system into an ordinary differential equation (ODE). Consequently, the evaluation of the coarse step is expected to be comparatively more efficient. However, it may introduce an inconsistency in mass balances, whose feasibility needs to be carefully evaluated.

Furthermore, the absolute computational time required for all optimization cases over a single hour time-span for the specific case (3.85 h with `parareal`, and 6.56 h with the fine integrator) are not reasonable if this is the temporal frame of receding horizon in a real-time optimal control application. However, if on the one hand the optimization time is expected to benefit dramatically from a reformulation in ODE or with MOR tools, on the other hand, what was commented on in section 5.2.2 holds true: the trade-off between length of time span and grid finesse must be tuned on a case-by-case basis, and a coarser grid may still provide acceptable predictions for the required control actions.

5.9 Chapter summary

"How does the inherent intermittency of renewable power affect design and operation of a Power-to-X plant?". This Question 3 from Section 1.3 implies the importance of identifying strategies to deliver reasonable product specifications, whenever a non-steady input is foreseen. A suitable plant configuration that fulfills product requirements must be optimally designed and controlled. In this first chapter on process flexibility, the concept of a Power-to-Syngas plant was taken from earlier discussions on process synthesis (Chapter 4), based on the idea that both ends of a water electrolyzer can be used to stabilise the quality of the product stream of a power-to-syngas plant, targeting the desired syngas flow rate and composition: H_2 feeds a RWGS reactor when cheap renewable energy is abundant, while O_2 is stored for later use when renewable energy is scarce and O_2 is fed to a tri-reforming reactor. Given reactor size based on the nominal load, their distributed models contribute to a DAE formulation of the underlying constraints for an optimal control problem that targets a syngas H_2 -to-CO ratio of 2 at a nominal flowrate. This raw syngas will be processed and purified in downstream process sections. This constitutes a suitable technical benchmark to test and evaluate a promising numerical approach for optimal control applications.

The performance of parallel computing based on the numerical approach `pararea1`, where integration results on the overall time span by means of a low-order, thus coarse, numerical scheme are corrected by the results of a higher order method, performed in parallel on multiple cores on a finer temporal grid, is compared with the fine integrator operating on the complete refined time grid. The fine and coarse integrators are of order 4 (Lobatto IIIC) and 1 (Implicit Euler), respectively. The computational time is reduced by a factor of 1.7 with `pararea1`, although the gain is significantly limited by the still too expensive coarse integration of this DAE system, which may be debottlenecked by a different mathematical formulation, as commented in Section 5.8.

From an engineering perspective, the proposed plant concept allows to provide the downstream Fischer-Tropsch synthesis reactor with a sufficiently stable syngas supply thanks to the utilization of the O_2 stream from the electrolyzer: as shown, the buffering of O_2 adds a negligible energy contribution (2.1% – 2.7%) to the dominant demand of the SOEC electrolyzer (Section 5.7.4). Nevertheless, wider fluctuations in renewable power supply will force the plant beyond its operability window, causing unit operations to go out of specification and flow distribution anomalies in reactors and heat exchangers, especially at very low loads. Typically, licensors set generous margins for the recommended lower operability threshold, up to 30% of the nominal load. Consequently, flexibility must be controlled within feasible ranges, either by introducing buffering devices to preserve a technical lower-bound to the admissible loads, or by resorting to make-up grid electricity, when required.

But how can this trade-off between buffering and process flexibility addressed in Question 4 of Section 1.3 be systematically and quantitatively evaluated? As reported earlier in this chapter

summary, plant sizing was attained by optimizing the reactors separately at the expected nominal load for the targeted syngas production. However, this approach assumes that optimality shall be extended at part-load, which may not be true. Furthermore, in the context of highly electrified plants possibly operating off-grid, the way in which the available renewable power is partitioned across the system affects process performance and product quality. This is a motivation to apply rigorous mathematical optimization to the entire interconnected plant, represented by detailed models (distributed in space if necessary), and taking into account partial loads.

The next chapter proposes the mathematical approach of multi-period design optimization to identify the optimal size and operation policies for a Power-to-Methanol plant based on detailed, temporally and spatially distributed equation models, thus ensuring feasibility over a number of discretized renewable energy loads throughout the year, weighted by their probability of occurrence. This concludes the analysis of the impact that intermittent renewable power supply has on design and operations of a plant (Question 3 in Section 1.3). This analysis is based on profitability, introduced for the first time in this work, as it allows to set a quantitative benchmark for the closing remarks on Question 4: profitability is a good indicator whether a reference solution for the flexible case is to be preferred over plant operation stabilized by large, expensive buffering devices over a given temporal domain.

Process flexibility (II) - Multi-period design optimization of a Power-to-Methanol Process

6.1 Introduction

Processes for the synthesis of green chemicals must take into account the intermittent nature of the renewable energy supply (load) in the medium and short term. As reported in the previous chapters, this aspect influences decision-making tools and results for the identification of candidate process topologies and operations. However, the implications of different extents of process flexibility on the detailed system design are yet to be incorporated in this work. It is the aim of this chapter to fill this gap.

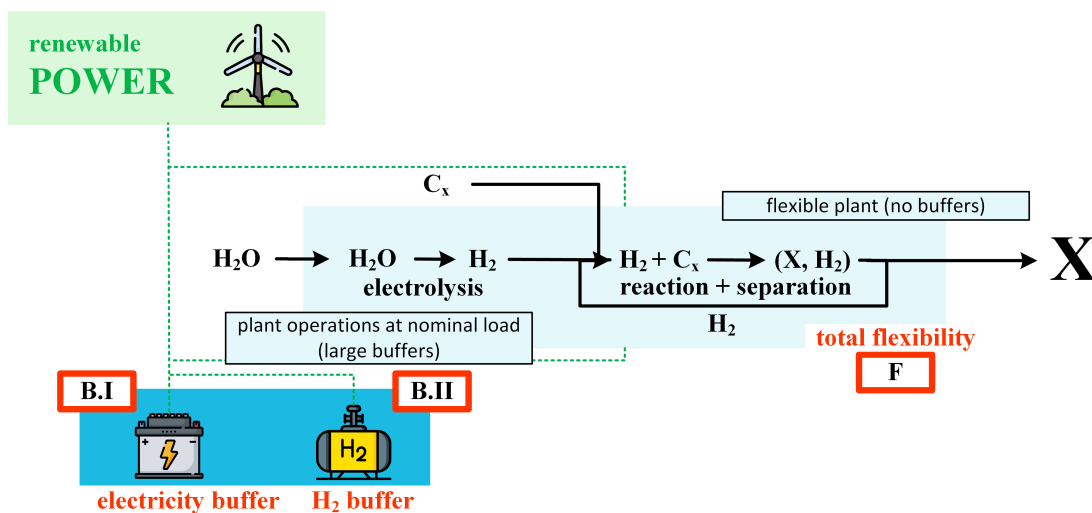


Figure 6.1.: Buffering strategies for a generic Power-to-X (P2X) process determine the extent of process flexibility involved. Electricity and hydrogen buffering strategies are denoted with B.I and B.II, respectively (plant design and operations at a single, nominal load). In contrast, the whole process can be operated flexibly (strategy F).

Figure 6.1 schematically illustrates the type of decisions involved in a preliminary project stage, where buffering strategies can be implemented along the production path for the conversion of renewable power, water and a carbon source into a generic valuable chemical component, X. It is assumed that a renewable energy park provides green electricity to a local Power-to-X facility.

In case B.I, a buffer for the storage of electricity is used before any chemical conversion process; in case B.II, hydrogen is stored after water electrolysis and before the chemical synthesis. The exact allocation of buffering devices along the process coordinate determines the extent of plant flexibility, i.e., the plant section which follows the buffer operates in steady state. Consequently, for case F where no buffers are involved, the P2X process is operated at the maximum flexibility.

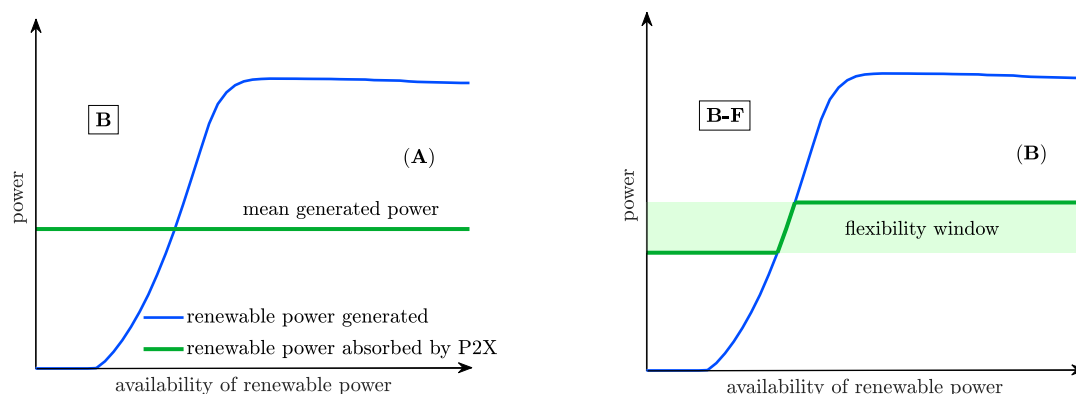


Figure 6.2.: (A) Large buffering devices determine a single operation mode at the mean generated power (buffering scenario B); (B) opening flexibility window with moderate buffering (transition from buffering scenario B towards the flexible case F). Generated renewable power in blue is retrieved from actual performance measurements of a wind turbine, where slightly declines before the cut off velocity is attained (cf. Table D.1).

The effect of implementing large buffering devices for the maximum stabilization of the process is shown qualitatively in Figure 6.2(A). Here, an unstable power supply is represented in blue. This is function of the availability of the renewable resource which generates and is expressed, e.g., as solar radiation or wind velocity. Energy is stored when this generation curve deviates positively from an average level that coincides with the nominal power demand of the operating chemical facility, in green. Excess power is then released when the deviation between supply and demand becomes negative.

For smaller buffering devices, operations at the average generated renewable power can no longer be ensured. This aspect is shown in Figure 6.2(B). The green patch here defines the flexibility window, a region delimited by a lower and an upper bound to the power supply that the plant can attain by adjusting its operating regime. Peak power supplies above the upper bound are stored, whereas supplies below the lower bound are integrated by the stored power.

Further reductions in the capacity of installed buffering devices result in a wider oscillation between operating modes, which may lead the system into a region where operations are not feasible. Therefore, the maximum achievable process flexibility is defined by the lowest power supply threshold below which the system cannot operate.

This suggests two possible operation strategies:

1. cyclic and frequent plant shutdowns with loads below the minimum threshold;
2. purchase of external power at reasonable negotiated prices.

Strategy 1. is not considered in this dissertation. It is economically unattractive due to loss of productivity, and technically demanding, as it implies that frequent and rapid shutdowns of reactors, compressors and electrolyzers are technically feasible. In addition, a certain amount of renewable power would not be utilized at low loads below the threshold. Instead, Strategy 2 is illustrated in Figure 6.3 and quantified in this last chapter dedicated to process flexibility.

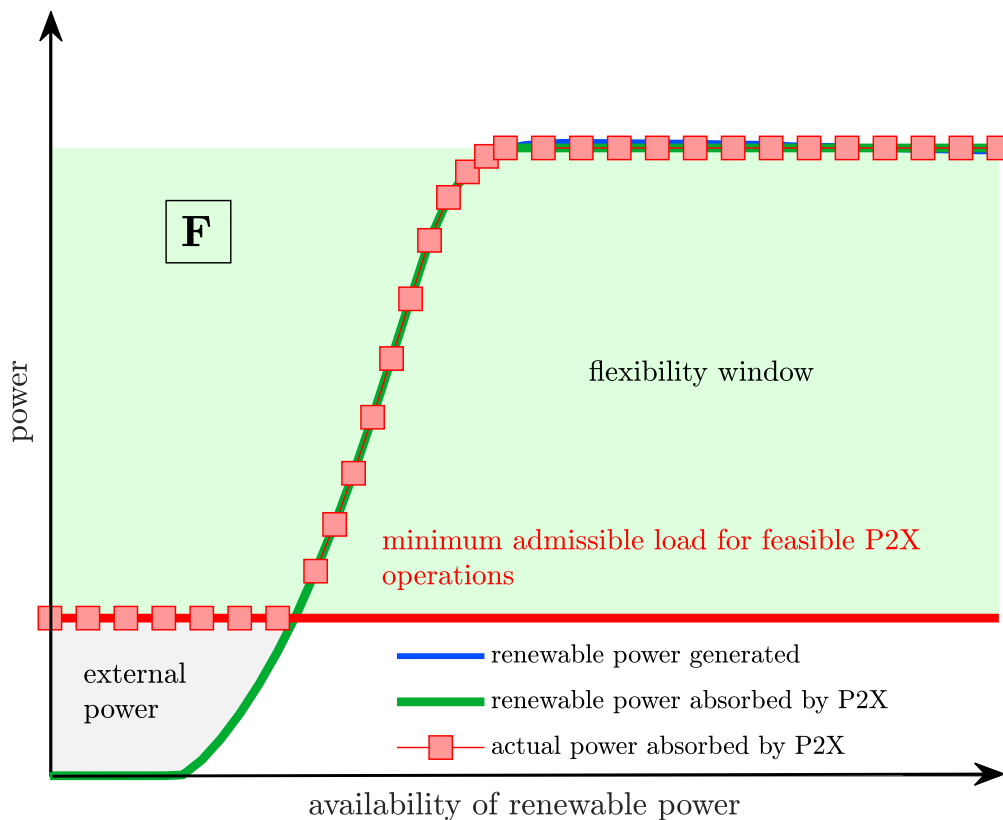


Figure 6.3.: Window for maximum plant flexibility. The renewable power generated at low wind velocities does not guarantee feasible plant operations, which are ensured via integration of external grid electricity.

Here, the power generated by a renewable resource is entirely absorbed by the chemical plant. Therefore, the renewable power supplied to the process coincides with the generated renewable power. Nevertheless, the minimum admissible load for feasible operations is crossed. For this reason, the curve representing the actual power supply to the process (red markers) coincides with the generation of renewable power until it stabilizes at the minimum admissible load. This occurs

when the natural resource only is too scarce to attain the minimum power threshold. Instead, an additional source must integrate the renewable input locally generated, e.g., from the grid or from a geographically displaced renewable energy source.

Based on this general background, a decision must be made on the flexibility window that can be reasonably imposed on the process. A decisive performance indicator which supports the final choice is profitability, crucial in industrial applications.

For flexible cases, the inherent fluctuations open important questions related to the best candidate design which can withstand load changes for the scenarios involved. Single units must preserve feasibility while the entire plant performs at the maximum profitability. This requires the implementation of detailed unit models associated with their feasibility constraints within an optimization framework for the identification of an optimum design. Different operating regimes and loads must be simultaneously included in the analysis.

Furthermore, any spike in the supply of local renewable electricity must be absorbed within the plant, e.g., by electrical heat exchangers, compressors, electrolyzers and electrified reactors for endothermic syntheses. Therefore, the final design of a highly electrified and flexible P2X plant is influenced by the distribution of the available power between the unit operations involved. Consequently, the optimization framework also needs to incorporate a description of the overall interconnected plant.

This chapter provides novel tools to formulate the profitability-based comparison between a flexible and a single-load design applied to an important syngas application: methanol synthesis. The tool for a detailed plant design in the flexible case is determined by means of multi-period optimization. The resulting profit is benchmarked with the reference case offered by the design of the same plant operated at a single, nominal load, average throughout the year, with large buffering devices. The outcomes determine a scenario, where the decision should be based on the price that can be negotiated for the supplementary energy supply at low loads. The proposed multi-period optimization framework represents a technical novelty, framed in the literature background presented in the next section.

6.1.1 Scaled profitability

The determination of a levelized cost of methanol is not the objective of the study. In this chapter, profitability is rather used to determine a methodological comparison between optimization scenarios. It is assumed that some units are unvaried between cases, such as compressors, electric heaters, flash drum. Therefore, the capital cost associated with these unit operations does not contribute to the system as the profit is not absolute but scaled.

6.2 Methodological background

Typical optimization techniques for the design of chemical plants with detailed models determine the size of process units for a single, nominal load. Nevertheless, there is no guarantee that the identified design is the best solution for loads other than nominal. Instead, dedicated optimization strategies should be implemented to account for flexible plant operations, where a detailed description of process units, interconnections and operating windows is incorporated. Furthermore, Bruns et al. [180] report on the definition and use in literature of the term flexibility, which has become increasingly important in the context of production processes in recent years, but lacks a comprehensive categorization. Their conclusions highlight that, although an enormous methodological development has been attained, literature still lacks the applications to complex and more realistic problems. Instead, it mainly focuses on quasi-convex feasibility domains, often far from a reasonable description of real production processes.

Grossmann and Sargent [19] define a problem class for plant design under uncertainty, where the probability of occurrence is associated to a given set of values of the uncertain parameters. The final objective function is given by a finite sum of single entries, each weighted by the corresponding value of probability. The solution of the weighted objective function is then combined with the nominal design solution, i.e., at the nominal value of the uncertain parameters, to obtain over-design factors. Nevertheless, the applications are restricted to monotonic equations. The authors introduce an important distinction between design variables (optimization variables shared across different sets of uncertain parameters), and control variables (adjusted in light of the actual prevailing operating conditions). The same group proposed a mixed-integer linear programming approach (MILP) for the synthesis and design of utility systems based on multi-period operations [181]. In their case-study, capital and operating costs are minimized in a linear programming framework. In addition, the correlation between problem size and number of periods is reported. More recently, Martín [182] proposed the application of multi-period MILP optimization to a renewables-to-methanol system, where the nonlinearity of detailed models is decoupled from the design under uncertainty of wind and solar farms. Surrogate models are incorporated into the final problem formulation, which account for actual patterns of wind and solar power supply. Furthermore, Peng et al. [183] proposed the application of simplified nonlinear models for superstructure optimization under intermittency introduced by predefined time series of renewable power supply. The authors distinguished between operating and design variables, the former are replicated and the latter are shared across the periods. Operating feasibility was ensured by the maximum equipment size required for any scenario. This approach is appropriate if the system does not include a detailed model. For instance, a reactor volume too large for the input power flowrate could lead to unattainable velocities or temperature hot spots. In a multi-period optimization application for superstructure networks of heat exchangers, Short et al. [184] highlighted the need to verify that design results shared among periods are always feasible. Once again, the authors decoupled detailed model evaluation from multi-period optimization by means of an iterative procedure. At each iteration of the optimization, the maximum achievable

size of the unit is selected and its feasibility across periods is checked before proceeding to a new iteration (decoupled approach).

In general, the implementation of simplified unit models or decoupled approaches in multi-period optimization frameworks allow to identify optimal solutions that do not guarantee the feasibility of flexible operations in the plant. More recently, Zimmermann et al. [185] included a detailed reactor and catalyst particle model within a multi-period approach for synthetic natural gas generation. In this article, the authors maximized the space-time yield of the methanation reactor subject to variable feed loads provided by renewable hydrogen. Unlike previous works, a detailed nonlinear model of the methanation reactor was directly included in the framework of multi-period design optimization. Therefore, design, catalyst concept and operating strategies for the unit operation are optimized.

From a methodological perspective, a systematic effort devoted to the simultaneous optimization of the detailed design and setpoints definition of an entire flexible and highly electrified Power-to-X and, in particular, methanol synthesis plant is a novel contribution to the existing literature.

6.2.1 The methanol synthesis

Methanol is a relevant key molecule in the chemical industry. Not only is it an important intermediate for further synthesis of chemicals, such as formaldehyde, acetic acid, and MTBE [186], but it is also blended with gasoline in internal combustion engines as an octane booster, or possibly in pure form, as reviewed in Verhelst et al. [187]. Methanol is produced industrially in large plants and cooled fixed-bed reactors. The conversion of carbon monoxide and carbon dioxide to methanol is moderately exothermic and proceeds with a decrease in the number of moles:



avored by high pressure and low temperature. As a side reaction, reverse water-gas shift contributes to the generation of carbon monoxide. Established technologies adopt fixed-/packed-bed reactors, typically on CuO/ZnO/Al₂O₃, cooled by boiling steam at a suitable pressure, as reviewed by Dieterich et al. [188]. An example is the first-stage of the Lurgi technology. Although these systems benefit from the economy of scale, the size of decentralized plants that take advantage of locally generated renewable power may be limited due to the area available for the installation of wind or solar parks. Furthermore, methanol can be easily stored as liquid at room temperature.

The next sections are dedicated to the description of the process layout and to the definition of the optimization setup, functional steps in the determination of modeling constraints and feasibility ranges.

6.3 Plant layout

Methanol is generated in a production section, followed by its separation from water. Figure 6.4 illustrates fine process details in terms of upstream and production, whereas the following separation (distillation) section is drafted as a simple input-output block. As a matter of fact, an unsteady power supply – green box for renewable energy (RE) – is to be absorbed via dynamic operations within the production section, whereas a separation, i.e., distillation, section can rely on a nominal feed and energy supply (F). By assumption, the plant relies solely on electricity, also to supply heat to process flows and conversion processes. For this purpose, electrical heat exchangers (HE) are implemented.

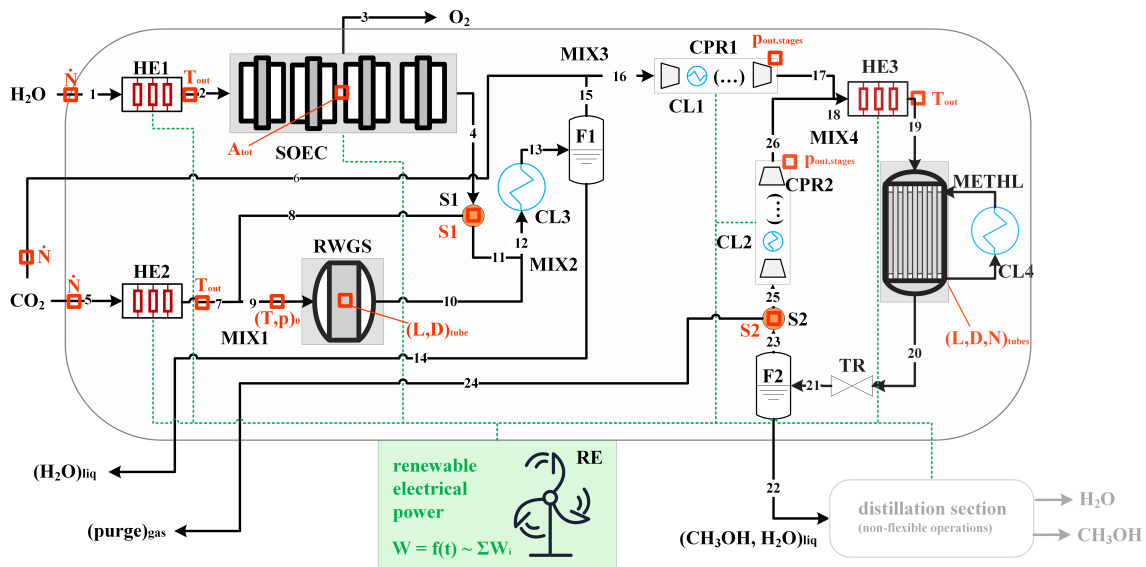


Figure 6.4.: Overall plant layout for the generation of a binary mixture of methanol and water. The final distillation section is not highlighted, as it operates independently of the unsteady power supply.

Figure 6.4 shows the process flow diagram, described in this section. A stream of deionized-desalinated water (stream 1) is vaporized and heated within HE1 up to the requirements of an efficient SOEC (solid oxide high-temperature steam electrolyzer), which generates oxygen at the anode (stream 3) and a mixture of water and hydrogen at the cathode (stream 4). A feed stream of carbon dioxide (stream 5) is heated in HE2. Its outlet stream 7 combines with stream 8 in mixer MIX1 (cathode outlets from SOEC) into stream 9 which feeds an adiabatic, single-staged reverse water-gas shift reactor (RWGS). Stream 8 is downstream of splitter S1, which allows to direct

stream 4, a mixture of hydrogen and water, either to RWGS (stream 8) or to the methanol loop (stream 11). As a consequence, if stream 11 is selected, and the bypass stream of carbon dioxide (stream 6) is selected over stream 5 (makeup carbon dioxide to RWGS), RWGS is bypassed and the methanol loop is fed exclusively with water, hydrogen and carbon dioxide after mixing. Stream 6 is fed directly to a compressor train CPR1, after the mixing with stream 15 in MIX3, vapor head of a knockout drum F1: water, formed in RWGS and possibly unconverted in SOEC, has to be removed before compression CPR1. Thus, stream 12, composed from stream 11 and stream 10 after mixing MIX2, is cooled in CL3 and subsequently flashed in F1. Five adiabatic compression stages are represented compactly by the dashed boxes CPR1 and CPR2 in Figure 6.4, which additionally include CL1 and CL2 and represent the intermediate coolers, three for each compressor group. Finally, outlet stream 17 feeds the methanol loop at mixer MIX4. Stream 18 is heated in HE3 to the required feed temperature in the multitubular, steam-cooled methanol reactor (METHL). Cooler CL4 cools the steam to its boiling point before recirculating in the reactor shell-side. The hot stream 20 is throttled (TR) and flashed in F2, which separates a cold liquid stream of water and methanol stream 22 from the gas stream stream 23, optionally purged by splitter S2 into stream 24, whereas stream 25 is recompressed in CPR2, then recycled as stream 26. In Figure 6.4, the degrees of freedom of the process are illustrated in red and denoted with small squares on the flowsheet. They can be sorted into design and operating decision variables. Variables such as the area of SOEC stacks, number of reactor tubes, as well as tube length, diameter and catalyst diameter are design decisions. Operating decisions are: flowrates of feed streams to the entire plant, i.e., stream 1 (water), 5 and 6 (carbon dioxide), the feed states of the reactors, outlet states of the compressor stages, the (electric) heat exchangers, the discharge pressure of the throttling valve, the extent of purge from splitter S2 in the methanol loop and the extent of bypass of RWGS via splitter S1.

6.4 Power supply and optimization setups

The available total electric power \dot{W}_{tot} is completely absorbed by the methanol plant and distributed according to the following constraint:

$$0 = \dot{W}_{\text{tot}}(v_{\text{wind}}) - \sum_{i \in I} \dot{W}_i(v_{\text{wind}}), \quad (\text{AE.Wtot})$$

where set I includes all power sinks within the upstream-reacting section of the plant, represented in Figure 6.4. Wind velocity constitutes a yearly time-series. Therefore, its time dependency can be expressed as $v_{\text{wind}} = v_{\text{wind}}(t)$. Consequently, the total power absorbed by the methanol plant is a function of the wind velocity, $\dot{W}_{\text{tot}}(v_{\text{wind}})$, and time, $\dot{W}_{\text{tot}}(t)$. The temporal dependency of the

total power $\dot{W}_{\text{tot}}(t)$ is not directly translated into dynamic models: for design purposes, dynamic transitions across periods do not need to be accounted for.

Wind velocities can be grouped into NP sub-domains, where the generic j -th sub-domain reads $(v_{\text{wind},j-1}, v_{\text{wind},j}]$ and is associated to a Period, Π_j . Over the complete domain, the total power input is discretized as:

$$\dot{W}_{\text{tot}}(v_{\text{wind}}) = \begin{cases} \dot{W}_{\text{tot},1} & \text{for } v_{\text{wind}} \in [0, v_{\text{wind},1}] \\ \dots & \\ \dot{W}_{\text{tot},\text{NP}} & \text{for } v_{\text{wind}} \in (v_{\text{wind},\text{NP}-1}, v_{\text{wind},\text{NP}}] \end{cases} \quad (6.4)$$

The integration of the frequency distribution over a generic sub-domain $(v_{\text{wind},j-1}, v_{\text{wind},j}]$ provides with the yearly probability of occurrence of period Π_j , and hence the yearly probability of occurrence of the total power, averaged for the current period, $\dot{W}_{\text{tot},j}$. The probability of occurrence of period Π_j is denoted by ω_j . In this Power-to-Methanol application, the Weibull distribution of wind velocities relates with the power curve generated by a wind park, whose rounded power output is 50 MW (actual output implemented: 50.5 MW) and is supplied by 24 wind turbines of 2.1 MW (nominal output). Data for the power curve are retrieved from a technical sheet – see Supplementary Section D. The Weibull distribution is generated from a mean wind velocity and from a shape factor of 2, representing rather variable winds from a scale of 1 (highly variable winds) to 4 (highly stable winds). The mean wind velocity adopted to define the distribution is scaled from a value of 4.46 m s^{-1} at 10 m above the ground (Supplementary Section D), to 8.9 m s^{-1} at 100 m, with a terrain rugosity factor of 0.3 (intermediate between the extreme values 0.2 and 0.4) applied to an exponential scaling rule: $v_{100 \text{ m}} = v_{10 \text{ m}} (100 \text{ m}/10 \text{ m})^{0.3}$. Details on the definition of the wind velocity frequency distribution can be found in Gualtieri et al. [189].

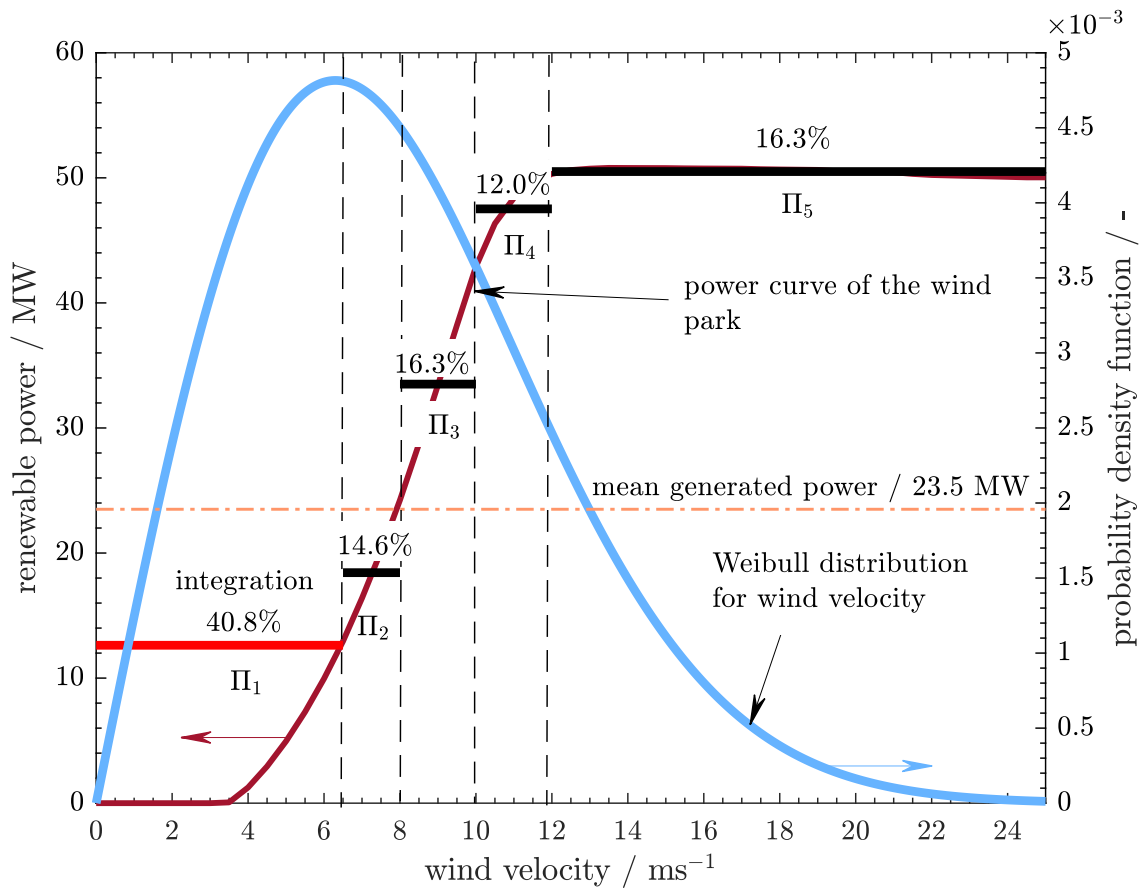


Figure 6.5.: Renewable power generated by the wind park in function of the wind velocity and probability density function. Periods are denoted by Π , and their probability of occurrence is given as a percentage value. Horizontal segments represent the mean power supply within a period. The integration of power from the grid required to ensure feasible operations for period Π_1 is indicated by the red segment. The dashed-dotted orange horizontal line represents the mean annual power generated (23.5 MW).

Figure 6.5 combines the Weibull distribution with the curve of the generated renewable power in function of the wind velocity. In addition, it shows how the periods are arranged for the current case. The first period is comprised between 0 and 6.45 m s^{-1} , the latter value representing the statistical mode of the Weibull distribution. In this first period, the power supplied by the wind park is not sufficient to ensure feasible plant operations. Therefore, power from an external source must be complementarily supplied to attain the minimum amount of power required. This power input of 12.625 MW, i.e., 25% of the maximum power supply provided by the wind park, is denoted by a red segment labeled as *integration*. The last period is defined for the power output of 50 MW, which is the rated power output, i.e., maximum, of the wind park. The remaining periods are set between $6.45 - 8$, $8 - 10$ and $10 - 12 \text{ m s}^{-1}$. Although this subdivision is arbitrary, it can provide a reasonable representation of the possible scenarios encountered during plant operations. The maximum number of periods is determined by the computational capacity of the machine

on which the optimization is performed and by the problem size, as it scales with the number of periods.

6.4.1 Design and operating variables

As discussed before, degrees of freedom labeled in red in Figure 6.4 are grouped into two classes of variables: operating and design variables. Operation variables are function of the loads, i.e., they change between periods, whereas the plant design is determined once for all periods. Design variables are denoted by superscript (π). All degrees of freedom are listed and described in Table 6.1 with their lower and upper bounds (LB, UB). As an example, the optimizer identifies a single solution value for $D_{T,METHL}^{(\pi)}$, the diameter of the methanol reactor tubes (design variable), while it identifies NP solutions (equal to the number of periods) for the cooling temperature T_{cool} (operation variable).

Table 6.1.: List of relevant decision variables for design problems and related bounds. Variables shared among periods are denoted with superscript (π).

Variable	LB	UB	description	unit (SI)
$A_{SOEC}^{(\pi)}$	0.5	19095	area SOEC	m ²
$L_{T,RWGS}^{(\pi)}$	0.1	2.1	tube length	m
$D_{T,RWGS}^{(\pi)}$	0.1	2.1	tube diameter	m
$N_{T,METHL}^{(\pi)}$	1	30000	number of tubes	—
$L_{T,METHL}^{(\pi)}$	1	15	tube length	m
$D_{T,METHL}^{(\pi)}$	0.02	0.15	tube diameter	m
$D_{cat,METHL}^{(\pi)}$	0	inf	catalyst diameter	m
$\dot{N}_{tot,1}$	0	inf	H ₂ O, feed SOEC	mol s ⁻¹
$\dot{N}_{tot,5}$	0	inf	CO ₂ , feed RWGS	mol s ⁻¹
$\dot{N}_{tot,6}$	0	inf	CO ₂ , bypass RWGS	mol s ⁻¹
$T_{out,HE1}$	1000	1300	feed temperature, SOEC	K
$T_{out,HE2}$	298	1010	feed temperature, RWGS	K
$T_{out,HE3}$	430	520	feed temperature, METHL	K
$\mathbf{p}_{out(stage),CPR1}$	1	100	vector of discharge pressures at each stage, CPR1	bar
$\mathbf{p}_{out(stage),CPR2}$	1	100	vector of discharge pressures at each stage, CPR2	bar
$p_{in,SOEC} \equiv p_{in,RWGS}$	1	5	pressure SOEC, RWGS (feed)	bar
$p_{in,METHL}$	20	100	feed pressure METHL	bar
T_{cool}	480	600	coolant temperature METHL	K
S1, S2	0	1	split factor: carbon dioxide to RWGS, purge	—

6.5 Mathematical models of process units

The system is modeled by means of zero- and one-dimensional representations of the process units, interconnected by node balances. Ideal gas law is adopted in low pressure, high temperature operations, i.e., from the feedstock to stream 16 entering the first compression sequence CPR1. Elsewhere, non-ideal gas behavior is described through the Redlich Kwong Soave equation of state (RKS), i.e., in compressors CPR1, CPR2 and within the methanol loop. The assumption of equal interactions between different molecules (Lewis-Randal) allows the composition of the gas to be disregarded when evaluating compressibility factors. This approach has been adopted by Graaf et al. [190] for the methanol reactor at high temperatures. Mixing rules are added to the RKS equation of state to model units at high pressure and low temperatures: compressors CPR1 and CPR2, and the flash separator F2 within the methanol loop. Where Lewis-Randal applies, molar total concentrations for gas mixtures at high pressure are expressed as:

$$C_{\text{gas}} = \frac{p \sum_{\alpha \in \mathcal{S}} \left(\frac{\zeta_{\alpha}}{Z_{\alpha, \text{gas}}} \right)}{R_{\text{gas}} T}. \quad (6.5)$$

Here, partial pressures are corrected by the component-related compressibility factors, $Z_{\alpha, \text{gas}}$, derived in D.3.6. Compressibility factors for mixtures, involved in the modeling of CPR1, CPR2 and F2, are denoted by $Z_{\text{mix, gas}}$ (D.3.7), $Z_{\text{mix, vapor}}$ and $Z_{\text{mix, liquid}}$ (D.3.2) for gas, vapor and liquid mixtures, respectively.

In the following sections, modeling equations will be denoted with AE/ODE.UNIT.NUMBER: algebraic or differential equation, unit operation, number of the equations, respectively. The following sections report on the modeling of the main unit operations, the SOEC and the methanol reactor. For heat exchangers, compressors and flash separators, cf. Supplementary Sections D.2.1, D.2.2 and D.3.2.

6.5.1 SOEC

The SOEC model is zero-dimensional and retrieves the relevant parameters from Udagawa et al. [191], reported in detail in D.3.1. The total power input to the stack (\dot{W}_{SOEC}) is expressed as a function of current density, total area and cell voltage:

$$0 = -\dot{W}_{\text{SOEC}} + V_{\text{tot, SOEC}} A_{\text{SOEC}}^{(\pi)} i_{\text{SOEC}}, \quad (\text{AE.SOEC.1})$$

where the total voltage $V_{\text{tot,SOEC}}$ is a summation of ideal (Nernst's) and nonideal contributions (ohmic losses, concentration overpotentials, cathode and anode activation potential), $A_{\text{SOEC}}^{(\pi)}$ is the total area of the SOEC, i_{SOEC} is the current density. To solve the system, the activation overpotential at the cathode and anode are expressed as constraints. They are nonlinear functions of exchange current densities $i_{\text{av,cat/an}}$ and activation overpotential losses $V_{\text{act,cat/an}}$ at cathode and anode, and read:

$$0 = i_{\text{SOEC}} + i_{\text{av,cat}} (\Lambda_1 \exp(\Lambda_2 V_{\text{act,cat}}) - \Lambda_3 \exp(\Lambda_4 V_{\text{act,cat}})), \quad (\text{AE.SOEC.2})$$

$$0 = i_{\text{SOEC}} + i_{\text{av,an}} (\exp(\Lambda_2 V_{\text{act,an}}) - \exp(\Lambda_4 V_{\text{act,an}})), \quad (\text{AE.SOEC.3})$$

where, for the sake of compactness, the lumping coefficients $\Lambda_{(1-4)}$ are introduced here and expanded in the D.3.1. Figure 6.6 (A) reports the polarization curves for the single voltage contributions.

Irreversible losses in the electrolyzer are offset by the endothermic reaction that occurs. Below the thermoneutral operating point, the energy consumed by the reaction is greater than the energy dissipated in irreversible losses, causing the temperature to decrease. In this regime, external thermal energy can be added to the stack. If this can be recovered from the plant itself, the overall efficiency is increased, although this coupling may not be available at the high operating temperatures of the electrolyzer. On the contrary, operation above the thermoneutral current density generates excess heat at high temperature suitable for steam generation [191, 192]. For steady-state operation, a cooling or heat recovery strategy can be implemented to take advantage of this system behavior. However, in flexible operation mode and for this particular plant, where no heat sources at such high temperatures are readily available within the battery limits, it was decided to opt for an adiabatic SOEC model with a constraint on the absolute temperature difference between the inlet and product streams. The adiabatic energy balance reads:

$$0 = -\dot{W}_{\text{SOEC}} + \dot{H}_{\text{out}}(T_{\text{out}}) - \dot{H}_{\text{in}}(T_{\text{in}}), \quad (\text{AE.SOEC.4})$$

where inlet and outlet stream enthalpies $\dot{H}_{\text{in,out}}$ are function of the inlet and outlet temperatures, respectively. Figure 6.6 (B) shows the outlet temperature, function of the power absorbed. The difference between the inlet and outlet temperatures of SOEC is conservatively constrained to an absolute value of 30 K to avoid extreme temperature gradients along the cathode, which could lead to degradation of the material [193]. The SOEC can operate at a pressure within a feasible

range of 1 to 5 bar and the ideal gas law applies. The input pressure at RWGS is constrained to the operating pressure of SOEC, as given in Table 6.1 ($p_{in,SOEC} \equiv p_{in,RWGS}$).

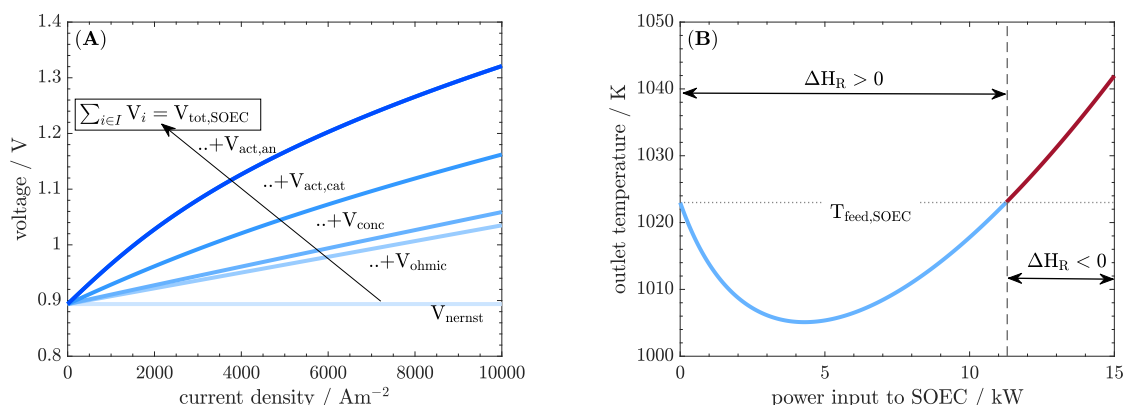
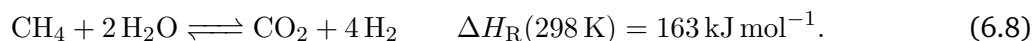
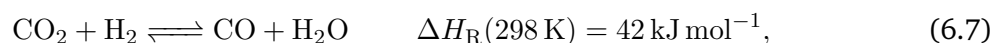
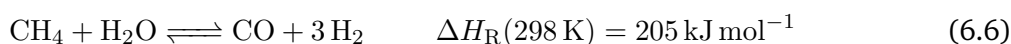


Figure 6.6.: (A) Cumulative definition of the polarization curves for the given cell parameters at 1023 K, as reported in D.3.1, from the ideal voltage (in the lightest blue) to the total voltage (in the darkest blue); (B) definition of the outlet temperature for a feed temperature of 1023 K, fixed cell parameters (Supplementary Section D.3), an area of 1 m² and a feed flowrate of 5.5 mol_{H₂O} s⁻¹, where the blue curve corresponds to endothermic operations, the dark red to exothermic operations.

6.5.2 Reactors

Tubular reactors are modeled with steady-state, one-dimensional mass and energy balances, discretized axially by means of the finite-difference upwind scheme with equally spaced nodes. Gas-phase dispersion is neglected. Therefore, it is sufficient to determine the states at the reactor inlet to define the axial profiles. This information comes from the upstream units in the process line. The pressure drop is described by the Ergun equation. Reactor METHL implements three kinetic contributions [194] related to Equations (6.1 - 6.3) (see D.3.6), whereas the RWGS reactor implements kinetics proposed first by Xu & Froment [170], where three reactions are involved: steam reforming, reverse water-gas shift, reverse methanation. For the latter, the chemical relations read, respectively:



The model equations in ordinary differential form in the axial coordinate z (labeled with the abbreviation ODE) read:

$$0 = -v \frac{d\zeta_\alpha}{dz} + \frac{1 - \epsilon}{\epsilon} \frac{\rho_{\text{cat}}}{C_{\text{gas}}} \left(\sigma_\alpha - \zeta_\alpha \sum_{\alpha \in \mathcal{S}} \sigma_\alpha \right), \quad (\text{ODE.RWGS.1, ODE.METHL.1})$$

$$0 = -v \epsilon C_{\text{tot}} \tilde{C}_{\text{p,gas}} \frac{dT}{dz} + (1 - \epsilon) \rho_{\text{cat}} \sum_{\alpha \in \mathcal{S}} -\tilde{H}_\alpha \sigma_\alpha, \quad (\text{ODE.RWGS.2})$$

$$0 = -v \epsilon C_{\text{tot}} \tilde{C}_{\text{p,gas}} \frac{dT}{dz} - 4 \frac{U}{D_{\text{T,METHL}}^{(\pi)}} (T - T_{\text{cool}}) + (1 - \epsilon) \rho_{\text{cat}} \sum_{\alpha \in \mathcal{S}} -\tilde{H}_\alpha \sigma_\alpha, \quad (\text{ODE.METHL.2})$$

$$0 = \frac{dp}{dz} + \frac{(1 - \epsilon)}{\epsilon^3} \left[150 v \frac{\epsilon (1 - \epsilon)}{\left(D_{\text{cat},k \in \{\text{RWGS,METHL}\}}^{(\pi)} \right)^2} \mu_{\text{mix}} + 1.75 \rho_{\text{gas}} \frac{v^2 \epsilon^2}{D_{\text{cat},k \in \{\text{RWGS,METHL}\}}^{(\pi)}} \right], \quad (\text{ODE.RWGS.3, ODE.METHL.3})$$

where ζ_α is the mole fraction of component α , ρ_{cat} is the catalyst density (1770 kg m^{-3} for METHL and 2355 kg m^{-3} for RWGS), $\tilde{C}_{\text{p,gas}}$ is the molar specific heat at constant pressure in bulk phase (molar average at the discretization node), C_{gas} is the total gas concentration, expressed as Equation (6.5) for METHL, whereas the ideal gas law applies for RWGS. Furthermore, σ_α is the source term related to component α , ϵ is the void fraction ($0.4 \text{ m}^3 \text{ m}^{-3}$), v is the interstitial velocity stemming from the total mass conservation (derived in D.3.9), U is the overall heat transfer coefficient, \tilde{H}_α is the component-related enthalpy of formation at system temperature, μ_{mix} the mixture viscosity obtained from the molar weighted average of component-viscosities at the discretization node.

The maximum pressure drop is set to 5% of the feed pressure. Mixing node MIX1 imposes that the pressure at the feed to RWGS equals the pressure of SOEC. Furthermore, stream 11 leaving S1 feeds MIX2. An isothermal expander is implicitly accounted for, as pressure of stream 11 should equal the pressure at stream 10, calculated from the Ergun equation of the RWGS reactor. The METHL reactor is discretized with 300 finite difference nodes, whereas the shorter RWGS adiabatic stage is discretized with 40 nodes (upwind scheme). Therefore, the discretized reactor models contribute to the final nonlinear set of algebraic constraints.

6.6 Optimization objectives, scenarios and solver

6.6.1 Objective functions

In this study, design and operation of a flexible Power-to-Methanol plant is compared with the results of a single-period optimization at the yearly-averaged nominal load, achieved by means of buffering strategies. This comparison is based on profitability, which is an important performance indicator when investigating industrial applications. Heat integration can help redefine the power distribution between plant units, thus influencing the resulting values of the optimization variables.

In addition, the plant can be designed at the maximum Power-to-Methanol efficiency, achievable regardless of the profit and independent of fixed costs. Based on this, three optimization objectives are defined:

1. maximum profit for flexible plant operations (multi-period);
2. maximum profit for plant operations in steady-state with large electricity or hydrogen buffers (single-period);
3. maximum Power-to-Methanol efficiency for steady state operations (single-period).

Objective 1. relating to the multi-period case reads:

$$\max_{\mathbf{x}^{(\pi)}, \bar{\mathbf{x}}} \sum_{j \in \{1, \text{NP}\}} \omega_j \left(\dot{C}_{22, \text{CH}_3\text{OH}, \Pi_j} - \sum_{i \in \text{UNITS}} \dot{C}_i^{(\pi)} \right), \quad (\text{OBJ.PROFIT.MP})$$

where $j \in \{1, \text{NP}\}$ and Π_j identify the period, $i \in \text{UNITS}$ the installation cost of reactor tubes and catalyst for METHL and RWGS, and the installation cost of SOEC based on the total power consumed. Vector $\mathbf{x}^{(\pi)}$ and $\bar{\mathbf{x}}$ include all design and operation variables for all periods, respectively, where the latter is intended as a collection of vectors for different periods and is indicated by a bar hat above the symbol. This vector reads:

$$\bar{\mathbf{x}} = [\tilde{\mathbf{x}}_1, \tilde{\mathbf{x}}_2, \dots, \tilde{\mathbf{x}}_{\text{NP}}], \quad (6.9)$$

where vector $\tilde{\mathbf{x}}_j$ is the set of operation variables and states for the generic j -th period. In addition, a tilde-hat distinguishes the full set of operation variables from the set of design variables. Heat exchangers, coolers, flash drums and compressors are assumed to be flexible so that they can always meet the requirement of each possible operating framework. Therefore, the selection of these units is independent on the optimization objectives and their costs do not contribute to OBJ.PROFIT.MP. For the modeling of capital costs of RWGS and METHL (reactor vessels and tubes), Guthrie and Timmerhaus cost functions are adopted, actualized to 2022 (CEPCI index) and annualized (fixed cost divided by the expected lifetime). Cost formula and prices follow in the Supplementary Section D.4.

For the single-period optimization but the same objective function, Objective 2. reads:

$$\max_{\mathbf{x}^{(\pi)}, \bar{\mathbf{x}}} \left(\dot{C}_{22, \text{CH}_3\text{OH}} - \sum_{i \in \text{UNITS}} \dot{C}_i^{(\pi)} \right), \quad (\text{OBJ.PROFIT.SP})$$

where now also operation variables are reported in vector form and the bar hat no longer appears. Therefore, Objective 3. is equivalent to maximizing the methanol flowrate in stream 22, outlet of the entire upstream-conversion section of the plant:

$$\max_{\mathbf{x}^{(\pi)}, \bar{\mathbf{x}}} (\eta_{\text{PtCH}_3\text{OH}}) = \max_{\mathbf{x}^{(\pi)}, \bar{\mathbf{x}}} \left(\frac{\dot{N}_{22, \text{CH}_3\text{OH}} \text{LHV}_{\text{CH}_3\text{OH}}}{\dot{W}_{\text{tot}}} \right) = \max_{\mathbf{x}^{(\pi)}, \bar{\mathbf{x}}} (\dot{N}_{22, \text{CH}_3\text{OH}}). \quad (\text{OBJ.EFF.SP})$$

Objective functions OBJ.PROFIT.MP, OBJ.PROFIT.SP and OBJ.EFF.SP are implemented to explore promising plant configurations and operational strategies in a rational sequence of case-studies.

6.6.2 Case-studies

Table 6.2.: Summary of the case-studies.

case study	objective	method	heat integration	buffering scheme
CASE.FLEX	OBJ.PROFIT.MP	multi-period	no	F
CASE.BUFF	OBJ.PROFIT.SP	single-period	no	B.I,B.II
CASE.EFF	OBJ.EFF.SP	single-period	no	B.I,B.II
CASE.FLEX.HI	OBJ.PROFIT.MP	multi-period	yes	F

At first, the design and operations for the maximum profit shall be identified in the context of buffering scenario F, in which maximum plant flexibility is involved – case-study: CASE.FLEX. Multi-period optimization is here applied. Thereafter, single-period optimization is applied to evaluate the buffering strategy B.I (electricity storage) and B.II (hydrogen storage) in case-study CASE.BUFF. Results of CASE.BUFF and CASE.FLEX are then compared. In CASE.BUFF, the plant is designed for a power rating of 23.5 MW, obtained by integration of the product between the probability density function and the power curve in Figure 6.5. In discretized form, it is the product between the average power delivered by the wind farm at consecutive discretization points along the abscissa (wind velocity), and the integral probability of occurrence for that segment, over the entire domain of wind velocities (from 0 m s^{-1} to 25 m s^{-1}). For the adopted set of 50 equally-spaced discretization nodes, it reduces to:

$$\dot{W}_{\text{tot(B.I,B.II)}} = \sum_{i \in \{2,50\}} \frac{(\dot{W}_{\text{tot},i} + \dot{W}_{\text{tot},i-1}) (\omega_i + \omega_{i-1}) (v_{\text{wind},i} - v_{\text{wind},i-1})}{4}, \quad (6.10)$$

where ω_i is the value at discretization point i of the probability density function (Figure 6.5), $\dot{W}_{\text{tot},i}$ and $v_{\text{wind},i}$ represent, respectively, the power generated by the wind park and the wind velocity. In Figure 6.5, this annual averaged power supply is identified by the dashed-dotted orange horizontal line.

The power integrated at period Π_1 for flexible operations (B.I) is obtained by subtracting the weighted integral of the renewable power curve within the period (as shown in Equation (6.10), between 0 m s^{-1} and 6.45 m s^{-1}) from the power actually supplied, stable at 25% of the nominal power supplied by the wind park (discussed at the beginning of Section 6.4).

For this analysis, installation costs of storage devices disregard the actual yearly wind velocity series: it is assumed that the maximum surplus of renewable energy can be determined by the longest time spent by the wind park at its nominal (i.e., maximum) power output at 50 MW, for wind velocities comprised between 12 m s^{-1} and 25 m s^{-1} . Afterwards, in a new scenario CASE.EFF, the Power-to-Methanol efficiency maximized for the single period at mean wind velocity (OBJ.EFF.SP) is compared with the corresponding value obtained in CASE.FLEX. This allows to indicate how efficiency is lost in the multi-period maximization of the profit (CASE.FLEX). Finally, the results of CASE.FLEX are reconsidered and compared within the same framework, that is, multi-period maximization of the profit, with the implementation of heat integration – case-study CASE.FLEX.HI. Here, the whole amount of thermal power recoverable from cold utilities within the plant is utilized for the vaporization of water and preheating at the inlet of SOEC. Table 6.2 summarizes relevant aspects related to the four optimization cases just described.

6.6.3 Formulation of multi-period design optimization problem

Modeling constraints, objective functions and scenario settings being introduced (Section 6.5 and 6.6.1, respectively), this section reports the final formulation of the NLP problems in differential form. Nonlinear problems are denoted by NLP.{FLEX,BUFF,EFF,FLEX.HI}, which translate case-studies CASE.{FLEX,BUFF,EFF,FLEX.HI} introduced in Section 6.6.2 into mathematical notation. The NLP associated with the first multi-period optimization scenario (CASE.FLEX) reads:

$$\begin{aligned}
& \max_{\mathbf{x}^{(\pi)}, \bar{\mathbf{x}}} \sum_{j \in \{1, \text{NP}\}} \omega_j \left(\dot{C}_{22, \text{CH}_3\text{OH}, \Pi_j} - \sum_{i \in \text{UNITS}} \dot{C}_i^{(\pi)} \right) \\
& \text{s.t.} \quad \mathbf{AE.Wtot}, \tag{NLP.FLEX} \\
& \mathbf{AE.SOEC}.(1, 2, 3, 4), \\
& \mathbf{DE.RWGS}.(1, 2, 3), \mathbf{DE.METHL}.(1, 2, 3), \\
& \mathbf{AE.MIX1}, \mathbf{AE.MIX2}, \mathbf{AE.MIX3}, \mathbf{AE.MIX4}, \\
& \mathbf{AE.HE1}, \mathbf{AE.HE2}, \mathbf{AE.HE3}, \\
& \mathbf{AE.CPR1}.(1, 2), \mathbf{AE.CPR2}.(1, 2), \\
& \mathbf{AE.F1.1}, \mathbf{AE.F2}.(1, 2, 3) \\
& |\mathbf{T}_{\text{out}, \text{SOEC}} - \mathbf{T}_{\text{in}, \text{SOEC}}| \leq 30 \text{ K}, \\
& \mathbf{p}_{\text{in}, \text{RWGS}} = \mathbf{p}_{\text{out}, \text{SOEC}}, \\
& \mathbf{p}_{\text{in}, (\text{RWGS}, \text{METHL})} - \mathbf{p}_{\text{out}, (\text{RWGS}, \text{METHL})} / \mathbf{p}_{\text{in}, (\text{RWGS}, \text{METHL})} \leq 0.05, \\
& 0.05 \text{ m s}^{-1} \leq \mathbf{v}_{(\text{RWGS}, \text{METHL})} \leq 3 \text{ m s}^{-1}, \\
& \mathbf{p}_{\text{out}, \text{CPR1}} = \mathbf{p}_{\text{out}, \text{CPR2}}, \\
& \mathbf{T}_{\text{METHL}} \leq 600 \text{ K}, \\
& \mathbf{T}_{\text{out}, \text{TR}} \geq 230 \text{ K}, \\
& \zeta_{\text{CH}_4, \text{METHL}} \leq 0.01. \\
& \{\mathbf{x}^{(\pi)}, \bar{\mathbf{x}}\} \leq \{\mathbf{UB}^{(\pi)}, \bar{\mathbf{UB}}\}, \\
& \{\mathbf{x}^{(\pi)}, \bar{\mathbf{x}}\} \geq \{\mathbf{LB}^{(\pi)}, \bar{\mathbf{LB}}\},
\end{aligned}$$

where bold entries constitute sets of constraints (**AE**, **DE**), vectors of system variables, the latter being denoted by a bar hat if they are not shared across periods, as discussed in Section 6.6.1. Set $\mathbf{AE.W}_{\text{tot}}$ collects replicas of Equation AE.Wtot across periods (AE.Wtot), where the total power is defined as in Equation (6.4).

The second and third optimization case, CASE.BUFF and CASE.EFF, refer to the same set of constraints in single-period, with different objective functions, respectively, OBJ.PROFIT.SP and OBJ.EFF.SP. In single-period optimization, constraints and operation variables are no longer replicated across periods. The NLPs read:

$$\begin{aligned}
& \max_{\mathbf{x}^{(\pi)}, \tilde{\mathbf{x}}} \left(\dot{C}_{22, \text{CH}_3\text{OH}} - \sum_{i \in \text{UNITS}} \dot{C}_i^{(\pi)} \right) \text{ and } (\dot{N}_{22, \text{CH}_3\text{OH}}) \\
& \text{s.t.} \quad \text{AE.Wtot}, \quad (\text{NLP.BUFF and NLP.EFF}) \\
& \quad \text{AE.SOEC.(1, 2, 3, 4)}, \\
& \quad \text{ODE.RWGS.(1, 2, 3), ODE.METHL.(1, 2, 3)}, \\
& \quad \text{AE.MIX1, AE.MIX2, AE.MIX3, AE.MIX4}, \\
& \quad \text{AE.HE1, AE.HE2, AE.HE3}, \\
& \quad \text{AE.CPR1.(1, 2), AE.CPR2.(1, 2)}, \\
& \quad \text{AE.F1.1, AE.F2.(1, 2, 3)} \\
& \quad |T_{\text{out,SOEC}} - T_{\text{in,SOEC}}| \leq 30 \text{ K}, \\
& \quad p_{\text{in,RWGS}} = p_{\text{out,SOEC}}, \\
& \quad p_{\text{in,(RWGS,METHL)}} - p_{\text{out,(RWGS,METHL)}} / p_{\text{in,(RWGS,METHL)}} \leq 0.05, \\
& \quad 0.05 \text{ m s}^{-1} \leq v_{\text{(RWGS,METHL)}} \leq 3 \text{ m s}^{-1}, \\
& \quad p_{\text{out,CPR1}} = p_{\text{out,CPR2}}, \\
& \quad T_{\text{METHL}} \leq 600 \text{ K}, \\
& \quad T_{\text{out,TR}} \geq 230 \text{ K}, \\
& \quad \zeta_{\text{CH}_4, \text{METHL}} \leq 0.01. \\
& \quad \{\mathbf{x}^{(\pi)}, \tilde{\mathbf{x}}\} \leq \{\mathbf{UB}^{(\pi)}, \widetilde{\mathbf{UB}}\}, \\
& \quad \{\mathbf{x}^{(\pi)}, \tilde{\mathbf{x}}\} \geq \{\mathbf{LB}^{(\pi)}, \widetilde{\mathbf{LB}}\}.
\end{aligned}$$

The formulation of the last multi-period problem with heat integration, NLP.FLEX.HI, is equivalent to the formulation of problem NLP.FLEX (multi-period, without heat integration). In addition, the power recovered from cold utilities is subtracted from the heating duty for HE1, the circulating heat exchanger SOEC inlet. Therefore, the constraint AE.HE1 for the heat exchanger at the SOEC inlet, becomes:

$$0 = \dot{W}_{\text{HE1}} - \left[\left(\int_{298 \text{ K}}^{T_{\text{SOEC}}} \tilde{C}_{\text{p,H}_2\text{O}} \dot{N}_{\text{in,H}_2\text{O}} dT \right) + \Delta H_{\text{ev}}(298 \text{ K}) - (\dot{Q}_{\text{CL1}} + \dot{Q}_{\text{CL2}} + \dot{Q}_{\text{CL3}} + \dot{Q}_{\text{CL4}}) \right], \quad (6.11)$$

which includes the sum of all recoverable thermal power output from the plant cooling devices, CL(1-4). The size of these NLPs is reported in Table 6.3.

Table 6.3.: Overview of the treated multi-period design optimization problems: number of variables, constraints and resulting degrees of freedom.

NLP problem	variables	equality constraints	degrees of freedom	number of variables: design, operation	number of periods
NLP.FLEX	13785	13675	110	10, 100	5
NLP.BUFF	2765	2735	30	10, 20	1
NLP.EFF	2765	2735	30	10, 20	1
NLP.FLEX.HI	13785	13675	110	10, 100	5

6.6.4 NLP solver

The system is modeled in MATLAB2018b, which invokes IPOPT [174] via CasADi [195, 173] v3.5.5 for the solution of large NLPs, running on the linear solver MA97 [196]. Computations are performed on a Linux machine, processor Intel^R CoreTM i7-6700 CPU @ 3.4 GHz , 4 cores, each provided with 8 GB RAM.

6.7 Optimization results

This section reports and discusses the optimization results obtained from the implementation of the four NLPs. A quantitative and comprehensive overview of the results of the different scenarios is reported in Table D.4 and Table D.5, which illustrate the resulting optimal design and operation variables, costs of the optimized units and revenues. From a topological perspective, RWGS is excluded from all optimization solutions. In fact, RWGS presents a negligible volume, splitter S1 deviates the whole SOEC outlet away from RWGS, and the feed stream of carbon dioxide bypasses the reactor. Consequently, split factor S2 enforces a closed recycle loop after METHL due to the fact that methane, an inert in METHL leading to hold-up to be purged, is not generated by the RWGS reactor, and that water is largely separated after throttling TR in the low-temperature flash F2. Furthermore, thermodynamics favor the reverse steam-reforming and methanation contributions within RWGS at high pressures as they proceed with a decreasing number of moles. For this reason, the optimal pressure selected at SOEC, and consequently at RWGS being above 4.5 bar, would enforce the generation of CH₄ at the temperature range considered. Although the RWGS step presents a negligible reacting volume, a stream of carbon monoxide is recirculated within the closed methanol loop, as discussed later on in the section.

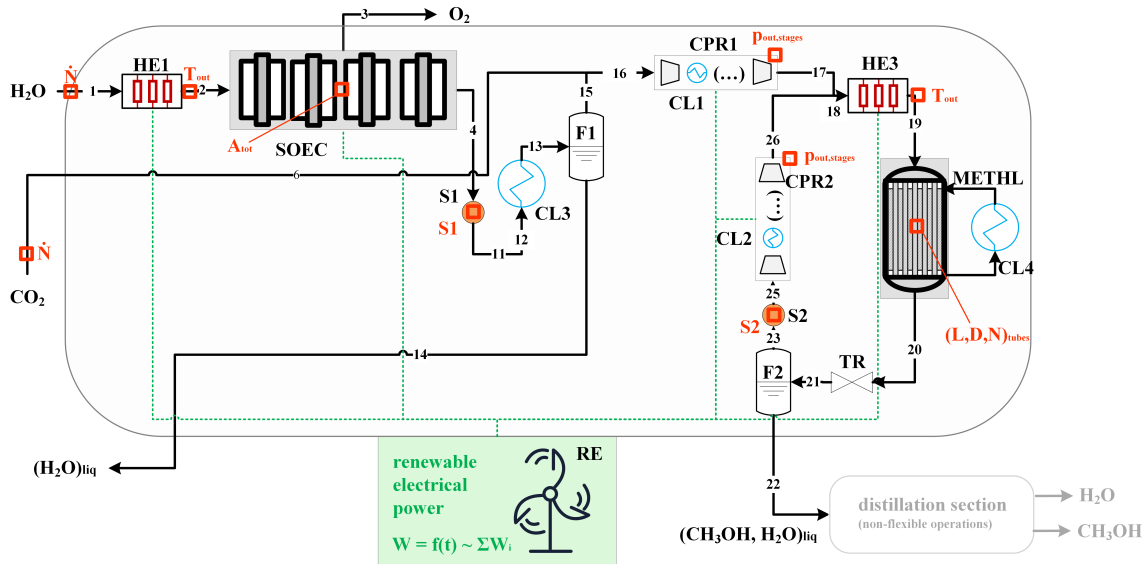


Figure 6.7.: Optimal P2Methanol plant topology shared by the four optimization cases. RWGS plays a negligible role, and thus can be bypassed by the process flows. The recycle loop of METHL is closed.

6.7.1 Results for CASE.FLEX: maximum flexibility without heat integration

The weighted maximization of the profits determines a process configuration where the methanol loop is essentially closed and carbon monoxide is recirculated within it. The presence of carbon monoxide is enforced for kinetic reasons, as it enhances the mass action related to its hydrogenation towards methanol as in Equation (6.2). At the same time, the reverse water-gas shift reaction contribution within the methanol reactor regenerates carbon monoxide so that its concentration along the axis is essentially preserved. This peculiar effect possibly depends on the kinetics chosen, combined with the minimization objective selected: the optimizer determines that it is more convenient to run the RWGS internally within the methanol loop, which also contributes in lowering the reaction temperatures due to the endothermic RWGS contribution. Therefore, a different catalyst more selective towards CO hydrogenation would enforce an additional RWGS steps.

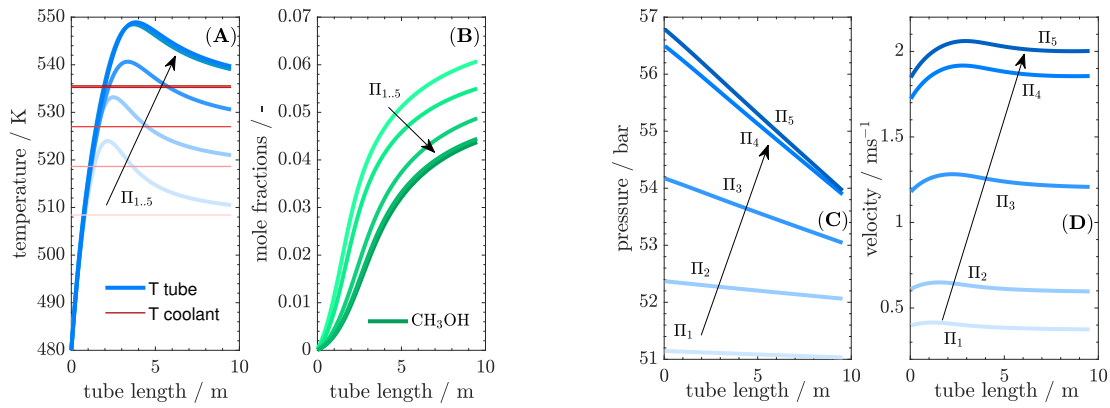


Figure 6.8.: Relevant profiles along the axial coordinate of METHL reactor for different periods for increasing loads, e.g., from Π_1 to Π_5 : temperature and molar fraction profiles, (A) and (B), pressure and velocity profiles, (C) and (D). Figure (A) reports the cooling temperature level in red, constant along the axis (boiling water).

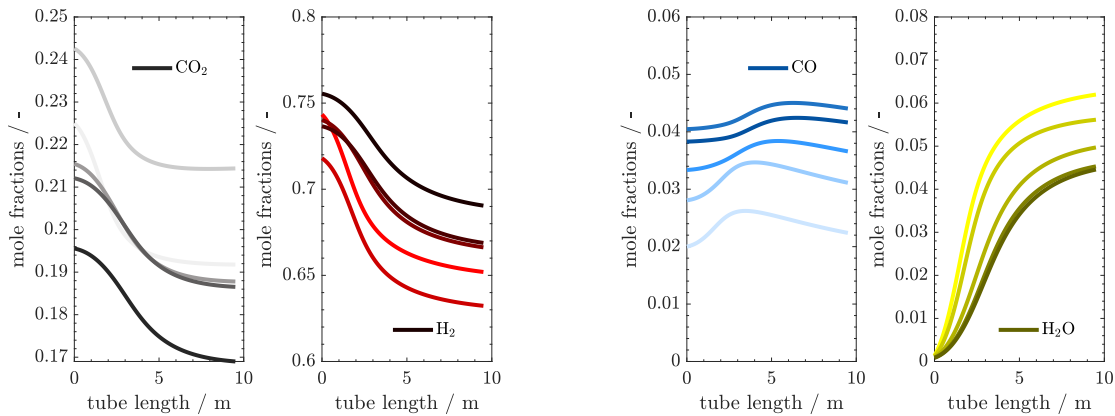


Figure 6.9.: Relevant profiles along the axial coordinate of METHL reactor for different periods for increasing loads, e.g., from Π_1 to Π_5 : darkening colors indicate increasing loads.

Figure 6.8 shows relevant trends along the axial coordinate of METHL for the different periods. Temperature profiles (tube side) and cooling temperatures (shell side) are directly proportional to the feed flowrates and to the velocity profiles, the latter determining proportional pressure drops. The feed pressure ranges between 51.1 bar and 56.8 bar. The cooling temperature ranges between 508 K and 536 K. The composition profiles show no qualitative differences for the different periods, as their trends are essentially preserved. The methanol yield per pass based on carbon dioxide, thus defined as the ratio between moles of carbon dioxide consumed and moles of methanol generated in the reactor, is unitary, although CO contributes to the system: this means that CO is generated from CO_2 (RWGS contribution in the first part of the reactor, until the hotspot is formed), and then it reacts in combination with H_2 to produce CH_3OH . The conversion of carbon dioxide and hydrogen per pass range within 20-25% and 17-21%, respectively. The outlet mole fraction of methanol ranges within 4.4% and 6% and is inversely proportional to the load, which is justified by the lower residence times at higher feed flowrates. The resulting design for METHL

consists of a bundle of 508 tubes of length 9.53 m and diameter 5.2 cm, with a total volume of 10.5 m³. The diameter of the catalyst particle is 1/10 of the tube diameter, due to a dedicated constrain.

SOEC is operated exclusively in the endothermic reaction regime, at the limit of the permitted temperature drop between inlet and outlet section, 30 K. This value exceeds the temperature difference range shown in Figure 6.6 (B), as it results from a different area of SOEC and feed flowrate from the simulation results of the single unit operation. Figure 6.10 shows the direct proportionality between the resulting current density, voltage, feed temperature and operating pressure with the corresponding period. In Table D.4, the supply temperature to the SOEC is equivalently reported as the outlet temperature from the first heat exchanger ($T_{out,HE1}$). The SOEC area is 2155 m².

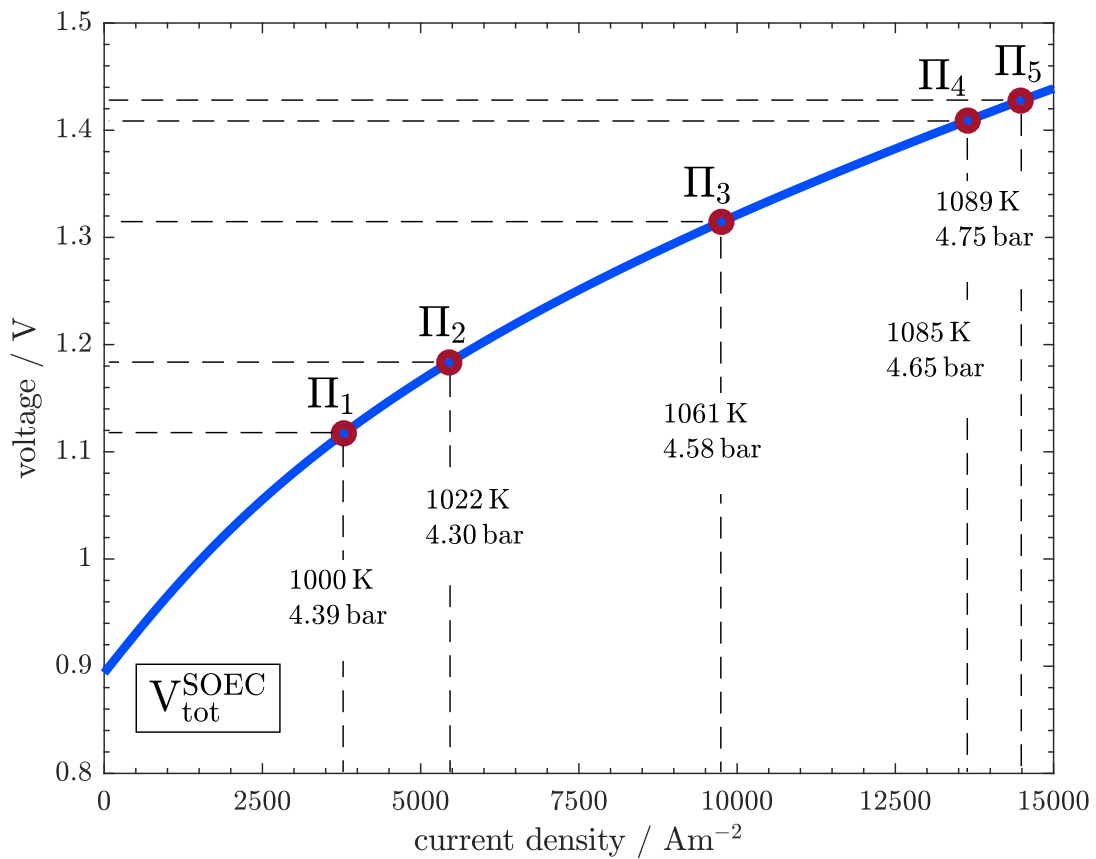


Figure 6.10.: This graph represents the current density and voltage resulting from NLP.FLEX. The points are labeled with the period identifier $\Pi_{i \in \{1, NP\}}$, the feed temperature and the operating pressure. The temperature drop is always equal to 30 K.

The flash separator F2 separates most of the condensable water and methanol due to the very low temperatures achievable with throttling, due to the low pressure attained after isenthalpic expansion of the off-gases from the METHL reactor. The pressure drop at the throttling valve is

comprised between 54% and 57% of its feed pressure. Figure 6.11 is a logarithmic representation of the partition of the total power in the plant among the unit operations. Clearly, the largest duty is reserved for SOEC operations. A large amount of energy is required for steam generation and preheating in the HE1 heat exchanger for SOEC supply. This bottleneck can be reduced if heat-integration is enforced with the cold process streams, as proposed for CASE.FLEX.HI.

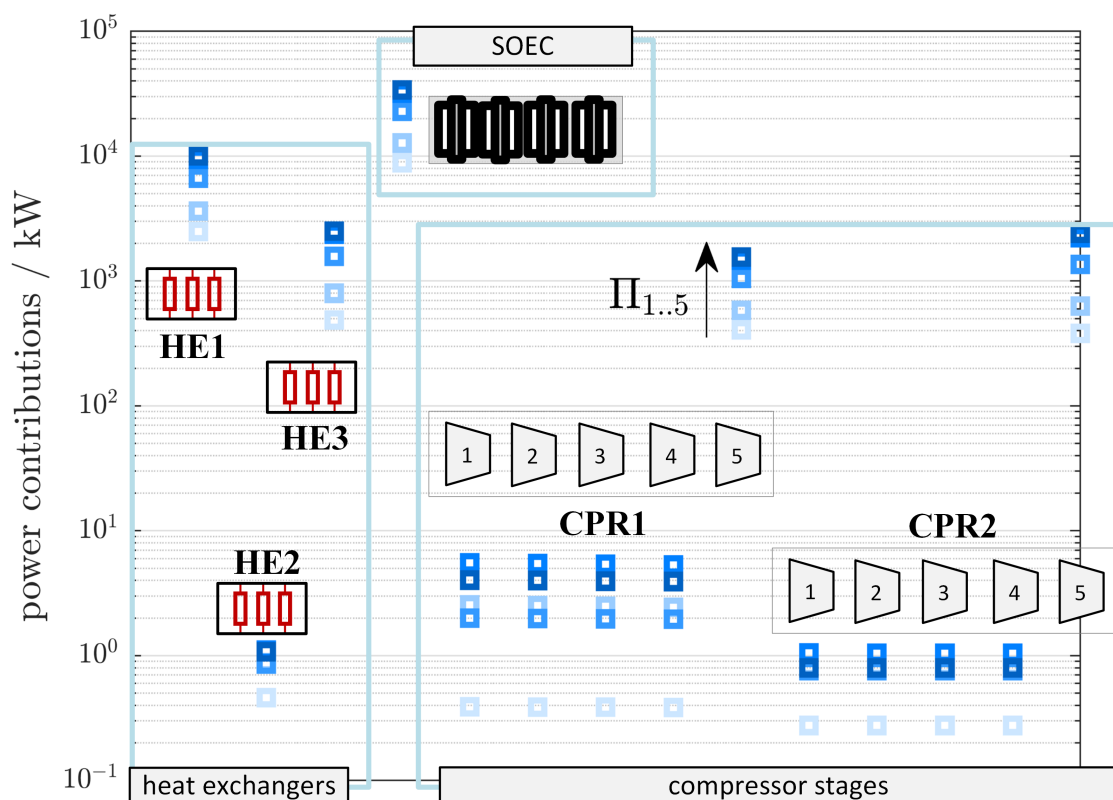


Figure 6.11.: Distribution of the power supplied within the plant, where the darker the blue, the larger the total power load to the plant, as illustrated by the arrow.

The achievable product flowrate from the plant ranges between 33 and 127 ton day⁻¹, where 69 ton day⁻¹ is the annual weighted average productivity. Considering a prevailing selling price of methanol of 580 € ton⁻¹, as in the first quarter of 2022 in Germany, the revenue reads as in Figure 6.12 (A), where the dashed horizontal line refers to average revenue (left y-axis) and average productivity (right y-axis).

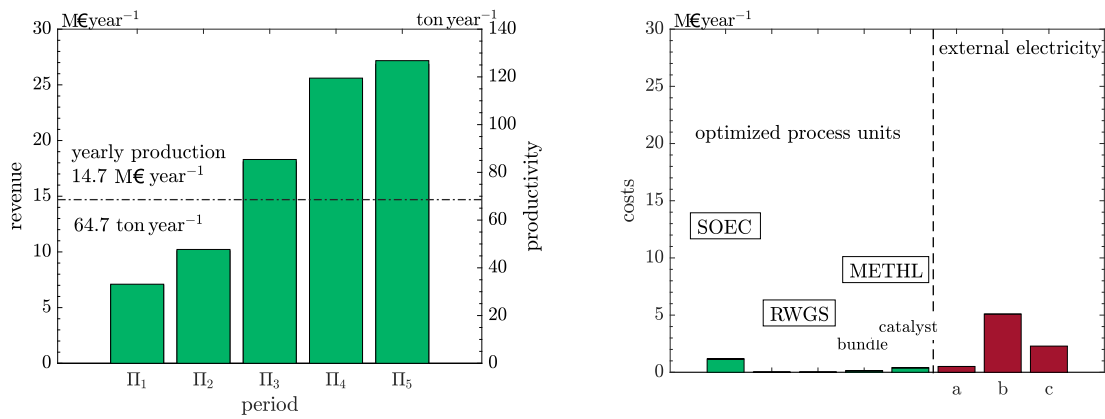


Figure 6.12.: (A) Revenues from the sale of methanol at 580 € ton^{-1} . The results for the period and annual average values are shown as bars and dashed horizontal line, respectively; (B) annualized and actualized costs of the optimized unit operations (green bars), annual cost of external power supply to ensure stable plant operations over the period Π_1 for different scenarios of electricity prices: a (20 €MWh), b (200 €MWh), c (90 €MWh).

Together with the revenues, results identify annualized and actualized installation costs for the optimized unit operations, represented by the green bars in Figure 6.12 (B) and reported in Table D.5. The cost of RWGS is negligible, whereas SOEC accounts for the largest contribution. This also derives from the higher turnover of unit replacement, 2 years, reported in Anghliante et al. [197].

Below the selected power level associated with Π_1 and equivalent to 25% of the maximum power supply, NLP.FLEX failed to identify a feasible solution. This indicates that, for loads lower than \dot{W}_{Π_1} , the constraints cannot be satisfied due to infeasible plant operations. The red bars shown in Figure 6.12 (B) represent the annual cost of external power, integrated to sustain plant operations for period Π_1 under three distinct pricing scenarios. The reason for different electricity prices shall be identified in the following Section in the comparative analysis of the current case-study (integration of external power to the plant) and the results of CASE.BUFF (implementation of electricity or hydrogen buffering, respectively, B.I and B.II).

6.7.2 Results for CASE.BUFF: steady-state operations without heat integration

Electricity (B.I) and hydrogen buffers (B.II) must be sized to ensure steady-state plant operations at the nominal, yearly-averaged power supply of 23.5 MW, despite the fluctuations of the renewable resource. The actual time series of a renewable power provision would allow for the rigorous identification of the maximum amount of electricity to be stored and, consequently, the exact size of buffers. Nevertheless, such level of detail in the sizing procedure is not accounted for, as the methodology and the quality of the comparison between buffering strategies remains essentially unchanged. Instead, the size of buffering devices is determined by the maximum time spent by the

wind park at its maximum power output within a single loading cycle, which is equal to 50 MW, i.e., 27 MW above the design load for the chemical plant. This information allows to estimate the maximum energy stored as $E_{\text{stored}} = 27 \text{ MW} t_{\text{buff}}$, where t_{buff} spans between 0 h and 24 h. Due to a further simplification related to hydrogen buffering analysis (strategy B.II), multi-period design optimization of the sole SOEC unit is neglected, although the electrolyzer should in this case follow the fluctuating trend of renewable power supply. For simplicity, the unit is set to a single load throughout the year.

The cost of lithium batteries is 137 € kWh^{-1} , as reported in Zakeri et al. [198]. In contrast, determining the amount of excess energy is not sufficient to estimate the fixed costs related to the storage of hydrogen. In fact, the surplus is to be shared among three power sinks: the preconditioning of steam at the SOEC (vaporization and preheating), the SOEC electrolysis itself and the compression work for the storage of hydrogen at 300 bar. The sum of precondition and electrolyzer power demand at SOEC is divided by the molar flowrate of hydrogen resulting from the unit to get λ_{SOEC} , which reads:

$$\lambda_{\text{SOEC}} = \frac{\dot{W}_{\text{HE1}} + \dot{W}_{\text{SOEC}}}{\dot{N}_{\text{prod,H}_2}} = 0.3156 \text{ MJ mol}_{\text{H}_2}^{-1}, \quad (6.12)$$

essentially constant for different scenarios, as verified from the analysis of results of NLP.FLEX at different loads. The specific molar compression work to store hydrogen at 300 bar is denoted by $\psi_{\text{compression,300 bar}} = 0.01942 \text{ MJ mol}_{\text{H}_2}^{-1}$. Therefore, the molar flowrate of buffered hydrogen reads:

$$\dot{N}_{\text{buff,H}_2} = \frac{50 \text{ MW}_{\text{peak}} - 23.5 \text{ MW}_{\text{nominal,plant}}}{(\lambda_{\text{SOEC}} + \psi_{\text{compression,300 bar}})}. \quad (6.13)$$

Ultimately, Equation 6.13 defines the amount of hydrogen produced with the maximum excess power, and accounts for the generation and preheating of steam, the SOEC demand and the hydrogen compression duty. Thus, it is possible to calculate the moles of hydrogen stored as a function of the maximum loading time, t_{buff} :

$$N_{\text{buff,H}_2}(t_{\text{buff}}) = \dot{N}_{\text{buff,H}_2} t_{\text{buff}}, \quad (6.14)$$

and on this basis it is possible to calculate compression costs from Timmerhaus (cf. Supplementary Section D.4) and buffer tank installation costs [199]. The tank installation cost, actualized from

2013 and annualized, is $C_{\text{H}_2,\text{tank}} = 1.3 \text{ € mol}_{\text{H}_2}^{-1}$. The final cost, which also accounts for the compressor (the compression power being evaluated as in Equation AE.CPR1.1, AE.CPR2.1, the cost as shown in D.4.3), reads:

$$C_{\text{H}_2,\text{buff}}(t_{\text{buff}}) = C_{\text{H}_2,\text{tank}} N_{\text{H}_2,\text{buff}}(t_{\text{buff}}) + C_{\text{H}_2,\text{compressor},300 \text{ bar}} \quad (6.15)$$

The estimate for the buffering costs given within this framework is shown in Figure 6.13. The size of the buffer increases linearly with the loading time at a total power input of 50 MW. The cost of the compressor is independent on the tank size: it exclusively depends on the excess of power generated by the wind park, constant throughout the domain. The cost of lithium batteries is dramatically higher than the costs of the hydrogen buffering system.

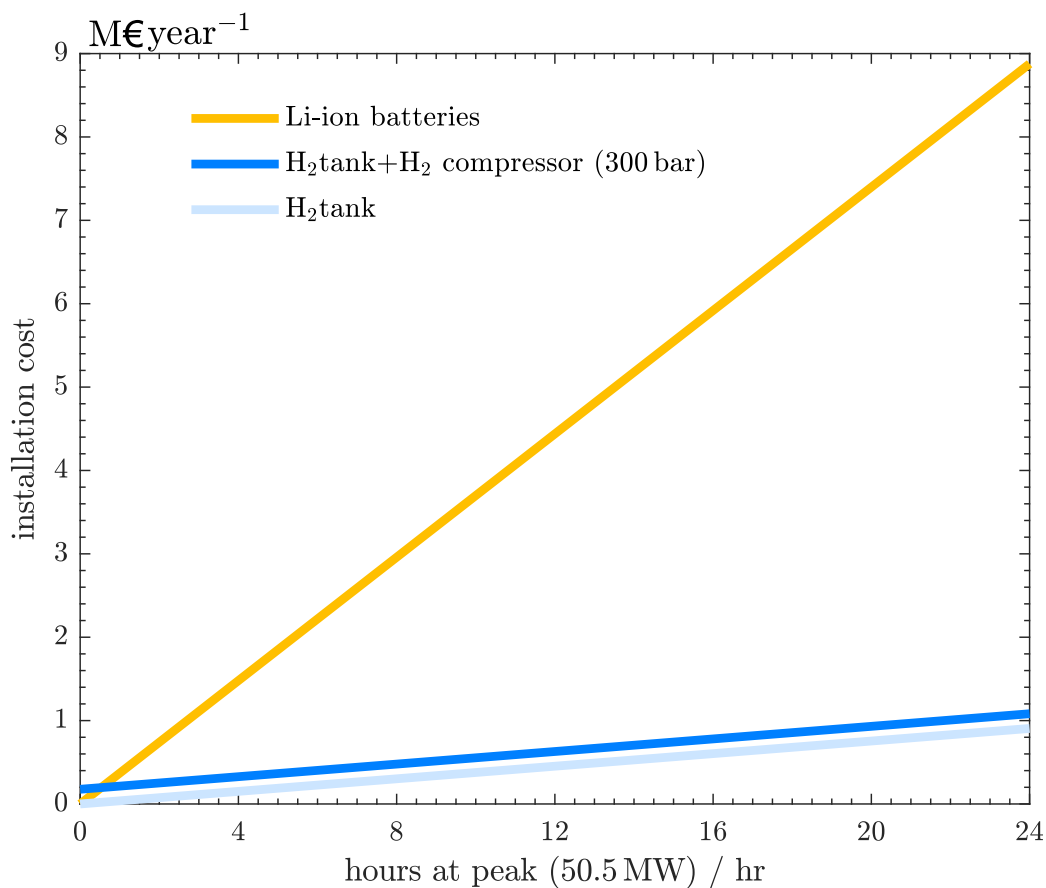


Figure 6.13.: Investment cost for buffering devices, calculated assuming the time (abscissa) spent by the wind park at 50 MW, 27 MW higher than the power absorbed by the methanol plant.

Given the trends in Figure 6.13 and the solution of NLP.BUFF, it is possible to determine topology, investment cost and operating regime of the plant for CASE.BUFF (Tables D.4 and D.5). The

Power-to-Methanol efficiency, 59.2%, lays between the efficiency at Π_2 (59.6%) and Π_3 (58.6%) of CASE.FLEX, reflecting the fact that the nominal load \dot{W}_{tot} for CASE.BUFF, 23.5 MW, is comprised between the load at Π_2 (18.4 MW) and at Π_3 (33.5 MW) for CASE.FLEX.

The SOEC area (3904 m²) is larger than the one identified in CASE.FLEX (2155 m²), although operating temperature and pressure (1000 K, 4.31 bar) are comparable with those identified for Π_1 of CASE.FLEX (period at the lowest power supply, where SOEC temperature and pressure are 1000 K and 4.39 bar, respectively). In contrast, the volume of the METHL for CASE.BUFF (8.22 m³) is smaller than for CASE.FLEX (10.5 m³), as it does not have to withstand the large peaks of feed flowrate attained during the high load periods of CASE.FLEX, where pipes with too small a diameter would lead to excessive pressure drops. Most relevantly, these results offer the tool to ascertain whether buffering strategy F can be more profitable than steady-state plant operations, where either electricity or hydrogen are buffered (B.I and B.II in CASE.BUFF). This particular aspect is dealt with in the next Section.

6.7.3 Role of the external electricity price on the competitiveness of the flexible process

The analysis is now restricted for a loading time comprised between 12 h and 24 h. Figure 6.14 reports the profits for the three buffering scenarios B.I, B.II, F as a function of the loading time. Profits are denoted by superscript *, as they exclude all process elements that are assumed to be in common among the three buffering strategies, e.g., wind park, process fluids compressors (excluding the compressor for the storage of hydrogen), heat exchangers, coolers, piping etc. The linearly decreasing trends are determined by the increasing sizes of the buffering devices (B.I and B.II). The green lines (F) are independent on the abscissas and are identified by different letters (a, b, c), which are related to the red bars in Figure 6.12 (B). These represent three prices of electricity integrated from external sources (grid) to support plant operations at period Π_1 for flexible plant operations (F). If the external electricity is supplied from a delocalized renewable source at 20 €/MWh⁻¹, flexible operations result in a more profitable process candidate. Nevertheless, this price is typical of renewable power plants allocated in the vicinity of the plant, which are therefore not dependent on the grid infrastructure, which might appear as an overly optimistic perspective. As for grid electricity, typical prices can reach and exceed 200 €/MWh⁻¹. In this case, it is clear that the profits from a strategy based on total flexibility are lower than those from buffering hydrogen, although this margin decreases as the buffer size increases. In a third framework c, the maximum electricity price that the company is willing to pay can be outlined against negotiations with the external electricity supplier, so that the flexible approach can be at least as profitable as strategy B.II. For this case-study, this price is 90 €/MWh⁻¹ for 12 h at the peak load.

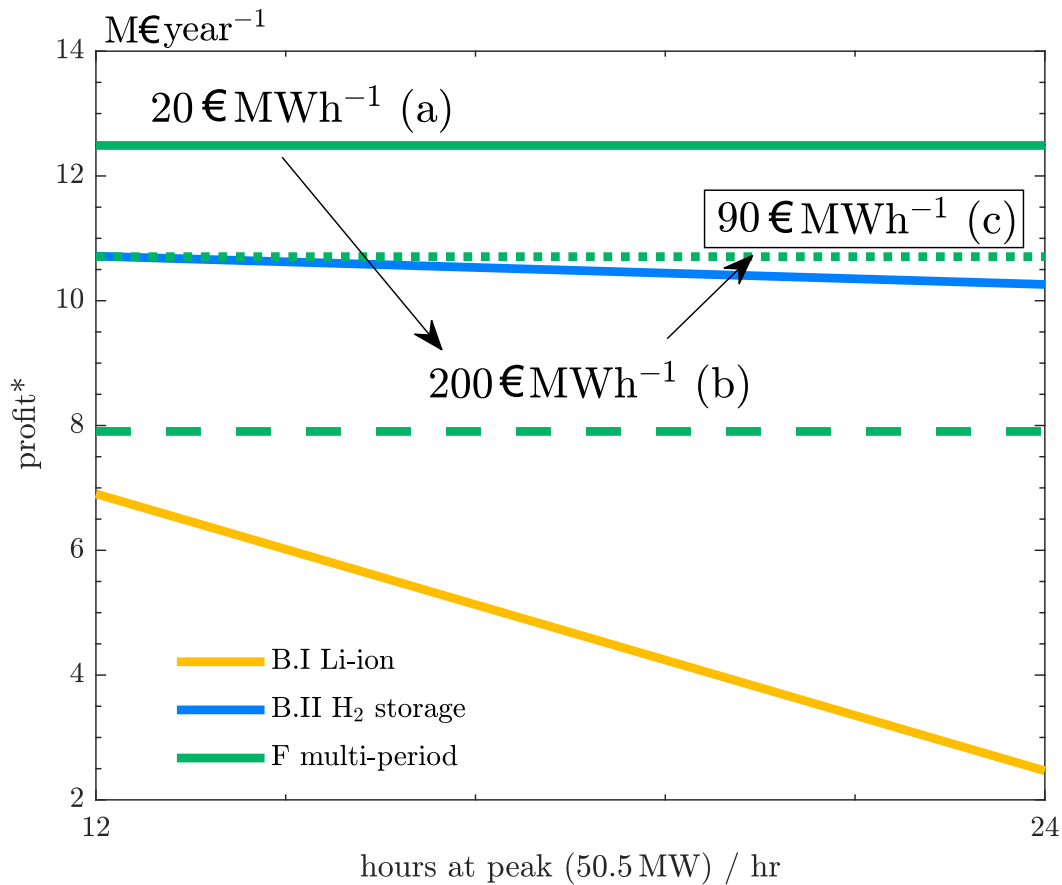


Figure 6.14.: Profit* versus loading time for the three buffering scenarios. The asterisk indicates that these values are built upon the optimized units (SOEC, RWGS, METHL), whereas all other process elements preserve their sizes and costs in the different cases. Profits for lithium batteries and hydrogen storage are inversely proportional to the size of the buffers. The profitability of the flexible setup F is highly dependent on the price of external electricity.

6.7.4 Results for CASE.EFF: maximum efficiency for B.I and B.II, no heat integration

The maximization of Power-to-Methanol efficiency for a plant operated at 23.5 MW – Objective OBJ.EFF.SP. – results in a gain of 3% over the corresponding value for CASE.BUFF at a significantly higher investment cost: the sum of actualized and annualized costs for the optimized units, i.e., SOEC, RWGS, METHL, is 4.6 times higher than in CASE.BUFF, which makes these results inapplicable.

6.7.5 Results for CASE.FLEX.HI: maximum profit with heat integration

Heat integration results in a higher Power-to-Methanol efficiency. Figure 6.15 (A) highlights the period-related gain in efficiency after heat integration: its mean annual value is almost 7% higher than the corresponding value obtained without heat integration (CASE.FLEX). Heat integration also results in a higher cost of the optimized units (SOEC, METHL), although revenues are largely improved. Consequently, the plant configuration with heat integration is more profitable, as shown in the comparison in Figure 6.15 (B).

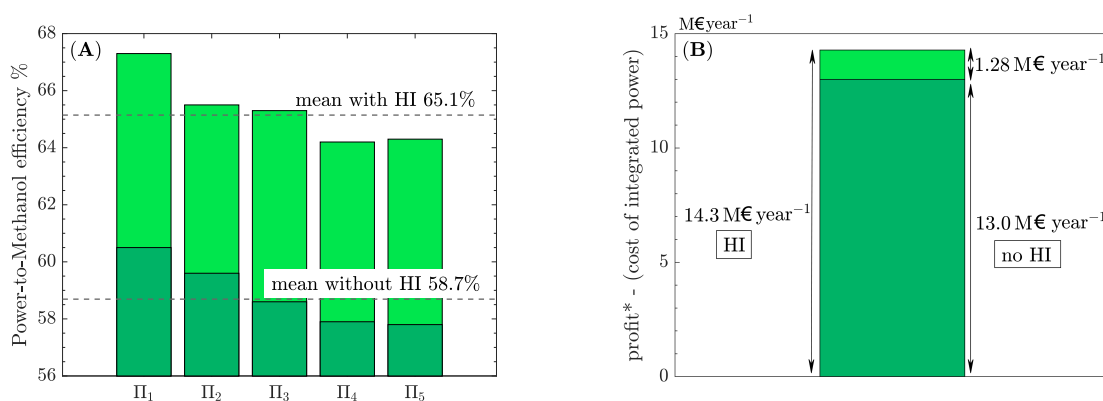


Figure 6.15.: (A) Period-related Power-to-Methanol efficiency in light and dark green with and without heat integration (HI), respectively. Dashed lines depict the annual mean values of efficiency; (B) comparison between pseudo-profits with and without heat integration, not accounting for the cost of the external electricity supply at Π_1 .

6.7.6 Desalination of seawater

Section 6.3 reports on the need for a preconditioned feed stream of water to SOEC. The source of water supplied to the plant influences the assessment of the overall plant energy requirement. Simoes et al. [61] examined the energy demands of different water purification technologies. Seawater offers an unlimited water supply, although its salinity (about 3.5%) imposes the installation of a desalination device (reverse osmosis, RO). Its energy requirement is the highest among the purification technologies reviewed (3-6 kWh m⁻³_{seawater}), and seawater losses occurring along the process reach up to 40%.

Since the purified water is collected in storage tanks before being heated in HE1, it is possible to decouple the energy analysis of a desalination process from the design procedure of a flexible Power-to-Methanol plant. Similarly to the latter, a flexible desalinators may be assumed, which thus follows the fluctuations in the renewable power. Alternatively, nominal, yearly-averaged operations can be ensured by means of a battery for electricity storage.

The flexible, heat integrated methanol plant (CASE.FLEX.HI) processes a annual average flowrate of purified water of $\sum_{j \in \{1, NP\}} \omega_j \dot{N}_{j, H_2O} = 84 \text{ mol s}^{-1}$. Accounting for seawater losses (40%), salinity (3.5%) and density (1028 kg m^{-3}), the total volumetric flowrate of processed seawater amounts to $2.558 \times 10^{-3} \text{ m}^3 \text{ s}^{-1}$. Consequently, a RO desalination device requiring $6 \text{ kWh m}_{\text{seawater}}^{-3}$ has to adsorb 55.24 kW and to be dimensioned accordingly. On the contrary, if flexibly operated, RO would have to withstand a peak power input of 101 kW , relatable with the maximum water intake for the flexible methanol plant (154 mol s^{-1}).

All this considered, the renewable power plant must ensure the production level by means of an additional wind turbine generating at least 0.1 MW at nominal regime, a negligible amount in comparison with the nominal power supplied to the methanol plant 50 MW .

6.8 Discussion

In the former section, results from the case of total flexibility (CASE.FLEX) were compared with buffering of electricity and hydrogen for steady-state operations (CASE.BUFF and CASE.EFF) due to the fact that fixed costs decrease proportionally with the size of buffering devices. As shown, negotiating on the price of the integrating external electricity supply for the low-load period Π_1 is the key to allow for a potentially competitive flexible process which does not resort to buffering devices. The relation between costs of different buffering strategies can be visualized qualitatively in Figure 6.16, where total and buffering costs of a generic P2X process are function of the extent of its flexibility.

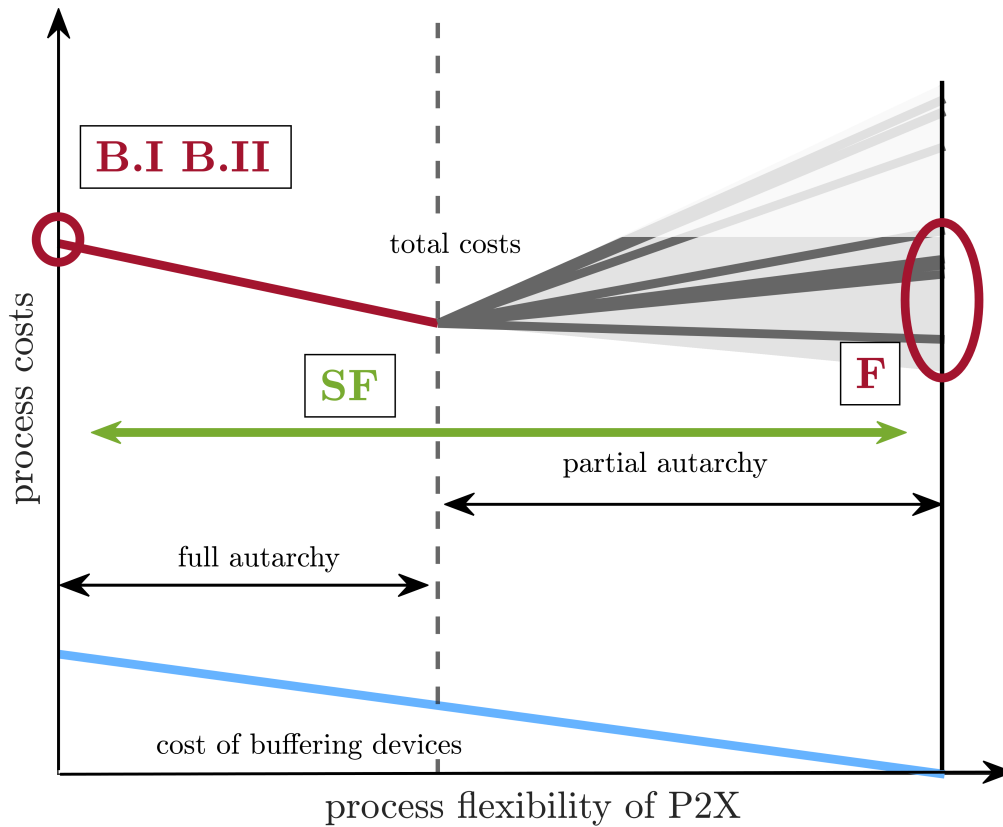


Figure 6.16.: Qualitative trend of process costs as a function of process flexibility for a generic Power-to-X system: flexible regime (F), Li-ion batteries and hydrogen buffering (B.I, B.II), semi-flexible plant (SF). The red line identifies costs in a regime of energy autarchy, where the renewable power is entirely produced and consumed within the chemical plant. Further to the right, the plant requires an external power input, as renewable power is not sufficient to support feasible operations. The costs of buffering devices are reported in blue.

At the origin of the abscissa, the process is operated at a nominal load throughout the year with large buffers (strategies B.I and B.II) in full energy autarchy, i.e., solely relying on the renewable power produced within the plant limits. Conversely, at the end of the abscissa, buffering devices are absent and the total cost is determined by the price of the complementary external electricity supply (strategy F). From the comparison with the single-period results in B.I and B.II, the maximum electricity price which plant owners should aim for during negotiations for a flexible, non buffered plant (F) is identified, as highlighted earlier in Section 6.7.3. If such price were not to be attained, intermediate solutions with small buffering devices and semi-flexible operations may be selected. This allows to run the plant with more expensive external electricity integrated at low-load (period Π_1), in partial energy autarchy and semi-flexible plant operations (denoted in the figure by a green arrow and labeled as strategy SF). The design of the P2X system should then be repeated for a reduced feasibility gap, implementing once again the multi-period design optimization approach highlighted in this chapter.

6.9 General remarks and outlook

The methodology presented in this work on multi-period optimization requires the formulation of a large NLP problem constrained by a number of replicas of steady-state modeling equations of the entire P2X production process. Operation variables resulting from the multi-period solution constitute set-point values which the plant attains to ensure optimal operations for the given period, i.e., power load. Nevertheless, the current multi-period optimization framework does not provide any information on how to manage the transition between different loads. Instead, if the time-scale to attain a new set point is comparable to the time of dynamic effects, an optimal control approach based on dynamic models should be formulated and solved in order to identify the fastest transition procedure and control values. Furthermore, a finer discretization of the power curve reported in Figure 6.5 would allow for a more accurate selection of design variables, as well as a more thorough overview of the range of set points to be attained during actual operations. Nonetheless, the number of discretization points is limited by the size of the problem and the machine used for the computations. A test with a purely parametric objective determined that 12 is the largest attainable number of periods for the given solver and modeling approach, although optimization results are reported for 5 periods: this allows a more agile workflow, which enables the NLP to be constructed by the solver in a reasonable time, about 15 min. Model order reduction (MOR) could allow, in a future application, a better approximation of the power curve by allowing the addition of more periods, without losing in modeling accuracy.

6.10 Chapter summary

This second chapter on process flexibility completes the discussion which addresses how the inherent intermittency of renewable power affects design and operation of a power-to-syngas plant (Cf. Question 3 in Section 1.3). In particular, by means of an effective CAPE tool (multiperiod design optimization), the chapter explores the profound implications that intermittent renewable power introduces into the analysis and selection of a suitable plant design in terms of sizing and operating policies within the feasibility ranges.

A novel multi-period optimization application is proposed to design and operate a flexible, highly electrified plant for the production of methanol from in-house generated fluctuating wind electricity. In contrast to the prevailing literature in the field of multi-period optimization of P2X systems, distributed models and detailed non-ideal gas relations constrain the nonlinear programs, which thus preserve a high fidelity representation of the system as a whole and ensure the feasibility of the identified design solutions. The conversion steps involved are SOEC-based water electrolysis, carbon monoxide generation in a reverse water-gas shift adiabatic reactor, and the methanol reactor. Side reactions are included in the kinetic models. In addition, two aspects carry significant consequences in the decision-making: the electrification of the entire process and the general purpose of P2X systems, which is to store fluctuating energy in chemical bounds without allowing

surplus energy. These key aspects introduce a relevant extent of interconnection between process units: they cannot be optimized separately prior to overall plant evaluations. Therefore, all process elements in the plant are simultaneously incorporated in the design optimization process. At the same time, process constraints, operation variables and states are replicated for five periods, approximating the power curve of the renewable power plant on an annual basis.

Firstly, a highly flexible plant designed in compliance with multi-period optimization results can compensate for the absence of buffering devices, provided that at low loads the process is supplied with integrated external power. In terms of topology, RWGS is never selected by the optimizer, although the presence of carbon monoxide in the recycle loop is beneficial to the methanol reaction kinetics. This is because the RWGS contribution occurs in the methanol synthesis step. Other kinetics that do not support the RWGS reaction may require this step to be present upstream of the synthesis reactor. Besides, SOEC operations and steam generation at its feed determine the highest power demand. Consequently, profitability and Power-to-Methanol efficiency are increased via heat integration, thus recovering thermal power within the plant.

The resulting process design represents the most cost attractive and technically feasible compromise across periods, which provides a valid benchmark to single-period optimization solutions. Here, plant design and operation variables are then identified based on this single yearly-averaged power supply. Large buffers for the storage of electricity and hydrogen are assumed. This comparison enables to address the final fundamental Question 4 in Section 1.3 presented in the introduction of this research work: "what is the trade-off between buffering and process flexibility?". Discussions highlighted how a highly flexible, non-buffered plant can be competitive with a buffered solution if the maximum threshold for the price of externally integrated power to sustain the plant base-load is identified and attained by negotiation. Intermediate process solutions with small buffers and moderate flexibility may offer interesting process candidates that can be identified using the same methodology for a narrower feasibility window. Such intermediate solutions are the only opportunity to benefit from flexible plant operations in remote locations, where grid power is not accessible and the plant relies exclusively on the local renewable sources, either produced by the plant itself or purchased by a different supplier which can ensure continuity in the supply.

Conclusions and impact of the thesis

The thesis aimed at the performance evaluation of Power-to-Syngas processes, optimized by means of novel methodological approaches applied to process synthesis, design and operations based on green feedstock and energy supply. Throughout this work, focus was attributed on the efficient utilization of energy and resources, whereas fixed costs have been introduced exclusively to support the methodological development and to formulate high-level statements about system load flexibility in the final chapter, which is dedicated to plant sizing and buffering policies. Chapter 1 highlighted the importance of computer-aided process engineering to assist decision-making in the course of a project, from the selection of technologies, to sizing and operation of new unit operations (retrofitting) or entirely new process systems. Mathematical tools and modeling approaches need to be adapted or newly developed to meet the needs imposed by the challenges of limited and fluctuating renewable resources, which are substantiated by the four fundamental questions formulated in Section 1.3.

To readily meet the emission reduction objectives, existing plant traditionally relying on fossil resources can be retrofitted to allow for the switch to sustainable feedstock and energy supply. This is reflected in the first fundamental research question, which sets its objective in the identification of energy and carbon efficient process topologies of a steam-reforming plant, revamped with a water electrolyzer and a reverse water-gas shift reactor in the first chapter dedicated to process synthesis. Degree of freedoms in the separation sequences after RWGS are allowed. Multi-objective optimizations to minimize total energy and absolute carbon emissions identified Pareto front of solutions that represent multiple optimal setpoints. The plant can switch from one to the other depending on the availability of renewable electricity and biogas, provided that load flexibility is technically feasible within the time window of resource intermittency. In particular, maximum electrification and minimum biogas utilization are achieved when the reverse water-gas shift reactor is implemented with the water electrolyzer and in the presence of an external source of CO_2 complementing the biogas supply, while different levels of integration between the pre-existing steam reforming, reverse water-gas shift and electrolysis ensure lower overall energy consumption levels, but require significantly more biogas as feedstock and additional biogas or fossil natural gas to meet the required heat demand. The optimal separation sequence recycles the binary mixture (CO_2, H_2) back to the RWGS inlet after condensation, membrane dehydration and vacuum pressure swing adsorption for the separation of CO. From a methodological perspective, this separation sequence represents the state-task network approach, where a single separation method corresponds to a given separation task. However, this selection is not exhaustive, as alternative separation methods may be available for a single task. This remark is directly translated

into the second fundamental question expressed in Section 1.3 and addressed in Chapter 4, the second chapter dedicated to process synthesis, where energy was minimized, assuming that biogas, a limited resource, should not be used to thermally sustain strongly endothermic processes such as steam and dry reforming. Here, the total energy (electric and thermal) was minimized in a scenario where renewable electricity is not available, whereas exclusively thermal energy is penalized where carbon-free green electricity is supplied. Results show that VPSA, membrane and cryogenic separators prevail over scrubbing and TSA (selected exclusively for hydroformylation) in all relevant scenario-settings. Combinations of reformers and electrolysis suggested viable solutions, where the electrification comes at high energy costs. In particular, partial oxidation processes normally run in air may be more conveniently fed by pure O₂ from water electrolysis, thus determining lower inert contents in the separation train and downstream conversion processes. Furthermore, the simultaneous valorization of both outlets of a water electrolyzer suggests a promising path towards an increased atom efficiency, provided that flexible operations and a certain extent of buffering is ensured. This approach was investigated under a dynamic scenario setting in Chapter 5 for the generation of a stream of syngas suitable for the Fischer-Tropsch synthesis, where a water electrolyzer, RWGS and a tri-reformer operated in adiabatic mode in pure O₂ are implemented.

Chapter 5 belongs to the second part of this thesis dedicated to process flexibility, where the remaining fundamental questions in Section 1.3 are addressed. How can a highly electrified system be sized and operated to account for the fluctuations in renewable energy?

The first study in Chapter 5 constituted an engineering benchmark for the performance evaluation of a fast optimal control approach and hinted at the need of a rigorous design for the plant, ensuring that feasible operations and optimal performances are attained in load-changing regime. This was eventually contextualized in Chapter 6 on multi-period design optimization of a flexible Power-to-Methanol plant. The methodology here presented is an extension of optimization approaches on simplified plants representations for scheduling problems and for single unit operations, now proposed for the entire plant. As a matter of fact, an extension of the method to the detailed representation of the overall system is required to account for the strong interdependency of different unit operations, a consequence of efficiently distributing the available, intermittent renewable power between highly electrified units, thus without any surplus.

This identifies the optimal rigorous plant design and set-points for the operations at changing loading regimes, concluding that the extent of flexibility allowed is not only constrained by the technical feasible region, but may be further limited by the purchase price of additional electricity below the minimum admissible load, thus preventing from cyclic plant shutdowns. In the case study, external electricity should not be purchased at a price higher than 90 € MWh⁻¹ to run a competitive flexible process without buffering devices. This sort of analysis may provide with reasonable steps for Power-to-X projects in the future, as multi-period optimization could be implemented for detailed full-plant descriptions, and thus for the systematic exploration of intermediate flexibility windows at a certain extent of buffering, possibly offering more profitable

options than in extreme-case scenarios. Such investigations would have to rely on project-related relevant information, e.g., the actual temporal trend in renewable energy supplies, the limitations in supply-chain flexibility and locally available feedstock, the detailed models and actual cost forecast of commercial units involved for the determination of feasible operating regimes.

In conclusion, this thesis has highlighted the profound impact that the nature of renewable energy has on the way we should synthesize, design and operate chemical plants, and aimed at contributing to the methodological development of relevant CAPE approaches. The multitude of process options and the high degree of interconnection that intermittent renewable power implies introduces the need for holistic approaches in the identification of best process candidates and in their fine design and operations, respectively. Optimization tools can ensure rational and feasible solutions in the context of the urgent problems we are called to face nowadays, not only to promptly retrofit existing processes, but also to identify new, non-intuitive plant concepts and to design and operate flexible systems.

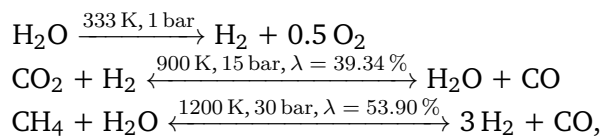
Appendix A

Supplement to Chapter 3

A.1 Equilibrium reactors and condensers

Conversion steps are fed with stoichiometric mixture. The extent of progression at equilibrium is indicated in percentage (λ , reported on the reaction arrow).

The chemical relation for EL, RWGS and SR read, respectively:



The ratio $\chi_{\text{H}_2\text{O}}$ between the flow rate of condensed water and the feed rate to the condenser reads:

$$\chi_{\text{H}_2\text{O}} = 1 - \frac{(z - 1)p^\circ}{(p^\circ - p)z}, \quad (\text{A.1})$$

where z denotes the molar fraction of water in the feed, p° the vapor pressure at the condensation temperature (ambient), p the preceding reactor pressure.

A.2 Modeling of surplus methane

Surplus CH_4 from the system is what remains after the combustion of surplus CH_4 from the process lines (synthesis):

$$\dot{N}_{\text{CH}_4, \text{surplus, system}} = \dot{N}_{\text{CH}_4, \text{surplus, synthesis}} - \dot{N}_{\text{CH}_4, \text{surplus, burned}}, \quad (\text{A.2})$$

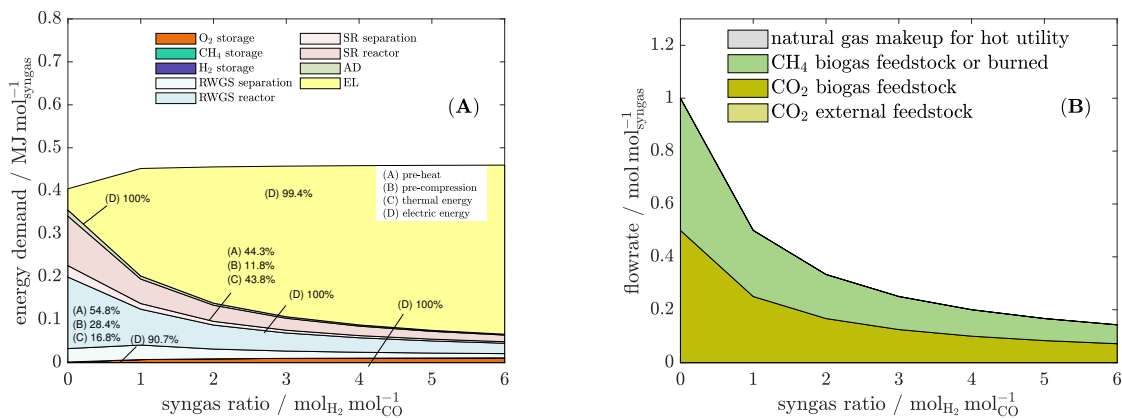
CH₄ burned shall not exceed CO₂ generated by all thermal contributions:

$$\dot{N}_{\text{CH}_4, \text{surplus, burned}} \leq \dot{N}_{\text{CO}_2, \text{th, tot}} \quad (\text{A.3})$$

Thus, the biogenic CO₂ generated from combustion of bio-CH₄ can be admitted into the feedstream node balance as makeup CO₂.

A.3 Inclusion in the objective function of CO₂ recycling stream from combustion gases

Figure A.1(A-F) report the whole set of results for the minimization of CEabs, including the recycle of bio-CO₂ from the hot utility exhaust gases back as reactor input. Figures (A,B) at $\omega = 0$, (C,D) $\omega = 1$, (C,D) at intermediate values of ω . The pseudocost ω has been discretized with 100 points, in all optimization cases. At the boundaries values of ω which identify a given process configuration, the discretization grid has been refined to identify possible intermediate configurations, not found.



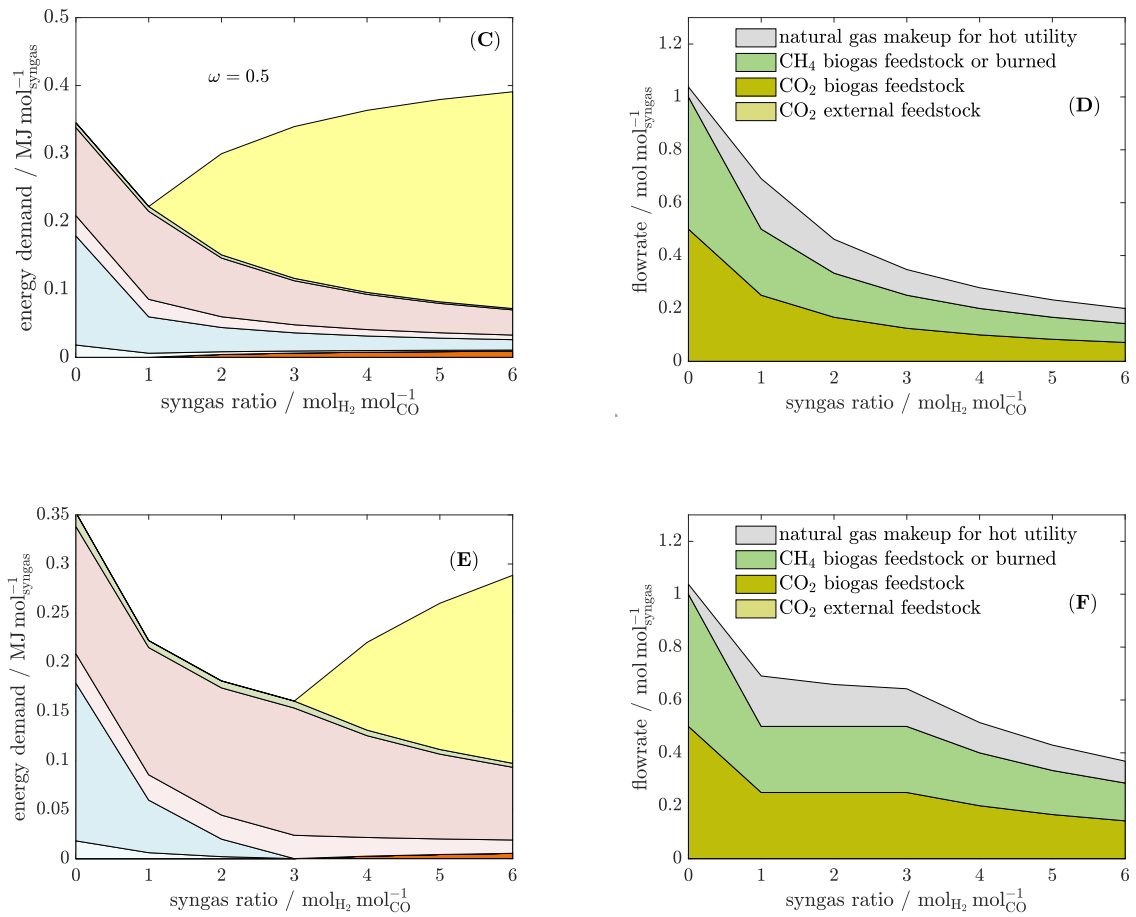


Figure A.1.: Complete results: minimization of CEabs, including the recycle of bio-CO₂ from the hot utility exhaust gases.

Appendix B

Supplement to Chapter 4

B.1 Modeling of interconnections between separators and component nodes

This supplementary section reports details for the modeling of the superstructure proposed in Chapter 4.

B.1.1 Interconnection of consecutive mixture blocks

Following the nomenclature introduced in Section 4.5.1, a generic stream $j \in J_1$ appearing in equations set Φ_1 for a given mixture ϕ_1 is then split in two outlets by the separator it supplies. These outlets constitute two new mixtures ϕ_2 and ϕ_3 , in turn associated with the sets of equations Φ_2 and Φ_3 , respectively. The three mixture blocks, ϕ_1 , ϕ_2 , ϕ_3 , must now be interconnected. The interconnection is ensured by means of two equality constraints, stating that stream \dot{N}_{j,ϕ_1} leaving mixture block ϕ_1 coincides with feed streams $\dot{N}_{i=1,\phi_2}$ and $\dot{N}_{i=2,\phi_3}$ feeding mixture blocks ϕ_2 and ϕ_3 , respectively, where it is implied that the given separator is named $i = 1$ in mixture block ϕ_2 and $i = 2$ in mixture block ϕ_3 . The block-connecting constraints read, respectively:

$$\dot{N}_{j,\phi_1} - \dot{N}_{i=1,\phi_2} = 0, \quad (\text{B.1})$$

$$\dot{N}_{j,\phi_1} - \dot{N}_{i=2,\phi_3} = 0. \quad (\text{B.2})$$

Figure B.1 illustrates the case. With such constraints, mass and energy balances related to all mixtures produced along the separation sequence are thus concatenated.

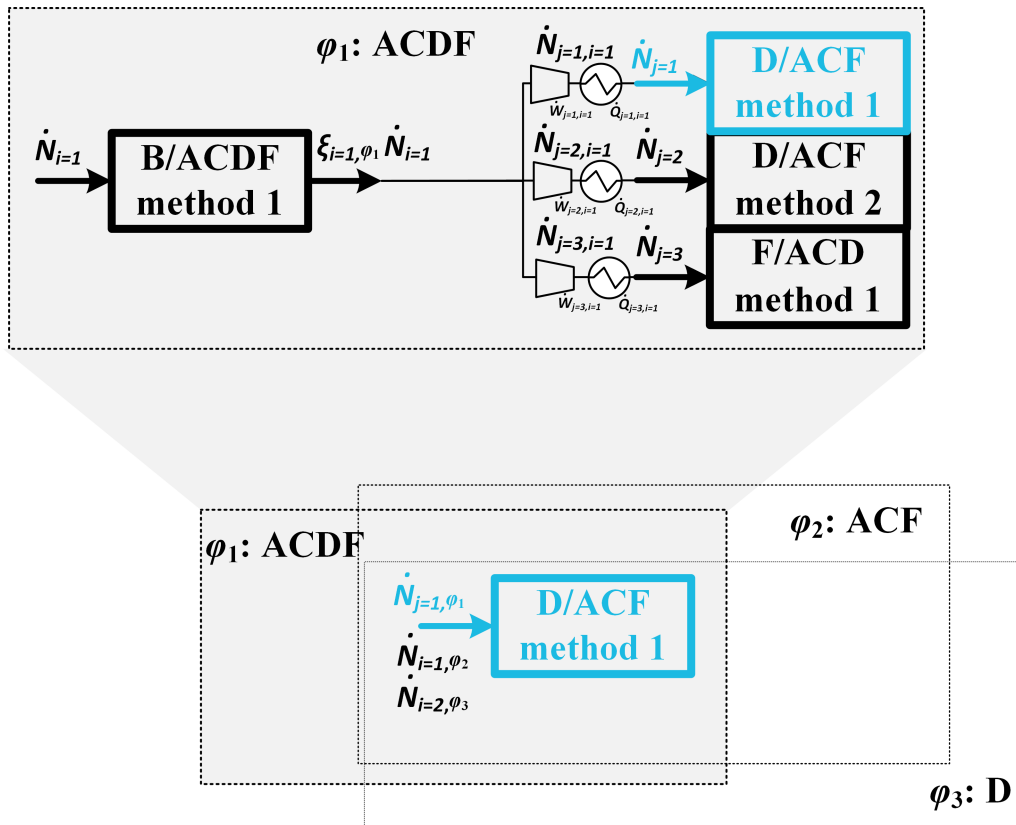


Figure B.1.: Compact representation of the interconnection between consecutive mixture blocks. In blue, the separator which delivers ACF to block ϕ_2 and D to block ϕ_3 .

B.1.2 Replicas of downstream separation systems

Separators involved in the downstream of a number of reformers are replicated in each downstream sequence within the superstructure. Furthermore, replicas of the same separator do not contribute within the same mixture block to Equations 4.22, 4.23, 4.24, and 4.25 belonging to a given mixture-block set Φ . This is illustrated in panel (A) of Figure B.2, where separator D/ACF is shared between two separation sequences after reactor R1 and R2.

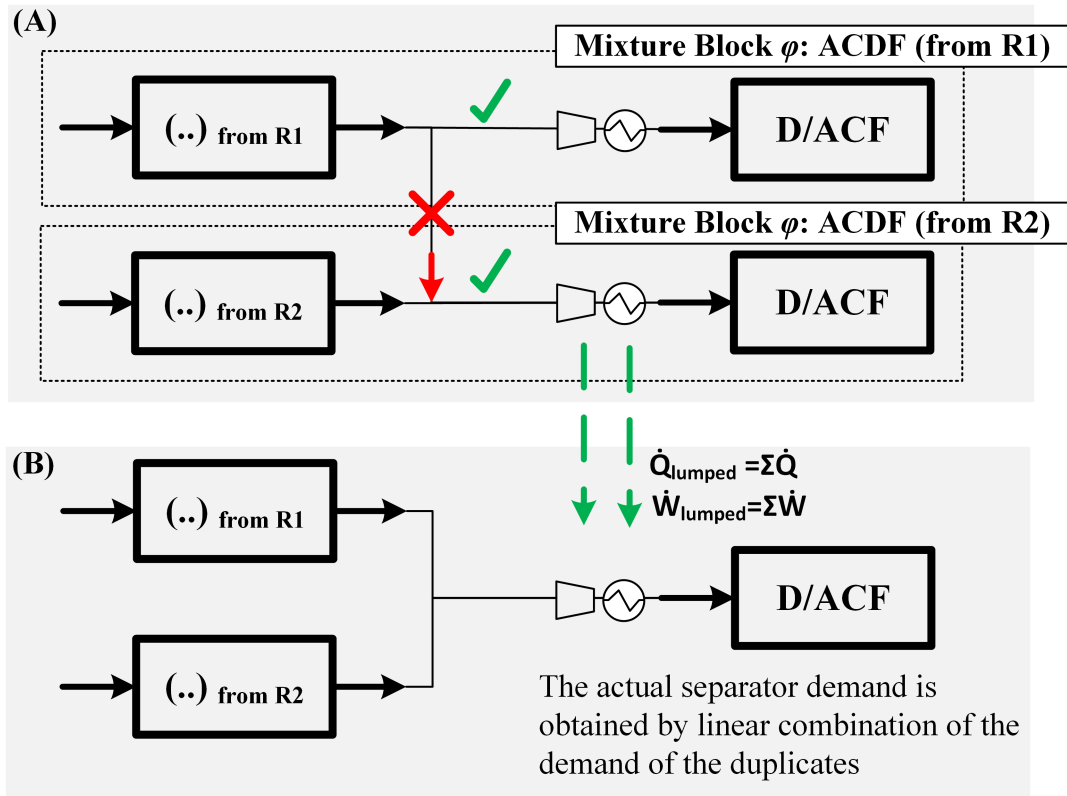


Figure B.2.: (A) separator D/ACF is replicated in the downstreams of reactor R1 and R2, not interconnected by any material stream; (B) if both separators are selected simultaneously by the optimizer, the resulting energy demand is obtained from the linear combination of single contributions, and the system is equivalent to a lumped representation.

The forbidden intersection marked in red would convert split factors $\xi_{D/(A,C,D,F)}$ and $\xi_{C,D,F/(A,C,D,F)}$ into system variables, function of the extent of mixing at the node indicated by a red arrow. Therefore, Equation 4.11 becomes nonlinear as the whole optimization set up.

Panel (B) highlights that replicas of the same separator in the superstructure, when simultaneously selected, approximate the energy demand of a lumped separator by linear combination of single linear contributions in Equation 4.24 and 4.25:

$$\dot{Q}_{D/ACF,lumped} = \sum_{\delta \in \Delta} \tilde{q}_{D/ACF,\delta} \dot{N}_{D/ACF,\delta}, \quad (\text{B.3})$$

$$\dot{W}_{D/ACF,lumped} = \sum_{\delta \in \Delta} \tilde{w}_{D/ACF,\delta} \dot{N}_{D/ACF,\delta}, \quad (\text{B.4})$$

where set Δ includes all reactor downstreams which share the separator. Additional energy demands discussed in Section 4.4.7 for the single methods are treated similarly, as they are also linear functions of the flowrates.

All this considered, although the superstructure of the separation system after each reactor is a network representation of the candidates, it is formally a tree-representation in terms of reactor-separator sequences: duplicates of separation trains follow different reactors which produce the same outlet mixture.

B.1.3 Substance nodes

Figure B.3 is a schematic representation of the substance-node balances at the reactors inlets, reporting nomenclature and indices for this section. Each chemical component is associated with a number of nodes that equals the number of reactors included in the superstructure. Reactors constitute set J . The substance node balance reads:

$$\dot{N}_{i,\text{ext}} - \sum_{j \in J} \dot{N}_{i,j}^{\text{makeup}} = 0. \quad (\text{B.5})$$

Equation B.5 indicates that component i can be delivered to any j^{th} reactor $\in J$ by means of a *makeup* stream, then preconditioned to attain pressure and temperature requirements at the reactor. Furthermore, for each reactor j and component i , a constraint is enforced to relate the feed to recycle and makeup streams:

$$\dot{N}_{i,j}^{\text{makeup}} + \sum_{k \in K} \dot{N}_{i,j,k}^{\text{recycle}} - \dot{N}_{i,j}^{\text{feed}} = 0, \quad (\text{B.6})$$

where $k \in K$ is a generic unit which separates pure i and recycle it back to the reactor feed.

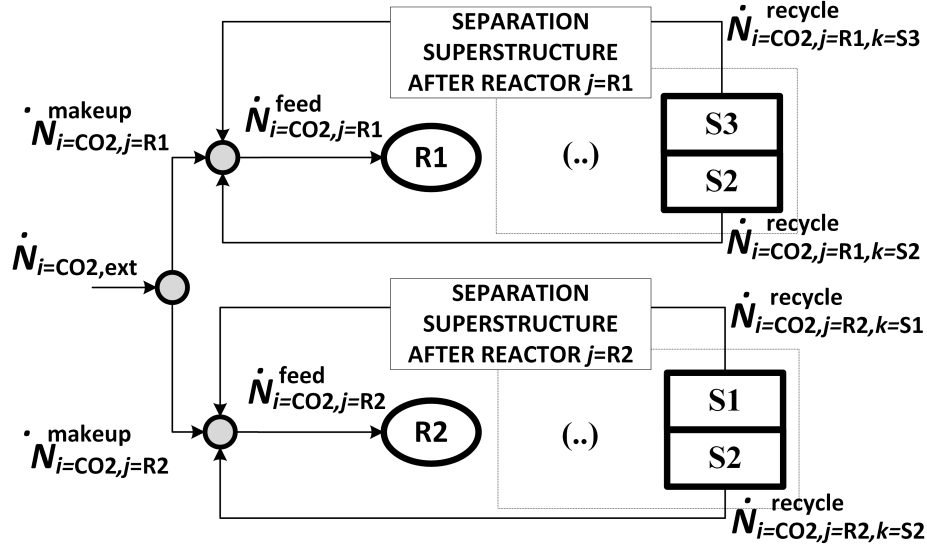


Figure B.3.: Representation of the substance-node balance associated to component $i = \text{CO}_2$ fed to the overall plant superstructure. Stream $\dot{N}_{i=\text{CO}_2,\text{ext}}$ is split into streams $\dot{N}_{i=\text{CO}_2,j=\{\text{RWGS,TRI},(\dots)\}}$, each contributing to the feed to reactor j : $\dot{N}_{i=\text{CO}_2,j}^{\text{feed}}$. Recycle component-streams $\dot{N}_{i,j,k}^{\text{recycle}}$ from the final separators along separation superstructure networks (here S1, S2 and S3) are also fed to these feed nodes.

B.1.4 Outlet and syngas nodes

As previously discussed in Section 4.3, excess H_2 and CH_4 can leave the plant after pressurization, whereas excess CO_2 , O_2 and H_2O can be released without any conditioning step. As surplus CO is not admitted, it is excluded from the set of components possibly released from the plant. For each component $i \neq \text{CO}$ leaving the plant, a node balance is introduced:

$$\sum_{o \in O} \dot{N}_{i,o} - \dot{N}_{i,\text{out}} = 0, \quad (\text{B.7})$$

where O is the set of process-units which produce or separate component i , which then leaves the plant. Similarly, the following syngas node balances are required:

$$\sum_{j \in J} \dot{N}_{\text{CO},\text{syngas},j} - \dot{N}_{\text{CO},\text{syngas}} = 0, \quad (\text{B.8})$$

$$\sum_{k \in K} \dot{N}_{\text{H}_2,\text{syngas},k} - \dot{N}_{\text{H}_2,\text{syngas}} = 0, \quad (\text{B.9})$$

$$\dot{N}_{\text{H}_2,\text{syngas}} - \psi \dot{N}_{\text{CO},\text{syngas}} = 0, \quad (\text{B.10})$$

where, in Equation B.8 and B.9, set J and K group all units which produce or separate pure CO and H₂, respectively.

Finally, Equation B.10 sets the syngas ratio to the desired value for downstream applications.

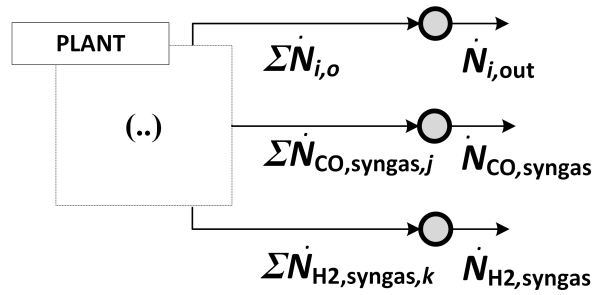


Figure B.4.: Representation of the outlet node balance for a generic component $i \neq \text{CO}$ and of the syngas nodes, for H₂ and CO. Streams of pure i provided by different units in the superstructure are collected into the outlet stream $\dot{N}_{i,\text{out}}$. Similarly, H₂ and CO streams from the superstructure to syngas are collected into $\dot{N}_{\text{H}_2,\text{syngas}}$ and $\dot{N}_{\text{CO},\text{syngas}}$, respectively. References are found in Equations B.7, B.8 and B.9. The syngas ratio is constrained via Equation B.10.

Appendix C

Supplement to Chapter 5

C.1 Process synthesis

Table C.1 reports the topological results obtained by enforcing that the minimum total energy is resulting from setting a maximum of 9 unit operations: 3 reactors (RWGS, TRI and AD-anaerobic digester), 4 separators for the downstream of TRI (5 components mixture), at most 3 separators after RWGS, and one separator for the upgrade of the biogas (CH_4, CO_2) mixture, possibly shared with the downstream of TRI, i.e., if one method in the downstream of TRI for the separation task CO_2/CH_4 is selected, logical constraints impose that the same will also be selected for biogas upgrade. Together, they constitute a single unit adding up to at most 9 unit (upper limit set for the complexity of the plant). Due to the feature of this superstructure optimization method, the downstream of RWGS and TRI cannot be merged as they do not share the same components in the feed mixture. Hence, from a methodological perspective, although a 4-components mixture (RWGS outlet) may share the same species with a 5-component mixture (TRI outlet), and from a technical perspective a single separator could accept both feeds, these units will be regarded as standalone systems in the computation of plant complexity, thus contributing to 2 units. Therefore, results need to be critically evaluated to address additional redundancies.

Table C.1.: Plant topology and power consumption for combined tri-reforming, reverse water-gas shift reactor and water electrolysis.

(a) $\min_{N,y} (\dot{Q} + \dot{W})$		
Reactor	Separators	Type
TRI	$(\text{H}_2\text{O})/(\text{CO}_2, \text{H}_2, \text{CO}, \text{CH}_4)$	VI (polymeric membrane)
	$(\text{CO})/(\text{CO}_2, \text{H}_2, \text{CH}_4)$	V (VPSA)
	$(\text{H}_2)/(\text{CO}_2, \text{CH}_4)$	V (VPSA)
AD, TRI	$(\text{CO}_2)/(\text{CH}_4)$	VI (membrane)
RWGS	$(\text{H}_2\text{O})/(\text{CO}_2, \text{H}_2, \text{CO})$	VI (polymeric membrane)
	$(\text{CO}_2)/(\text{H}_2, \text{CO})$	V (VPSA)
	(H_2, CO)	directly to the product

In Table C.1 it can be noted that membrane separators for dehydration (highlighted in blue) can be performed in the same unit operation without expecting technical issues. Therefore, the first separator in RWGS train shall not constitute an additional CAPEX expense. Furthermore,

the ternary mixture in the retentate of this membrane separator after RWGS can be processed similarly by the two VPSA in the TRI train, as all components but CH₄ are shared. Thus, the PSA (CO₂)/(H₂, CO) after RWGS (highlighted in red) is redundant and shall be disregarded from the final topology presented in Chapter 5. The final topology consisting of 6 units is then reported in Table C.2.

Table C.2.: Plant topology and power consumption for combined tri-reforming, reverse water-gas shift reactor and water electrolysis.

(a) $\min_{N,y} (\dot{Q} + \dot{W})$		
Reactor	Separators	Type
TRI,RWGS	(H ₂ O)/(CO ₂ ,H ₂ ,CO,CH ₄)	VI (polymeric membrane)
	(CO)/(CO ₂ ,H ₂ ,CH ₄)	V (VPSA)
	(H ₂)/(CO ₂ ,CH ₄)	V (VPSA)
AD,TRI	(CO ₂)/(CH ₄)	VI (membrane)

C.2 Reaction rates for tri-reforming of methane

The parameters [170] are reported in Table C.3. The governing kinetic expressions are

- $$\text{DEN} = \left(1 + K_{\text{CO}} p_{\text{CO,bar}} + K_{\text{H}_2} p_{\text{H}_2,bar} + K_{\text{CH}_4} p_{\text{CH}_4,bar} + K_{\text{H}_2\text{O}} \frac{x_{\text{H}_2\text{O}}}{x_{\text{H}_2}} \right),$$
- $$R_{\text{SR}} = 10^3 \frac{k_{\text{SR}}}{p_{\text{H}_2,bar}^{2.5}} \frac{\left(p_{\text{CH}_4,bar} p_{\text{H}_2\text{O,bar}} - p_{\text{H}_2,bar}^3 \frac{p_{\text{CO,bar}}}{K_{\text{eqSR}}} \right)}{\text{DEN}^2},$$
- $$R_{\text{WGS}} = 10^3 \frac{k_{\text{WGS}}}{p_{\text{H}_2,bar}} \frac{\left(p_{\text{CO,bar}} p_{\text{H}_2\text{O,bar}} - p_{\text{H}_2,bar} \frac{p_{\text{CO}_2,bar}}{K_{\text{eqWGS}}} \right)}{\text{DEN}^2},$$
- $$R_{\text{RMETH}} = 10^3 \frac{k_{\text{RMETH}}}{p_{\text{H}_2,bar}^{3.5}} \frac{\left(p_{\text{CH}_4,bar} p_{\text{H}_2\text{O,bar}}^2 - p_{\text{H}_2,bar}^4 \frac{p_{\text{CO}_2,bar}}{K_{\text{eqRMETH}}} \right)}{\text{DEN}^2},$$
- $$R_{\text{COMB}} = \frac{k_{a,\text{COMB}} p_{\text{CH}_4,bar} p_{\text{O}_2,bar}}{\left(1 + K_{\text{CH}_4,\text{COMB}} p_{\text{CH}_4,bar} + K_{\text{O}_2,\text{COMB}} p_{\text{O}_2,bar} \right)^2} + \frac{k_{b,\text{COMB}} p_{\text{CH}_4,bar} p_{\text{O}_2,bar}}{\left(1 + K_{\text{CH}_4,\text{COMB}} p_{\text{CH}_4,bar} + K_{\text{O}_2,\text{COMB}} p_{\text{O}_2,bar} \right)},$$

where the kinetics parameters k_i and K_j related to reaction and adsorption result from the following Arrhenius-like relations

$$k_i = A(k_i) \exp\left(-\frac{E(k_i)}{R_{\text{gas}}T}\right) \quad \text{and} \quad K_j = A(K_j) \exp\left(-\frac{E(K_j)}{R_{\text{gas}}T}\right). \quad (\text{C.1})$$

Values of coefficients $A(k_i, K_j)$ and $E(k_i, K_j)$ are listed in Table C.3.

Table C.3.: List of parameters for TRI kinetics: pre-exponential and activation energies.

$A(k_i)/A(K_i)$	Value	unit (SI)	$E(k_i)/E(K_i)$	Value	unit (SI)
$A(k_{\text{SR}})$	1.17×10^{12}	$\text{kmol bar}^{0.5} \text{kg}_{\text{cat}}^{-1} \text{s}^{-1}$	$E(k_{\text{SR}})$	2.40×10^5	
$A(k_{\text{WGS}})$	5.43×10^2	$\text{kmol bar}^{-1} \text{kg}_{\text{cat}}^{-1} \text{s}^{-1}$	$E(k_{\text{WGS}})$	6.71×10^4	
$A(k_{\text{RMETH}})$	2.83×10^{11}	$\text{kmol bar}^{0.5} \text{kg}_{\text{cat}}^{-1} \text{s}^{-1}$	$E(k_{\text{RMETH}})$	2.44×10^5	
$A(k_{a,\text{COMB}})$	8.11×10^5	$\text{mol bar}^{-2} \text{kg}_{\text{cat}}^{-1} \text{s}^{-1}$	$E(k_{a,\text{COMB}})$	8.60×10^4	
$A(k_{b,\text{COMB}})$	6.82×10^5	$\text{mol bar}^{-2} \text{kg}_{\text{cat}}^{-1} \text{s}^{-1}$	$E(k_{b,\text{COMB}})$	8.60×10^4	
$A(K_{\text{CH}_4})$	6.65×10^{-4}	bar^{-1}	$E(K_{\text{CH}_4})$	-3.83×10^4	J mol^{-1}
$A(K_{\text{H}_2\text{O}})$	1.75×10^5	–	$E(K_{\text{H}_2\text{O}})$	8.87×10^4	
$A(K_{\text{CO}})$	8.23×10^{-5}	bar^{-1}	$E(K_{\text{CO}})$	-7.07×10^4	
$A(K_{\text{H}_2})$	6.12×10^{-9}	bar^{-1}	$E(K_{\text{H}_2})$	-8.29×10^4	
$A(K_{\text{CH}_4,\text{COMB}})$	1.26×10^{-1}	bar^{-1}	$E(K_{\text{CH}_4,\text{COMB}})$	-2.73×10^4	
$A(K_{\text{O}_2,\text{COMB}})$	7.87×10^{-7}	bar^{-1}	$E(K_{\text{O}_2,\text{COMB}})$	-9.28×10^4	

C.3 Reaction rates for RWGS

RWGS kinetics are adapted from Richardson et al. [33]

$$\text{DEN} = (1 + K_{\text{CO}_2}p_{\text{CO}_2,\text{atm}} + K_{\text{H}_2}p_{\text{H}_2,\text{atm}}) \quad (\text{C.2})$$

and

$$R_{\text{RWGS}} = 10^3 k_{\text{RWGS}} K_{\text{CO}_2} K_{\text{H}_2} \left(p_{\text{CO}_2,\text{atm}} p_{\text{H}_2,\text{atm}} - \frac{p_{\text{CO},\text{atm}} p_{\text{H}_2\text{O},\text{atm}}}{K_{\text{eqRWGS}}} \right) / \text{DEN}^2, \quad (\text{C.3})$$

where kinetics parameters k_i and K_j related to reaction and adsorption, result from Arrhenius-like relations

$$k_{\text{RWGS}} = 350 \exp\left(\frac{-81030}{R_{\text{gas}}T}\right), K_{\text{CO}_2} = 0.5771 \exp\left(\frac{9262}{R_{\text{gas}}T}\right), K_{\text{H}_2} = 1.494 \exp\left(\frac{6025}{R_{\text{gas}}T}\right). \quad (\text{C.4})$$

Effectiveness factor is set to 0.3 [33].

C.4 Overall heat transfer coefficient RWGS

The overall heat transfer coefficient reads

$$U = \left(\frac{1}{\alpha_{\text{eff}}} \right)^{-1}. \quad (\text{C.5})$$

The shell-side heat transfer coefficient is not accounted for. Instead, a constant skin temperature is assumed along the pipe. The definition of α_{eff} for non-adiabatic packed-bed reactors is provided by Martin et al. [200]

$$\frac{1}{\alpha_{\text{eff}}} = \left(\frac{1}{\alpha_w} + \frac{D_T}{8\Lambda_r} \right). \quad (\text{C.6})$$

Here, α_w and Λ_r are retrieved from [201] and discussed by [202] as well as [200]

$$\alpha_w = \left[\left(1.3 + \frac{5}{D_T/d_p} \right) \frac{\lambda_{\text{bed}}}{\lambda_{\text{mix}}} + 0.19 \left[\rho_{\text{gas}} v \epsilon \frac{d_p}{\mu_{\text{mix}}} \right]^{0.75} \left[\mu_{\text{mix}} \frac{\tilde{C}_{p,\text{gas}}}{\lambda_{\text{mix}}} \right]^{0.33} \right] \frac{\lambda_{\text{mix}}}{d_p} \quad (\text{C.7})$$

and

$$\Lambda_r = \left[\lambda_{\text{bed}} + \frac{v \epsilon c_T \tilde{C}_{p,\text{gas}} d_p}{8 \left[2 - \left(1 - \frac{2}{D_T/d_p} \right)^2 \right]} \right]. \quad (\text{C.8})$$

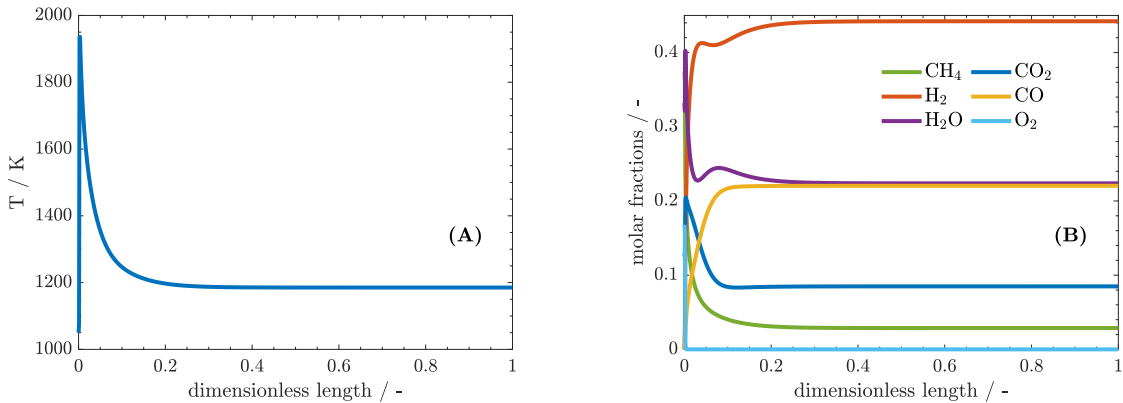
Embedded in the definition of α_w , the heat conductivity across the packed-bed λ_{bed} is defined by the following steps [202]:

- $\lambda_{\text{bed}} = k_{\text{bed}} \lambda_{\text{mix}}$,
- $k_{\text{bed}} = (1 - \sqrt{1 - \epsilon}) \epsilon \left[\left(\epsilon - 1 + \frac{1}{k_G} \right)^{-1} + k_{\text{rad}} \right] + \sqrt{1 - \epsilon} (\phi k_p + (1 - \phi) k_C)$,
- $\phi = 0.0077$ [-] spheres,

- $k_C = \frac{2}{N} \left(\frac{B(k_p + k_{\text{rad}} - 1)}{N^2 \cdot k_G \cdot k_p} \log \left(\frac{k_p + k_{\text{rad}}}{B(k_G + (1 - k_G) \cdot (k_p + k_{\text{rad}}))} \right) + \frac{B + 1}{2B} \left(\frac{k_{\text{rad}}}{k_G} - B \left(1 + \frac{1 - k_G}{k_G} k_{\text{rad}} \right) \right) - \frac{B - 1}{N \cdot k_G} \right)$
- $k_{\text{rad}} = \frac{4\sigma_{\text{SB}}}{2/\epsilon_E - 1} t_{\text{end}}^3 \frac{d_p}{\lambda_{\text{mix}}}$, $\sigma_{\text{SB}} = 5.67 \cdot 10^{-8} [\text{W m}^{-2} \text{K}^{-4}]$, $\epsilon_E = 0.4 [-]$, $k_G = 1 [-]$,
- $B = 1.25 \left(\frac{1 - \epsilon}{\epsilon} \right)^{(10/9)}$, and $k_p = \frac{\lambda_{\text{cat}}}{\lambda_{\text{mix}}}$.

C.5 Graphical results optimal TRI and RWGS configurations

Tri-reforming reactor profiles reflect the typical adiabatic operation: non-zero gradients are reported at the beginning, flattening out to zero once the energy input from the catalyzed combustion of CH_4 is exhausted by the endothermic reactions. The selected NLP formulation and objective determine a solution for the reactor length at its upper bound, although the gradients flatten out before its first half. Consequently, the reactor length is reduced by 90 % of the upper bound, whereas the value of the remaining optimization variables is set to their optimum. Steady-state simulation profiles are reported in Figure C.1: reforming contributions exploit the heat from catalyzed combustion within the very first reactor section. After the adiabatic peak, temperature decreases and stabilizes around 1200 K. The short reactor length determines a negligible pressure drop, in agreement with Chein et al. [40], and the velocity reflects the temperature profile. Position and magnitude of the high-temperature peak at the very inlet of the reactor is consistent with scenarios presented by Chein et al. [40], Aboosadi et al. [39], and Rezaei et al. [37].



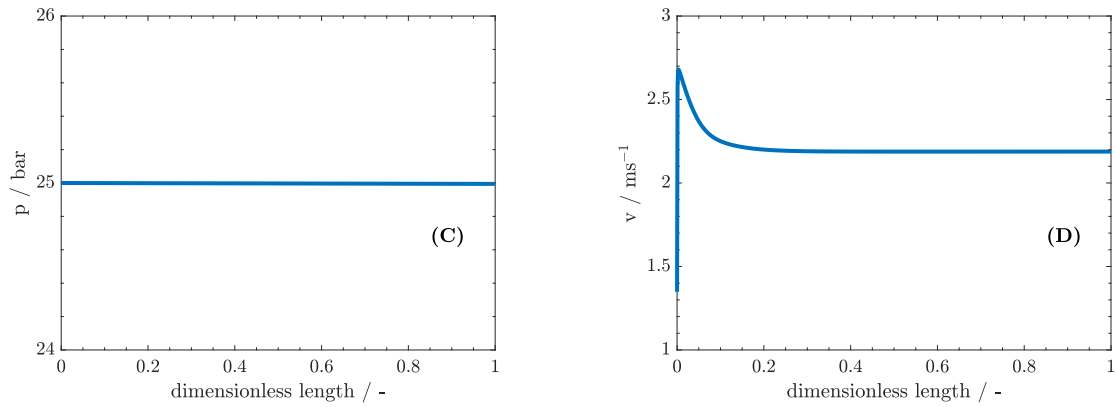


Figure C.1.: TRI temperature (A), composition (B), pressure (C), and velocity profile (D) at steady-state and nominal flowrate.

For the RWGS reactor, simulation results indicate a single-pass conversion of 44.7%.

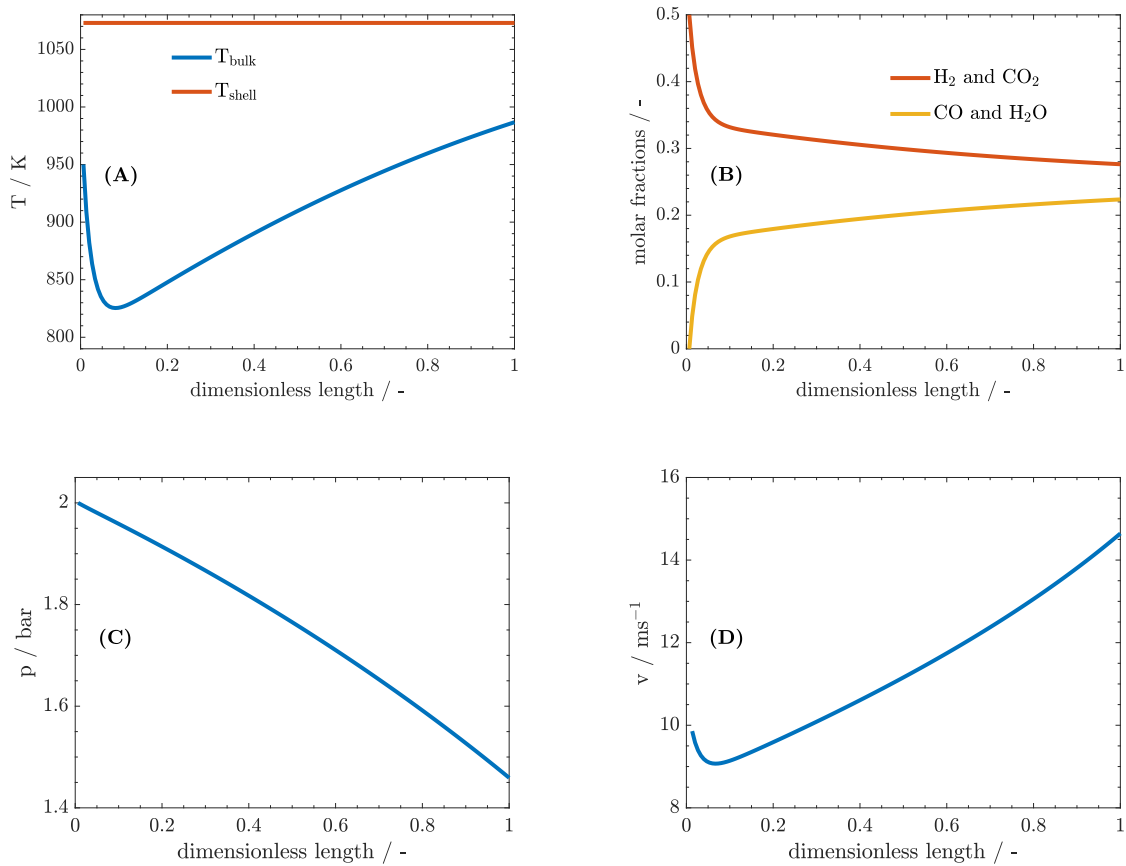


Figure C.2.: RWGS bulk and shell temperature (A), composition (B), pressure (C) and velocity profile (D) at steady-state nominal flowrate.

Appendix D

Supplement to Chapter 6

D.1 Wind park parametrization

D.1.1 Wind turbine power curve

Data for the definition of the power curve generated by the wind park are reported in Table D.1 and retrieved the technical sheet of a 2.1 MW wind turbine [203].

Table D.1.: Data are retrieved from the technical sheet of a wind turbine (2.1 MW S95 Sulzon).

m s^{-1}	3.0	3.5	4.0	4.5	5.0	5.5	6.0	6.5	7.0	7.5
kW	0.0	2.6	52.3	122.5	206.4	304.0	414.9	539.5	683.1	839.2
m s^{-1}	8.0	8.5	9.0	9.5	10.0	10.5	11.0	11.5	12.0	12.5
kW	1010.0	1197.1	1393.2	1592.4	1787.7	1931.2	2016.3	2068.3	2096.4	2109.2
m s^{-1}	13.0	13.5	14.0	14.5	15.0	15.5	16.0	16.5	17.0	17.5
kW	2114	2116.5	2116.2	2116	2115.8	2115	2114.5	2114.2	2113.87	2112.2
m s^{-1}	18.0	18.5	19.0	19.5	20.0	20.5	21.0	21.5	22.0	22.5
kW	2111.2	2110.5	2109.8	2105.5	2104.4	2103.2	2102	2096.4	2092.8	2091.2
m s^{-1}	23.0	23.5	24.0	24.5	25.0					
kW	2089.7	2088.2	2086.6	2084.9	2084.9					

D.1.2 Monthly wind velocity

The monthly average wind velocity in Magdeburg is retrieved from [204] and reported here:

Table D.2.: Average monthly wind velocities in Magdeburg, Germany.

	Jan.	Feb.	Mar.	Apr.	May	Jun.	Jul.	Aug.	Sep.	Oct.	Nov.	Dec.
km hr^{-1}	19.2	18.5	17.7	15.3	14.2	14.1	14.0	13.9	14.9	15.9	16.9	18.3

D.2 Mixers, heat exchangers, compressors, flash separator

D.2.1 Mixers, heat exchangers, compressors

In this section, some of the constraints apply with the same formulation to different unit operations in the plant. With an abuse of mathematical notation, such constraints shall be "evaluated at" (vertical bar symbol) the related process elements, whose identifiers are also reported in brackets on the right.

At each stream junction (MIX) represented in Figure 6.4, an energy balance determines the outlet temperature:

$$0 = \sum_{i \in I} \sum_{\alpha \in \mathcal{S}} \tilde{H}_{i,\alpha} \dot{N}_{i,\alpha} - \sum_{\alpha \in \mathcal{S}} \tilde{H}_{o,\alpha} \dot{N}_{o,\alpha} \Big|_{\text{MIX}(1-4)} \quad (\text{AE.MIX1, AE.MIX2, AE.MIX3, AE.MIX4})$$

where set I includes all streams entering the node, set \mathcal{S} includes all chemical components, and the index o denotes the outflow. Mixers feed temperatures are not pre-assigned, but result from the solution of the system.

Electric heat exchangers are modeled as functions of two system variables: the outlet temperature and the power input. These units are assumed to be extremely efficient. Therefore, all electric power is converted into thermal energy intended for the process stream. The governing equation reads:

$$0 = -\dot{W}_{\text{HE}} + \sum_{\alpha \in \mathcal{S}} \left(\int_{T_{\text{in}}}^{T_{\text{out}}} \tilde{C}_{p,\alpha} \dot{N}_{\text{in},\alpha} dT \right) \Big|_{\text{HE}(1-3)} \quad (\text{AE.HE1, AE.HE2, AE.HE3})$$

with the addition of the latent heat of vaporization of water at 298 K for the case of HE1: $\Delta H_{\text{ev}}(298 \text{ K})$.

Compressors are modeled as a sequence of isentropic compression stages. Two governing equations express the relation among three system variables: power input, discharge temperatures and pressure. The first defines the power required by the individual stage of compressor CPR1 and CPR2:

$$0 = -\dot{W}_{\text{CPR}(\text{stage})} + \left(\sum_{\alpha \in \mathcal{S}} \dot{N}_{\text{in},\alpha} \right) R_{\text{gas}} T_{\text{in}} Z_{\text{mix,gas}} \frac{\gamma_{\text{av}}}{\gamma_{\text{av}} - 1} \left[\left(\frac{p_{\text{out}}}{p_{\text{in}}} \right)^{\left(\frac{\gamma_{\text{av}} - 1}{\gamma_{\text{av}}} \right)} - 1 \right] \Bigg|_{\text{CPR}(1,2)} \quad (\text{AE.CPR1.1, AE.CPR2.1})$$

where the cubic equation of state is solved analytically for the compressibility factor of the mixture, $Z_{\text{mix,gas}}$ (see D.3.6), and the ratio of the temperature-dependent specific heat capacities at constant pressure and at constant temperature determines γ at the inlet and at the outlet. The average value of γ between inlet and outlet stream is denoted as γ_{av} . The second relation reads:

$$0 = T_{\text{out}} - T_{\text{in}} \left(\frac{p_{\text{out}}}{p_{\text{in}}} \right)^{\frac{\gamma_{\text{av}} - 1}{\gamma_{\text{av}}}} \Bigg|_{\text{CPR}(1,2)} \quad (\text{AE.CPR1.2 AE.CPR2.2})$$

and binds the temperature and pressure ratios of inlet and outlet flows. Equations (AE.CPR1.1, AE.CPR2.1) and (AE.MIX1, AE.MIX2, AE.MIX3, AE.MIX4) are repeated for the number of compression stages for CPR1 and CPR2.

The intermediate coolers are not modeled directly, since it is assumed that enough cold utility is available to bring the temperature of the feed to the next compression stage to 298 K. This decision does not apply to the last compression stage, whose isentropic outlet temperature is directly exploited by the next process item – heat exchanger HE3.

D.2.2 Flash separators

Flash F1 is run at a pressure range comparable to that of RWGS and SOEC. The preceding cooling step CL3 allows the temperature to drop to ambient temperature before the separator F1.

The Rachford-Rice equation in ξ , namely, the ratio between vapor and feed flowrates, is implemented to allow partial separation of water from all other components:

$$0 = \sum_{c \in \mathcal{C}} \frac{\zeta_{\text{feed},c} (K_c - 1)}{\alpha K_c + (1 - \xi)} + \frac{\sum_{i \in \mathcal{I}} z_i}{\xi} \Bigg|_{\text{FR}(1,2)} \quad (\text{AE.F1.1, AE.F2.1})$$

where set I includes the incondensable components, whereas set C includes exclusively water (condensable component). Due to the low pressure range, Raoult's law applies for the determination of the distribution coefficient K_c .

Flash F2 comes after throttling. The attained pressure level is higher than for F1. Consequently and also due to the low temperature, mixing rules are applied to RKS. In flash F2, set C includes water and methanol. For this flash separator, the equilibrium constant K_c results from a direct approach:

$$K_c = \frac{\Phi_{c,\text{liquid}}}{\Phi_{c,\text{vapor}}}, \quad (\text{D.1})$$

where the fugacity coefficient for component c in liquid and vapor phase are determined as reported in D.3.2, Equation (D.7). In addition to the Rachford Rice equation (AE.F2.1), this model incorporates two cubic equations in the compressibility factor $Z_{\text{mix,vap/liq}}$, one initialized with a higher value (largest root for vapor phase, unitary), the other with a low value (smaller root for liquid phase, a positive infinitesimal). They read:

$$0 = Z_{\text{mix,vap}}^3 + \alpha_{\text{mix,vap}} Z_{\text{mix,vap}}^2 + \beta_{\text{mix,vap}} Z_{\text{mix,vap}} + \gamma_{\text{mix,vap}}, \quad (\text{AE.F2.2})$$

$$0 = Z_{\text{mix,liq}}^3 + \alpha_{\text{mix,liq}} Z_{\text{mix,liq}}^2 + \beta_{\text{mix,liq}} Z_{\text{mix,liq}} + \gamma_{\text{mix,liq}}. \quad (\text{AE.F2.3})$$

Coefficients for the cubic equations are based on mixing rules and expanded in Supplementary Section D.3.

D.3 System models parametrization

D.3.1 Modeling of SOEC

Factors in Equation AE.SOEC.2, AE.SOEC.3:

$$\Lambda_1 = \frac{\zeta_{\text{av,H}_2,\text{TPB}}}{\zeta_{\text{av,H}_2}}, \quad \Lambda_2 = \frac{\mathcal{E}_{\text{faraday}}}{R_{\text{gas}} T_{\text{av}}}, \quad \Lambda_3 = \frac{\zeta_{\text{av,H}_2\text{O},\text{TPB}}}{\zeta_{\text{av,H}_2\text{O}}}, \quad \Lambda_4 = \frac{-\mathcal{E}_{\text{faraday}}}{R_{\text{gas}} T_{\text{av}}}, \quad (\text{D.2})$$

where subscript "av" denotes an average value between inlet and outlet of SOEC, R_{gas} the universal gas constant ($8.314 \text{ J mol}^{-1} \text{ K}^{-1}$), $\mathcal{E}_{\text{faraday}}$ the Faraday constant, subscript "TPB" denotes the concentration at the triple phase boundary. Mole fractions $\zeta_{\text{av},i \in \{\text{H}_2, \text{H}_2\text{O}\}}$ at the cathode read:

$$\zeta_{\text{av},\text{H}_2} = \frac{\dot{N}_{\text{av},\text{H}_2}}{\dot{N}_{\text{av},\text{H}_2} + \dot{N}_{\text{av},\text{H}_2\text{O}}}, \quad \zeta_{\text{av},\text{H}_2\text{O}} = \frac{\dot{N}_{\text{av},\text{H}_2\text{O}}}{\dot{N}_{\text{av},\text{H}_2} + \dot{N}_{\text{av},\text{H}_2\text{O}}}. \quad (\text{D.3})$$

Other terms appearing in Equation D.2 are expanded here:

$$\zeta_{\text{av},\text{H}_2,\text{TPB}} = \zeta_{\text{av},\text{H}_2} + \frac{\tau_{\text{cat}}}{2\mathcal{E}_{\text{faraday}}D_{\text{eff},\text{cat}}C_{\text{tot},\text{av}}}i_{\text{SOEC}}, \quad (\text{D.4})$$

$$\zeta_{\text{av},\text{H}_2\text{O},\text{TPB}} = \zeta_{\text{av},\text{H}_2\text{O}} - \frac{\tau_{\text{cat}}}{2\mathcal{E}_{\text{faraday}}D_{\text{eff},\text{cat}}C_{\text{tot},\text{av}}}i_{\text{SOEC}}, \quad (\text{D.5})$$

where $C_{\text{tot},\text{av}}$ is the ideal gas average concentration between inlet and outlet of SOEC, τ_{cat} is the cathode thickness ($500 \times 10^{-6} \text{ m}$), $D_{\text{eff},\text{cat}}$ is the average effective diffusivity coefficient of the cathode ($36.6 \times 10^{-6} \text{ m}^2 \text{ s}^{-1}$).

The total voltage is given by the sum of reversible and irreversible contributions.

$$V_{\text{tot}}^{\text{SOEC}} = V_{\text{nernst}} + V_{\text{ohm}} + V_{\text{conc}} + V_{\text{act},\text{cat}} + V_{\text{act},\text{an}}, \quad (\text{D.6})$$

$$V_{\text{nernst}} = -\frac{g_{\text{f},\text{H}_2\text{O}}^0(T_{\text{in}})}{2\mathcal{E}_{\text{faraday}}} - R_{\text{gas}}\frac{T_{\text{av}}}{2\mathcal{E}_{\text{faraday}}}\ln\left(\frac{\zeta_{\text{av},\text{H}_2\text{O}}}{\zeta_{\text{av},\text{H}_2}\zeta_{\text{av},\text{O}_2}^{0.5}}\right),$$

$$V_{\text{ohm}} = i_{\text{SOEC}}\left(\frac{\tau_{\text{cat}}}{\sigma_{\text{cat}}} + \frac{\tau_{\text{el}}}{\sigma_{\text{el}}} + \frac{\tau_{\text{an}}}{\sigma_{\text{an}}}\right),$$

$$V_{\text{conc}} = R_{\text{gas}}\frac{T_{\text{av}}}{2\mathcal{E}_{\text{faraday}}}\ln\left(\zeta_{\text{av},\text{H}_2,\text{TPB}}\frac{\zeta_{\text{av},\text{H}_2\text{O}}}{\zeta_{\text{av},\text{H}_2}\zeta_{\text{av},\text{H}_2\text{O},\text{TPB}}}\right)$$

whereas $V_{\text{act},\text{cat}}$ and $V_{\text{act},\text{an}}$ are implicit dependencies of other variables and must be calculated as NLP constraints, AE.SOEC.2 and AE.SOEC.3. In Equation D.6; T_{av} is the average temperature between the inlet and outlet of SOEC, $g_{\text{f},\text{H}_2\text{O}}^0(T_{\text{in}})$ is the Gibbs free energy of formation of water at the feed temperature to SOEC; $\zeta_{\text{av},\text{O}_2}$ is the mole fraction of oxygen in the sweep gas (pure, thus unitary); $\zeta_{\text{av},\text{H}_2\text{O}}$ and $\zeta_{\text{av},\text{H}_2}$ are average component compositions at the cathode (see Equation

D.3); τ_{cat} , τ_{el} and τ_{an} are the cathode, the electrolyte and the anode thickness (500×10^{-6} m, 20×10^{-6} m, 50×10^{-6} m, respectively). The cathode electric conductivity, the electrolyte ionic conductivity and the anode electric conductivity are denoted by σ_{cat} , σ_{el} and σ_{an} ($80 \times 10^3 \Omega^{-1} \text{ m}^{-1}$, $33400 \exp(-10300/T_s) \Omega^{-1} \text{ m}^{-1}$, $8400 \Omega^{-1} \text{ m}^{-1}$, respectively).

D.3.2 Modeling of flash separator F2 (methanol recycle loop)

Mixture fugacity coefficient $\Phi_{\alpha, \text{phase} \in \{\text{vap}, \text{liq}\}}$ for condensable components ($\alpha \in \{\text{H}_2\text{O}, \text{CH}_3\text{OH}\}$) in liquid and vapor phase read:

$$\Phi_{\alpha, \text{phase}} = \exp \left(\frac{b_{\alpha, \text{phase}}}{b_{\text{mix}, \text{phase}}} (Z_{\text{mix}, \text{phase}} - 1) - \log(|Z_{\text{mix}, \text{phase}} - B_{\text{EOS}, \text{phase}}|) - \dots \right) \quad (\text{D.7})$$

$$\frac{A_{\text{EOS}, \text{phase}}}{B_{\text{EOS}, \text{phase}}} \left(2 \cdot \sqrt{\left(\frac{a_{\alpha, \text{phase}}}{a_{\text{mix}, \text{phase}}} \right)} - \frac{b_{\alpha, \text{phase}}}{b_{\text{mix}, \text{phase}}} \log \left(1 + \frac{B_{\text{EOS}, \text{phase}}}{Z_{\text{mix}, \text{phase}}} \right) \right).$$

Coefficients for the cubic Equations AE.F2.2, AE.F2.3 (flash in the methanol reactor loop) read:

$$\begin{aligned} \alpha_{\text{mix}, \text{phase}} &= -1, \\ \beta_{\text{mix}, \text{phase}} &= A_{\text{EOS}, \text{phase}} - B_{\text{EOS}, \text{phase}} - B_{\text{EOS}, \text{phase}}^2, \\ \gamma_{\text{mix}, \text{phase}} &= -A_{\text{EOS}, \text{phase}} B_{\text{EOS}, \text{phase}}, \end{aligned} \quad (\text{D.8})$$

where

$$\begin{aligned} A_{\text{EOS}, \text{phase}} &= a_{\text{mix}, \text{phase}} \frac{p}{(R_{\text{gas}} T)^2}, \\ B_{\text{EOS}, \text{phase}} &= b_{\text{mix}, \text{phase}} \frac{p}{(R_{\text{gas}} T)}, \end{aligned} \quad (\text{D.9})$$

and, introducing two new indices for components in the mixture i and j to explore binary interactions,

$$a_{\text{mix,phase}} = \sum_{i \in I} \sum_{j \in J} \zeta_{i,j,\text{phase}} a_{i,j,\text{phase}}, \quad (\text{D.10})$$

$$b_{\text{mix,phase}} = \sum_{i \in I} \zeta_{i,\text{phase}} b_{i,\text{phase}},$$

and

$$a_{i,j,\text{phase}} = \sqrt{a_{i,\text{phase}} a_{j,\text{phase}}} (1 - K_{i,j}), \quad (\text{D.11})$$

where coefficient $K_{i,j}$ denote the binary interaction between component i and j and is retrieved from [205], whereas coefficients $a_{i,\text{phase}}$ and $b_{i,\text{phase}}$ for a generic pure component i in the phase read:

$$a_{\alpha,\text{phase}} = 0.42748 \frac{(R_{\text{gas}} T_{\text{critical}})^2}{p_{\text{critical}}} k_{\alpha}, \quad (\text{D.12})$$

$$b_{\alpha,\text{phase}} = 0.08664 \frac{R_{\text{gas}} T_{\text{critical}}}{p_{\text{critical}}},$$

For water and methanol (condensable components) they read: $K_{\text{H}_2\text{O}-\text{H}_2\text{O}} = 0$, $K_{\text{CH}_3\text{OH}-\text{CH}_3\text{OH}} = 0$, $K_{\text{CH}_3\text{OH}-\text{H}_2\text{O}} = -0.0789$, whereas k_i reads $\left(1 + S \left(1 - \sqrt{T_{\text{reduced},\alpha}}\right)\right)^2$, with $S = s_1 + s_2\omega + s_3\omega^2$, $\omega = -\log_{10}(p_{\text{pitzer}}/p_{\text{critical}}) - 1$. The pressure utilized for the evaluation of Pitzer's acentric factor reads

$$p_{\text{pitzer}} (\text{Pa}) = 10^{(A+B/T_{\text{pitzer}} + C \log_{10}(T_{\text{pitzer}}) + DT_{\text{pitzer}} + ET_{\text{pitzer}}^2)} \frac{101325}{760} \quad T_{\text{pitzer}} = 0.7 \cdot T_{\text{critical}}. \quad (\text{D.13})$$

D.3.3 Source term σ_{α} in reactor models

The generation of component α in ODE.RWGS.1, ODE.METHL.1 and 3 is expressed by the source term σ_{α} , which reads:

$$\sigma_\alpha = \sum_{k \in K} \nu_{\alpha,k} R_k, \quad (\text{D.14})$$

where the stoichiometric coefficient $\nu_{\alpha,k}$ multiplies the reaction rate of reaction R_k ($\text{mol kg}_{\text{cat}}^{-1} \text{s}^{-1}$). Reaction rates for RWGS and METHL are reported in the following Sections of this Appendix.

D.3.4 Reaction rates for reverse water-gas shift (RWGS)

The parameters are selected from [170] and reported in Table D.3. The governing kinetic expressions are

$$\begin{aligned} \text{DEN} &= \left(1 + K_{\text{CO}} p_{\text{CO,bar}} + K_{\text{H}_2} p_{\text{H}_2,\text{bar}} + K_{\text{CH}_4} p_{\text{CH}_4,\text{bar}} + K_{\text{H}_2\text{O}} \frac{x_{\text{H}_2\text{O}}}{x_{\text{H}_2}} \right), \quad (\text{D.15}) \\ R_{\text{SR}} &= 10^3 \frac{k_{\text{SR}}}{p_{\text{H}_2,\text{bar}}^{2.5}} \frac{\left(p_{\text{CH}_4,\text{bar}} p_{\text{H}_2\text{O,bar}} - p_{\text{H}_2,\text{bar}}^3 \frac{p_{\text{CO,bar}}}{K_{\text{eq,SR}}} \right)}{\text{DEN}^2}, \\ R_{\text{WGS}} &= 10^3 \frac{k_{\text{WGS}}}{p_{\text{H}_2,\text{bar}}} \frac{\left(p_{\text{CO,bar}} p_{\text{H}_2\text{O,bar}} - p_{\text{H}_2,\text{bar}} \frac{p_{\text{CO}_2,\text{bar}}}{K_{\text{eq,WGS}}} \right)}{\text{DEN}^2}, \\ R_{\text{RMETH}} &= 10^3 \frac{k_{\text{RMETH}}}{p_{\text{H}_2,\text{bar}}^{3.5}} \frac{\left(p_{\text{CH}_4,\text{bar}} p_{\text{H}_2\text{O,bar}}^2 - p_{\text{H}_2,\text{bar}}^4 \frac{p_{\text{CO}_2,\text{bar}}}{K_{\text{eq,RMET}}} \right)}{\text{DEN}^2}, \end{aligned}$$

where the kinetics parameters k_i and K_j related to reaction and adsorption result from the following relations

$$k_i = A(k_i) \exp\left(-\frac{E(k_i)}{R_{\text{gas}} T}\right) \quad \text{and} \quad K_j = A(K_j) \exp\left(-\frac{E(K_j)}{R_{\text{gas}} T}\right). \quad (\text{D.16})$$

Values of coefficients $A(k_i, K_j)$ and $E(k_i, K_j)$ are listed in Table D.3.

Table D.3.: List of parameters for RWGS kinetics.

$A(k_i)$ and $A(K_i)$	Value	unit (SI)	$E(k_i)$ and $E(K_i)$	Value	unit (SI)
$A(k_{\text{SR}})$	1.17×10^{12}	$\text{kmol bar}^{0.5} \text{kg}_{\text{cat}}^{-1} \text{s}^{-1}$	$E(k_{\text{SR}})$	2.40×10^5	
$A(k_{\text{WGS}})$	5.43×10^2	$\text{kmol bar}^{-1} \text{kg}_{\text{cat}}^{-1} \text{s}^{-1}$	$E(k_{\text{WGS}})$	6.71×10^4	
$A(k_{\text{RMETH}})$	2.83×10^{11}	$\text{kmol bar}^{0.5} \text{kg}_{\text{cat}}^{-1} \text{s}^{-1}$	$E(k_{\text{RMETH}})$	2.44×10^5	
$A(K_{\text{CH}_4})$	6.65×10^{-4}	bar^{-1}	$E(K_{\text{CH}_4})$	-3.83×10^4	J mol^{-1}
$A(K_{\text{H}_2\text{O}})$	1.75×10^5	–	$E(K_{\text{H}_2\text{O}})$	8.87×10^4	
$A(K_{\text{CO}})$	8.23×10^{-5}	bar^{-1}	$E(K_{\text{CO}})$	-7.07×10^4	
$A(K_{\text{H}_2})$	6.12×10^{-9}	bar^{-1}	$E(K_{\text{H}_2})$	-8.29×10^4	

D.3.5 Reaction rates for methanol reactor (METHL)

METHL kinetics are adapted from [194] and determined as $\text{mol kg}_{\text{cat}}^{-1} \text{s}^{-1}$.

$$\text{DEN} = (1 + K_{\text{CO}}f_{\text{CO,bar}} + K_{\text{CO}_2}f_{\text{CO}_2,\text{bar}}) \left[f_{\text{H}_2}^{0.5} + (K_{\text{H}_2\text{O}}/K_{\text{H}_2}^{0.5}) f_{\text{H}_2\text{O}} \right], \quad (\text{D.17})$$

$$R_{\text{CO} \rightarrow \text{CH}_3\text{OH}} = k_{\text{A3}} K_{\text{CO}} \frac{\left(f_{\text{CO,bar}} f_{\text{H}_2,\text{bar}}^{3/2} - \frac{f_{\text{CH}_3\text{OH,bar}}}{f_{\text{H}_2,\text{bar}}^{0.5} K_{\text{eqCO} \rightarrow \text{CH}_3\text{OH}}} \right)}{\text{DEN}},$$

$$R_{\text{RWGS}} = k_{\text{B2}} K_{\text{CO}_2} \frac{\left(f_{\text{CO}_2,\text{bar}} f_{\text{H}_2,\text{bar}} - \frac{f_{\text{H}_2\text{O,bar}} f_{\text{CO,bar}}}{K_{\text{eqRWGS}}} \right)}{\text{DEN}},$$

$$R_{\text{CO}_2 \rightarrow \text{CH}_3\text{OH}} = k_{\text{C3}} K_{\text{CO}_2} \frac{\left(f_{\text{CO}_2,\text{bar}} f_{\text{H}_2,\text{bar}}^{3/2} - \frac{f_{\text{CH}_3\text{OH,bar}} f_{\text{H}_2\text{O,bar}}}{f_{\text{H}_2,\text{bar}}^{1.5} K_{\text{eqCO}_2 \rightarrow \text{CH}_3\text{OH}}} \right)}{\text{DEN}},$$

and

$$k_{\text{A3}} = 2.69 \times 10^7 \exp\left(\frac{-109900}{R_{\text{gas}}T}\right), \quad k_{\text{B2}} = 7.31 \times 10^8 \exp\left(\frac{-123400}{R_{\text{gas}}T}\right), \quad (\text{D.18})$$

$$k_{\text{C3}} = 4.36 \times 10^2 \exp\left(\frac{-65200}{R_{\text{gas}}T}\right), \quad K_{\text{CO}} = 7.99 \times 10^{-7} \exp\left(\frac{58100}{R_{\text{gas}}T}\right),$$

$$K_{\text{CO}_2} = 1.02 \times 10^{-7} \exp\left(\frac{67400}{R_{\text{gas}}T}\right), \quad K_{\text{H}_2\text{O}} \sqrt{K_{\text{H}_2}} = 4.13 \times 10^{-11} \exp\left(\frac{104500}{R_{\text{gas}}T}\right),$$

$$K_{\text{H}_2} = 1.494 \exp\left(\frac{6025}{R_{\text{gas}}T}\right).$$

Catalyst effectiveness factor is set to 1 for both fixed-bed reactors.

D.3.6 Analytical solution for the compressibility factor in gas phase (METHL)

RKS is adopted for the modeling of the methanol reactor METHL as recommended in the sources, where mixing rules are not implemented (Lewis-Randall approximation: real gases as pure components within a mixture). The reactor operates at gas phase conditions. Therefore, the analytic solution at each discretization point for the compressibility factor $Z_{\alpha \in S, k \in K, \text{gas}}$, where set S includes the components, set K the discretization points, reads:

$$Z_{\alpha, \text{gas}, k} = \text{sgn}(\Theta_{1, (\alpha, k)}) |\Theta_{1, \alpha, k}|^{1/3} + \text{sgn}(\Theta_{2, \alpha, k}) |\Theta_{2, \alpha, k}|^{1/3} - \frac{\alpha_{\alpha, k}}{3} \quad (\text{D.19})$$

where

$$\begin{aligned} \Theta_{1, \alpha, k} &= -\frac{q_{\alpha, k}}{2} + \sqrt{D_{\alpha, k}} \\ \Theta_{2, \alpha, k} &= -\frac{q_{\alpha, k}}{2} - \sqrt{D_{\alpha, k}} \\ D_{\alpha, k} &= \frac{q_{\alpha, k}^2}{4} + \frac{p_{\alpha, k}^3}{27} \\ q_{\alpha, k} &= 2\frac{\alpha_{\alpha, k}^3}{27} - \alpha_{\alpha, k} \frac{\beta_{\alpha, k}}{3} + \gamma_{\alpha, k} \\ p_{\alpha, k} &= \beta_{\alpha, k} - \frac{\alpha_{\alpha, k}^2}{3} \end{aligned} \quad (\text{D.20})$$

where $\alpha_{\alpha, k}$, $\beta_{\alpha, k}$ and $\gamma_{\alpha, k}$ are calculated as in D.3.2 in function of $a_{\alpha, k}$ and $b_{\alpha, k}$ for pure components along the axial coordinate k , therefore without accounting for the mixing rules:

$$\begin{aligned} A_{\text{EOS}, \alpha, k} &= a_{\alpha, k} \frac{p_k}{(R_{\text{gas}} T_k)^2}, \\ B_{\text{EOS}, \alpha, k} &= b_{\alpha, k} \frac{p_k}{(R_{\text{gas}} T_k)}. \end{aligned} \quad (\text{D.21})$$

Reference is found in Rota [206].

The fugacity is obtained multiplying the fugacity coefficient with the partial pressure of component i at each discretization point k :

$$f_{\alpha,k} = \Phi_{\alpha,k} p_{\text{tot},k} \zeta_{\alpha,k} \quad (\text{D.22})$$

and the fugacity coefficient $\Phi_{\alpha,k}$ for pure components (Lewis Randall approximation of equal interactions among real components in gas phase) reads:

$$\Phi_{\alpha,k} = \exp \left(Z_{\alpha,\text{gas},k} - 1 - \frac{A_{\text{EOS},\alpha,k}}{B_{\text{EOS},\alpha,k}} \log \left(Z_{\alpha,\text{gas},k} + \frac{B_{\text{EOS},\alpha,k}}{Z_{\alpha,\text{gas},k}} \right) - \log (Z_{\alpha,\text{gas},k} - B_{\text{EOS},\alpha,k}) \right). \quad (\text{D.23})$$

Similarly to $\alpha_{\alpha,k}$ and $\beta_{\alpha,k}$, $A_{\text{EOS},\alpha,k}$ and $B_{\text{EOS},\alpha,k}$ rely on pure component calculations.

D.3.7 Analytical solution for the compressibility factor in gas phase (COMPR)

The compressibility factor is calculated analytically as shown in Appendix D.3.6, with the difference that coefficients α , β , γ are derived accounting for the mixing rules, as in Equation D.8 in Appendix D.3.2.

D.3.8 Overall heat transfer coefficient U (METHL)

The overall heat transfer coefficient depending on the axial discretization point along the methanol reactor reads

$$U = \left(\frac{1}{\alpha_{\text{eff}}} \right)^{-1}, \quad (\text{D.24})$$

where α_{eff} is the effective heat transfer coefficient. Here, the shell-side heat transfer coefficient is not accounted for. Instead, a constant skin temperature is assumed along the pipe. The definition of α_{eff} for non-adiabatic packed-bed reactors is provided by Martin and Nilles [200]:

$$\frac{1}{\alpha_{\text{eff}}} = \left(\frac{1}{\alpha_w} + \frac{D_{t,\text{METHL}}}{8\Lambda_r} \right). \quad (\text{D.25})$$

Here, α_w and Λ_r , respectively, wall heat transfer coefficient and radial heat conductivity, are retrieved from Bauer et al.[201] and discussed by Tsotsas [202] and Martin and Nilles [200]

$$\alpha_w = \left\{ \left(1.3 + \frac{5}{D_{T,\text{METHL}}/D_{\text{cat},\text{METHL}}} \right) \frac{\lambda_{\text{bed}}}{\lambda_{\text{mix}}} + 0.19 \left[\rho_{\text{gas}} v \epsilon \frac{D_{\text{cat},\text{METHL}}}{\mu_{\text{mix}}} \right]^{0.75} \left[\mu_{\text{mix}} \frac{\tilde{C}_{p,\text{gas}}}{\lambda_{\text{mix}}} \right]^{0.33} \right\} \frac{\lambda_{\text{mix}}}{D_{\text{cat},\text{METHL}}}, \quad (\text{D.26})$$

$$\Lambda_r = \left\{ \lambda_{\text{bed}} + \frac{v \epsilon C_{\text{tot}} \tilde{C}_{p,\text{gas}} D_{\text{cat},\text{METHL}}}{8 \left[2 - \left(1 - \frac{2}{D_{T,\text{METHL}}/D_{\text{cat},\text{METHL}}} \right)^2 \right]} \right\}. \quad (\text{D.27})$$

Embedded in the definition of α_w , the heat conductivity across the packed-bed λ_{bed} is defined by the following steps [202]:

$$\lambda_{\text{bed}} = k_{\text{bed}} \lambda_{\text{mix}}, \quad (\text{D.28})$$

$$k_{\text{bed}} = \left(1 - \sqrt{1 - \epsilon}\right) \epsilon \left[\left(\epsilon - 1 + \frac{1}{k_G} \right)^{-1} + k_{\text{rad}} \right] + \sqrt{1 - \epsilon} (\phi k_p + (1 - \phi) k_C), \quad (\text{D.29})$$

$$\phi = 0.0077 \quad [-] \quad \text{spheres}, \quad (\text{D.30})$$

$$k_C = \frac{2}{N} \left\{ \frac{B(k_p + k_{\text{rad}} - 1)}{N^2 \cdot k_G \cdot k_p} \log \left(\frac{k_p + k_{\text{rad}}}{B(k_G + (1 - k_G) \cdot (k_p + k_{\text{rad}}))} \right) + \frac{B + 1}{2B} \left[\frac{k_{\text{rad}}}{k_G} - B \left(1 + \frac{1 - k_G}{k_G} k_{\text{rad}} \right) \right] - \frac{B - 1}{N \cdot k_G} \right\}, \quad (\text{D.31})$$

$$k_{\text{rad}} = \frac{4\sigma_{\text{SB}}}{2/\epsilon_E - 1} T^3 \frac{D_{\text{cat,METHL}}}{\lambda_{\text{mix}}}, \quad \sigma_{\text{SB}} = 5.67 \cdot 10^{-8} [\text{W m}^{-2} \text{K}^{-4}], \quad \epsilon_E = 0.4 [-], \quad k_G = 1 [-], \quad (\text{D.32})$$

$$B = 1.25 \left(\frac{1 - \epsilon}{\epsilon} \right)^{(10/9)}, \quad \text{and} \quad k_p = \frac{\lambda_{\text{cat}}}{\lambda_{\text{mix}}}. \quad (\text{D.33})$$

$$N = \frac{1}{k_G} \left(1 + \frac{k_{\text{rad}} - B \cdot k_G}{k_p} \right) - B \left(\frac{1}{k_G} - 1 \right) \left(1 + \frac{k_{\text{rad}}}{k_p} \right). \quad (\text{D.34})$$

For a thorough description of the single coefficients reported above, see sources.

D.3.9 Interstitial velocity for tubular reactors (METHL and RWGS)

The interstitial velocity profile is derived in fulfillment of the total mass balance between inlet and current section of the reactor tube. At a given section along the reactor tube, interstitial velocity reads:

$$v = \frac{\sum_{\alpha \in \mathcal{S}} (\dot{N}_{\text{in},\alpha} M_\alpha)}{C_{\text{gas}} A_{\text{cross}} \epsilon \sum_{\alpha \in \mathcal{S}} (\zeta_\alpha M_\alpha)}, \quad (\text{D.35})$$

where $\dot{N}_{0,\alpha}$ is the feed flowrate of component α and M_α its molecular weight, C_{tot} is the total concentration at the current reactor section defined as in Equation 6.5, A_{cross} is the cross sectional area without voids, ϵ the void fraction, ζ_α the mole fraction at the point.

D.4 Cost functions

CEPCI cost indices have been retrieved. They are used to actualize the original cost functions. For 1968, 1987, 2013 and 2022 they are 113.6, 323.8, 567.3 and 906.3, respectively. Sources are found on websites [207, 208]. Lifetimes for units and components are reported in Table D.5. For hydrogen compressor, a lifetime of 10 years is assumed.

D.4.1 Tubular reactors

The cost correlation for tubular bundle reactors (METHL) is the same for shell and tubes heat exchangers and is retrieved from Timmerhaus [209]. It reads:

$$C_{\text{METHL,vessel,\$}} = 4.9 \times 10^3 (0.10764 \cdot A_{\text{METHL,tot}})^{0.68} 1.61 \left(2.7 + \left(\frac{2.7}{100} \right)^{0.07} \right) \left(\frac{\text{CEPCI}_{2022}}{\text{CEPCI}_{1987}} \right), \quad (\text{D.36})$$

and is defined for stainless steel shell and tubes heat exchangers; $A_{\text{METHL,tot}}$ is the total area of exchange, from tubes to reactor coolant. The formula is adapted from a graphical diagram, and converted to use SI units of measurement.

The cost of an adiabatic RWGS stage is given by Guthrie [70] and reads:

$$C_{\text{RWGS,vessel,\$}} = 101.9 (3.28084 \cdot D_{\text{t,RWGS}})^{1.066} (3.28084 L_{\text{t,RWGS}})^{0.802} (2.18 + 1) \left(\frac{\text{CEPCI}_{2022}}{\text{CEPCI}_{1968}} \right), \quad (\text{D.37})$$

defined for carbon steel at low pressure. Both, Equation D.36 and D.37, are expressed in Dollar, which is converted to Euro according to the prevailing change at the time of the computations 1 € / 1.05 \$. Similarly for all prices adopted in the Contribution.

For RWGS, a standard industrial nickel catalyst on alumina support has been selected. Its estimated cost: 13 \$ kg⁻¹. For the methanol reactor catalyst a price of 45 \$ kg⁻¹ is assumed. Both references are averaged values from online sources [210, 211].

D.4.2 SOEC

In absence of a reliable cost per unit of SOEC area, a cost per unit of power input is adopted: 0.1253 € W^{-1} [197].

D.4.3 Compressor

The hydrogen compressor installation cost is retrieved from a graphical diagram in Timmerhaus [209]:

$$C_{\text{CPR,H}_2,\$} = 21 \times 10^3 \left(\frac{\dot{W}_{\text{CPR}}}{29840} \right)^{0.8} \left(\frac{\text{CEPCI}_{2022}}{\text{CEPCI}_{1987}} \right)^{1.49}. \quad (\text{D.38})$$

Table D.4.: Optimization results for the case-studies listed in Table 6.2. Reactor volumes, reported in brackets, are calculated from the results, i.e., they do not constitute decision variables. The table continues under the thicker dividing-line, where $\dot{N}_{tot,(1,5,6)}$ represent, respectively, the feed stream of water, carbon dioxide to RWGS, carbon dioxide to the methanol loop.

case-study	Π	P_{CH_3OH} ton $_{CH_3OH}$ day $^{-1}$	Design Variables $^{(\pi)}$								
			$A_{SOEC}^{(\pi)}$ m 2	$L_{T,RWGS}^{(\pi)}$ m	$D_{T,RWGS}^{(\pi)}$ m	$(V_{RWGS}^{(\pi)})$ m 3	$N_{T,METHL}^{(\pi)}$ –	$L_{T,METHL}^{(\pi)}$ m	$D_{T,METHL}^{(\pi)}$ m	$(V_{METHL}^{(\pi)})$ m 3	
CASE.FLEX	1	33.142	2155	1.024	1.00×10^{-1}	(8.1×10^{-3})	508	9.537	5.2×10^{-2}	(10.471)	
	2	47.700									
	3	85.396									
	4	119.483									
	5	126.802									
	annual	69.412									
CASE.BUFF (23.5 MW)	1	60.404	3904	1.254	1.01×10^{-1}	(1×10^{-2})	321	13.4	4.9×10^{-2}	(8.22)	
CASE.EFF (23.5 MW)	1	63.457	4129	1.7	1.00×10^{-1}	(1.32×10^{-2})	3039	15	6.8×10^{-2}	(165.9)	
CASE.FLEX.HI	1	36.875	2375	1.75	1.00×10^{-1}	(1.38×10^{-2})	64	15	1.49×10^{-1}	(16.9)	
	2	52.387									
	3	94.977									
	4	132.461									
	5	140.932									
	annual	77.042									
Operation Variables											
	Π	Operation Variables									
		$\dot{N}_{tot,(1,5,6)}$ mol s $^{-1}$	$T_{out,HE1,2,3}$ K	$P_{out,(stage),CPR1}$ bar	$P_{out,(stage),CPR2}$ bar	$P_{in,SOEC,RWGS}$ bar	$P_{in,METHL}$ bar	$T_{cool,METHL}$ K	S1 –	S2 –	
CASE.FLEX	1	36.2, 0.014, 12.0	1000, 1001, 478	4.4 (1-4), 51.1 (5)	23.0 (1-3), 23.1 (4), 51.1 (5)	4.39	51.1	508	3.9 $\times 10^{-4}$	1.3 $\times 10^{-4}$	
	2	52.2, 0.027, 17.2	1022, 994, 478	4.4 (1-2), 4.5 (3), 4.6 (4), 51.1 (5)	23.0 (1-2), 23.1 (3-4), 52.4 (5)	4.30	52.4	519	6.0 $\times 10^{-4}$	2.7 $\times 10^{-4}$	
	3	93.3, 0.026, 30.9	1061, 995, 478	4.6 (1-2), 4.7 (3-4), 54.2 (5)	23.0 (1-4), 54.2 (5)	4.58	54.2	527	3.2 $\times 10^{-4}$	4.8 $\times 10^{-5}$	
	4	130.5, 0.034, 43.2	1085, 992, 478	4.7 (1), 4.8 (2-3), 4.9 (4), 56.5 (5)	23 (1-4), 56.5 (5)	4.65	56.5	535	3.0 $\times 10^{-4}$	3.0 $\times 10^{-5}$	
	5	138.5, 0.033, 45.8	1089, 993, 478	4.8 (1-2), 4.9 (3-4), 56.8 (5)	23.0 (1-4), 56.8 (5)	4.75	56.8	536	2.8 $\times 10^{-4}$	7.2 $\times 10^{-6}$	
CASE.BUFF (23.5 MW)	1	66.1, 0.034, 21.8	1000, 992, 477	4.4 (1), 4.6 (2), 4.7 (3), 4.9 (4), 55.8 (5)	23.0 (1), 23.1 (2-4), 55.8 (5)	4.31	55.8	529	6.1 $\times 10^{-4}$	2.8 $\times 10^{-4}$	
CASE.EFF (23.5 MW)	1	69.3, 0.010, 22.9	1000, 1009, 477	5.0 (1-4), 48.0 (5)	23.0 (1-4), 48.0 (5)	4.95	48.0	480	6.8 $\times 10^{-5}$	1.6 $\times 10^{-7}$	
CASE.FLEX.HI	1	40.5, 0.044, 13.3	1000, 976, 519	10.1, 17.5, 25.7, 35.0, 49.9	27.1, 31.6, 36.3, 41.4, 49.9	3.09	49.9	492	1.3 $\times 10^{-3}$	8.9 $\times 10^{-4}$	
	2	57.7, 0.063, 19.0	1020, 858, 519	9.5, 17.2, 25.9, 35.9, 51.4	27.3, 31.9, 36.8, 42.2, 51.4	3.04	51.4	506	1.4 $\times 10^{-3}$	1.1 $\times 10^{-3}$	
	3	104.3, 0.064, 34.4	1061, 868, 519	10.5, 18.4, 27.1, 37.0, 52.2	27.4, 32.0, 37.1, 42.5, 52.2	3.25	52.2	504	8.0 $\times 10^{-4}$	5.0 $\times 10^{-4}$	
	4	145.4, 0.070, 47.9	1084, 809, 519	10.8, 18.9, 28.0, 38.4, 53.9	27.6, 32.4, 37.7, 43.4, 53.9	3.32	53.9	511	6.4 $\times 10^{-4}$	3.9 $\times 10^{-4}$	
	5	154.5, 0.067, 51.0	1089, 864, 519	11.8, 19.8, 28.7, 38.9, 54.0	27.6, 32.4, 37.7, 43.4, 54.0	3.45	54.0	510	5.6 $\times 10^{-4}$	2.7 $\times 10^{-4}$	

Table D.5.: Optimization results. \dot{C}_{22,CH_3OH} annual revenue from selling methanol at 580 € ton^{-1} , prevailing price for the first quarter of 2022 in Germany [212]. Cost \dot{C}_{Plant}^{Δ} incorporates the process units subject to optimization (SOEC, RWGS, METHL). All costs are annualized, i.e., the absolute cost divided the expected number of years of operations.

case-study	Π	\dot{C}_{22,CH_3OH}	η_{PtCH_3OH}	\dot{C}_{Plant}^{Δ}	$\dot{C}_{SOEC}^{(\pi)}$ 2 years	$\dot{C}_{RWGS}^{(\pi)}$		$\dot{C}_{METHL}^{(\pi)}$		$\dot{C}_{buffering\ device}^{(\pi)}$ 12 h peak ⁽¹⁾ 24 h peak ⁽²⁾		
						tube 10 years	catalyst 2 years	tube bundle 10 years	catalyst 2 years	Li-ion ^(a) 10 years	H ₂ tank ^(b) 10 years	
CASE.FLEX	1	7 016 230	60.5%	1 696 183	1 164 294	177	117	134 443	397 152	-	-	
	2	10 098 010	59.6%									
	3	18 078 350	58.6%									
	4	25 294 736	57.9%									
	5	26 844 032	57.8%									
annual	14 694 648											
CASE.BUFF (23.5 MW)	1	12 787 612	59.2%	5 882 874 ^(a1) 10 321 674 ^(a2)	2 073 244 ^(b1) 2 526 118 ^(b2)	1 012 730	210	147	119 051	311 936	4 438 800 8 877 600	629 170 1 082 044
CASE.EFF (23.5 MW)	1	13 433 982	62.2%	12 532 238 ^(a1) 16 971 038 ^(a2)	8 722 608 ^(b1) 9 175 482 ^(b2)	1 062 601	262	192	736 959	6 293 424	4 438 800 8 877 600	629 170 1 082 044
CASE.FLEX.HI	1	7 806 601	67.3%	2 028 551	1 294 898	272	202	91 435	641 744	-	-	
	2	11 090 451	65.5%									
	3	20 106 823	65.3%									
	4	28 042 199	64.2%									
	5	29 835 414	64.3%									
annual	16 309 948											

Bibliography

- [1] Svante Arrhenius. “On the influence of carbonic acid in the air upon the temperature of the ground”. In: *The London, Edinburgh, and Dublin Philosophical Magazine and Journal of Science* 41.251 (1896), pp. 237–276. DOI: 10.1080/14786449608620846 (cit. on p. 1).
- [2] Mikael Höök and Xu Tang. “Depletion of fossil fuels and anthropogenic climate change: A review”. In: *Energy Policy* 52 (2013), pp. 797–809. DOI: 10.1016/j.enpol.2012.10.046 (cit. on p. 1).
- [3] Intergovernmental Panel on Climate Change (IPCC). *Synthesis report of the sixth assessment report*. 2022. URL: <https://www.ipcc.ch/ar6-syr/> (visited on Dec. 30, 2022) (cit. on p. 1).
- [4] United Nations. *The Paris Agreement*. URL: <https://unfccc.int/process-and-meetings/the-paris-agreement/the-paris-agreement> (visited on Dec. 30, 2022) (cit. on p. 1).
- [5] Carlo Buontempo and Samantha Burgess. *Copernicus: 2024 is the first year to exceed 1.5°C above pre-industrial level*. 2025. URL: <https://climate.copernicus.eu> (visited on Jan. 14, 2025) (cit. on p. 1).
- [6] GDO. *Drought in Europe - GDO Analytical Report*. 2022. URL: https://edo.jrc.ec.europa.eu/documents/news/GDO-EDODroughtNews202208_Europe.pdf (visited on Dec. 30, 2022) (cit. on p. 1).
- [7] EPA. *Global greenhouse gas emissions data*. URL: <https://www.epa.gov/ghgemissions/global-greenhouse-gas-emissions-data> (cit. on p. 1).
- [8] Priyadarshi R. Shukla, Jim Skea, and Andy Reisinger. *IPCC climate change 2022: mitigation of climate change*. URL: https://www.ipcc.ch/report/ar6/wg3/downloads/report/IPCC_AR6_WGIII_SPM.pdf (cit. on p. 1).
- [9] Agora. *European energy transition 2030: the big picture. Ten Priorities for the next European Commission to meet the EU’s 2030 targets and accelerate towards 2050*. URL: https://www.agora-energiewende.de/fileadmin/Projekte/2019/EU_Big_Picture/153_EU-Big-Pic_WEB.pdf (cit. on p. 2).
- [10] *Renewable Power Generation Costs in 2020*. 2021. URL: https://edo.jrc.ec.europa.eu/documents/news/GDO-EDODroughtNews202208_Europe.pdf (visited on Apr. 1, 2023) (cit. on pp. 3, 23).
- [11] IRENA. *Renewable Power Generation Costs in 2021*. 2022. URL: https://www.irena.org/-/media/Files/IRENA/Agency/Publication/2022/Jul/IRENA_Power_Generation_Costs_2021.pdf (cit. on p. 3).
- [12] Luis Puigjaner and Georges Heyen. *Computer Aided Process and Product Engineering (CAPE)*. John Wiley & Sons, 2007 (cit. on p. 4).

- [13]Lorenz T. Biegler, Ignacio E. Grossmann, and Arthur W. Westerberg. *Systematic Methods of Chemical Process Design*. English. Prentice Hall international series in the physical and chemical engineering sciences. Upper Saddle River, N.J.: Prentice Hall PTR, 1997. ISBN: 0134924223 (cit. on pp. 4, 17, 18, 20, 61, 68).
- [14]M. Soledad Diaz and Alberto Bandoni. “A mixed integer optimization strategy for a large scale chemical plant in operation”. In: *Computers & Chemical Engineering* 20.5 (1996), pp. 531–545. DOI: 10.1016/0098-1354(95)00209-X (cit. on p. 5).
- [15]Miguel A. Navarro-Amorós, Rubén Ruiz-Femenia, and José A. Caballero. “Integration of modular process simulators under the Generalized Disjunctive Programming framework for the structural flowsheet optimization”. In: *Computers & Chemical Engineering* 67 (2014), pp. 13–25. DOI: 10.1016/j.compchemeng.2014.03.014 (cit. on p. 5).
- [16]José Antonio Vazquez-Castillo, Josué Addiel Venegas-Sánchez, Juan Gabriel Segovia-Hernández, Héctor Hernández-Escoto, Salvador Hernandez, Claudia Gutiérrez-Antonio, and Abel Briones-Ramírez. “Design and optimization, using genetic algorithms, of intensified distillation systems for a class of quaternary mixtures”. In: *Computers & Chemical Engineering* 33.11 (2009), pp. 1841–1850. DOI: 10.1016/j.compchemeng.2016.02.009 (cit. on p. 5).
- [17]John C. Eslick and David C. Miller. “A multi-objective analysis for the retrofit of a pulverized coal power plant with a CO₂ capture and compression process”. In: *Computers & Chemical Engineering* 35.8 (2011), pp. 1488–1500. DOI: 10.1016/j.compchemeng.2011.03.020 (cit. on p. 5).
- [18]Michele Corbetta, Ignacio E. Grossmann, and Flavio Manenti. “Process simulator-based optimization of biorefinery downstream processes under the Generalized Disjunctive Programming framework”. In: *Computers & Chemical Engineering* 88 (2016), pp. 73–85. DOI: 10.1016/j.compchemeng.2016.02.009 (cit. on p. 5).
- [19]Ignacio E. Grossmann and Roger W. H. Sargent. “Optimum design of chemical plants with uncertain parameters”. In: *AIChE Journal* 24.6 (1978), pp. 1021–1028. DOI: 10.1002/aic.690240612 (cit. on pp. 7, 120).
- [20]Pamela L. Spath and David C. Dayton. *Preliminary Screening–Technical and Economic Assessment of Synthesis Gas to Fuels and Chemicals with Emphasis on the Potential for Biomass-derived Syngas*. Tech. rep. National Renewable Energy Lab., Golden, CO.(US), 2003. DOI: 10.2172/15006100 (cit. on p. 8).
- [21]Marcus Wenzel, Liisa Rihko-Struckmann, and Kai Sundmacher. “Thermodynamic analysis and optimization of RWGS processes for solar syngas production from CO₂.” In: *AIChE Journal* 63.1 (2017), pp. 15–22. DOI: DOI10.1002/aic.15445. URL: <https://doi.org/10.1002/aic.15445> (cit. on p. 8).
- [22]Wolfgang Schneider and Werner Diller. “Phosgene”. In: *Ullmann’s Encyclopedia of Industrial Chemistry* (2000). DOI: 10.1002/14356007.a19_411 (cit. on p. 8).
- [23]Carole Le Berre, Philippe Serp, Philippe Kalck, and G. Paull Torrence. “Acetic acid”. In: *Ullmann’s Encyclopedia of Industrial Chemistry* (2014). DOI: 10.1002/14356007.a01_045.pub3 (cit. on p. 8).
- [24]Robert Franke, Detlef Selent, and Armin Börner. “Applied hydroformylation”. In: *Chemical Reviews* 112.11 (2012), pp. 5675–5732. DOI: 10.1021/cr3001803 (cit. on p. 8).
- [25]Mohammed Liaket Ali, Quentin Fradet, and Uwe Riedel. “Kinetic mechanism development for the direct reduction of single hematite pellets in H₂/CO atmospheres”. In: *Steel Research International* (2022), p. 2200043. DOI: 10.1002/srin.202200043 (cit. on p. 8).
- [26]Shaobin Wang. “Application of solid ash based catalysts in heterogeneous catalysis”. In: *Environmental Science & Technology* 42.19 (2008), pp. 7055–7063. DOI: 10.1002/14356007.o05_o03 (cit. on p. 8).

- [27]Jorg Ott, Veronika Gronemann, Florian Pontzen, Eckhard Fiedler, Georg Grossmann, D. Burkhard Kersebohm, Günther Weiss, and Claus Witte. “Methanol”. In: *Ullmann’s Encyclopedia of Industrial Chemistry* (2012). DOI: 10.1002/14356007.a16_465.pub3 (cit. on p. 8).
- [28]CRH De Smet, MHJM De Croon, RJ Berger, GB Marin, and JC Schouten. “Design of adiabatic fixed-bed reactors for the partial oxidation of methane to synthesis gas. Application to production of methanol and hydrogen-for-fuel-cells”. In: *Chemical Engineering Science* 56.16 (2001), pp. 4849–4861. DOI: 10.1016/s0009-2509(01)00130-0 (cit. on pp. 10, 102).
- [29]Mariana M.V.M. Souza and Martin Schmal. “Autothermal reforming of methane over Pt/ZrO₂/Al₂O₃ catalysts”. In: *Applied Catalysis A: General* 281.1-2 (2005), pp. 19–24. DOI: 10.1016/j.apcata.2004.11.007 (cit. on p. 10).
- [30]S.S. Bharadwaj and Lanny D. Schmidt. “Catalytic partial oxidation of natural gas to syngas”. In: *Fuel Processing Technology* 42.2-3 (1995), pp. 109–127 (cit. on p. 10).
- [31]Philipp Kaiser, Rajabhau Bajirao Unde, Christoph Kern, and Andreas Jess. “Production of liquid hydrocarbons with CO₂ as carbon source based on reverse water-gas shift and Fischer-Tropsch synthesis”. In: *Chemie Ingenieur Technik* 85.4 (2013), pp. 489–499. DOI: 10.1002/cite.201200179 (cit. on p. 10).
- [32]Yolanda A. Daza and John N. Kuhn. “CO₂ conversion by reverse water gas shift catalysis: comparison of catalysts, mechanisms and their consequences for CO₂ conversion to liquid fuels”. In: *RSC Advances* 6.55 (2016), pp. 49675–49691. DOI: 10.1039/c6ra05414e (cit. on p. 11).
- [33]Jamest T. Richardson and S.A. Paripatyadar. “Carbon dioxide reforming of methane with supported rhodium”. In: *Applied Catalysis* 61.1 (1990), pp. 293–309. DOI: 10.1016/s0166-9834(00)82152-1 (cit. on pp. 11, 102, 104, 165).
- [34]Shalini Arora and R. Prasad. “An overview on dry reforming of methane: strategies to reduce carbonaceous deactivation of catalysts.” In: *RSC Advances* 6.110 (2016), pp. 108668–108688. DOI: 10.1039/C6RA20450C (cit. on p. 11).
- [35]Doan Pham Minh, Xuan-Huynh Pham, Tan Ji Siang, and Dai-Viet N Vo. “Review on the catalytic tri-reforming of methane-Part I: impact of operating conditions, catalyst deactivation and regeneration”. In: *Applied Catalysis A: General* 621 (2021), p. 118202. DOI: 10.1016/j.apcata.2021.11820 (cit. on p. 12).
- [36]Lidia Pino, Antonio Vita, Massimo Lagana, and Vincenzo Recupero. “Hydrogen from biogas: catalytic tri-reforming process with Ni/LaCeO mixed oxides.” In: *Applied Catalysis B: Environmental* 148 (2014), pp. 91–105 (cit. on p. 12).
- [37]Ebrahim Rezaei and Lionel J.J. Catalan. “Evaluation of CO₂ utilization for methanol production via tri-reforming of methane”. In: *Journal of CO₂ Utilization* 42 (2020), p. 101272. DOI: 10.1016/j.jcou.2020.101272 (cit. on pp. 12, 167).
- [38]Doan Pham Minh, Tan Ji Siang, Dai-Viet N Vo, Thanh Son Phan, Cyrille Ridart, Ange Nzihou, and Didier Grouset. “Hydrogen production from biogas reforming: an overview of steam reforming, dry reforming, dual reforming, and tri-reforming of methane”. In: *Hydrogen Supply Chains* (2018), pp. 111–166 (cit. on p. 12).
- [39]Z. Arab Aboosadi, Abdolhossein Jahanmiri, and Mohammad Reza Rahimpour. “Optimization of tri-reformer reactor to produce synthesis gas for methanol production using differential evolution (DE) method”. In: *Applied Energy* 88.8 (2011), pp. 2691–2701. DOI: 10.1016/j.apenergy.2011.02.017 (cit. on pp. 12, 167).

- [40]Rei-Yu Chein, Chien-Yu Wang, and Ching-Tsung Yu. “Parametric study on catalytic tri-reforming of methane for syngas production”. In: *Energy* 118 (2017), pp. 1–17. DOI: 10.1016/j.energy.2016.11.147 (cit. on pp. 12, 167).
- [41]Rajib Kumar Singha, Astha Shukla, Aditya Yadav, Shubhadeep Adak, Zafar Iqbal, Nazia Siddiqui, and Rajaram Bal. “Energy efficient methane tri-reforming for synthesis gas production over highly coke resistant nanocrystalline Ni/ZrO₂ catalyst.” In: *Applied Energy* 178 (2016), pp. 110–125 (cit. on p. 12).
- [42]Giuseppe Pantaleo, Valeria La Parola, Francesca Deganello, Rajib Kumar Singha, Rajaram Bal, and A.M. Venezia. “Ni/CeO₂ catalysts for methane partial oxidation: synthesis driven structural and catalytic effects.” In: *Applied Catalysis B: Environmental* 189 (2016), pp. 233–241. DOI: 10.1016/j.apcatb.2016.02.064. URL: <https://doi.org/10.1016/j.apcatb.2016.02.064> (cit. on p. 12).
- [43]Dohyung Kang, Hyun Suk Lim, Minbeom Lee, and Jae W Lee. “Syngas production on a Ni-enhanced Fe₂O₃/Al₂O₃ oxygen carrier via chemical looping partial oxidation with dry reforming of methane.” In: *Applied Energy* 211 (2018), pp. 174–186 (cit. on p. 12).
- [44]Maximilian Schalenbach, Aleksandar R Zeradjanin, Olga Kasian, Serhiy Cherevko, and Karl JJ Mayrhofer. “A perspective on low-temperature water electrolysis—challenges in alkaline and acidic technology”. In: *International Journal of Electrochemical Science* 13.2 (2018), pp. 1173–1226 (cit. on pp. 12, 13).
- [45]Kai Zeng and Dongke Zhang. “Recent progress in alkaline water electrolysis for hydrogen production and applications”. In: *Progress in Energy and Combustion Science* 36.3 (2010), pp. 307–326 (cit. on p. 12).
- [46]Marcelo Carmo, David L. Fritz, Jürgen Mergel, and Detlef Stolten. “A comprehensive review on PEM water electrolysis”. In: *International Journal of Hydrogen Energy* 38.12 (2013), pp. 4901–4934. DOI: 10.1016/j.ijhydene.2013.01.151 (cit. on pp. 12, 13).
- [47]Jörn Brauns and Thomas Turek. “Alkaline water electrolysis powered by renewable energy: A review”. In: *Processes* 8.2 (2020), p. 248 (cit. on pp. 12, 13).
- [48]Senan F Amireh, Niels N Heineman, Paul Vermeulen, Rodrigo Lira Garcia Barros, Dongsheng Yang, John van der Schaaf, and Matheus T de Groot. “Impact of power supply fluctuation and part load operation on the efficiency of alkaline water electrolysis”. In: *Journal of Power Sources* 560 (2023), p. 232629 (cit. on p. 12).
- [49]Martín David, Carlos Ocampo-Martínez, and Ricardo Sánchez-Peña. “Advances in alkaline water electrolyzers: A review”. In: *Journal of Energy Storage* 23 (2019), pp. 392–403 (cit. on pp. 12, 13).
- [50]Pierre Millet, R. Ngameni, Sergey Grigoriev, N. Mbemba, F. Brisset, Alireza RANJBARI, and C. Etiévant. “PEM water electrolyzers: from electrocatalysis to stack development”. In: *International Journal of Hydrogen Energy* 35.10 (2010), pp. 5043–5052. DOI: 10.1016/j.ijhydene.2009.09.015 (cit. on pp. 13, 26).
- [51]Ragnhild Hancke, Thomas Holm, and Øystein Ulleberg. “The case for high-pressure PEM water electrolysis”. In: *Energy Conversion and Management* 261 (2022), p. 115642 (cit. on p. 13).
- [52]Geert Tjarks, Andrej Gibelhaus, Franz Lanzerath, Martin Müller, André Bardow, and Detlef Stolten. “Energetically-optimal PEM electrolyzer pressure in power-to-gas plants”. In: *Applied Energy* 218 (2018), pp. 192–198 (cit. on p. 13).
- [53]Ragnhild Hancke, Piotr Bujlo, Thomas Holm, and Øystein Ulleberg. “High-pressure PEM water electrolyser performance up to 180 bar differential pressure”. In: *Journal of Power Sources* 601 (2024), p. 234271 (cit. on p. 13).

- [54]Anne Hauch, Rainer Küngas, Peter Blennow, Anders Bavnhøj Hansen, John Bøgild Hansen, Brian Vad Mathiesen, and Mogens Bjerg Mogensen. “Recent advances in solid oxide cell technology for electrolysis”. In: *Science* 370.6513 (2020), eaba6118 (cit. on p. 13).
- [55]*Green hydrogen cost reduction: scaling up electrolyzers to meet the 1.5 °C climate goal*. 2020. URL: https://www.irena.org/-/media/Files/IRENA/Agency/Publication/2020/Dec/IRENA_Green_hydrogen_cost_2020.pdf (visited on Apr. 13, 2023) (cit. on p. 13).
- [56]Philipp Haug, Matthias Koj, and Thomas Turek. “Influence of process conditions on gas purity in alkaline water electrolysis”. In: *International Journal of Hydrogen Energy* 42.15 (2017), pp. 9406–9418 (cit. on p. 13).
- [57]International Energy Agency. *Biogas upgrading and utilisation*. 1999. URL: http://213.229.136.11/bases/ainia_probiogas.nsf (visited on Apr. 13, 2023) (cit. on p. 14).
- [58]Eline Ryckebosch, Margriet Drouillon, and Han Vervaeren. “Techniques for transformation of biogas to biomethane”. In: *Biomass and Bioenergy* 35.5 (2011), pp. 1633–1645. DOI: 10.1016/j.biombioe.2011.02.033 (cit. on p. 14).
- [59]Qie Sun, Hailong Li, Jinying Yan, Longcheng Liu, Zhixin Yu, and Xinhai Yu. “Selection of appropriate biogas upgrading technology—a review of biogas cleaning, upgrading and utilisation”. In: *Renewable and Sustainable Energy Reviews* 51 (2015), pp. 521–532. DOI: 10.1016/j.rser.2015.06.029 (cit. on p. 14).
- [60]Nicolas Abatzoglou and Steve Boivin. “A review of biogas purification processes”. In: *Biofuels, Bioproducts and Biorefining* 3.1 (2009), pp. 42–71. DOI: 10.1002/bbb.117 (cit. on p. 14).
- [61]Sofia G. Simoes, Justina Catarino, Ana Picado, Tiago F Lopes, Santino Di Berardino, Filipa Amorim, Francisco Giro, CM Rangel, and Teresa Ponce de Leao. “Water availability and water usage solutions for electrolysis in hydrogen production”. In: *Journal of Cleaner Production* 315 (2021), p. 128124. DOI: /10.1016/j.jclepro.2021.128124 (cit. on pp. 14, 146).
- [62]Jungbin Kim, Kiho Park, Dae Ryook Yang, and Seungkwon Hong. “A comprehensive review of energy consumption of seawater reverse osmosis desalination plants”. In: *Applied Energy* 254 (2019), p. 113652. DOI: 10.1016/j.apenergy.2019.113652 (cit. on p. 14).
- [63]Nikolay Voutchkov. “Energy use for membrane seawater desalination—current status and trends”. In: *Desalination* 431 (2018), pp. 2–14. DOI: 10.1016/j.desal.2017.10.033 (cit. on p. 14).
- [64]Stefan Rabe, Thanh-Binh Truong, and Frédéric Vogel. “Catalytic autothermal reforming of methane: Performance of a kW scale reformer using pure oxygen as oxidant”. In: *Applied Catalysis A: General* 318 (2007), pp. 54–62. DOI: 10.1016/j.apcata.2006.10.043 (cit. on p. 14).
- [65]Medhat A. Nemitallah, Mohamed A. Habib, Hassan M. Badr, Syed A. Said, Aqil Jamal, Rached Ben-Mansour, Esmail M.A. Mokheimer, and K. Mezghani. “Oxy-fuel combustion technology: current status, applications, and trends”. In: *International Journal of Energy Research* 41.12 (2017), pp. 1670–1708. DOI: <https://doi.org/10.1002/er.3722> (cit. on pp. 14, 15).
- [66]Alexandre C Dimian and Costin Sorin Bildea. *Chemical Process Design: Computer-aided Case Studies*. John Wiley & Sons, 2008. Chap. 3 (cit. on p. 15).
- [67]Andreas Jess and Peter Wasserscheid. *Chemical Technology: from Principles to Products*. John Wiley & Sons, 2020. Chap. 3. ISBN: 978-3-527-34421-5 (cit. on p. 15).
- [68]Warren D. Seider, Daniel R. Lewin, and J. D. Seader. *Process Design Principles: Synthesis, Analysis, and Evaluation*. John Wiley & Sons, Inc., 1999. ISBN: 978-1-119-28263-1 (cit. on pp. 17, 18, 20).

- [69]Naonori Nishida, George Stephanopoulos, and Arthur W Westerberg. “A review of process synthesis”. In: *AIChE Journal* 27.3 (1981), pp. 321–351. DOI: 10.1002/aic.690270302 (cit. on p. 18).
- [70]James Merrill Douglas. *Conceptual Design of Chemical Processes*. Vol. 1110. McGraw-Hill New York, 1988 (cit. on pp. 18, 182).
- [71]Mark M. Daichendt and Ignacio E. Grossmann. “Integration of hierarchical decomposition and mathematical programming for the synthesis of process flowsheets”. In: *Computers & Chemical Engineering* 22.1-2 (1998), pp. 147–175 (cit. on p. 18).
- [72]Tong Zhang, Nikolaos V Sahinidis, and Jeffrey J Siirola. “Pattern recognition in chemical process flowsheets”. In: *AIChE Journal* 65.2 (2019), pp. 592–603 (cit. on p. 18).
- [73]Thibaut Neveux. “Ab-initio process synthesis using evolutionary programming”. In: *Chemical Engineering Science* 185 (2018), pp. 209–221 (cit. on p. 18).
- [74]Tomio Umeda, Akira Hirai, and Atsunobu Ichikawa. “Synthesis of optimal processing system by an integrated approach”. In: *Chemical Engineering Science* 27.4 (1972), pp. 795–804 (cit. on p. 19).
- [75]RWH Sargent. “Optimum design of plate distillation columns”. In: *Optimization in Action* 58 (1976), p. 267 (cit. on p. 19).
- [76]Ignacio E. Grossmann and RWH Sargent. “Optimum design of heat exchanger networks”. In: *Computers & Chemical Engineering* 2.1 (1978), pp. 1–7. DOI: 10.1016/0098-1354(78)80001-5 (cit. on p. 19).
- [77]Jaime Cerda and Arthur W Westerburg. “Synthesizing heat exchanger networks having restricted stream/stream matches using transportation problem formulations”. In: *Chemical Engineering Science* 38.10 (1983), pp. 1723–1740 (cit. on p. 19).
- [78]Soterios A. Papoulias and Ignacio E. Grossmann. “A structural optimization approach in process synthesis - II: Heat recovery networks”. In: *Computers & Chemical Engineering* 7.6 (1983), pp. 707–721 (cit. on p. 19).
- [79]Christodoulos A. Floudas, Amy R. Ciric, and Ignacio E. Grossmann. “Automatic synthesis of optimum heat exchanger network configurations”. In: *AIChE Journal* 32.2 (1986), pp. 276–290 (cit. on p. 19).
- [80]Alok K. Saboo, Manfred A. Morari, and Richard D. Colberg. “RESHEX: An interactive software package for the synthesis and analysis of resilient heat-exchanger networks—I: Program description and application”. In: *Computers & Chemical Engineering* 10.6 (1986), pp. 577–589 (cit. on p. 19).
- [81]Mark J. Andreovich and Arthur W. Westerberg. “A simple synthesis method based on utility bounding for heat-integrated distillation sequences”. In: *AIChE Journal* 31.3 (1985), pp. 363–375 (cit. on p. 19).
- [82]Avanish Aggarwal and Christodoulos A. Floudas. “Synthesis of general distillation sequences—nonsharp separations”. In: *Computers & Chemical Engineering* 14.6 (1990), pp. 631–653. DOI: 10.1016/0098-1354(90)87033-L (cit. on p. 19).
- [83]Arthur W. Westerberg. “The synthesis of distillation-based separation systems”. In: *Computers & Chemical Engineering* 9.5 (1985), pp. 421–429. DOI: 10.1016/0098-1354(85)80020-X (cit. on p. 19).
- [84]Hector Yeomans and Ignacio E. Grossmann. “A systematic modeling framework of superstructure optimization in process synthesis”. In: *Computers & Chemical Engineering* 23.6 (1999), pp. 709–731. DOI: 10.1002/aic.690240612 (cit. on p. 19).

- [85]Ramesh Raman and Ignacio E. Grossmann. “Relation between MILP modelling and logical inference for chemical process synthesis”. In: *Computers & Chemical Engineering* 15.2 (1991), pp. 73–84 (cit. on p. 19).
- [86]Ramesh Raman and Ignacio E. Grossmann. “Modelling and computational techniques for logic based integer programming”. In: *Computers & Chemical Engineering* 18.7 (1994), pp. 563–578. DOI: 10.1016/0098-1354(93)E0010-7 (cit. on p. 19).
- [87]Sangbum Lee and Ignacio E. Grossmann. “New algorithms for nonlinear generalized disjunctive programming”. In: *Computers & Chemical Engineering* 24.9-10 (2000), pp. 2125–2141. DOI: 10.1016/S0098-1354(00)00581-0 (cit. on p. 19).
- [88]Richard Turton, Richard C Bailie, Wallace B Whiting, and Joseph A Shaeiwitz. *Analysis, Synthesis, and Design of Chemical Processes*. English. 4. ed., international ed. Prentice Hall international series in the physical and chemical engineering sciences. Upper Saddle River, NJ (US): Pearson Education International, 2013. ISBN: 0132940299 (cit. on pp. 20, 21).
- [89]Thomas F. Edgar, David Mautner Himmelblau, and Leon S. Lasdon. *Optimization of Chemical Processes*. McGraw Hill, 2001. ISBN: 0070393591 (cit. on p. 20).
- [90]Jacques Richalet. “Industrial applications of model based predictive control”. In: *Automatica* 29.5 (1993), pp. 1251–1274. DOI: 10.1016/0005-1098(93)90049-Y (cit. on p. 20).
- [91]Carlos E Garcia, David M Prett, and Manfred Morari. “Model predictive control: Theory and practice — A survey”. In: *Automatica* 25.3 (1989), pp. 335–348. DOI: 10.1016/0005-1098(89)90002-2 (cit. on p. 20).
- [92]S Joe Qin and Thomas A Badgwell. “An overview of industrial model predictive control technology”. In: *AIChE Symposium Series*. Vol. 93. 316. New York, NY: American Institute of Chemical Engineers, 1971-c2002. 1997, pp. 232–256 (cit. on p. 20).
- [93]Jan L.A. Koolen. *Design of Simple and Robust Process Plants*. John Wiley & Sons, 2001. ISBN: 3527297847 (cit. on p. 21).
- [94]Rajesh Jugulum and Daniel D Frey. “Toward a taxonomy of concept designs for improved robustness”. In: *Journal of Engineering Design* 18.2 (2007), pp. 139–156 (cit. on p. 21).
- [95]Bundesnetzagentur. *Bundesnetzagentur veröffentlicht Daten zum Strommarkt*. 2022. URL: https://www.bundesnetzagentur.de/SharedDocs/Pressemitteilungen/DE/2023/20230104_smard.html (visited on Dec. 30, 2022) (cit. on p. 23).
- [96]Eurostat. *Shedding light on energy in the EU*. 2022. URL: https://ec.europa.eu/eurostat/cache/infographs/energy/img/pdf/shedding-light-in-the-EU-2022_en.pdf (visited on Apr. 1, 2023) (cit. on p. 23).
- [97]Rainer Reimert, Friedemann Marschner, Hans-Joachim Renner, Walter Boll, Emil Supp, Miron Brejc, Waldemar Liebner, and Georg Schaub. *Gas Production, 2. Processes*. John Wiley & Sons, Ltd, 2011. Chap. 2. ISBN: 9783527306732. DOI: 10.1002/14356007.o12_o01 (cit. on p. 24).
- [98]Boris Bensmann, Richard Hanke-Rauschenbach, IK Pena Arias, and Kai Sundmacher. “Energetic evaluation of high pressure PEM electrolyzer systems for intermediate storage of renewable energies.” In: *Electrochimica Acta* 110 (2013), pp. 570–580. DOI: 10.1016/j.electacta.2013.05.102 (cit. on pp. 26, 59).
- [99]Peter Häussinger, Reiner Lohmüller, and Allan M. Watson. “Hydrogen, 2. Production”. In: *Ullmann’s Encyclopedia of Industrial Chemistry*. John Wiley & Sons, Ltd, 2011. ISBN: 9783527306732. DOI: https://doi.org/10.1002/14356007.o13_o03 (cit. on p. 27).

- [100] Mamata Mukhopadhyay. *Fundamentals of Cryogenic Engineering*. PHI Learning Pvt. Ltd., 2010 (cit. on p. 29).
- [101] Jennifer Uebbing, Liisa K Rihko-Struckmann, and Kai Sundmacher. “Exergetic assessment of CO₂ methanation processes for the chemical storage of renewable energies.” In: *Applied Energy* 233 (2019), pp. 271–282. DOI: 10.1016/j.apenergy.2018.10.014 (cit. on pp. 29, 66).
- [102] Sybrand J. Metz, Wilbert J.C. van de Ven, Jens Potreck, Marcel H.V. Mulder, and Matthias Wessling. “Transport of water vapor and inert gas mixtures through highly selective and highly permeable polymer membranes.” In: *Journal of Membrane Science* 251.1-2 (2005), pp. 29–41. DOI: 10.1016/j.memsci.2004.08.036 (cit. on pp. 29, 66).
- [103] Timothy C. Merkel, Raghubir Gupta, B.S. Turk, and Benny Freeman. “Mixed-gas permeation of syngas components in poly (dimethylsiloxane) and poly (1-trimethylsilyl-1-propyne) at elevated temperatures.” In: *Journal of Membrane Science* 191.1-2 (2001), pp. 85–94. DOI: 10.1016/S0376-7388(01)00452-5 (cit. on pp. 29, 66).
- [104] Sepideh Ziaei, Stuart Cohen, Gary T Rochelle, Thomas F Edgar, and Michael E Webber. “Dynamic operation of amine scrubbing in response to electricity demand and pricing.” In: *Energy Procedia* 1.1 (2009), pp. 4047–4053. DOI: 10.1016/j.egypro.2009.02.211 (cit. on pp. 29, 65, 66).
- [105] Seong-Cheol Jang, Se-Il Yang, Seong-Geun Oh, and Dae-Ki Choi. “Adsorption dynamics and effects of carbon to zeolite ratio of layered beds for multicomponent gas adsorption.” In: *Korean Journal of Chemical Engineering* 28.2 (2011), pp. 583–590. DOI: 10.1007/s11814-010-0399-9 (cit. on pp. 29, 66).
- [106] Fei Gao, Shougui Wang, Weiwen Wang, Jihai Duan, Jipeng Dong, and Guanghui Chen. “Adsorption separation of CO from syngas with CuCl@ AC adsorbent by a VPSA process.” In: *RSC Advances* 8.69 (2018), pp. 39362–39370. DOI: 10.1039/C8RA08578A (cit. on pp. 29, 66).
- [107] Fei Gao, Yaquan Wang, Xiao Wang, and Shuhai Wang. “Selective CO adsorbent CuCl/AC prepared using CuCl₂ as a precursor by a facile method.” In: *RSC Advances* 6.41 (2016), pp. 34439–34446. DOI: 10.1039/C6RA03116A (cit. on pp. 29, 66).
- [108] Robin Smith. *Chemical Process: Design and Integration*. John Wiley & Sons, 2005. ISBN: 0-471-48681-7 (cit. on pp. 30, 63).
- [109] Roongrat Sakwattanapong, Adisorn Aroonwilas, and Amornvadee Veawab. “Behavior of reboiler heat duty for CO₂ capture plants using regenerable single and blended alkanolamines”. In: *Industrial & Engineering Chemistry Research* 44.12 (2005), pp. 4465–4473. DOI: 10.1021/ie050063w (cit. on p. 30).
- [110] C Descamps, Chakib Bouallou, and Mohamed Kanniche. “Efficiency of an integrated gasification combined cycle (IGCC) power plant including CO₂ removal”. In: *Energy* 33.6 (2008), pp. 874–881. DOI: 10.1016/j.energy.2007.07.013 (cit. on p. 32).
- [111] Luca Mencarelli, Qi Chen, Alexandre Pagot, and Ignacio E. Grossmann. “A review on superstructure optimization approaches in process system engineering”. In: *Computers & Chemical Engineering* 136 (2020), p. 106808. DOI: 10.1016/j.compchemeng.2020.106808 (cit. on p. 52).
- [112] Mariano Martín and Thomas A. Adams II. “Future directions in process and product synthesis and design”. In: 44 (2018), pp. 1–10 (cit. on p. 52).
- [113] Scott D. Barnicki and Jeffrey J. Siirola. “Process synthesis prospective”. In: *Computers & Chemical Engineering* 28.4 (2004), pp. 441–446 (cit. on p. 52).

- [114]Sireethorn Satchatippavarn, Elias Martinez-Hernandez, Melissa Yuling Leung Pah Hang, Matthew Leach, and Aidong Yang. “Urban biorefinery for waste processing”. In: *Chemical Engineering Research and Design* 107 (2016), pp. 81–90 (cit. on p. 52).
- [115]Omar Morsy, Farzad Hourfar, Qinqin Zhu, Ali Almansoori, and Ali Elkamel. “A Superstructure Mixed-Integer Nonlinear Programming Optimization for the Optimal Processing Pathway Selection of Sludge-to-Energy Technologies”. In: *Sustainability* 15.5 (2023), p. 4023 (cit. on p. 52).
- [116]Muhammad Rizwan, Jay H Lee, and Rafiqul Gani. “Optimal processing pathway for the production of biodiesel from microalgal biomass: a superstructure based approach”. In: *Computers & Chemical Engineering* 58 (2013), pp. 305–314 (cit. on p. 52).
- [117]Philipp Kenkel, Timo Wassermann, and Edwin Zondervan. “Renewable fuels from Integrated Power- and Biomass-to-X Processes: A Superstructure Optimization Study”. In: *Processes* 10.7 (2022), p. 1298 (cit. on p. 53).
- [118]Joonjae Ryu, Lingxun Kong, Arthur E Pastore de Lima, and Christos T Maravelias. “A generalized superstructure-based framework for process synthesis”. In: *Computers & Chemical Engineering* 133 (2020), p. 106653 (cit. on p. 53).
- [119]Christodoulos A Floudas and Spiros H Anastasiadis. “Synthesis of distillation sequences with several multicomponent feed and product streams”. In: *Chemical Engineering Science* 43.9 (1988), pp. 2407–2419 (cit. on p. 53).
- [120]Dominik Schack and Kai Sundmacher. “Techno-ökonomische Optimierung des Produktionsnetzwerkes für die Synthese von Ameisensäure aus erneuerbaren Ressourcen”. In: *Chemie Ingenieur Technik* 90.1-2 (2018), pp. 256–266. DOI: 10.1002/cite.201700163 (cit. on p. 53).
- [121]Dominik Schack, Liisa Rihko-Struckmann, and Kai Sundmacher. “Linear programming approach for structure optimization of Renewable-to-Chemicals (R2Chem) production networks”. In: *Industrial & Engineering Chemistry Research* 57.30 (2018), pp. 9889–9902. DOI: doi.org/10.1021/acs.iecr.7b05305 (cit. on p. 53).
- [122]Jennifer Uebbing, Liisa Rihko-Struckmann, Sebastian Sager, and Kai Sundmacher. “CO₂ methanation process synthesis by superstructure optimization”. In: *Journal of CO₂ Utilization* 40 (2020), p. 101228 (cit. on p. 53).
- [123]Valerio Paolini, Francesco Petracchini, Marco Segreto, Laura Tomassetti, Nour Naja, and Angelo Cecinato. “Environmental impact of biogas: A short review of current knowledge.” In: *Journal of Environmental Science and Health, Part A* 53.10 (2018), pp. 899–906. DOI: 10.1080/10934529.2018.1459076 (cit. on p. 54).
- [124]Pietro Di Profio, Simone Arca, Federico Rossi, and Mirko Filippini. “Comparison of hHydrogen hydrates with existing hydrogen storage technologies: energetic and economic evaluations.” In: *International Journal of Hydrogen Energy* 34.22 (2009), pp. 9173–9180. DOI: 10.1016/j.ijhydene.2009.09.056 (cit. on p. 55).
- [125]Chunshan Song and Wei Pan. “Tri-reforming of methane: a novel concept for catalytic production of industrially useful synthesis gas with desired H₂/CO ratios”. In: *Catalysis Today* 98.4 (2004), pp. 463–484. DOI: 10.1016/j.cattod.2004.09.054 (cit. on pp. 57, 58).
- [126]Carlos A Grande and Alírio E Rodrigues. “Layered vacuum pressure-swing adsorption for biogas upgrading.” In: *Industrial & Engineering Chemistry Research* 46.23 (2007), pp. 7844–7848. DOI: 10.1021/ie070942d. URL: https://doi.org/10.1021/ie070942d (cit. on p. 63).

- [127] Yu Huang, Tim C Merkel, and Richard W Baker. "Pressure ratio and its impact on membrane gas separation processes." In: *Journal of Membrane Science* 463 (2014), pp. 33–40. DOI: 10.1016/j.memsci.2014.03.016. URL: <https://doi.org/10.1016/j.memsci.2014.03.016> (cit. on p. 63).
- [128] Michal Netusil and Pavel Dittl. "Comparison of three methods for natural gas dehydration." In: *Journal of Natural Gas Chemistry* 20.5 (2011), pp. 471–476. eprint: [https://doi.org/10.1016/S1003-9953\(10\)60218-6](https://doi.org/10.1016/S1003-9953(10)60218-6) (cit. on pp. 65, 66).
- [129] Kunimitsu Morishige. "Adsorption and separation of CO₂/CH₄ on amorphous silica molecular sieve." In: *The Journal of Physical Chemistry C* 115.19 (2011), pp. 9713–9718. DOI: 10.1021/jp202572w (cit. on p. 65).
- [130] Xin Li, Zhong Li, Qibin Xia, and Hongxia Xi. "Effects of pore sizes of porous silica gels on desorption activation energy of water vapour." In: *Applied Thermal Engineering* 27.5-6 (2007), pp. 869–876. DOI: 10.1016/j.applthermaleng.2006.09.010 (cit. on p. 65).
- [131] Alireza Bahadori and Hari B Vuthaluru. "Simple methodology for sizing of absorbers for TEG (triethylene glycol) gas dehydration systems." In: *Energy* 34.11 (2009), pp. 1910–1916. DOI: 10.1016/j.energy.2009.07.047 (cit. on p. 65).
- [132] Li Sun and Robin Smith. "Rectisol wash process simulation and analysis." In: *Journal of Cleaner Production* 39 (2013), pp. 321–328. DOI: 10.1016/j.jclepro.2012.05.049 (cit. on p. 65).
- [133] Khuram Maqsood, Aditi Mullick, Abulhassan Ali, Kajari Kargupta, and Saibal Ganguly. "Cryogenic carbon dioxide separation from natural gas: a review based on conventional and novel emerging technologies." In: *Reviews in Chemical Engineering* 30.5 (2014), pp. 453–477. DOI: 10.1515/revce-2014-0009 (cit. on pp. 65, 66).
- [134] NN Dutta and GS Patil. "Developments in CO separation". In: *Gas Separation & Purification* 9.4 (1995), pp. 277–283 (cit. on p. 66).
- [135] Anwu Li, Weiqiang Liang, and Ronald Hughes. "The effect of carbon monoxide and steam on the hydrogen permeability of a Pd/stainless steel membrane." In: *Journal of Membrane Science* 165.1 (2000), pp. 135–141. DOI: 10.1016/S0376-7388(99)00223-9 (cit. on p. 66).
- [136] Hylke Sijbesma, Kitty Nymeyer, Rob van Marwijk, Rob Heijboer, Jens Potreck, and Matthias Wessling. "Flue gas dehydration using polymer membranes." In: *Journal of Membrane Science* 313.1-2 (2008), pp. 263–276. DOI: 10.1016/j.memsci.2008.01.024 (cit. on p. 66).
- [137] Colin A Scholes, Joannelle Bacus, George Q Chen, Wen X Tao, Gang Li, Abdul Qader, Geoff W Stevens, and Sandra E Kentish. "Pilot plant performance of rubbery polymeric membranes for carbon dioxide separation from syngas." In: *Journal of Membrane Science* 389 (2012), pp. 470–477. DOI: 10.1016/j.memsci.2011.11.011 (cit. on p. 66).
- [138] Yu Wang and M Douglas LeVan. "Adsorption equilibrium of carbon dioxide and water vapor on zeolites 5A and 13X and silica gel: pure components." In: *Journal of Chemical & Engineering Data* 54.10 (2009), pp. 2839–2844. DOI: 10.1021/je800900a (cit. on p. 66).
- [139] José A. Delgado, Vicente I. Águeda, María A. Uguina, Jose L. Sotelo, Pilar Brea, and Carlos A. Grande. "Adsorption and diffusion of H₂, CO, CH₄, and CO₂ in BPL activated carbon and 13X zeolite: evaluation of performance in pressure swing adsorption hydrogen purification by simulation." In: *Industrial & Engineering Chemistry Research* 53.40 (2014), pp. 15414–15426. DOI: 10.1021/ie403744u (cit. on p. 66).
- [140] Jeeban Poudel, Ja Hyung Choi, and Sea Cheon Oh. "Process design characteristics of syngas (CO/H₂) separation using composite membrane." In: *Sustainability* 11.3 (2019), p. 703. DOI: 10.3390/su11030703 (cit. on p. 66).

- [141] Peter Häussinger, Reiner Lohmüller, and Allan M Watson. "Hydrogen, 3. Purification." In: *Ullmann's Encyclopedia of Industrial Chemistry*. American Cancer Society, 2011. DOI: 10.1002/14356007.o13_o04 (cit. on p. 66).
- [142] Anshul Agarwal, Lorenz T Biegler, and Stephen E Zitney. "A superstructure-based optimal synthesis of PSA cycles for post-combustion CO₂ capture." In: *AIChE Journal* 56.7 (2010), pp. 1813–1828. DOI: 10.1002/aic.12107 (cit. on p. 66).
- [143] Jan Andre Wurzbacher, Christoph Gebald, Nicolas Piatkowski, and Aldo Steinfeld. "Concurrent separation of CO₂ and H₂O from air by a temperature-vacuum swing adsorption/desorption cycle." In: *Environmental Science & Technology* 46.16 (2012), pp. 9191–9198. DOI: 10.1021/es301953k (cit. on p. 66).
- [144] James A Ritter and Armin D Ebner. "State-of-the-art adsorption and membrane separation processes for hydrogen production in the chemical and petrochemical industries." In: *Separation Science and Technology* 42.6 (2007), pp. 1123–1193. DOI: 10.1080/01496390701242194 (cit. on p. 66).
- [145] S.P. DiMartino, Jerome L. Glazer, Carlton Douglas Houston, and Mark E. Schott. "Hydrogen/Carbon Monoxide Separation with Cellulose Acetate Membranes." In: *Gas Separation & Purification* 2.3 (1988), pp. 120–125. DOI: 10.1016/0950-4214(88)80027-6 (cit. on p. 66).
- [146] Bo Wang, Adrien P. Côté, Hiroyasu Furukawa, Michael O'Keeffe, and Omar M. Yaghi. "Colossal cages in zeolitic imidazolate frameworks as selective carbon dioxide reservoirs." In: *Nature* 453.7192 (2008), pp. 207–211. DOI: 10.1038/nature06900 (cit. on p. 66).
- [147] Barry Burr and Lili Lyddon. "A Comparison of Physical Solvents for Acid Gas Removal". 2008 (cit. on p. 66).
- [148] G Hochgesand. "Rectisol and Purisol". In: *Industrial & Engineering Chemistry* 62.7 (1970), pp. 37–43. DOI: 10.1021/ie50727a007 (cit. on p. 66).
- [149] Rainer Reimert, Friedemann Marschner, Hans-Joachim Renner, Walter Boll, Emil Supp, Miron Brejc, Waldemar Liebner, and Georg Schaub. "Ullmann's Energy: Resources, Processes, Products." In: Wiley-VCH, 2015. Chap. Gas Production, 2. Processes: Natural Gas. ISBN: 978-3-527-33370-7 (cit. on p. 66).
- [150] Vinay Mulgundmath and F Handan Tezel. "Optimisation of carbon dioxide recovery from flue gas in a TPSA system." In: *Adsorption* 16.6 (2010), pp. 587–598. DOI: 10.1007/s10450-010-9255-9 (cit. on p. 66).
- [151] Hyo Won Kim, Hee Wook Yoon, Seon-Mi Yoon, Byung Min Yoo, Byung Kook Ahn, Young Hoon Cho, Hye Jin Shin, Hoichang Yang, Ungyu Paik, Soongeun Kwon, et al. "Selective gas transport through few-layered graphene and graphene oxide membranes." In: *Science* 342.6154 (2013), pp. 91–95. DOI: 10.1126/science.1236098 (cit. on p. 66).
- [152] S. Sircar and Timothy Golden. "Purification of hydrogen by pressure swing adsorption." In: *Separation Science and Technology* 35.5 (2000), pp. 667–687. DOI: 10.1081/SS-100100183 (cit. on p. 66).
- [153] Haiqing Lin, Scott M Thompson, Adrian Serbanescu-Martin, Johannes G Wijmans, Karl D Amo, Kaaeid A Lokhandwala, and Timothy C Merkel. "Dehydration of natural gas using membranes. Part I: composite membranes." In: *Journal of Membrane Science* 413 (2012), pp. 70–81. DOI: 10.1016/j.memsci.2012.04.009 (cit. on p. 66).
- [154] Carlos A. Grande, Richard Blom, Kari Anne Andreassen, and Ruth E. Stensrød. "Experimental results of pressure swing adsorption (PSA) for pre-combustion CO₂ capture with metal organic frameworks." In: *Energy Procedia* 114 (2017), pp. 2265–2270. DOI: 10.1016/j.egypro.2017.03.1364 (cit. on p. 66).

- [155] Monoj Kumar Mondal, Hemant Kumar Balsora, and Prachi Varshney. “Progress and trends in CO₂ capture/separation technologies: a review.” In: *Energy* 46.1 (2012), pp. 431–441. DOI: 10.1016/j.energy.2012.08.006 (cit. on p. 66).
- [156] Jong-Ho Park, Jong-Nam Kim, and Soon-Haeng Cho. “Performance analysis of four-bed H₂ PSA process using layered beds.” In: *AIChE Journal* 46.4 (2000), pp. 790–802. DOI: 10.1002/aic.690460413 (cit. on p. 66).
- [157] Jaeyoung Yang, Chang-Ha Lee, and Jay-Woo Chang. “Separation of hydrogen mixtures by a two-bed pressure swing adsorption process using zeolite 5A.” In: *Industrial & Engineering Chemistry Research* 36.7 (1997), pp. 2789–2798. DOI: 10.1021/ie960728h (cit. on p. 66).
- [158] Svenskt Gastekniskt Center AB (SGC). *Basic Data on Biogas*. 2012. ISBN: 978-91-85207-10-7 (cit. on p. 66).
- [159] Chonghun Han, Umer Zahid, Jinjoo An, Kyeongsu Kim, and Changsoo Kim. “CO₂ transport: design considerations and project outlook.” In: *Current Opinion in Chemical Engineering* 10 (2015), pp. 42–48. DOI: 10.1016/j.coche.2015.08.001 (cit. on p. 66).
- [160] M.J. Battrum and W. John Thomas. “Carbon monoxide recovery by pressure swing adsorption.” In: *Chemical Engineering Research & Design* 69.A2 (1991), pp. 119–129 (cit. on p. 66).
- [161] Mahdi Fasihi, Olga Efimova, and Christian Breyer. “Techno-economic assessment of CO₂ direct air capture plants”. In: *Journal of Cleaner Production* 224 (2019), pp. 957–980. DOI: <https://doi.org/10.1016/j.jclepro.2019.03.086> (cit. on p. 86).
- [162] Carlo Giorgio Visconti, Luca Lietti, Enrico Tronconi, Pio Forzatti, Roberto Zennaro, and Elisabetta Finocchio. “Fischer–Tropsch synthesis on a Co/Al₂O₃ catalyst with CO₂ containing syngas”. In: *Applied Catalysis A: General* 355.1-2 (2009), pp. 61–68. DOI: 10.1016/j.apcata.2008.11.027 (cit. on p. 93).
- [163] Jacques-Louis Lions, Yvon Maday, and Gabriel Turinici. “Résolution d’EDP par un schéma en temps «pararéel»”. In: *Comptes Rendus de l’Académie des Sciences - Series I - Mathematics* 332.7 (2001), pp. 661–668. DOI: 10.1016/S0764-4442(00)01793-6 (cit. on p. 98).
- [164] Leonardo Baffico, Stephane Bernard, Yvon Maday, Gabriel Turinici, and Gilles Zérah. “Parallel-in-time molecular-dynamics simulations”. In: *Physical Review E* 66.5 (2002), p. 057701. DOI: 10.1103/PhysRevE.66.057701 (cit. on p. 98).
- [165] Yang Cao, Shengtai Li, and Linda Petzold. “Adjoint sensitivity analysis for differential-algebraic equations: algorithms and software”. In: *Journal of Computational and Applied Mathematics* 149.1 (2002), pp. 171–191. DOI: 10.1016/S0377-0427(02)00528-9 (cit. on p. 98).
- [166] Yang Cao, Shengtai Li, Linda Petzold, and Radu Serban. “Adjoint sensitivity analysis for differential-algebraic equations: The adjoint DAE system and its numerical solution”. In: *SIAM Journal on Scientific Computing* 24.3 (2003), pp. 1076–1089. DOI: 10.1137/S1064827501380630 (cit. on p. 98).
- [167] European Biogas Association. *About Biogas and Biomethane*. 2021. URL: <https://www.europeanbiogas.eu/about-biogas-and-biomethane> (visited on June 30, 2021) (cit. on p. 100).
- [168] International Energy Agency. *Report Extract: an Introduction to Biogas and Biomethane*. 2021. URL: <https://www.iea.org/reports/outlook-for-biogas-and-biomethane-prospects-for-organic-growth/an-introduction-to-biogas-and-biomethane> (visited on June 30, 2021) (cit. on p. 100).

- [169]Andrea Maggi, Dominik Garmatter, Sebastian Sager, Martin Stoll, and Kai Sundmacher. “Power-to-Syngas: A Parareal Optimal Control Approach”. In: *Frontiers in Energy Research* 9 (2021), p. 720489. DOI: 10.3389/fenrg.2021.720489 (cit. on p. 100).
- [170]Jianguo Xu and Gilbert F Froment. “Methane steam reforming, methanation and water-gas shift: I. Intrinsic kinetics”. In: *AIChE Journal* 35.1 (1989), pp. 88–96. DOI: 10.1002/aic.690350109 (cit. on pp. 102, 129, 164, 176).
- [171]Ann M De Groote and Gilbert F Froment. “The role of coke formation in catalytic partial oxidation for synthesis gas production”. In: *Catalysis today* 37.3 (1997), pp. 309–329. DOI: 10.1016/S0920-5861(97)00013-8 (cit. on pp. 102, 103).
- [172]David L Trimm and Chi-Wai Lam. “The combustion of methane on platinum—alumina fibre catalysts—I”. In: *Chemical Engineering Science* 35.6 (1980), pp. 1405–1413. DOI: 10.1016/0009-2509(80)85134-7 (cit. on p. 102).
- [173]Joel AE Andersson, Joris Gillis, Greg Horn, James B Rawlings, and Moritz Diehl. “CasADi: a software framework for nonlinear optimization and optimal control”. In: *Mathematical Programming Computation* 11.1 (2019), pp. 1–36. DOI: 10.1007/s12532-018-0139-4 (cit. on pp. 103, 136).
- [174]Andreas Wächter and Lorenz T Biegler. “On the implementation of an interior-point filter line-search algorithm for large-scale nonlinear programming”. In: *Mathematical Programming* 106.1 (2006), pp. 25–57. DOI: 10.1007/s10107-004-0559-y (cit. on pp. 103, 136).
- [175]Oliver Posdziech, Konstantin Schwarze, and Jörg Brabandt. “Efficient hydrogen production for industry and electricity storage via high-temperature electrolysis”. In: *International Journal of Hydrogen Energy* 44.35 (2019), pp. 19089–19101. DOI: 10.1016/j.ijhydene.2018.05.169 (cit. on p. 104).
- [176]John D. Lambert. *Numerical Methods for Ordinary Differential Systems: the Initial Value Problem*. English. Reprint. Wiley, 1995. ISBN: 0471929905 (cit. on p. 108).
- [177]Christian H. Bischof, H. Martin Bücker, Bruno Lang, Arno Rasch, and Andre Vehreschild. “Combining Source Transformation and Operator Overloading Techniques to Compute Derivatives for MATLAB Programs”. In: *Proceedings of the Second IEEE International Workshop on Source Code Analysis and Manipulation (SCAM 2002)*. IEEE Computer Society, 2002, pp. 65–72. DOI: 10.1109/SCAM.2002.1134106 (cit. on p. 109).
- [178]Sebastiano Boscarino. “Error analysis of IMEX Runge–Kutta methods derived from differential-algebraic systems”. In: *SIAM Journal on Numerical Analysis* 45.4 (2007), pp. 1600–1621. DOI: 10.1137/060656929 (cit. on p. 113).
- [179]Johannes Steiner, Daniel Ruprecht, Robert Speck, and Rolf Krause. “Convergence of Parareal for the Navier–Stokes Equations Depending on the Reynolds Number”. In: *Lecture Notes in Computational Science and Engineering*. Springer International Publishing, 2014, pp. 195–202. DOI: 10.1007/978-3-319-10705-9_19 (cit. on p. 113).
- [180]Bastian Bruns, Felix Herrmann, Maria Polyakova, Marcus Grünewald, and Julia Riese. “A systematic approach to define flexibility in chemical engineering”. In: *Journal of Advanced Manufacturing and Processing* 2 (2020), e10063. DOI: 10.1002/amp2.10063 (cit. on p. 120).
- [181]R.R. Iyer and Ignacio E. Grossmann. “Synthesis and operational planning of utility systems for multiperiod operation”. In: *Computers & Chemical Engineering* 22.7-8 (1998), pp. 979–993. DOI: 10.1016/S0098-1354(97)00270-6 (cit. on p. 120).
- [182]Mariano Martín. “Methodology for solar and wind energy chemical storage facilities design under uncertainty: methanol production from CO₂ and hydrogen”. In: *Computers & Chemical Engineering* 92 (2016), pp. 43–54. DOI: 10.1016/j.compchemeng.2016.05.001 (cit. on p. 120).

- [183]Xinyue Peng, Thatcher W Root, and Christos T Maravelias. “Optimization-based process synthesis under seasonal and daily variability: application to concentrating solar power”. In: *AIChE Journal* 65.7 (2019), e16458. DOI: 10.1002/aic.16458 (cit. on p. 120).
- [184]Michael Short, Adeniyi J Isafiade, Duncan M Fraser, and Zdravko Kravanja. “Two-step hybrid approach for the synthesis of multi-period heat exchanger networks with detailed exchanger design”. In: *Applied Thermal Engineering* 105 (2016), pp. 807–821. DOI: 10.1016/j.applthermaleng.2016.05.065 (cit. on p. 120).
- [185]Ronny Tobias Zimmermann, Jens Bremer, and Kai Sundmacher. “Load-flexible fixed-bed reactors by multi-period design optimization”. In: *Chemical Engineering Journal* 428 (2022), p. 130771. DOI: 10.1016/j.cej.2021.130771 (cit. on p. 121).
- [186]Amjad Riaz, Gholamreza Zahedi, and Jiří Jaromír Klemeš. “A review of cleaner production methods for the manufacture of methanol”. In: *Journal of Cleaner Production* 57 (2013), pp. 19–37. DOI: 10.1016/j.jclepro.2013.06.017 (cit. on p. 121).
- [187]Sebastian Verhelst, James WG Turner, Louis Sileghem, and Jeroen Vancoillie. “Methanol as a fuel for internal combustion engines”. In: *Progress in Energy and Combustion Science* 70 (2019), pp. 43–88. DOI: 10.1016/j.pecs.2018.10.001 (cit. on p. 121).
- [188]Vincent Dieterich, Alexander Buttler, Andreas Hanel, Hartmut Spliethoff, and Sebastian Fendt. “Power-to-liquid via synthesis of methanol, DME or Fischer–Tropsch-fuels: a review”. In: *Energy & Environmental Science* 13.10 (2020), pp. 3207–3252. DOI: 10.1039/D0EE01187H (cit. on p. 121).
- [189]Giovanni Gualtieri and Sauro Secci. “Methods to extrapolate wind resource to the turbine hub height based on power law: a 1-h wind speed vs. Weibull distribution extrapolation comparison”. In: *Renewable Energy* 43 (2012), pp. 183–200. DOI: 10.1016/j.renene.2011.12.022 (cit. on p. 124).
- [190]Geert H. Graaf. “Chemical equilibria in methanol synthesis”. In: *Chemical Engineering Science* 41.11 (1986), pp. 2883–2890. DOI: 10.1016/0009-2509(86)80019-7 (cit. on p. 127).
- [191]J Udagawa, P Aguiar, and NP Brandon. “Hydrogen production through steam electrolysis: model-based steady state performance of a cathode-supported intermediate temperature solid oxide electrolysis cell”. In: *Journal of Power Sources* 166.1 (2007), pp. 127–136. DOI: 10.1016/j.jpowsour.2006.12.081 (cit. on pp. 127, 128).
- [192]Marius Mueller, Markus Klinsmann, Ulrich Sauter, Jean-Claude Njodzefon, and André Weber. “High Temperature Solid Oxide Electrolysis–Technology and Modeling”. In: *Chemie Ingenieur Technik* 96.1-2 (2024), pp. 143–166 (cit. on p. 128).
- [193]Floriane Petipas, Annabelle Brisse, and Chakib Bouallou. “Model-based behaviour of a high temperature electrolyser system operated at various loads”. In: *Journal of Power Sources* 239 (2013), pp. 584–595. DOI: 10.1016/j.jpowsour.2013.03.027 (cit. on p. 128).
- [194]Geert H. Graaf, Eize J. Stamhuis, and Anthonius A.C.M. Beenackers. “Kinetics of low-pressure methanol synthesis.” In: *Chemical Engineering Science* 43.12 (1988), pp. 3185–3195. DOI: 10.1016/0009-2509(88)85127-3 (cit. on pp. 129, 177).
- [195]Joel Andersson. *A general-purpose software framework for dynamic optimization (Een algemene softwareomgeving voor dynamische optimalisatie)*. PhD dissertation, KU Leuven, 2013 (cit. on p. 136).
- [196]Harwell Subroutine Library. *A collection of Fortran codes for large scale scientific computation*. 2007. URL: <https://www.hs1.rl.ac.uk/catalogue/> (visited on Apr. 13, 2023) (cit. on p. 136).

- [197] Régis Anghilante, David Colomar, Annabelle Brisse, and Mathieu Marrony. “Bottom-up cost evaluation of SOEC systems in the range of 10–100 MW”. In: *International Journal of Hydrogen Energy* 43.45 (2018), pp. 20309–20322. DOI: 10.1016/j.ijhydene.2018.08.161 (cit. on pp. 141, 183).
- [198] Behnam Zakeri and Sanna Syri. “Electrical energy storage systems: A comparative life cycle cost analysis”. In: *Renewable and Sustainable Energy Reviews* 42 (2015), pp. 569–596. DOI: 10.1016/j.rser.2014.10.011 (cit. on p. 142).
- [199] U.S. Department of Energy. *Hydrogen storage cost analysis final public report*. 2013. URL: <https://www.osti.gov/servlets/purl/1082754> (cit. on p. 142).
- [200] Holger Martin and Michael Nilles. “Radiale Wärmeleitung in durchströmten Schüttungsrohren”. In: *Chemie Ingenieur Technik* 65.12 (1993), pp. 1468–1477. DOI: 10.1002/cite.330651206 (cit. on pp. 166, 180).
- [201] Ralf Bauer and Ernst Ullrich Schluender. “Effektive radiale Wärmeleitfähigkeit gasdurchströmter Schüttungen aus Partikeln unterschiedlicher Form”. In: *Chemie Ingenieur Technik* 48.3 (1976), pp. 227–228. DOI: 10.1002/cite.330480309 (cit. on pp. 166, 180).
- [202] Evangelos Tsotsas. “Heat and Mass Transfer in Packed Beds with Fluid Flow”. In: *VDI Heat Atlas*. Springer Berlin Heidelberg, 2010, pp. 1327–1342. DOI: 10.1007/978-3-540-77877-6_100 (cit. on pp. 166, 180, 181).
- [203] SULZON Energy GmbH. *Sulzon S95-2.1 MW. Wind Turbine Generator Technical Specification*. 2012. URL: https://environment.govmu.org/Documents/eia/eiareports/suzlon_windfarm/annex8.pdf (visited on Dec. 14, 2022) (cit. on p. 169).
- [204] Weather Spark. *Das Wetter das ganze Jahr über an einem beliebigen Ort der Erde*. 2022. URL: <https://de.weatherspark.com/y/71338/Durchschnittswetter-in-Magdeburg-Deutschland-das-ganze-Jahr-%C3%BCber#Figures-WindSpeed> (cit. on p. 169).
- [205] Ingvild Løvik. *Modelling, estimation and optimization of the methanol synthesis with catalyst deactivation*. PhD dissertation, NTNU, Department of Chemical Engineering, 2001 (cit. on p. 175).
- [206] Renato Rota. *Fondamenti di Termodinamica dell’Ingegneria Chimica*. Pitagora Editore, 2015. ISBN: 8837119089 (cit. on p. 179).
- [207] William D. Baasel. *Preliminary Chemical Engineering Plant Design*. Vol. 2. Van Nostrand Reinhold – New York, 1990 (cit. on p. 182).
- [208] Chemical Engineering Plant Cost Index. *Cost Indices*. 2022. URL: <https://www.toweringskills.com/financial-analysis/cost-indices/> (cit. on p. 182).
- [209] Max Stone Peters, Klaus D. Timmerhaus, Ronald Emmett West, et al. *Plant Design and Economics for Chemical Engineers*. Vol. 3. McGraw-Hill – New York, 2003 (cit. on pp. 182, 183).
- [210] *MS-2 methanol catalyst*. 2022. URL: https://www.alibaba.com/product-detail/MS-2-Methanol-catalyst_1600191862387.html?spm=a2700.7724857.0.0.619d20c7AnFt31 (cit. on p. 182).
- [211] *Nickel-alumina catalyst for hydrogenation*. 2022. URL: https://www.alibaba.com/product-detail/Nickel-Alumina-Catalyst-Factory-Price-For_62039092901.html?spm=a2700.details.0.0.70491d7eJSNs7Q1 (cit. on p. 182).
- [212] *Methanol price trend and forecast*. URL: <https://www.chemanalyst.com/Pricing-data/methanol-1> (cit. on p. 185).

List of Figures

3.1	Schematic representation of the separators involved after each reactor. Temperature and pressure levels are reported in orange. Abbreviations: electrolyzer (EL), reverse water-gas shift (RWGS), anaerobic digestion (AD), steam methane reformer (SR).	26
3.2	Fully connected superstructure. Substance nodes (grey circles) accept feedstock and recycles, to be delivered to the reactors (ovals). Excess H ₂ , O ₂ and CH ₄ are stored (dashed boxes). Water and syngas (SG) leave the plant as co-product and product, respectively. Acronyms for process units: electrolyzer (EL), anaerobic digester (AD), steam reformer (SR), vacuum pressure swing adsorption (VPSA), water condenser (CD), membrane separator (MS), amine absorption (AA), cryogenic separator (CR).	28
3.3	Renewable electricity is available: multi-objective optimization results combining total energy and absolute carbon emissions minimization by means of a weight factor ω . At extreme values of ω , the multi-objective optimization results are indicated with colors, where the objective function coincides with the minimization of Objective (A) (total energy, for $\omega = 1$, in purple) and (B) (absolute carbon emissions, for $\omega = 0$, in green), respectively. Different ω values generate two sets of intermediate solutions (in red and within the black rectangle). Discretization of ω : 1×10^4 points. The H ₂ -to-CO ratio is indicated with r	35
3.4	Minimum absolute carbon emissions and relatively inexpensive, available renewable power – Objective (B) ($\omega = 0$): power contributions of reactors, separation sections, and storage systems for surplus O ₂ , CH ₄	36
3.5	(A) Relevant specific molar flowrates as a function of the syngas ratio for minimum absolute carbon emissions in presence of renewable power – Objective (B); (B) feed policies for CH ₄ (from biogas or from natural gas), and CO ₂ , from biogas or external.	37
3.6	Optimal topology for the separation train (Objective (B)).	38
3.7	The optimal topology for intermediate Pareto-optimal solutions at $\omega \in [0.01, 0.21]$ is highlighted in orange, for any value of the syngas ratio r	39
3.8	(A) Feed policies for CH ₄ (from biogas or from natural gas), and CO ₂ , from biogas or external at $\omega \in [0.01, 0.21]$; (B) energy demand.	39
3.9	Energy demands for minimum total power – Objective (A) ($\omega = 1$): power contributions of reactors, separation sections, and storage systems for surplus O ₂ and CH ₄	41

3.10	(A) Molar flowrates of the H ₂ streams: total H ₂ from the steam reformer outlet (H ₂ from SR), share of H ₂ from SR fed to the RWGS reactor for CO ₂ reduction (SR to RWGS), and to the product stream (SR to Syngas). In green, H ₂ stream to the product (H ₂ to Syngas) and from EL to syngas (blue square markers); (B) CO flowrates to the product (CO to Syngas), from the reformers outlets to Syngas (CO from SR and RWGS to Syngas); (C) CH ₄ and CO ₂ feedstock to the reactors (in tones of green), where excess CH ₄ , if available, can be burned to produce thermal energy.	42
3.11	Absolute carbon emissions by contribution. In dark blue, CO ₂ is produced by combustion processes for thermal energy generation; an intermediate tone of blue indicates the excess CO ₂ from the synthesis, therefore not being reduced to CO. In light blue, CH ₄ surplus not utilized in the synthesis which is preferably burned and, if the thermal demand is then completely fulfilled, the remaining is stored.	43
3.12	Pareto-optimal solutions for $\omega \in [0.21, 0.62]$ and H ₂ -to-CO $r > 1$. The region $r \leq 1$ is labeled with $\equiv \omega = 1$: for syngas ratios $r \leq 1$, results at $\omega \in [0.21, 0.62]$ coincide with results at $\omega = 1$ (minimum total energy). Therefore, process configurations and related energy demands at $r \leq 1$ are the same for any value of the weight factor $\omega \geq 0.21$	44
3.13	Renewable electricity is not available: multi-objective (A)+(C). The Pareto-front is absent, as the minimization of energy and carbon efficiency identify the same configurations: as indicated within the figure, results from the minimization of Objective A and C coincide.	45
3.14	(A) Absolute carbon emissions by contribution. From the darkest tone of blue: CO ₂ generated from the combustion of CH ₄ in a powerplant for electricity generation, CO ₂ produced by combustion processes for thermal energy generation, excess CO ₂ from the synthesis not being reduced to CO, CH ₄ surplus not utilized in the synthesis and preferably burned (not present); (B) combustion of natural gas and of surplus bio-CH ₄ : if biogas availability is constrained, the plant should resort to natural gas for heat generation. In this case, no surplus CH ₄ from the synthesis is available for the purpose of heat generation.	46
3.15	Total power demand and net CO ₂ emission if the most sustainable process solution in presence of renewable power were to be operated with natural gas-based electricity from power plant.	47
3.16	Multi-objective solutions, renewable power is available. Recycle of bio-CO ₂ from the utility stream is admitted at the reactors feed and favored in the objective function for the minimization of absolute carbon emissions.	48
3.17	Energy (A), CO ₂ and CH ₄ demand (B) for the process at minimum absolute carbon emissions with renewable electricity and inclusion of recycled bio-CO ₂ from the hot utility within the objective function.	49
4.1	Illustrative process flowsheet. EL = electrolyzer; RWGS = reverse water-gas-shift reactor; SR = steam reforming of methane; POX = partial oxidation of methane; DR = dry reforming of methane; TRI = tri-reforming of methane; TPSA,TSA,VPSA = temperature/pressure/vacuum swing adsorption; TEG = ethylene glycol absorption; MEA = mono-ethanol amine.	55

4.2	Exemplification of separation tasks and methods embedded in the superstructure. For instance, the task of separating CO ₂ from H ₂ can be accomplished by five separation methods: VPSA, palladium membrane, polymeric membrane, chemical and physical absorption. Temperature and pressure are adjusted at the feed to each separation method from the previous temperature and pressure level, i.e., from the previous separator or reactor. Method-specific energy requirements can be accounted for (red and blue arrow for thermal and electrical input, respectively).	56
4.3	Representation of a mixture block delivering mixture ϕ (lowercase) with a single sharp-split separator.	67
4.4	Compact representation of a mixture block delivering mixture ϕ with two sharp-split separators.	68
4.5	(A) Superstructure approach adopted in this chapter, where replicas of the downstream sections are fed by the same components (mixture ϕ) with different composition, pressure and temperature (ζ, T, p) from reactor R1 and R2, respectively; (B) reference formulation not replicating the separators.	69
4.6	(A) Qualitative representation of a possible solution from an energy-based objective function, where different feed states to the separation trains define two redundant units; (B) no redundant units are allowed in the solution due to the problem formulation; (C) equivalent representation without redundancies.	70
4.7	Contributions to the total power requirements for $\min_{N,y} (\dot{Q} + \dot{W})$, biogas as feedstock. Plant complexity is constrained in the separation system, but two or more reformers can be selected simultaneously and interact at the minimum energy demand. The entry "flowrate" indicates the summation of feed flowrates to the reactors.	76
4.8	Yield to CO and molar carbon content in the syngas stream. For syngas applications at low syngas ratios r , RWGS and DR are active. This combination determines the lowest yield and the highest processed flowrates to the reactors, which justifies the increased energy consumption for preconditioning of the inlet, as shown in Figure 4.7.	77
4.9	Atom efficiency for Problem (A) $\min_{N,y} (\dot{Q} + \dot{W})$ and (B) $\min_{N,y} (\dot{Q})$ for constrained topological complexity in the separation train (no redundancy in the separators), where multiple reformers can be active at the same time (cf. Figure 4.7).	80
4.10	Contributions to the total power requirements for $\min_{N,y} \dot{Q}$, biogas as feedstock. Plant complexity is constrained in the separation system and more reactors can be selected simultaneously.	81
4.11	Net thermal power demand and CO ₂ generation for the two objectives, $\min_{N,y} (\dot{Q} + \dot{W})$ and $\min_{N,y} \dot{Q}$ and constrained complexity with possible interactions among reformers. Biogas is the only carbon source, and surplus bio-CH ₄ is optionally burned to recover clean energy. Electricity is generated in a gas-fired power-plant of 60% efficiency in a worst-case scenario of unavailable renewable power. In green, net CO ₂ generation when the net energy requirement is negative.	82

4.12	Contributions to the total power requirements for $\min_{\dot{N},y} (\dot{Q} + \dot{W})$, biogas as feedstock. The solution is constrained to a single reformer, optionally with EL. In green, the reference solution for constrained plant complexity (c.c.), where more reformers (m.r., indicated in the green boxes) can be selected and interact, also reported in Table 4.7, and in Figure 4.7.	85
4.13	Energy demand if exclusively CO ₂ from DAC is fed to the plant for $\min_{\dot{N},y} (\dot{Q} + \dot{W})$. A maximum of 5 units is allowed by complexity constraint Equation 4.29. The contributions in this figure do not include DAC energy requirements.	87
4.14	Total thermal requirements. Comparison of the interaction between reformers at the minimum total energy, with biogas as feedstock to multiple reformers without redundant separators (in green, extracted from the results in Table 4.7) and with direct air-captured CO ₂ to the combination of EL and RWGS (in blue, from Table 4.10(A)). The latter accounts also for the thermal input requirement at DAC, which is a conservative assumption: the selected DAC technology requires a considerable amount of thermal energy, while many DAC systems proposed on the market can be fully electrified or thermally integrated within the system with waste heat at low temperatures.	88
4.15	Oxygen can be supplied to the oxy-combustion chamber of the RWGS reactor, where heat is supplied to allow the endothermic reaction to take place (in purple). The remaining O ₂ , while valuable, has no use in the system (in blue).	90
5.1	Plant layout: the RWGS and TRI reactors produce raw syngas, where H ₂ and O ₂ are supplied <i>via</i> electrolysis, e.g., an efficient SOEC. H ₂ may be fed to RWGS and/or bypass the reactor to the syngas product stream whereas excess O ₂ may be stored in a buffering device. CO ₂ could be obtained from biogas using a suitable separation strategy.	95
5.2	Plant operation when electricity is scarce and RWGS is supplied with H ₂ from EL. Methane from biogas can provide heat to the RWGS reaction.	96
5.3	Plant operation when electricity is scarce and Tri-reforming is combined with stored O ₂	97
5.4	Plant operation with low electricity input. TRI is sustained <i>via</i> injection of O ₂ from the buffering device.	98
5.5	Temporal trend of the electricity supply and molar feed flowrate to SOEC.	99
5.6	Setpoint attainment with parareal: (A) syngas ratio; (B) flowrate of CO in the syngas stream.	110
5.7	(A) Power demand at SOEC (\dot{W}_{SOEC}), for the compression to the Fischer-Tropsch reactor requirements ($\dot{W}_{\text{FTS,compr}}$) and to buffer O ₂ at 300 bar in gaseous form ($\dot{W}_{\text{O}_2,\text{buff}}$); (B) total feed flowrate to RWGS and TRI, flowrate for the integration of H ₂ directly to the syngas stream ($\dot{N}_{\text{H}_2,\text{int}}$), accumulation rate of O ₂ in the buffering device ($\dot{N}_{\text{O}_2,\text{buff}}$).	111
5.8	Molar flowrates at the outlet of RWGS (A) and TRI (B) and in the syngas stream (C) over the time domain at the optimum.	112
6.1	Buffering strategies for a generic Power-to-X (P2X) process determine the extent of process flexibility involved. Electricity and hydrogen buffering strategies are denoted with B.I and B.II, respectively (plant design and operations at a single, nominal load). In contrast, the whole process can be operated flexibly (strategy F).	116

6.2	(A) Large buffering devices determine a single operation mode at the mean generated power (buffering scenario B); (B) opening flexibility window with moderate buffering (transition from buffering scenario B towards the flexible case F). Generated renewable power in blue is retrieved from actual performance measurements of a wind turbine, where slightly declines before the cut off velocity is attained (cf. Table D.1).	117
6.3	Window for maximum plant flexibility. The renewable power generated at low wind velocities does not guarantee feasible plant operations, which are ensured via integration of external grid electricity.	118
6.4	Overall plant layout for the generation of a binary mixture of methanol and water. The final distillation section is not highlighted, as it operates independently of the unsteady power supply.	122
6.5	Renewable power generated by the wind park in function of the wind velocity and probability density function. Periods are denoted by Π , and their probability of occurrence is given as a percentage value. Horizontal segments represent the mean power supply within a period. The integration of power from the grid required to ensure feasible operations for period Π_1 is indicated by the red segment. The dashed-dotted orange horizontal line represents the mean annual power generated (23.5 MW).	125
6.6	(A) Cumulative definition of the polarization curves for the given cell parameters at 1023 K, as reported in D.3.1, from the ideal voltage (in the lightest blue) to the total voltage (in the darkest blue); (B) definition of the outlet temperature for a feed temperature of 1023 K, fixed cell parameters (Supplementary Section D.3), an area of 1 m^2 and a feed flowrate of $5.5 \text{ mol}_{\text{H}_2\text{O}} \text{ s}^{-1}$, where the blue curve corresponds to endothermic operations, the dark red to exothermic operations.	129
6.7	Optimal P2Methanol plant topology shared by the four optimization cases. RWGS plays a negligible role, and thus can be bypassed by the process flows. The recycle loop of METHL is closed.	137
6.8	Relevant profiles along the axial coordinate of METHL reactor for different periods for increasing loads, e.g., from Π_1 to Π_5 : temperature and molar fraction profiles, (A) and (B), pressure and velocity profiles, (C) and (D). Figure (A) reports the cooling temperature level in red, constant along the axis (boiling water).	138
6.9	Relevant profiles along the axial coordinate of METHL reactor for different periods for increasing loads, e.g., from Π_1 to Π_5 : darkening colors indicate increasing loads.	138
6.10	This graph represents the current density and voltage resulting from NLP.FLEX. The points are labeled with the period identifier $\Pi_{i \in \{1, \text{NP}\}}$, the feed temperature and the operating pressure. The temperature drop is always equal to 30 K.	139
6.11	Distribution of the power supplied within the plant, where the darker the blue, the larger the total power load to the plant, as illustrated by the arrow.	140
6.12	(A) Revenues from the sale of methanol at 580 € ton^{-1} . The results for the period and annual average values are shown as bars and dashed horizontal line, respectively; (B) annualized and actualized costs of the optimized unit operations (green bars), annual cost of external power supply to ensure stable plant operations over the period Π_1 for different scenarios of electricity prices: a (20 €MWh), b (200 €MWh), c (90 €MWh).	141

6.13	Investment cost for buffering devices, calculated assuming the time (abscissa) spent by the wind park at 50 MW, 27 MW higher than the power absorbed by the methanol plant.	143
6.14	Profit* versus loading time for the three buffering scenarios. The asterisk indicates that these values are built upon the optimized units (SOEC, RWGS, METHL), whereas all other process elements preserve their sizes and costs in the different cases. Profits for lithium batteries and hydrogen storage are inversely proportional to the size of the buffers. The profitability of the flexible setup F is highly dependent on the price of external electricity.	145
6.15	(A) Period-related Power-to-Methanol efficiency in light and dark green with and without heat integration (HI), respectively. Dashed lines depict the annual mean values of efficiency; (B) comparison between pseudo-profits with and without heat integration, not accounting for the cost of the external electricity supply at Π_1	146
6.16	Qualitative trend of process costs as a function of process flexibility for a generic Power-to-X system: flexible regime (F), Li-ion batteries and hydrogen buffering (B.I, B.II), semi-flexible plant (SF). The red line identifies costs in a regime of energy autarchy, where the renewable power is entirely produced and consumed within the chemical plant. Further to the right, the plant requires an external power input, as renewable power is not sufficient to support feasible operations. The costs of buffering devices are reported in blue.	148
A.1	Complete results: minimization of CEabs, including the recycle of bio-CO ₂ from the hot utility exhaust gases.	156
B.1	Compact representation of the interconnection between consecutive mixture blocks. In blue, the separator which delivers ACF to block ϕ_2 and D to block ϕ_3	158
B.2	(A) separator D/ACF is replicated in the downstreams of reactor R1 and R2, not interconnected by any material stream; (B) if both separators are selected simultaneously by the optimizer, the resulting energy demand is obtained from the linear combination of single contributions, and the system is equivalent to a lumped representation.	159
B.3	Representation of the substance-node balance associated to component $i = \text{CO}_2$ fed to the overall plant superstructure. Stream $\dot{N}_{i=\text{CO}_2,\text{ext}}$ is split into streams $\dot{N}_{i=\text{CO}_2,j=\{\text{RWGS,TRI},(\cdot)\}}^{\text{makeup}}$, each contributing to the feed to reactor j : $\dot{N}_{i=\text{CO}_2,j}^{\text{feed}}$. Recycle component-streams $\dot{N}_{i,j,k}^{\text{recycle}}$ from the final separators along separation superstructure networks (here S1, S2 and S3) are also fed to these feed nodes.	161
B.4	Representation of the outlet node balance for a generic component $i \neq \text{CO}$ and of the syngas nodes, for H ₂ and CO. Streams of pure i provided by different units in the superstructure are collected into the outlet stream $\dot{N}_{i,\text{out}}$. Similarly, H ₂ and CO streams from the superstructure to syngas are collected into $\dot{N}_{\text{H}_2,\text{syngas}}$ and $\dot{N}_{\text{CO},\text{syngas}}$, respectively. References are found in Equations B.7, B.8 and B.9. The syngas ratio is constrained via Equation B.10.	162
C.1	TRI temperature (A), composition (B), pressure (C), and velocity profile (D) at steady-state and nominal flowrate.	168
C.2	RWGS bulk and shell temperature (A), composition (B), pressure (C) and velocity profile (D) at steady-state nominal flowrate.	168

List of Tables

2.1	Syngas downstream applications, molar ratios, temperature and pressure requirements [21].	8
4.1	Syngas downstream applications, molar ratios, temperature and pressure requirements. Data are retrieved and adapted from Table 2.1.	54
4.2	Parameters for the description of reactors. θ represents the ratio between extent of reaction and feed flowrate. Specific heat demand (\bar{q}) and electrical energy demands (\bar{w}) per mole-flowrate of feed are included.	60
4.3	The separation tasks are here sorted by the number of components in the feed, N_{spec} , and reactor type. Reactors DR, SR, TRI, POX share the same separation tasks. A single asterisk * indicates the separation tasks whose methods are shared between DR, SR, TRI, POX. Double asterisk those shared between RWGS and the other reformers **. The task of separating biogas into CH_4 and CO_2 and possibly adopted in the downstream of the reformers DR, SR, TRI, POX, is indicated by a triple asterisk ***. Details on the separation methods available are collected in Table 4.5.	62
4.4	Separation methods and identifiers adopted in Table 4.5. Deviations from the reported values for (T (K), p (bar)) are possibly implemented in the constraints, e.g. membranes for H_2 separation adjacent to the reactor are operated at temperatures higher than 298 K (Pd membrane, polymeric membrane).	65
4.5	Numbered list of splits allowed in the superstructure and available separation methods. (*) MEDAL™ Air Liquide - hydrogen purification; (**) MEDAL™ Air Liquide - biogas purification.	66
4.6	Topological results for unconstrained plant complexity, where multiple reformers can be selected simultaneously and interact with each other. The number of redundant units is derived according to the criteria presented in Section 4.6.	73
4.7	Plant topology and power consumption when more reactor can be simultaneously selected but redundancies in the separation systems are removed. The total number of units allowed is iteratively constrained to a maximum N_{max} , until the first configuration without redundant units is identified. The percent value of thermal energy (T%), electrical energy (E%) and the total energy in $\text{kJ mol}_{\text{syngas}}^{-1}$ (tot.) are reported. Biogas is the only feedstock.	75
4.8	Plant topology and power consumption when more reactor can be simultaneously selected but the number of units allowed is iteratively constrained to a maximum N_{max} , until the first configuration without redundant units is identified. The percent value of thermal energy (T%), electrical energy (E%) and the total energy in $\text{kJ mol}_{\text{syngas}}^{-1}$ (tot.) are reported. Biogas is the only feedstock.	79

4.9	Plant topology and power consumption for the minimization of the total power demand (Problem A), biogas as feedstock. When not indicated, biogas is fed without upgrading to the reactor. In this case, only one reformer can be selected, possibly in conjunction with EL. Maximum number of units: 6.	84
4.10	Plant topology and power consumption, divided into thermal percentage (T%), electrical percentage (E%) and total power for the syngas plant (tot.). Additionally, consumptions for direct air-capture (DAC) are reported.	86
5.1	List of relevant optimization variables for design problems, bounds, and results for TRI.	103
5.2	List of design parameters and nominal operating conditions for RWGS.	104
6.1	List of relevant decision variables for design problems and related bounds. Variables shared among periods are denoted with superscript (π).	126
6.2	Summary of the case-studies.	132
6.3	Overview of the treated multi-period design optimization problems: number of variables, constraints and resulting degrees of freedom.	136
C.1	Plant topology and power consumption for combined tri-reforming, reverse water-gas shift reactor and water electrolysis.	163
C.2	Plant topology and power consumption for combined tri-reforming, reverse water-gas shift reactor and water electrolysis.	164
C.3	List of parameters for TRI kinetics: pre-exponential and activation energies.	165
D.1	Data are retrieved from the technical sheet of a wind turbine (2.1 MW S95 Sulzon). .	169
D.2	Average monthly wind velocities in Magdeburg, Germany.	169
D.3	List of parameters for RWGS kinetics.	177
D.4	Optimization results for the case-studies listed in Table 6.2. Reactor volumes, reported in brackets, are calculated from the results, i.e., they do not constitute decision variables. The table continues under the thicker dividing-line, where $\dot{N}_{\text{tot},(1,5,6)}$ represent, respectively, the feed stream of water, carbon dioxide to RWGS, carbon dioxide to the methanol loop.	184
D.5	Optimization results. $\dot{C}_{22,\text{CH}_3\text{OH}}$ annual revenue from selling methanol at 580 € ton ⁻¹ , prevailing price for the first quarter of 2022 in Germany [212]. Cost $\dot{C}_{\text{Plant}}^{\Delta}$ incorporates the process units subject to optimization (SOEC, RWGS, METHL). All costs are annualized, i.e., the absolute cost divided the expected number of years of operations.	185

Colophon

This thesis was typeset with $\text{\LaTeX}2_{\epsilon}$. It uses the *Clean Thesis* style developed by Ricardo Langner. The design of the *Clean Thesis* style is inspired by user guide documents from Apple Inc.

Download the *Clean Thesis* style at <http://cleanthesis.der-ric.de/>.

Publications and statements of authorship

List of scientific contributions

During the doctoral studies, a number of scientific articles were published in peer-reviewed journals. For the preparation of this dissertation, some of the published material was adapted or expanded. The numbered list of peer-reviewed publications and conference contributions is included below.

- The multi-objective optimization approach proposed in Chapter 3 is partly retrieved from (1.). However, methods and results have been significantly extended.
- Methods and results adopted in Chapter 4 on the extended process synthesis framework are retrieved from (2.). All plots have been regenerated and the result section expanded with additional analyses, which now incorporates yield and atom efficiency of different configurations and energy requirement of single-reactor optimal layouts compared with results allowing for multiple reformers. Furthermore, in the sake of clarity, the methodological background has been significantly extended.
- Methods and results reported in Chapter 5 on synthesis and control of a flexible Power-to-Syngas plant for Fischer-Tropsch synthesis applications are retrieved from (4.). Nonetheless, the contextualization of this chapter has been enriched to highlight its logical connection within the dissertation. In particular, the complete biogas-to-syngas reactor-separation sequence for Fischer-Tropsch applications has been derived by setting the modeling tool developed for in Chapter 4 to select a RWGS reactor in combination with the Tri-reforming reactor simultaneously. Furthermore, the application of `pararea1` in optimal control reported in Section 5.7 is resized and adapted to the scope of this work (Section 5.7). It is hereby to a acknowledge that Dr. Dominik Garmatter (formerly at TU Chemnitz) developed the `pararea1` calculation framework and ran the related optimization on a multicore machine.
- Methods and results from Chapter 6 on the multi-period design optimization of a flexible methanol plant are retrieved from a peer-reviewed contribution published in Chemical Engineering Science (5.). The contextualization concerning process flexibility is adapted to the scope of the dissertation.

Peer-reviewed publications

1. Andrea Maggi[†], Marcus Wenzel, and Kai Sundmacher. “Power-to-Syngas Processes by Reactor-Separator Superstructure Optimization”. In: *Computer Aided Chemical Engineering*. Elsevier, 48 (2020), pp. 1387–1392.
2. Andrea Maggi[†], Marcus Wenzel, and Kai Sundmacher. “Mixed-integer linear programming (MILP) approach for the synthesis of efficient power-to-syngas processes”. In: *Frontiers in Energy Research*. 8 (2020), p. 161.
3. Dominik Garmatter[†], Andrea Maggi[†], Marcus Wenzel, Shaimaa Monem, Mirko Hahn, Martin Stoll, Sebastian Sager, Peter Benner, and Kai Sundmacher. “Power-to-chemicals: a superstructure problem for sustainable syngas production”. In: *Mathematical Modeling, Simulation and Optimization for Power Engineering and Management*. Springer, 2021, pp. 145–168.
4. Andrea Maggi[†], Dominik Garmatter[†], Sebastian Sager, Martin Stoll, and Kai Sundmacher. “Power-to-Syngas: A Parareal Optimal Control Approach”. In: *Frontiers in Energy Research*. 9 (2021), Article 720489.
5. Andrea Maggi[†], Jens Bremer, and Kai Sundmacher. “Multi-period optimization for the design and operation of a flexible power-to-methanol process”. In: *Chemical Engineering Science*. 281 (2023), Article 119202.

[†]First author; co-first authors.

Conference contributions

6. Andrea Maggi[†], Marcus Wenzel, and Kai Sundmacher. "Power-to-Syngas Processes by Reactor-Separator Superstructure Optimization". Poster presented at the 12th European Congress of Chemical Engineering (ECCE 12). Florence, Italy, 2019.
7. Andrea Maggi[†], Marcus Wenzel, and Kai Sundmacher. "Power-to-Syngas Processes by Reactor-Separator Optimization". Talk presented at the European Symposium on Computer Aided Process Engineering (ESCAPE 30). Milan, Italy, 2020.
8. Andrea Maggi[†], Jens Bremer, and Kai Sundmacher. "Multiperiod Design Optimization of a Flexible Power-to-Methanol Process". Talk presented at the 26th International Congress of Chemical and Process Engineering (CHISA). Prague, Czech Republic, 2022.
9. Andrea Maggi[†], Jens Bremer, and Kai Sundmacher. "Multiperiod Design Optimization of a Flexible Power-to-Methanol Process". Talk presented at the Annual Meeting of the American Institute of Chemical Engineers (AIChE). Phoenix, United States of America, 2022.

Declaration of honor

I hereby declare that I produced this thesis without prohibited external assistance and that none other than the listed references and tools have been used. In the case of co-authorship, especially in the context of a cumulative dissertation, the own contribution is correctly and completely stated. I did not make use of any commercial consultant concerning graduation. A third party did not receive any nonmonetary perquisites neither directly nor indirectly for activities which are connected with the contents of the presented thesis. All sources of information are clearly marked, including my own publications.

In particular I have not consciously:

- Fabricated data or rejected undesired results,
- Misused statistical methods with the aim of drawing other conclusions than those warranted by the available data,
- Plagiarized data or publications,
- Presented the results of other researchers in a distorted way.

I do know that violations of copyright may lead to injunction and damage claims of the author and also to prosecution by the law enforcement authorities.

I hereby agree that the thesis may need to be reviewed with an electronic data processing for plagiarism.

This work has not yet been submitted as a doctoral thesis in the same or a similar form in Germany or in any other country. It has not yet been published as a whole.